Synthesis and Gas-Expanded Liquid (GXL) Processing of Metal and Metal Oxide Nanoparticles: Fundamentals and Application

by

Pranav Shekhar Vengsarkar

A dissertation submitted to the Graduate Faculty of
Auburn University
in partial fulfillment of the
requirements for the Degree of
Doctor of Philosophy

Auburn, Alabama
August 1, 2015

Keywords: nanoparticles, gas-expanded liquids, iron oxide, catalysis, emulsions, fundamentals

Approved by
Christopher Roberts, Dean, College of Engineering
Mario Eden, Department Chair, Chemical Engineering
Robert Ashurst, Associate Department Chair, Chemical Engineering
Jeffrey Fergus, Associate Dean, College of Engineering

Abstract

This dissertation involves a detailed discussion into the design of metal and metal oxide nanoparticles along with associated gas-expanded liquid (GXL) processing technologies for use in various industrially relevant applications. Nanoparticles have unique size-dependent physicochemical properties which need to be harnessed for their efficient use in the aforementioned applications. These size-dependent properties necessitate the presence of monodisperse nanoparticles in any nanoparticle-based system being investigated. The typical way to obtain monodisperse nanoparticles is through the use of specialized synthesis methods or through the post-synthesis processing of polydisperse nanoparticles. However, the methods to synthesize monodisperse nanoparticles are usually tedious and expensive, while the processing methods are often solvent intensive and lack large throughputs. To overcome these issues, our lab previously designed a process to effectively fractionate metal nanoparticles based upon their size using gas-expanded liquids. GXLs are tunable solvents whose properties can be manipulated by varying applied gas pressure. While the GXL nanoparticle fractionation process can successfully separate metal nanoparticles based upon their size, it still suffers from a few drawbacks such as requiring relatively high CO_2 operating pressures and an inability to separate large quantities of nanoparticles in a scalable manner. The studies described in this dissertation aim to eliminate these drawbacks in the GXL nanoparticle processing system through the use of various nanoparticle systems and through the design of a completely new fractionation apparatus which is scalable in nature. The GXL system

is also then extended to metal oxide nanoparticles and their use in industrially relevant applications such as catalysis and environmental remediation.

To eliminate the drawback of high operating pressures required in the GXL fractionation process, this dissertation contains a study which shows that the use nanoparticle systems with sterically hindered solvent/ligand combinations can reduce operating pressures significantly. Through the investigation of gold nanoparticles coated with dodecanethiol and its tertiary isomer along with various isomers of hexane, it was shown that the system using gold nanoparticles coated with *tert*-dodecanethiol dispersed in 2,2-dimethylbutane (the most sterically hindered isomer of hexane) resulted in six-fold reduction in operating pressures (41.4 bar to 6.9 bar). Furthermore, the fractionation of iron oxide nanoparticles coated with oleic acid was also successfully attempted in the cascaded-vessel apparatus, thus proving that the GXL process can be extended to metal oxide nanoparticles. The GXL fractionation system was then modified using a Parr reactor to enable the fractionation of large quantities of metal and metal oxide nanoparticles. Oleic acid-coated iron oxide nanoparticles, synthesized using the coprecipitation method, were successfully fractionated into various distinct size-fractions using this scalable apparatus. The design of this apparatus enables the fractionation and processing of large quantities of nanoparticles, thereby allowing application-based studies on the size effects of nanoparticle systems.

These fundamental studies into the synthesis and processing of metal and metal oxide nanoparticles pave the path forward towards the use of the GXL system in various relevant applications. In this dissertation the possible use of the GXL system in the fields of environmental remediation and catalysis is investigated. While an attempt to use GXL

system to study the size effect of iron oxide nanoparticles in the formation of oil-in-water (O/W) emulsions for oil spill remediation was unsuccessful due to the inherent nature of hydrophobic nanoparticles required for the GXL fractionation process, a system to effectively stabilize O/W emulsions using stearoyl lactylate (SL) bilayer coated iron oxide nanoparticles was developed using a coprecipitation-based synthesis technique. The Parr-reactor apparatus was also used to deposit iron oxide nanoparticles onto various support materials in a GXL to generate supported iron catalysts for Fischer Tropsch Synthesis (FTS). The catalysts generated using this method were then used along with catalysts synthesized using traditional techniques in a FTS system to study their effectiveness. It was observed that the catalysts generated using the GXL method gave stable performance and higher conversion than their traditional counterparts in the FTS system. Analysis of the GXL catalyst using various characterization techniques indicated lower support-metal interactions as the cause of this higher activity.

Hence, as a whole, the research presented in this dissertation improves and increases the versatility the GXL nanoparticle fractionation process. It has demonstrated that the initial fundamental studies into the GXL fractionation process resulted into significant improvements in the process, which was in turn used to generate nanomaterials for fields such as catalysis. Eventually, the GXL nanoparticle processing technique which provides several advantages over conventional solvent techniques can be used in the generation of advanced nanoparticle systems and nanomaterials.

Acknowledgements

First and foremost, I would like to thank my advisor Dr. Christopher B. Roberts for providing me with the opportunity to join his research group at Auburn University and for his continued support and guidance. I would especially like to thank him for giving me the independence to pursue my research goals in a way I saw fit, while at the same time ensuring I had the end result in sight. His priceless advice and guidance regarding all work and non-work related issues has resulted into me learning several life lessons which no-doubt would be useful to me in future. His work-ethic has always been an inspiration to me and the fact that he thinks and cares about his students like family has always been my motivation for working hard. I sincerely appreciate the time he takes out of extremely busy schedule to help his students out and I cannot say how proud I am to have been a part of his research group.

I would like to thank my committee members Dr. Jeffrey Fergus, Dr. Mario Eden, and Dr. Robert Ashurst for their guidance and help throughout my Ph.D. and in making this dissertation a worthy document. I would also like to thank Dr. Xinyu Zhang for undertaking the role as the outside reader for my dissertation. I would also like to thank Dr. Michael Miller for help with the transmission electron microscope and Dr. Alan David for help with particle analysis. This dissertation would not have been possible without the hard work and assistance of Dr. Rui Xu whose expertise in Fischer-Tropsch synthesis and catalyst characterization was invaluable. I would like to thank Brian

Schwieker for his excellent assistance in the development and maintenance of the reactor system and Steven Moore for his help with particle characterization. I would also like to thank Karen Cochran, Elaine Jimmerson and Georgetta Dennis for their help in various matters over the years.

I would like to thank current and past members of the Roberts Research Group including, but not limited to, Steven Saunders, Rui Xu, Helena (Sihe) Zhang, Jie Zhong, Jennifer Duggan, Charlotte Stewart and David Roe. I would like to especially thank Jennifer for being an awesome friend, for helping me out countless times, and for always being there for me. Her honesty and work-ethic have always been an inspiration to me. Also, I am grateful to Charlotte and David for being awesome office mates/friends and for entertaining my questions about Fischer-Tropsch synthesis. Thank you all members of the Wilmore 200 office for making sure that the last four years were some of the best in my life. I also like to appreciate the friendship of and express my gratitude to my fellow graduate students, including but not limited to Hema Ramsurn, Courtney Ober, Matt Kayatin, Shaima Nahreen, Achin Sujan, Shantanu Pradhan, Vikrant Dev, Jessica Larsen, Alex Kelly, Alan Hanley, Liana Wuchte, Kyle Stone, Steven Montgomery, Zan Haywood, Brianna Smith and Will Hand. There were countless others who made my time at Auburn memorable and I would like to thank them again for their friendship.

Most importantly, I would like to thank my parents, Aparna Vengsarkar and Shekhar Vengsarkar for being a beacon of support and for always being there for me. Their encouragement has been very helpful during my time at Auburn. The values they have imparted in me throughout my life have made me who I am today and I will be eternally grateful.

Table of Contents

List of Figures

List of tables

List of Abbreviations

AOT	Aerosol OT (or dioctyl sodium sulfosuccinate)
A_x	Hamaker constant of 'x'
ASF	Anderson-Schulz-Flory (plots)
BET	Brunauer–Emmett–Teller (surface are analysis)
CMC	carboxymethyl cellulose
DELOS	Depressurization of an Expanded Liquid Organic Solution
DIUF	deionized ultra-filtered
DLS	Dynamic Light Scattering
FDA	Food and Drug Administration
$Fe(acac)_3$	Tris(acetylacetonato) iron(III)
FeNP	iron oxide nanoparticle
FTIR	Fourier Transform Infrared spectroscopy
FT	Fischer-Tropsch
FTS	Fischer-Tropsch Synthesis
FID	flame ionization detector
GAS	Gas Anti-Solvent
GHSV	gas hourly space velocity
GXL	Gas-eXpanded Liquid
HPLC	High-Pressure liquid chromatography
HR-TEM	high-resolution transmission electron microscopy

ICP	inductively coupled plasma emission spectroscopy
LSAS	Liquid Solvent-Antisolvent
MFFF	magnetic field flow fractionation
MRI	magnetic resonance imaging
O/W	oil-in-water
SANS	small angle neutron scattering
SPR	surface plasmon resonance
PR-EOS	Peng-Robinson Equation of State
PDI	polydispersity index
P_i	pressure of incipient precipitation
SSL	sodium stearoyl lactylate
SL	stearoyl lactylate
$scCO_2$	supercritical CO_2
TOABr	tetraoctylammonium bromide
TOF	turn over frequency
TCD	thermal conductivity detector
TEM	Transmission Electron Microscopy
TGA	thermogravimetric analysis
TMAOH	Tetramethylammonium hydroxide
UV-Vis	UV-Visible
VLE	vapor-liquid equilibrium
VOC	volatile organic compounds
V_{vdW}	van der Waals interaction free energy
W/O	water-in-oil
XRD	X-ray diffractometer

Chapter 1

Introduction

1.1 Introduction to Nanotechnology

Nano, derived from the Greek word for *dwarf*, when combined with *technology* gives rise to the word *nanotechnology* which signifies operations occurring on the scale of 10^{-9} meters (Selin, 2007). The term nanotechnology is employed to describe the creation and exploitation of materials with structural features in between those of atoms and bulk materials, with at least one dimension in the nanometer range (1 nm = 10^{-9} m) (C. Rao, Müller, & Cheetham, 2006). It also involves the study of two and three dimensional assemblies of molecular scale building blocks into well-defined nanostructures or nanomaterials (Ju-Nam & Lead, 2008). Nanotechnology is an important topic in modern research due to its multidisciplinary applicability and future potential in many applications such as environmental remediation, catalysis and biomedicine.

Even though nanotechnology has only recently attracted a lot of media attention, people have known about nanoparticles and used the properties of nanomaterials for many centuries. The oldest known item is the Lycurgus chalice from 5th century Rome, which contains gold nanoparticles (Freestone, Meeks, Sax, & Higgitt, 2007). Johann Kunckel (1638- ?) is credited by many for developing the first systematic procedures for

incorporating gold into molten silica to make ruby glass, which is similar to the glass used in the Lycurgus chalice (Fedlheim & Foss, 2001). There are also many examples of nanomaterials such as halloysite nanotubes (Du, Guo, & Jia, 2010) and organic nanoparticles (Xia, Lenaghan, Zhang, Zhang, & Li, 2010) which occur naturally in the environment. The research in the field of nanotechnology picked up pace again in the mid to late 1900's when researchers like Richard Feynman, Heinrich Rohrer, Sir Harold Kroto and George Whitesides amongst others developed and implemented ideas to manipulate individual atoms to generate atomic assemblies (ex. fullerenes) with unique properties. This surging interest in nanoscale materials has continued into current times, where nanotechnology is one of the most popular fields in academic and industrial research across the globe. The impact of nanotechnology can be felt in all aspects of current life since many common household items such as paints, cosmetics and pharmaceuticals (Tegart, 2004) contain nanomaterials in one form or the other. The support of the federal government and the increasing collaboration between universities and nanotechnology companies had caused a tremendous increase in nanotechnology-based firms (in the US) in the early 2000's as can be seen in Figure 1.1 (J. Wang & Shapira, 2009). The field of nanotechnology has shown tremendous growth in modern times as can be seen from the fact that the federal funding for nanotechnology R&D has increased from $116 million in 1997 to an estimated $1.8 billion in 2013. The cumulative NNI (National Nanotechnology Initiative) investment since fiscal year 2001, including the 2014 request, now totals almost $20 billion while investments in nanotechnology-related environmental, health, and safety research since 2006 now total nearly $750 million.(http://www.nano.gov/about-nni/what/funding, n.d.)

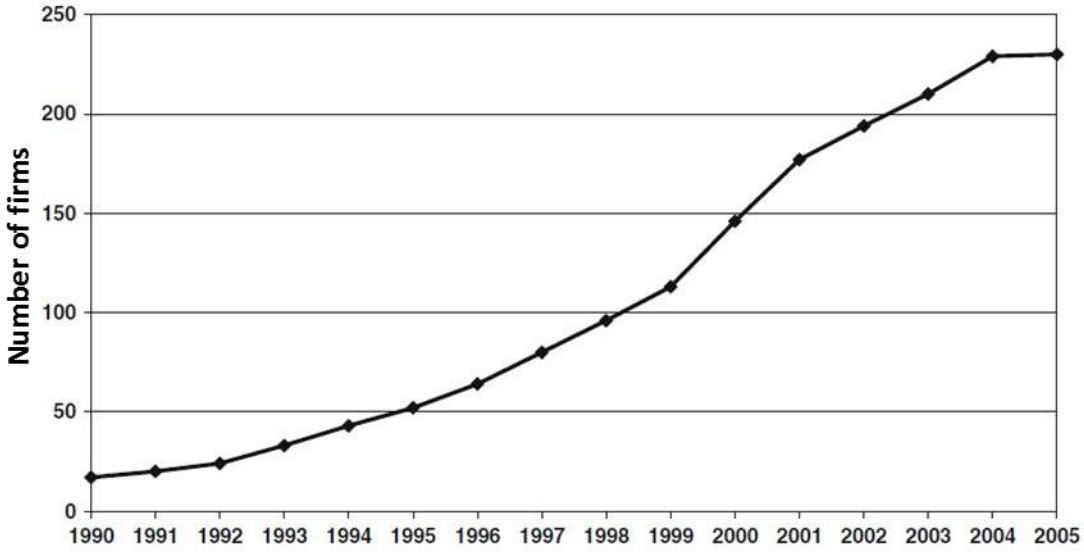

Figure 1.1 Number of new nanotechnology-based firms, USA, classified by year of founding, 1990-2005 (J. Wang & Shapira, 2009)

Nanotechnology as a science encompasses a variety of fields and the chart showing the distribution of the main research fields of nanotechnology is shown in Figure 1.2 (Coccia, Finardi, & Margon, 2011). Nanoparticles of metals (e.g. gold) and metal oxides (e.g. iron oxide) are major areas of research in these fields of study due to their breadth of application in disciplines such as biomedicine (Pankhurst, Connolly, Jones, & Dobson, 2003; Tartaj, Morales, Veintemillas-Verdaguer, Gonz lez-Carre o, & Serna, 2003), surface technology (K. M. Hurst, Roberts, & Ashurst, 2011) and catalysis (Daniel & Astruc, 2004; Haruta & Daté, 2001). For example, gold nanoparticles can be useful as drug delivery agents and in hydrogenation/redox catalysis (Daniel & Astruc, 2004) while iron oxide nanoparticles have been used in various applications like Fischer-Tropsch catalysis (Mahajan, Gütlich, & Ensling, 2003) and as contrast agents for MRI (Teja & Koh, 2009). Nanoparticles have also been used in various other applications like in the formation of particle stabilized emulsions (Pickering emulsions) (Melle, Lask, & Fuller, 2005) and magnetoliposomes (Gonzales & Krishnan, 2005) which are useful in environmental and biomedical applications. Materials with dimensions at these length scales exhibit very unique electrical, optical, magnetic, mechanical and catalytic properties which deviate from the properties of their bulk constituent material. (Poole Jr. & Owens, 2003) This nonconformity between the macroscopic properties and nanoscale properties is due to quantum effects that dominate over other effects at these small dimensions (El-Sayed, 2004) as well as the high surface area to volume ratio that is present at this scale. Detailed information about the unique size-dependent properties of nanoparticles, synthesis procedures for nanoparticles, post-processing methods and nanoparticle applications is provided in the oncoming sections.

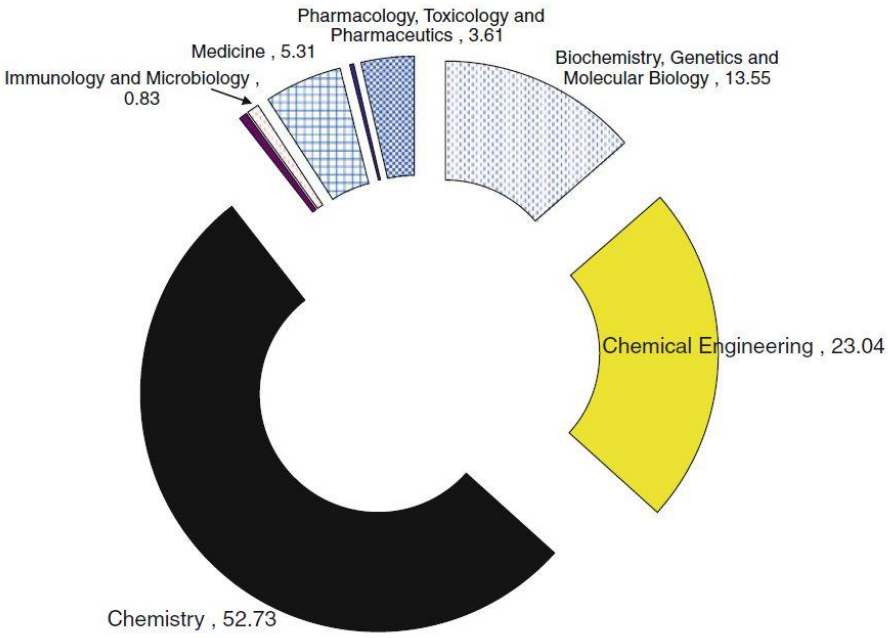

Figure 1.2 Percent value of the main research fields of nanotechnology (Coccia et al., 2011)

1.1.1 Unique Size-Dependent Properties of Nanoparticles

The physical and chemical properties of a material are determined by the type of motion allowed for its electrons to execute. (El-Sayed, 2004) For small particles, the electronic energy levels are not continuous as in bulk materials, but discrete, because of the confinement of the electron wavefunction caused by the physical dimensions of the particles. In Figure 1.3, one can observe how the electronic structures of metal and semiconductor nanocrystals contrast from those of bulk materials and isolated atoms. (C. N. R. Rao, Kulkarni, Thomas, & Edwards, 2002) These discrete electron energy levels are one of the main reasons behind the uniqueness in thermo-physical properties observed in nanoparticles. For example, surface plasmon resonance (oscillation of conduction electrons) which is observed for some metal (gold, platinum, etc.) nanoparticles can be explained by the fact that when a small spherical metallic nanoparticle is irradiated by light, the oscillating electric field causes the conduction electrons to oscillate coherently. The oscillation frequency is usually in the visible region for gold and silver, giving rise to the strong surface plasmon resonance absorption. (Eustis & el-Sayed, 2006; Kelly & Coronado, 2003) The red color of gold nanoparticle solutions also arises because of this phenomenon. This surface plasmon resonance absorption, shown by some nanoparticles, is a very convenient phenomenon which can be used to characterize nanoparticles using simple techniques like UV-Vis spectroscopy. The most visual of the size-dependent effects, is the change in optical properties of semiconductor nanoparticles (e.g. quantum dots) shown in Figure 1.4. These quantum dots are useful in various electronic applications like sensors and LEDs (Light-Emitting Diodes). The domination of these

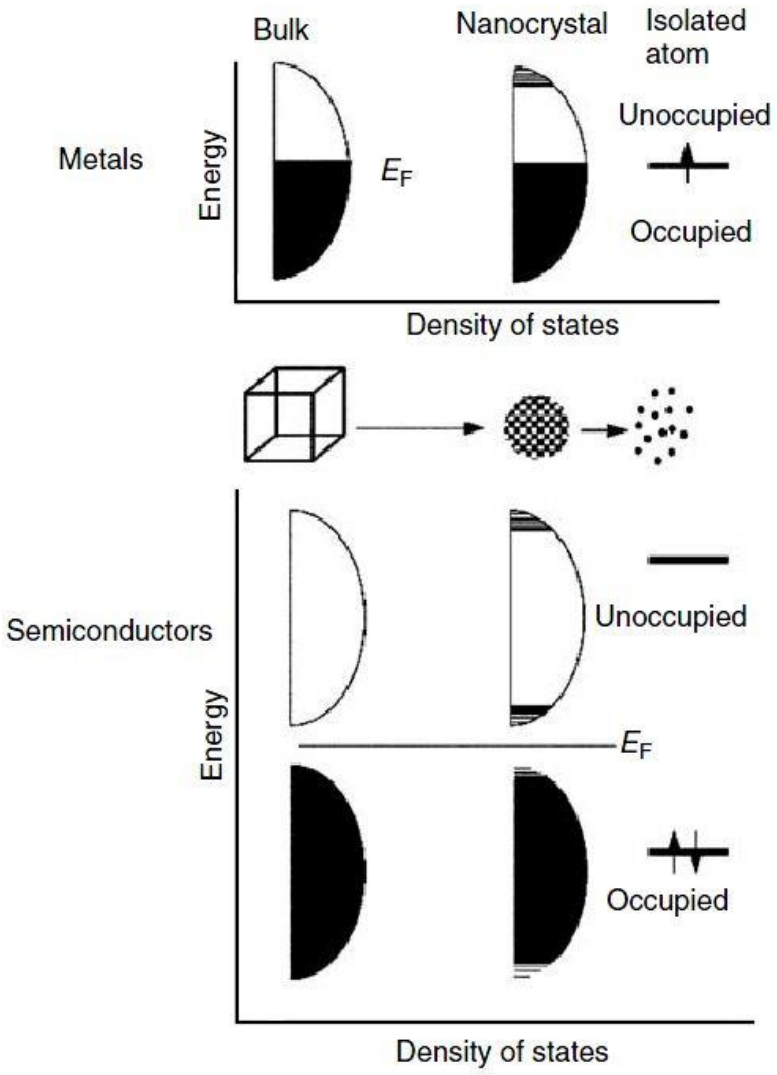

Figure 1.3 Density of states for metal and semiconductor nanocrystals compared to those of the bulk and of isolated atoms (C. N. R. Rao et al., 2002)

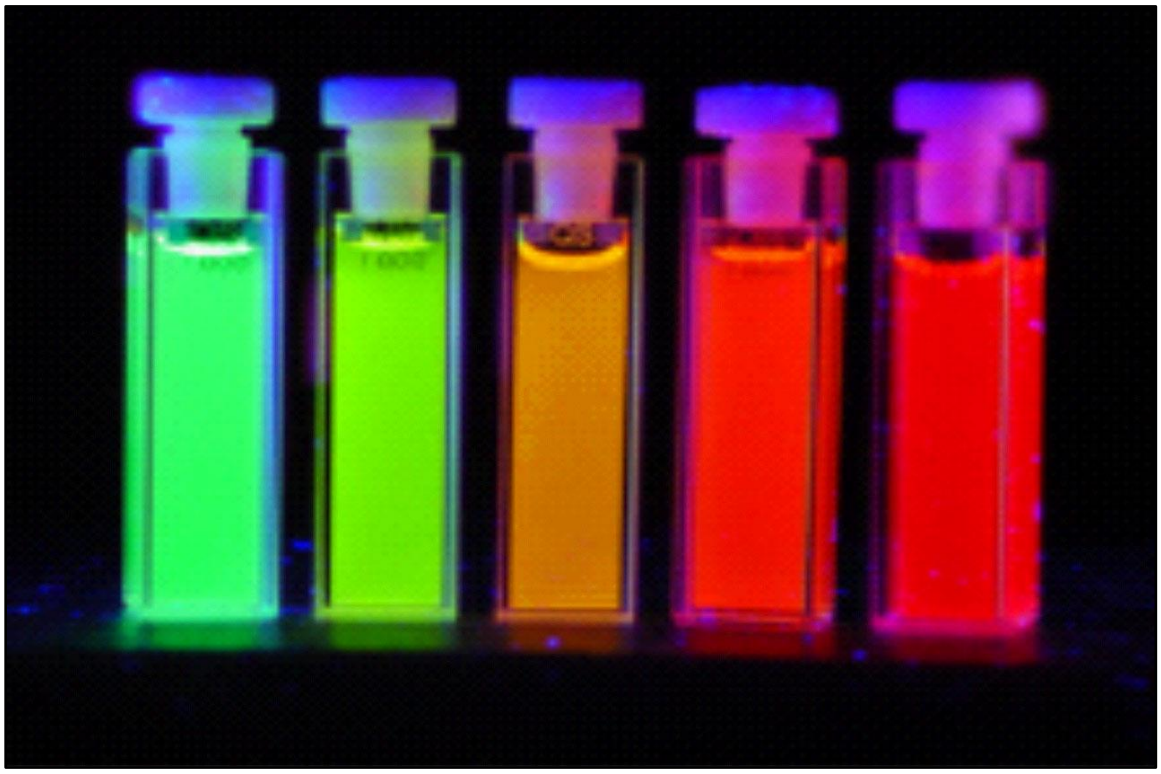

Figure 1.4 Particles of inorganic semiconducting (quantum dots) with nanometer scale dimensions of different sizes

(***Source****: Philips* http://www.research.philips.com/downloads/pictures/downloads/ldm-nanotech_04-0_h.jpg *, Last accessed 06/10/2014) Free license*

quantum effects over other effects at the nanoscale also results into change in melting point, absorption spectra and other properties with size. Another phenomenon which causes nanoparticles to have extremely unique and size-dependent properties is the high surface area to volume ratio which nanometer sized particles of have. As you go down in particle size, the percentage of atoms at the surface compared to the atoms within the particle increases drastically. These surface atoms usually have dangling/unsatisfied bonds which cause a net inward force which causes a subsequent increase in surface energy. This increased surface energy is the reason most nanostructured materials are thermodynamically unstable or metastable. (Cao, 2004) This effect can be visualized from data in Table 1.1 which illustrates the variation in surface energy with size for sodium chloride particles.

For metal and metal oxide nanoparticles, their magnetic properties have an important effect on their preparation and applications. The properties of materials composed of magnetic nanoparticles are a result of both the intrinsic properties of the particles and the interactions between particles. (Kodama, 1999) If the phenomenon of magnetism is discussed on the basis of the domain theory, we can understand why nanoparticles have unique size-dependent magnetic properties. Magnetic domains are regions in a material where the moments of all atoms of that material are aligned and the region has uniform magnetism. In absence of an external magnetic field, the magnetic domains are randomly oriented and the magnetic flux circuit lies almost entirely within the specimen.(Kittel, 1946) However, when an external magnetic field is applied, these domains align themselves in the direction of the magnetic field. As the particle size approaches a certain minimum critical size, often in the nanoscale range, the formation of

Table 1.1 Variation of surface energy of sodium chloride with particle size. (Cao, 2004)

Side (cm)	**Total surface area (cm^2)**	**Total edge (cm)**	**Surface energy (J/g)**	**Edge energy (J/g)**
0.77	3.6	9.3	7.2×10^{-5}	2.8×10^{-12}
0.1	28	550	5.6×10^{-4}	1.7×10^{-10}
0.01	280	5.5×10^{4}	5.6×10^{-3}	1.7×10^{-8}
0.001	2.8×10^{3}	5.5×10^{6}	5.6×10^{-2}	1.7×10^{-6}
10^{-4} (1 μm)	2.8×10^{4}	5.5×10^{8}	0.56	1.7×10^{-4}
10^{-7} (1 nm)	2.8×10^{7}	5.5×10^{14}	560	170

domain walls becomes energetically unfavorable. (Varadan, Chen, & Xie, 2008) Changes in magnetization occur through the rotation of spins rather than through the motion of domain walls. Particles exhibiting these properties are called single domain. As particle size is decreased further, spins are affected by thermal fluctuations and the particles become superparamagnetic (Vatta, Sanderson, & Koch, 2006). Iron and cobalt nanoparticles can occur in multiple crystal phases (ex. magnetite, hematite, etc. for iron oxide), which can result in large differences in the magnetic moment and crystalline anisotropy. This appears to be a size effect related to the balance of surface and bulk free energies for the various possible crystal structures, and consequently depends on the particle size and matrix material. (Kodama, 1999)

These size-dependent properties can be effectively harnessed by either using specialized synthesis techniques that yield monodisperse nanoparticles, or by employing sensitive processing (e.g. size-selective separation) techniques to generate monodisperse nanoparticle samples from polydisperse systems (as explained in detail in the next section).

1.1.2 Synthesis of Nanomaterials

There are two approaches to the effective synthesis of small particles: (1) the top-down approach were larger particles are divided repeatedly using various techniques to give small particles and (2) the bottom-up approach where the small particles are grown from individual atoms. (Rotello, 2004) These approaches are usually designed in a way so as to effectively control the size, shape and structure of the particles. In the top-down approach mechanical size-reduction techniques like milling and grinding are typically used to generate nanoparticles from minerals and metals. These particles are also usually synthesized in the presence of colloidal stabilizers to prevent aggregation during the size-reduction process (Nagarajan & Hatton, 2008).

The bottom-up approach is however preferred for the synthesis of nanoparticles because it is based on the reduction in Gibbs free-energy and hence ordinarily provides particles which have less defects, are chemically more homogeneous and have more ordering. (Nagarajan & Hatton, 2008) The typical methods involved in the bottom-up approach include chemical precipitation, reduction and acid/base reactions; where metal ions are reduced, subsequently nucleate, and then grow into nanoparticles. Metal and metal oxide nanoparticles, which are the subject of this study, can summarily aggregate due to formation of bonds on the surface between two or more particles. There are two main approaches to prevent the aggregation of these particles namely (a) Steric hindrance which involves surrounding the nanoparticle with an inert agent like a polymer or surfactant thus preventing its surface from having contact with any other particle and (b) Electrostatic repulsion which involves working away from the zero-charge point and thus

giving the particles a net charge. The neighboring particles then remain separated from each other due to electrostatic repulsion (Bréchignac, Houdy, & Lahmani, 2008).

A popular method of synthesizing nanoparticles is through the reduction of metal salts in an appropriate solvent. The reduction can be performed using a variety of methods including, but not limited to the use of chemical agents (M. Brust, Fink, Bethell, Schiffrin, & Kiely, 1995; Mathias Brust, Walker, Bethell, Schiffrin, & Whyman, 1994; Guzmán, Dille, & Godet, 2008), thermolysis (Tuchscherer, Schaarschmidt, Schulze, Hietschold, & Lang, 2012; Yamamoto, 2009) and photochemical agents (Eustis, Hsu, & El-Sayed, 2005; Arnim Henglein, 1998; Kéki, Török, Deák, Daróczi, & Zsuga, 2000). The metal ion, which is present when the salt is dissolved in the solvent, is reduced to a zerovalent state when the reduction is complete. After the formation of these zerovalent atoms, which are highly reactive, these species then nucleate to form the initial nanoclusters which are also very reactive in nature (Belloni, 1996; A Henglein, 1989, 1993; N. Jana, Gearheart, & Murphy, 2001; Nikhil R. Jana, Gearheart, & Murphy, 2001). These ‘nanoparticle seeds’ can then be used to generate nanoparticles which can be very uniform and monodisperse in nature.

1.1.2.1 *Gold nanoparticle synthesis methods*

Two popular methods for synthesizing gold-nanoparticles are the one step citrate reduction method in an aqueous media by Turkevich et al. (Turkevich, Stevenson, & Hillier, 1951) and the two-step synthesis method in an organic solvent as described by Brust et al. (Mathias Brust et al., 1994). In the citrate-reduction method chloroauric acid ($HAuCl_4 \cdot 3H_2O$) is used as the metal salt and sodium citrate is used as the reducing agent. The citrate also acts as a stabilizer for the nanoparticles. The method initially

produced nanoparticle seeds of about 50Å in size and can produce particles of desired sizes (5-20 nm) using modifications and reaction/reactant conditions suggested by Frens (Frens, 1973) and Chow & Zukoski (Chow & Zukoski, 1994). It has been shown from the kinetics of extinction spectra that multiple clustering steps occur after nucleation to give polycrystallite nanoparticles and that the resulting nanoparticles are of similar nature irrespective of energy source used to provide energy to the solution (thermal or UV) (Kimling et al., 2006).

However, the particles synthesized by the citrate-reduction method suffer from the disadvantage of not being redispersible after being removed from the solvent (water). This restricts the use of these nanoparticles in applications like thin film processing and hence organic solvent based methods like the Brust-Schiffrin method (M. Brust et al., 1995; Mathias Brust et al., 1994) are also used. In the Brust-Schiffrin method, a solution of chloroauric acid is used along with a phase transfer agent tetraoctylammonium bromide (TOAB). Sodium borohydride ($NaBH_4$) is used as the reducing agent in this method. There are many advantages of this method over other methods, including the fact that the kinetics of the nanocluster formation are dictated by surface coverage such that the reaction conditions what affect cluster size and not metal ion reduction kinetics (M. Brust et al., 1995). The TOAB, however, binds weakly to the nanoparticles and hence is a weak stabilizing agent for the nanoparticles which causes the particles to start falling out of solution within a few weeks. To prevent this, the process can be supplemented with the addition of thiol (e.g. dodecanethiol) as a capping ligand to passivate the surface of the particles and prevent nanoparticle aggregation (Manna et al., 2003). The TOAB forms metal complexes which act as precursors for nanoparticle formation and these can be

further manipulated to give more monodisperse samples (Goulet & Lennox, 2010). The latest accepted explanation behind the chemical mechanism which is occurring during the Brust synthesis method is shown in Figure 1.5. The Brust synthesis process gives more polydisperse particles (around the size range of 5 nm) when compared to the citrate-reduction method. But, the particles synthesized from the Brust method are redispersible in other non-polar solvents and can be isolated from the solvents to obtain a waxy-powder like nanoparticle sample. While the original methods described above are the most popular methods for synthesizing gold nanoparticles, there are many other modifications of the above methods to synthesize gold nanoparticles which use different reducing agents like hydroquinone (Jing Li et al., 2011) or use amines (K. R. Brown, Walter, & Natan, 2000) in the process. The Brust method of synthesis has been adapted to various other metals like ruthenium and platinum to prepare, for example, alkylamine stabilized nanoparticles(J. Yang, Lee, Deivaraj, & Too, 2004).

There are several other approaches to synthesize gold nanoparticles including through the use of microemulsions and by using various seed mediated growth methods. In the microemulsion methods, synthesis usually involves a two-phase system with a surfactant that causes the formation of the microemulsion or a micelle generating a favorable microenvironment together with the extraction of metal ions from the aqueous phase to the organic phase (Daniel & Astruc, 2004). Several of these microemulsion based methods (F. Chen, Xu, & Hor, 2003; Manna, Imae, Yogo, Aoi, & Okazaki, 2002; Spatz, Mößmer, & Möller, 2006) have resulted into gold nanoparticles with favorable properties and are still being perfected to yield better results. Seed mediated growth methods control the growth and nucleation steps in the nanoparticle growth phenomenon

to yield monodisperse nanoparticles.(N. R. Jana, Gearheart, & Murphy, 2001; Nikhil R. Jana et al., 2001) Seed mediated growth methods have been used Jana et al. to successfully synthesize gold nanoparticles and nanorods,(N. Jana et al., 2001; N. R. Jana et al., 2001; Nikhil R. Jana et al., 2001) while extremely monodisperse palladium nanoparticles have also been synthesized by Liu et al. to be used in various applications like catalysis.(J. Liu, Duggan, Morgan, & Roberts, 2012; J. Liu, He, Gunn, Zhao, & Roberts, 2009)

1.1.2.2 *Iron oxide nanoparticle synthesis methods*

The simplest and the most inexpensive method to synthesize iron oxide nanoparticles (Fe_3O_4 and γ-Fe_2O_3) is the co-precipitation method. It involves co-precipitating stoichiometric amounts of ferric and ferrous salts in an aqueous medium followed by addition of a base and subsequent heating. The thermodynamics of the system dictates that the stoichiometric ratio is 2:1 for the Fe^{2+}/Fe^{3+} salts and that the pH of the system is basic (8 to 12). To prevent the oxidation of ions before precipitation the entire reaction is carried out over an inert atmosphere like nitrogen or argon. A black precipitate of iron oxide nanoparticles can be obtained later by freeze-drying the resultant solution. (Bee, 1995; Lodhia, Mandarano, Ferris, Eu, & Cowell, 2010) This method is useful because it can synthesize large quantities of nanoparticles but suffers from the

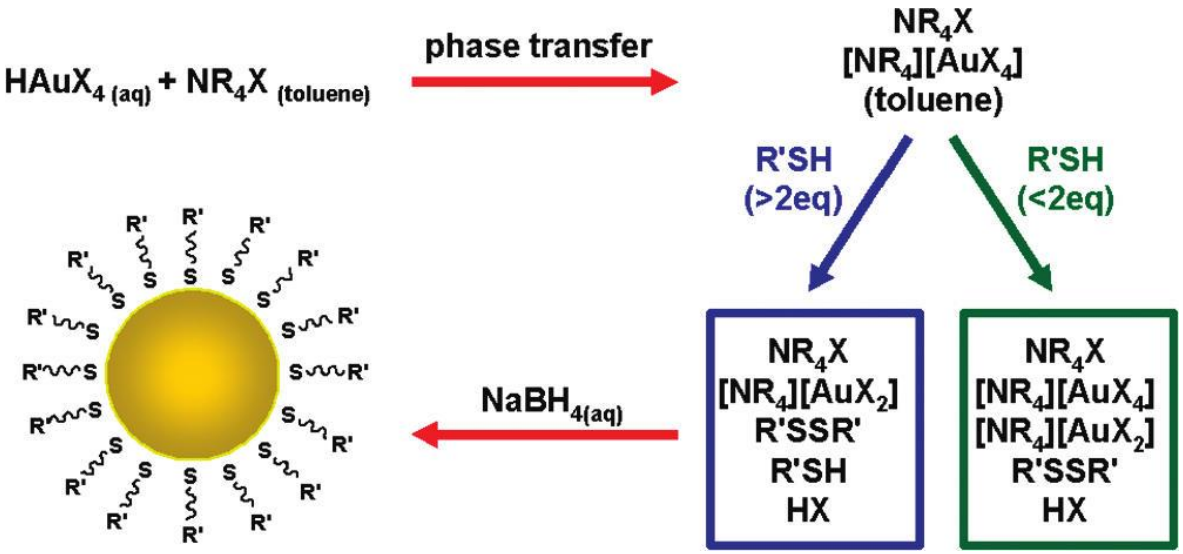

Figure 1.5 Overview of the mechanism behind the Brust-Schiffrin Au nanoparticle synthesis method (Goulet & Lennox, 2010)

disadvantage of producing samples with a large size-distribution. Many modifications and enhancements of this method have been published in literature, aiming to create a more monodisperse samples or changing the surface functionality (D.K. Kim, Zhang, Voit, Rao, & Muhammed, 2001; Do Kyung Kim, Mikhaylova, Zhang, & Muhammed, 2003; Predoi, 2007).

The other main methods to synthesize monodisperse iron oxide nanoparticles include the reverse micelle (Iida, Nakanishi, Takada, & Osaka, 2006; Y. Lee et al., 2005) and high-temperature approaches (Hyeon, Lee, Park, Chung, & Na, 2001; Shouheng Sun & Zeng, 2002). The reverse micelle methods usually suffer from drawbacks like having low yields, low crystallinity and possible aggregation, but there are methods available in literature (Y. Lee et al., 2005) which try to diminish some of these drawbacks. The high temperature methods available in literature are excellent for having significant size-control, crystallinity and shape uniformity in obtained samples. Extremely monodisperse magnetite nanoparticles have been synthesized by high-temperature solution-phase reaction of $Fe(acac)_3$ in phenyl ether with alcohol, oleic acid, and oleylamine (Shouheng Sun & Zeng, 2002) and through the use of iron pentacarbonyl as a precursor (Hyeon et al., 2001).

1.1.3 Size-Selective Nanomaterial Separation Methods

There are currently several processing techniques available to effectively generate monodisperse nanoparticles (Deng et al., 2005; S. Sun, 2000; Shouheng Sun & Zeng, 2002; Y. Sun & Xia, 2002) however, many of these suffer from several disadvantages such as the use of large amounts of solvents, high temperatures, expensive reagents and also the use of certain stabilizing ligands that limit surface access/functionality. With

regard to post synthesis techniques, the methods currently available include magnetic separation (Yavuz et al., 2006), size-exclusion chromatography (Siebrands, Giersig, Mulvaney, & Fischer, 1993; G. T. Wei, Liu, & Wang, 1999), centrifugation (Novak, Nickerson, Franzen, & Feldheim, 2001), electrophoresis (Surugau & Urban, 2009) and solvent/antisolvent precipitation (Thorat & Dalvi, 2012).

The methods based upon magnetic separation work by separating particles based upon their magnetic susceptibilities and/or sizes. Currently, particles of iron-oxide and cobalt have been separated based upon their size using methods like high gradient magnetic separation (HGMS) (Moeser, Roach, Green, Alan Hatton, & Laibinis, 2004) and by using capillary magnetic field flow fractionation (MFFF) (Latham, Freitas, Schiffer, & Williams, 2005). Studies comparing the effectiveness of these magnetic separation strategies to other techniques are also available in literature (Rheinländer & Kötitz, 2000). The chromatographic separation methods are based on mobile phase of mixtures passing through a stationary phase where separation is achieved through differences in the partition coefficients of the mobile and stationary phases. Size-exclusion chromatography has been used to effectively separate gold, silver and semiconductor nanoparticles based upon their size and shape (Al-Somali, Krueger, Falkner, & Colvin, 2004; FK Liu & Wei, 2004; Siebrands et al., 1993; G. T. Wei et al., 1999). However, these methods do require careful selection of the mobile phase and stationary phase to be effective and hence need to be tuned significantly before being applied.

Centrifugation techniques and electrophoresis are also popular methods for size-based nanoparticle separation. Centrifugation is centrifugal force-assisted separation of

nanoparticles based upon their densities and nanomaterials have been successfully separated based upon their size using both isopynic (Arnold, Stupp, & Hersam, 2005) and rate-zonal centrifugation (shown in Figure 1.6) (X. Sun et al., 2009). Electrophoretic techniques use an electric field to separate particles based upon their size/charge and currently gold, silver and CdSe semiconductor nanoparticles have been successfully separated based upon their size using gel and capillary electrophoresis (Hanauer, Pierrat, Zins, Lotz, & Sönnichsen, 2007; Oszwałdowski, Zawistowska-Gibuła, & Roberts, 2011; Surugau & Urban, 2009). Other methods for nanoparticle fractionation include membrane separation and extraction. These methods, though not frequently used, are capable of effectively and consistently separating nanoparticles based upon their size/shape.

The most common method of size-selectively fractionating nanoparticles is through an antisolvent precipitation technique (Mathias Brust et al., 1994; Murray, C.B. Kagan, Bawendi, & Murray, 2000; Sigman, Saunders, & Korgel, 2004). This technique, useful for organic dispersions of nanoparticles, involves the drop-wise addition of a poor solvent (antisolvent) like ethanol to an organic stable dispersion (Mathias Brust et al., 1994). With increasing amount of antisolvent being added to the dispersion, the solvent strength of the mixture drops to the point where the particles can no longer remain thermodynamically stable in the solvent mixture. The nanoparticles with the largest size exhibit the largest van der Waals forces of attraction and tend to agglomerate first while leaving the smaller nanoparticles in a stable dispersion (Murray, C.B. Kagan et al., 2000). Centrifugation is required to assist the agglomeration and precipitation of the nanoparticles from the dispersion.

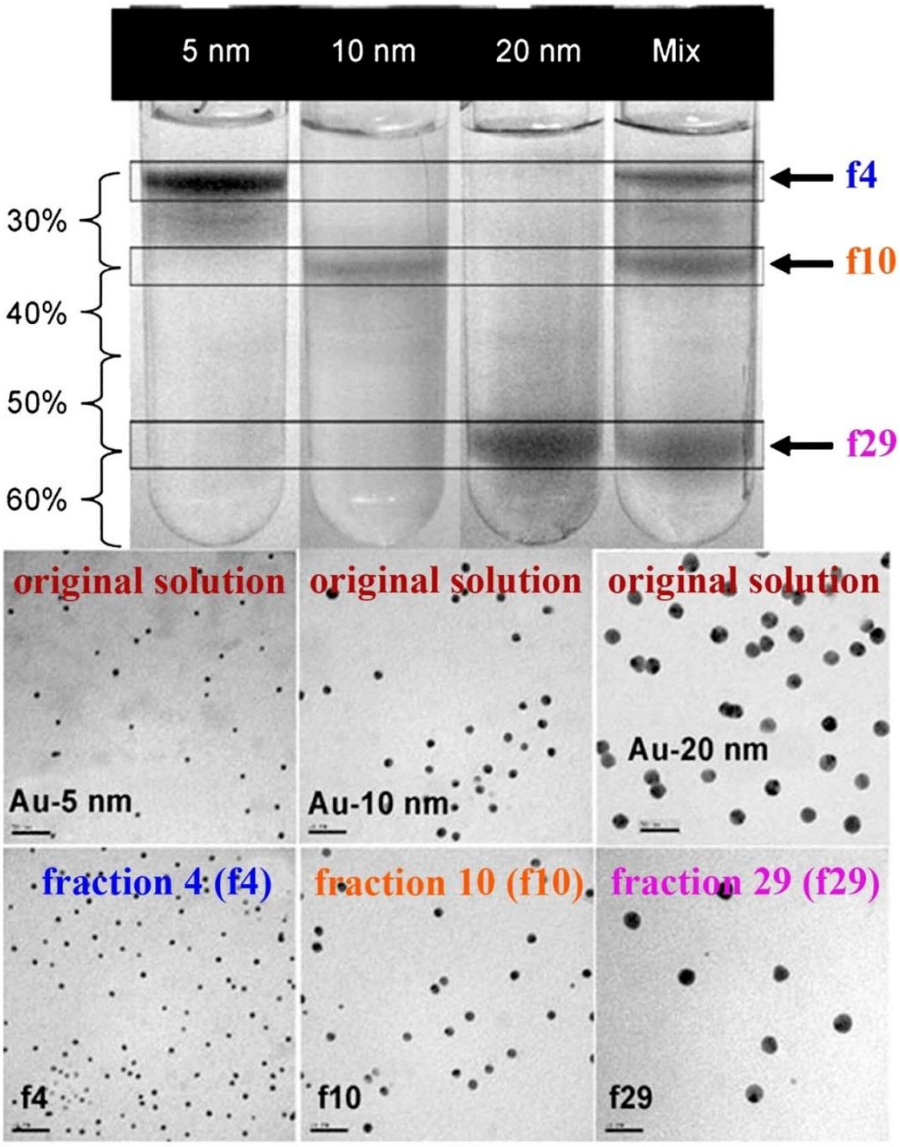

Figure 1.6 Optical and TEM images showing the separation of gold nanoparticles using the rate-zonal centrifugation technique (Kowalczyk, Lagzi, & Grzybowski, 2011)

The solvent mixture can be decanted; leaving the largest nanoparticles precipitated which can then be redispersed by addition of pure solvent. The smaller nanoparticles which are still dispersed in the supernatant can be fractionated further by adding more antisolvent. Through repeated addition of solvent and antisolvent, the fractionated nanoparticles can be separated into narrow size distributions. This technique is used in many laboratories due to its simplicity and easy availability of chemicals and required equipment.

However, most of these techniques are constrained by certain operational drawbacks. For example, limited size-dependent applicability in case of magnetic separation methods (Bishop, Wilmer, Soh, & Grzybowski, 2009; Fletcher, 1991), pore blockages and irreversible adsorption of nanoparticles in case of chromatographic methods (Kowalczyk et al., 2011) and the inherent energy-intensiveness of centrifugation methods.. Other problems include large amounts of solvents required, low throughputs, and expensive equipment required for the processes (S R Saunders & Roberts, 2009). One of the methods that was developed to overcome some of the problems includes the use of gas-expanded liquid (GXL) systems (Anand, Odom, & Roberts, 2007; McLeod, Anand, Kitchens, & Roberts, 2005; S R Saunders & Roberts, 2009) in a modified solvent-antisolvent process. This process is referred to as the GXL size selective fractionation process. In this method a liquid solvent and a gaseous (CO_2) antisolvent are used to precipitate nanoparticles of progressively smaller size from solution using increasing amounts of applied CO_2 pressure. This method will be discussed in detail in following sections of this document.

1.1.4 Applications of Metal and Metal-oxide nanoparticles

Metal and metal oxide nanoparticles are an area of continuous research in industry and academia due to the previously mentioned benefits they offer in physicochemical properties. The most common fields for nanoparticle use include biomedical engineering, nano-composites, catalysis and environmental remediation. The application of metal and metal oxide nanoparticles in these fields is highly dependent on controlling the various parameters associated with a nanoparticle, such as size, shape, coating agent, etc., some of which are shown in Figure 1.7. Nanoparticles are especially useful in the medical industry since the small size of the particles allows easy interaction of nanoparticles with cells (10-100 μm), viruses (20 – 450 nm), proteins (5 – 50 nm) or genes (2 nm wide and 10-100 nm long) (Pankhurst et al., 2003). For example, nanoparticles are being developed for applications such as targeted intracellular delivery (Chou, Ming, & Chan, 2010; Jain, Morales, Sahoo, Leslie-Pelecky, & Labhasetwar, 2005; Nativo, Prior, & Brust, 2008) and as magnetic resonance imaging (MRI) contrast agents (Babes, Denizot, Tanguy, Le Jeune JJ, & Jallet, 1999; Kwak, 2005; R. Qiao, Yang, & Gao, 2009; Tassa, Shaw, & Weissleder, 2011) require design of particles having good biocompatibility and magnetism. Nanoparticles also play in the field of catalysis due their surface area/volume ratio advantages and due to the unique physicochemical properties present at the sub-micron scale. Several metal and metal oxide nanoparticles like gold, cobalt and iron oxide have been used as catalysts for various reactions. The applications of these nanoparticles include industrially relevant processes like hydrogenation of various compounds and Fischer-Tropsch synthesis.

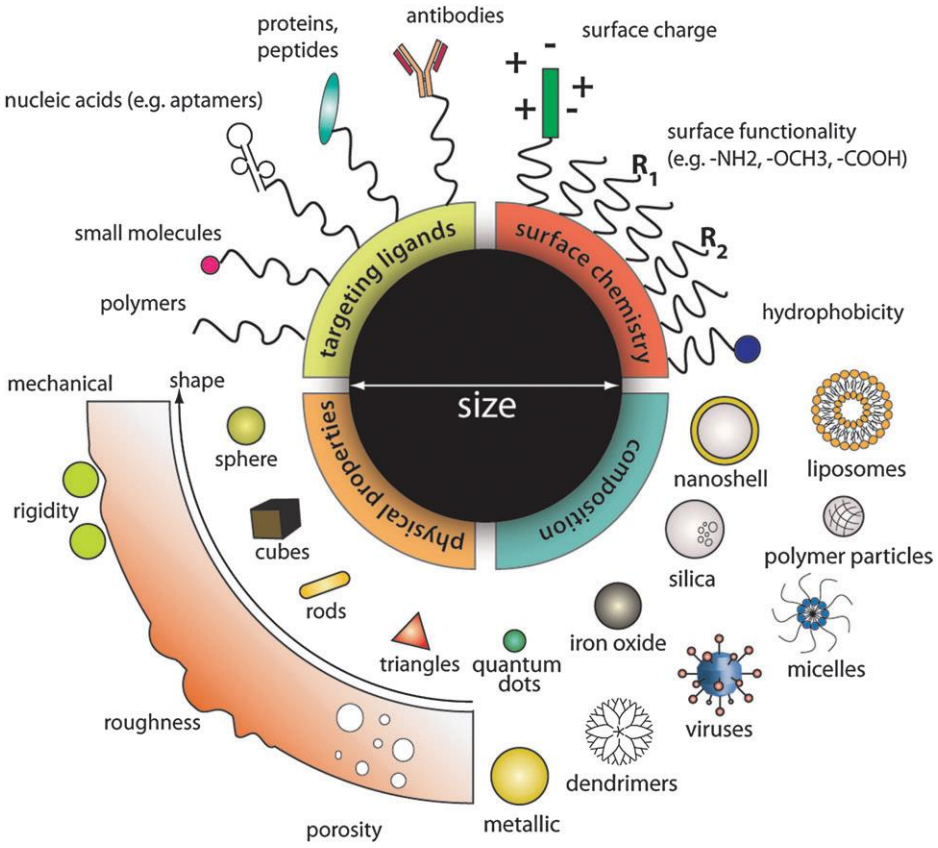

Figure 1.7 Different types of parameters which can be varied for nanoparticles (Chou et al., 2010)

Gold nanoparticles which have been deposited on a support have been shown to be effective catalysts for reactions such as the epoxidation of propene and hydrogenation of unsaturated substrates like acrolein to allylic alcohols (Daniel & Astruc, 2004). Supported nickel nanoparticles are particularly useful for the hydrogenation of aromatic compounds like methylbenzene (R. J. White, Luque, Budarin, Clark, & Macquarrie, 2009). Cobalt and iron nanoparticles deposited on various supports like alumina (J.-Y. Park et al., 2010; Torres Galvis, Bitter, Khare, et al., 2012) and carbon nanotubes (Bezemer, Falke, van Dillen, & de Jong, 2005; van Steen & Prinsloo, 2002) have been shown to be efficient at catalysis Fischer-Tropsch reactions at various conditions. The size of the nanoparticles has also shown to play an important part in controlling the selectivity and activity of the Fischer-Tropsch reactions (Nakhaei Pour, Housaindokht, Behroozsarand, & Khodagholi, 2013; J.-Y. Park et al., 2010).

Environmental applications like ground water purification and oil-spill remediation are also popular avenues for nanoparticle use, due to the interfacial properties of nanoparticles and the ability to modify nanoparticle surfaces to target certain contaminants. Since, nanoparticles can be effectively transported through groundwater, metallic nanoparticles like zerovalent iron (Fe^0) have been developed for various purposes like dechlorination, detoxification of pesticides and for removal of heavy metals.(Y.-P. Sun, Li, Cao, Zhang, & Wang, 2006; W. Zhang, 2003) Metal nanoparticles like CMC stabilized palladium (J. Liu, He, Durham, Zhao, & Roberts, 2008) and iron oxide (Mayo et al., 2007) can also be used to degrade toxic trichloroethylene and arsenic respectively from the environment.

The interfacial properties of nanoparticles can also be manipulated to generate particles which aggregate at oil-water interfaces and help disperse oil spills. These emulsions called Pickering emulsions, which initially were used primarily in the food industry are being now increasingly used in environmental and biomedical applications due their various advantages. Emulsions stabilized by particles also tend to be stabilized to a higher extent than surfactant stabilized emulsions due to their large interfacial energy (Melle et al., 2005). Carbon black (Katepalli, John, & Bose, 2013), silica (Eskandar, Simovic, & Prestidge, 2007), soy protein (Fu Liu & Tang, 2013) and iron oxide nanoparticles (Orbell, Godhino, Bigger, Nguyen, & Ngeh, 1997) are few of the nanoparticle systems that have been designed to help achieve this goal. A more detailed discussion about Pickering emulsions will be provided in Chapter 6 which deals exclusively with their design and use.

1.2 Introduction to Gas-Expanded Liquids (GXLs) and Supercritical Fluids

During the last several decades there has been a large volume of research being carried out with the aim to find out better media to carry chemical reactions in. This quest for systems with unique and tunable properties has resulted into a spur of research into supercritical fluids, gas-expanded liquids and ionic liquids. Every stable compound has a triple and critical point at which the properties of the liquid and gas phases become identical. Any gaseous compound reaches a supercritical state when pressurized to a pressure higher than the critical pressure (P_c) and a temperature higher than the critical temperature (T_c) (Noyori, 1999). A phase diagram showing the details of the phases for supercritical CO_2 ($sc CO_2$) is shown in Figure 1.8.

Supercritical fluids can serve as alternatives to volatile organic compounds (VOCs) that are used as solvents in many applications. These organic solvents are usually toxic, flammable and pose various environmental hazards during and after their use. Compressed (liquefied or supercritical) fluids like CO_2 are being researched as alternatives to such VOCs. The critical point for CO_2 is characterized by the critical temperature (T_c) of 31.0 °C, the critical pressure (P_c) of 73.8 bar, and the corresponding critical density (d_c) of 0.466 g mL^{-1}. Beyond this point, no distinct liquid or vapor phase can exist, and the new supercritical phase exhibits properties that are reminiscent of both states (Leitner, 2002). CO_2 is often preferred as a supercritical fluid because of the fact that it's a nonflammable, relatively nontoxic and inert gas, readily available, miscible with a variety of low molecular weight organic liquids, environmentally benign and inexpensive. Also, the critical temperature and pressure of CO_2 are easily accessible which makes lab scale operation safer and easier.

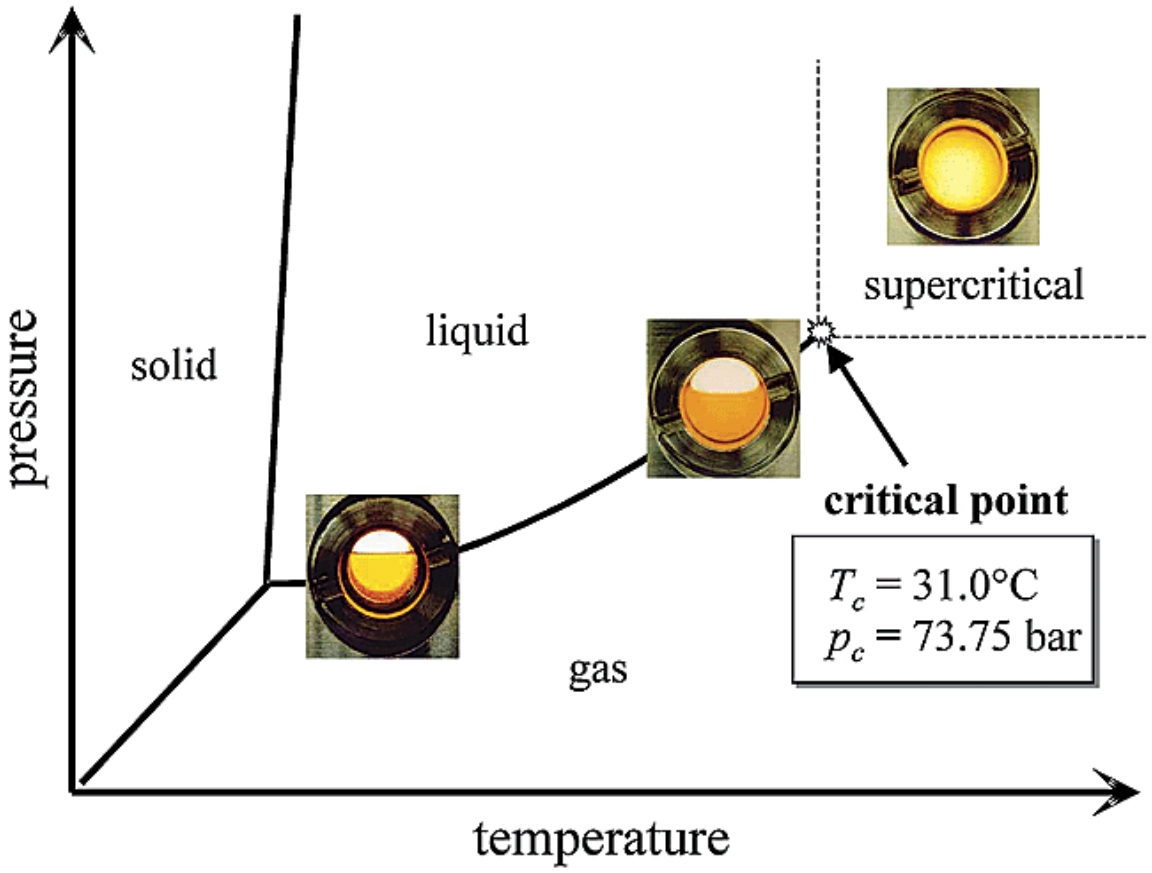

Figure 1.8 Schematic phase diagram of CO_2 with snapshots of the transition from the liquid/gas region to the supercritical region in presence of a CO_2-philic dye. (Leitner, 2002)

While *sc*CO2 has been used in various applications like particle generation for pharmaceutical processes (B Subramaniam, Rajewski, & Snavely, 1997), catalysis (Leitner, 2002) and food processing (Palmer & Ting, 1995), it has several disadvantages which has hampered its widespread use. These include only marginal increase in reaction rate benefits compared to the high pressure operation and its associated cost as well as a reduced solubility of reagents and catalysts in *sc*CO_2 compared to many organic counterparts, which reduce its economic and environmental benefits (Jessop & Subramaniam, 2007).

An alternative type of system being developed to overcome some of these disadvantages is through the use of a new type of solvent called a gas-expanded liquid (GXL). A GXL is a mixed solvent composed of a compressible gas like CO_2 or ethane dissolved in an organic solvent (Jessop & Subramaniam, 2007). GXLs exhibit pressure tunable properties due to the expansion of the liquid-organic solvent upon gas dissolution. Several properties of the gas-expanded mixture such as viscosity, diffusivity and solubility are affected by this pressure tunable solvent expansion. The physicochemical properties of the system can be varied between that of the pure solvent and that of the pure compressible gas simply by manipulating the applied pressure on the system. The most popular choice of gas for a gas expanded liquid is CO_2 because it's economically viable and safe for most applications. The gas expanded liquids expanded using CO_2 can be broadly classified into three categories as described by Subramaniam and Jessop: A) Class I liquids like water in which CO_2 is poorly soluble and for which expansion on pressurization is minimal to absent, B) Class II liquids like hexane, methanol and other organic solvents which undergo great volumetric expansion and

change in physicochemical properties upon addition of CO_2 and C) Class III liquids like ionic liquids and crude oil which expand only moderately upon applied CO_2 pressure, which in turn results into a change in only a few properties like viscosity (Jessop & Subramaniam, 2007). A comparison between the different classes of solvents and their expansion data is given in Table 1.1.

Gas expanded liquids, including those expanded using CO_2, have been used in various applications in a multitude of research fields. The most popular use of GXLs is in the fields of catalysis and particle processing. In the field of catalysis, a tunable solvent system has been used for example to increase the turnover frequency of a water-soluble catalyst system by a factor of 85 for the hydroformylation of 1-octene (Hallett et al., 2008). Also, in the ethylene oxide manufacture process, through judicious choice of catalyst and a modest modification of process conditions, the solubility of gaseous ethylene in the liquid reaction phase (a gas-expanded liquid) could be substantially increased under pressure to enhance the reaction and prevent formation of CO_2 as a byproduct (ethylene oxide manufacturing process is one of the most CO_2 generating process in industry) (H.-J. Lee, Ghanta, Busch, & Subramaniam, 2010). CO_2 expanded alcohols have also been used as a catalytic media for the cyclohexanone acetal formation, to reduce the use of toxic acid catalysts (Xie, Liotta, & Eckert, 2004). In the area of particle processing, ultrafine particles of biomedically useful substances like cholesterol have been synthesized using organic solvents and subcritical CO_2 (Dalvi & Mukhopadhyay, 2009). Many particle processing processes like GAS (Gas Anti-Solvent) and DELOS (Depressurization of an Expanded Liquid Organic Solution) employ gas-expanded liquids (or similar systems) and are designed to give fine monodisperse

particles of various substances (Jessop & Subramaniam, 2007; B Subramaniam et al., 1997). Other than the common applications mentioned above GXLs are also used in various niche applications. For example, GXLs (CO_2 expanded ethanol) have been used for cleaning or residue removal approaches that overcome some of the drawbacks of current surface preparation methods including the removal of polyhydroxystyrene photoresist films during manufacture of integrated circuits (Song, Spuller, Levitin, & Hess, 2006). CO_2-expanded liquids are also used to coat microelectromechanical systems (MEMS) with uniform, wide area nanoparticle films of ligand stabilized nanoparticles to act as a durable anti-stiction coating (K. Hurst & Ansari, 2011; McLeod, Kitchens, & Roberts, 2005).

At moderate pressures (between 3 and 8 MPa), gaseous CO_2 has a considerable solubility in many of the Class II solvents mentioned above, which provides the opportunity to alter the physicochemical properties of the solvent such as the polarity and hydrogen-bonding. A short overview of the tunable properties of GXLs as a whole and especially CO_2 expanded liquids is given henceforth.

class	solvent	P, bar	volumetric expansion, %	wt. % CO_2	mol. % CO_2
I	H2O	70	n/a	4.8	2.0
II	MeCN	69	387	83	82
II	1,4-dioxane	69	954	79	89
II	DMF	69	281	52	65
III	[bmim]BF_4[a]	70	17	15	47
III	PEG-400	80	25	16	63
III	PPG-2700[b]	60	25	12	89

Table 1.2 A Comparison of Different Classes of Solvents and their Expansion Behavior at 40°C under CO_2 Pressure (Jessop & Subramaniam, 2007) [a] Interpolated from literature data. [b] At 35 °C

.

1.2.1 Tunable Properties of GXLs

Gas expanded liquids; especially Class II GXLs, show a wide variation in physicochemical properties with applied gas pressure. Solution properties like solvent polarity and viscosity are primarily affected. For example, at moderate pressures, CO_2 undergoes a substantial change in physicochemical properties of the solvent such as the polarity and hydrogen-bonding and these have been researched using solvatochromic solvent parameters calculated using solvatochromic dyes by Wyatt *et al.* for CO_2-acetone and methanol systems (Wyatt et al., 2005). Sih *et al.* studied properties like viscosity of CO_2 expanded systems (the CO_2-methanol system and CO_2-ethanol system) using the falling-weight viscometry technique to show that increase in the degree of volume expansion of the liquid phase brings about a dramatic initial reduction in liquid phase viscosity (Sih, Armenti, Mammucari, Dehghani, & Foster, 2008; Sih, Dehghani, & Foster, 2007). Volume expansion of GXLs has also been critically studied using various optical techniques like UV-Vis spectroscopy by various researchers, for different gas-solvent systems, which in turn can be used to determine other synergetic physicochemical properties of GXLs (Aida, Aizawa, Kanakubo, & Nanjo, 2010; Elvassore, Bertucco, & Di Noto, 2002; Fuente, Peters, & Arons, 2000; Jun Li, Rodrigues, Matos, & Gomes de Azevedo, 2005).

Transport properties of gas-expanded liquid show marked improvement upon application of gas pressure and these properties are the main reason why GXLs are advantageous over other solvent systems in catalysis and other applications. For example, a four to five fold increase in diffusivity of benzene was reported by Sassiat et al. in a CO_2-methanol system upon pressurization with CO_2 (Sassiat, Mourier, Caude, & Rosset,

1987). Also, via molecular simulation studies GXLs (CO_2-acetone and CO_2-methanol) were found to exhibit local density enhancements similar but lower than supercritical fluids (C. Shukla & Hallett, 2006). Other properties like surface tension, conductivity, and acidity also vary significantly in GXLs and they have been reported in literature and one can refer to the extensive review by Jessop and Subramaniam (Jessop & Subramaniam, 2007) for more information.

1.2.2 Nanoparticle Processing using GXLs

Due to the easily tunable properties of GXLs, they have seen much use for the synthesis and processing of nanoparticles. GXLs also have the added advantage of being able to dissolve inorganic metal precursors, phase transfer agents, reducing agents and stabilizing ligands critical to nanoparticle synthesis and processing. For example, ZnS nanoparticles stabilized in AOT reverse-micelles have been recovered using compressed CO_2 using isooctane as the expandable solvent (J. Zhang et al., 2001). During nanomaterial fabrication for biomedical application, which insists upon the control of size and morphology of drug powder and its multidimensional structure that is very essential to control the activity and drug delivery, subcritical and supercritical CO_2 and H_2O based processes have proved to be of much use (Byrappa, Ohara, & Adschiri, 2008). For post-processing methods to obtain nanoparticles, supercritical ethane has been shown to be effective in size-selectively separating alkanethiol-coated gold nanoparticles by density tuning (Clarke, Waters, Johnson, Satherley, & Schiffrin, 2001; Shah, Holmes, Johnston, & Korgel, 2002). For the processing of polydisperse nanoparticle populations using GXLs, its was showed by McLeod et al. that dodecanethiol capped gold nanoparticles could be size-selectively separated using CO_2-expanded liquids (McLeod, Anand, et al.,

2005). To precipitate nanoparticles populations of different sizes in succession, a spiral tube apparatus as shown in Figure 1.9 was developed by McLeod et al.(Anand et al., 2007) The initial polydisperse gold nanoparticle dispersion is added to one end of the spiral tube and the pressure of the system is increased to a predefined value so that a fraction of the gold nanoparticles precipitate out of the solution due to reduction in solvation of the ligands. This decrease in the solvation of ligands is caused by the reduction in solvent strength of the system by the addition of CO_2 which makes the system behave more like a gas than the solvent. However, the aliphatic ligands do not dissolve in CO_2 and hence collapse upon themselves as proved by recent small angle neutron scattering (SANS) studies (G Von White & Kitchens, 2010). Using this method, multiple nanoparticle fractions can be separated rapidly while obtaining greater monodispersity than the original sample all in one step. However, one of the disadvantages of this method was that very small amount of sample (1-2 ml) could be fractionated using this spiral tube apparatus. Also, the cleaning and reuse of this spiral tube apparatus is time consuming and individual fractions cannot be easily recovered.

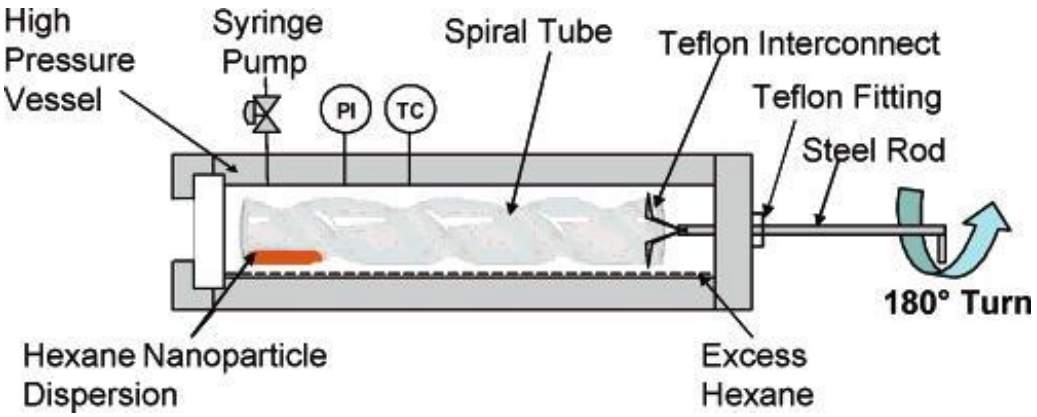

Figure 1.9 Spiral tube apparatus for the size-selective fractionation of nanoparticles using GXLs (Anand et al., 2007).

A modified application scale apparatus using a cascaded series of Jerguson gages was then developed by Saunders & Roberts so as increase the processing volume and to decrease the downtime necessary for cleaning. (S R Saunders & Roberts, 2009) In short, the apparatus consists of three stainless steel Jerguson® site gages (i.e. high pressure vessels- J_1, J_2, J_3) which are connected to each other vertically (in series) and are compartmentalized with high pressure valves (V_1, V_2, V_3) and tubing, as illustrated in Figure 1.10. In addition, each vessel has a glass-tube insert which is attached to the bottom of the vessel with a liquid tight seal. This allows for easy removal of nanoparticles that will be deposited onto its surface through the course of the following process. A pressure transducer is connected to the top of the first vessel (J_1) to allow for the measurement of the CO_2 pressure.

In a typical experiment, a sample of the liquid nanoparticle dispersion (up to 20 ml) is loaded into the top vessel (J_1), the valve V_1 is closed so as to isolate the solution in J_1 and CO_2 is passed through the entire system (vessels J_1, J_2 & J_3) to purge the system of air and saturate it with hexane vapor. The system is then pressurized to the first (the lowest) pressure which is below the vapor pressure of CO_2 and allowed to equilibrate such that the first fraction of nanoparticles (the largest) is precipitated from the solution onto the walls of the inner glass tube in vessel J_1, leaving the smaller nanoparticles still dispersed in the solution mixture (solvent + CO_2). The valve (V_1) connecting the first and second vessel is slowly opened to allow the remaining dispersed particles to flow into the second vessel (J_2) via gravity. It must be noted that vessels J_2 & J_3 are equipped with side ports that allow for removal of CO_2 gas that must be displaced during the transfer of a

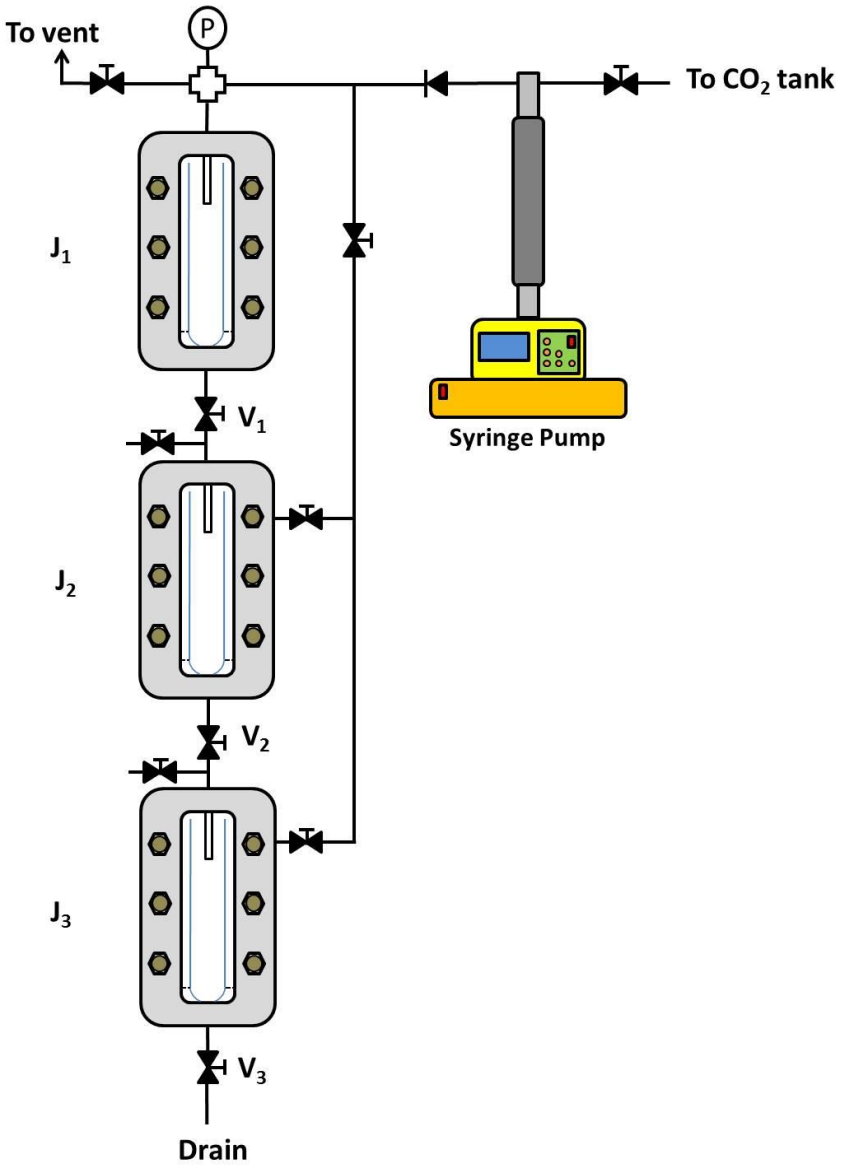

Figure 1.10 Cascaded vessel apparatus for the size-selective fractionation of nanoparticles using GXLs (S R Saunders & Roberts, 2009).

liquid dispersion from one vessel to the next at constant pressure (i.e. as a liquid sample is moved from one vessel to the next through the high pressure valves and tubing, a commensurate volume of gas must be displaced into the former vessel at the same pressure). After complete transfer of the liquid dispersion to the second vessel (J_2), the system is then pressurized to the second higher pressure which further induces the precipitation of another fraction of the nanoparticles (with sizes smaller than the first fraction). The remaining nanoparticle solution mixture, containing the still dispersed smallest nanoparticles, is then transferred (via V_2) to the last vessel (J_3) and then the system is depressurized slowly. The smallest nanoparticles are obtained as a dispersion by simply draining the solution from the last vessel (via V_3) while the other fractions can be obtained as dispersions by simply isolating and washing each vessel in succession (J_3 → J_2 → J_1) with the solvent being used (thereby redispersing the precipitated nanoparticles in neat solvent).

This apparatus was shown to be successful in fractionating gold nanoparticles dispersed in organic solvents (S R Saunders & Roberts, 2009) and organic solvents combined with a co-solvent (Steven R. Saunders & Roberts, 2011). This apparatus and the above mentioned procedure along with some modifications were used as the primary size-selective fractionation apparatus for most of the theoretical experiments in this study due to its easy operability and effectiveness in delivering monodisperse nanoparticles for dilute samples.

1.3 Summary of chapters

Given the foregoing background, the following chapters in this dissertation deal with two primary areas related to the GXL fractionation process; a) process enhancement, and b) process application. The main areas where process enhancement is being implemented include a) decreasing the process operating pressures, b) increasing process capacity, and c) increasing process versatility. The process pressures are tuned by manipulating the solvent-ligand interactions in the GXL-nanoparticle system using branched ligands and solvents, as shown in Chapter 2. An attempt to increase the process versatility by using a relatively complex system of iron-oxide nanoparticles (compared to the common system of gold nanoparticles) is shown in Chapter 3. Work regarding an attempt at converting the cascaded vessel apparatus mentioned above into a packed column in order to increase processing capacity, along with a successful scaled-up redesign of the GXL fractionation system is also discussed in Chapter 4. An application of the GXL process to generate viable supported Fischer-Tropsch (FT) catalysts will be explained in Chapters 5 along with experiments testing the effectiveness of the synthesized catalyst in an actual FT process. Chapter 6 shows our attempt to study the effect of nanoparticle size on Pickering emulsion formation using processed iron-oxide nanoparticles. A study using iron oxide nanoparticles coated with a FDA approved ligand in order to create stable oil-in-water emulsions is also shown in Chapter 6.

Chapter 2

Understanding the Effect of Ligand and Solvent Structure on Size-Selective Nanoparticle Dispersability and Fractionation of Gold Nanoparticles in (GXL) Systems

2.1 Introduction

With the use of the cascaded vessel apparatus described in the Section 1.2.2 and in Figure 1.9 it is possible to separate metallic nanoparticles based upon their size using CO_2 gas-expanded liquids. This apparatus has been shown to yield monodisperse fractions of nanoparticles using alkanethiol capped particles dispersed in organic solvents like hexane (S R Saunders & Roberts, 2009; Steven R. Saunders & Roberts, 2011). However, while this process gives relatively monodisperse particles, it is still necessary to subject the system to significant applied pressures of CO_2. Usually, applied CO_2 pressures of around 35 bar are required to begin the precipitation of gold nanoparticles coated with dodecanethiol dispersed in *n*-hexane (McLeod, Anand, et al., 2005). In this study, the pressure at which the nanoparticles start to precipitate from the solvent dispersion will be referred to as the pressure of incipient precipitation (P_i). It has been shown in previous studies (Anand, McLeod, Bell, & Roberts, 2005; Steven R. Saunders & Roberts, 2011) that reduction of P_i values is feasible by modifying solvent ligand interactions and this was obtained using short-chain solvents (ex. pentane), short-chain

ligands (ex. hexanethiol) and co-solvents (ex. acetone). However, insignificant P_i reduction was obtained using short-chain solvents and only moderate P_i reduction was obtained using short-chain ligands (Anand et al., 2005). Also, non-spherical particles were observed due to the use of these short-chain ligands which can be explained by the possible insufficient steric stabilization provided by these ligands after the growth phase during the synthesis procedure. By using co-solvents combined with short-chain ligands the P_i values were tuned successfully from 35 bar to 5 bar to still obtain monodisperse nanoparticles.(Steven R. Saunders & Roberts, 2011) While the use of co-solvents and shorter ligands is advantageous to reduce pressures it is also difficult to control and predict sizes obtained due to presence of the co-solvent, which adds an extra variable to the entire system. Also, since short-chain ligands were used again with the co-solvents, the problem with misshapen particles was observed again with these systems. (Steven R. Saunders & Roberts, 2011)

The main aim of this study is to check the feasibility of reducing the operating pressures in the GXL fractionation process with the goal for making this process more economically viable, through the modification of the ligand and solvent steric structures and manipulation of the solvent-ligand interactions. Moreover, this study should be critical in furthering our understanding of the changes in solvent-ligand interactions due to change in ligand and solvent structure and how these interactions affect nanoparticle dispersability in gas-expanded liquids.

2.2 Experimental Section

2.2.1 Materials

Gold (III) chloride trihydrate ($HAuCl_4 \cdot 3H_2O$, 99.9%), sodium borohydride ($NaBH_4$, >98.0%), tetraoctylammonium bromide (TOABr, $[CH_3(CH_2)_7]_4NBr$, 98%), 1-dodecanethiol ($CH_3(CH_2)_{11}SH$, 98%), and *tert*-dodecanethiol (mixture of isomers) ($CH_3(CH_2)_8C(CH_3)_2SH$, 98.5%), were obtained from Aldrich. *n*-hexane (HPLC grade, 95%), 2-methylpentane (99+%), 3-methylpentane (99+%), 2,2-dimethylbutane (99%) and 2,3-dimethylbutane (99+%) was obtained from Alfa-Aesar. Ethanol (94.0-96.0%) was obtained from Mallinckrodt Chemicals. Toluene (HPLC grade, 99.9%) and (deionized ultra-filtered) DIUF water were obtained from Fisher. Carbon dioxide (SFC/SFE grade) was obtained from Airgas. All chemicals were used as received without further purification.

2.2.2 Gold Nanoparticle Synthesis

For the synthesis of dodecanethiol capped gold nanoparticles dispersed in an organic solvent the two-phase arrested precipitation method developed by Brust et al.(Mathias Brust et al., 1994; Goulet & Lennox, 2010) and then modified by Sigman et al.(Sigman et al., 2004) was used. A solution of gold salt was initially prepared by dissolving 0.36 g of $HAuCl_4 \cdot 3H_2O$ to 36 ml of water. Also, a solution TOABr was prepared by completely dissolving 2.7 g of TOABr in 24.5 ml of toluene. The gold salt solution was then slowly added to the TOABr solution on a magnetic stir plate and a color change was observed. This mixture was then vigorously stirred for an hour and then the aqueous phase was removed using a pipette. A solution of $NaBH_4$ (0.5 g of $NaBH_4$ in 30 mL DIUF water) was then slowly added over a period of 1 minute to the remaining

organic mixture ,while still being stirred, in order to induce reduction of the salt. This mixture was allowed to stir, at room temperature, for 8 hours and then the new aqueous layer was removed. Following complete aqueous layer removal, 240 μL of 1-dodecanethiol (or *tert*-dodecanethiol as appropriate) was added to the solution and was stirred for a further 4 hours. To purify the sample 40 mL of ethanol was first added to precipitate the nanoparticles. The solution was then centrifuged (Labnet Hermle Z200A) at 5000 rpm for 5 minutes and the supernatant was discarded. This purification process with ethanol was performed thrice in succession to remove any impurities from solution such as excess 1-dodecanethiol. The solution was then dried using nitrogen and then redispersed in the solvent of choice.

2.2.3 Monitoring nanoparticle dispersability using UV-Vis spectroscopy

The absorption spectra of metallic gold nanoparticles is characterized by a strong broad absorption band at around 520 nm that is absent in the bulk metal spectra.(Amendola & Meneghetti, 2009; Haiss, Thanh, Aveyard, & Fernig, 2007) This absorption band can be used to determine the dispersability of gold nanoparticles in solution. The conditions present in an expanding GXL containing gold nanoparticles can also be traced effectively by using this surface plasmon resonance (SPR) band of the gold nanoparticles.(McLeod, Anand, et al., 2005) This unique absorbance band is credited to the collective oscillation of the conduction electrons in the gold nanoparticles in response to external optical excitation.(Alvarez et al., 1997) The presence of this band in the visible region of the spectrum is responsible for the striking colors of dilute colloidal solutions of noble metals like gold and silver.(Creighton & Eadon, 1991) The change in intensity of this band can be used to track the precipitation of the gold nanoparticles from

the GXL, where greater intensity of the SPR band corresponds to the dispersability of more nanoparticles (i.e. greater concentration) in the solvent mixture (i.e. *n*-hexane + CO_2). (Anand et al., 2005; McLeod, Anand, et al., 2005; S R Saunders & Roberts, 2009) These UV-Vis measurements are performed through the use of a high pressure vessel fitted with quartz windows and the entire apparatus is fitted within a UV-Vis spectrophotometer (Cary 3E) in order to obtain *in-situ* readings of the absorption spectra as a function of applied CO_2 pressure. (Anand et al., 2005; McLeod, Anand, et al., 2005) Specifically, the gold nanoparticle dispersion was added to a 1cm × 1cm quartz cuvette and this cuvette was inserted into the high pressure vessel in alignment with the quartz windows such that an absorption spectrum of the contents of the cuvette can be collected *in-situ*. The vessel is purged of air and then pressurized to a desired pressure using CO_2 from a high pressure syringe pump (ISCO 260D). This initial pressure was chosen such that a certain fraction (the largest particles) of the nanoparticles would precipitate upon dissolution of CO_2 into the solvent so as to form a solvent + CO_2 mixture. The concentration of CO_2 in this mixture is dependent on the CO_2 pressure applied on the system. For the sake of consistency, the change in applied pressure between successive readings was chosen to be 50 psig (i.e. 3.45 bar). The CO_2 pressure within the system was monitored using a pressure transducer attached to the top of the high pressure vessel and another that was present inline between the pump and the vessel. The system was then allowed to reach equilibrium as evidenced by a consistent UV-Vis spectrum as a function of time at that pressure. The system was then pressurized to a subsequent higher pressure so as to further precipitate more nanoparticles (the next smaller sized set of particles) and the UV-Vis spectrum was collected again once equilibrium was obtained. This process

was continued until the SPR band had completely diminished in the obtained spectra which meant that all the particles had precipitated from the solution.

As an example, the UV-Vis spectrum for the dodecanethiol capped gold nanoparticles dispersed in *n*-hexane system is shown in Figure 2.1. The change in intensity of the SPR band (specifically, the absorbance at 520 nm) is then plotted as a function of applied CO_2 pressure after correcting the initial value for the volume expansion that occurs in the GXL system (details for correction shown in Appendix 1). This plot then allows for determination of the pressures required to initiate nanoparticle precipitation and the pressure range over which the precipitation occurs. These particular plots are referred to as 'precipitation curves' within the remainder of this document. A generic representation of a precipitation curve of this type is shown in Figure 2.2. As an example, the precipitation curve for the system where dodecanethiol capped gold nanoparticles are dispersed in *n*-hexane, is shown in Figure 2.3.

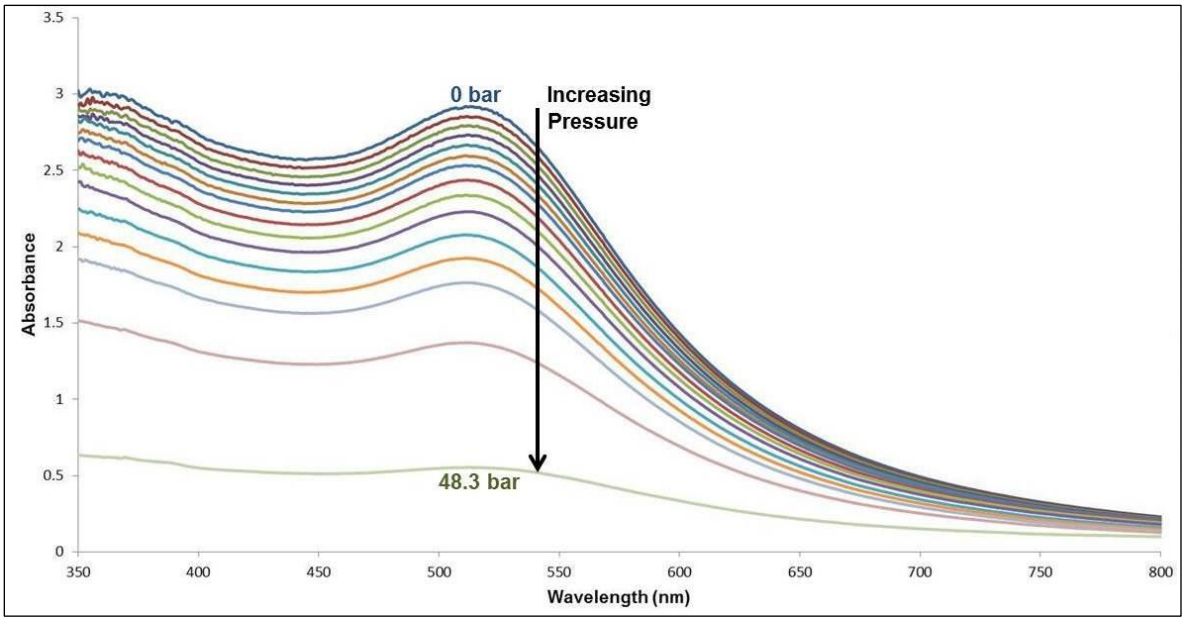

Figure 2.1 UV-Vis spectra for dodecanethiol coated gold nanoparticles dispersed in n-hexane at different applied CO_2 pressures in 3.45 bar intervals (i.e. 50 psig).

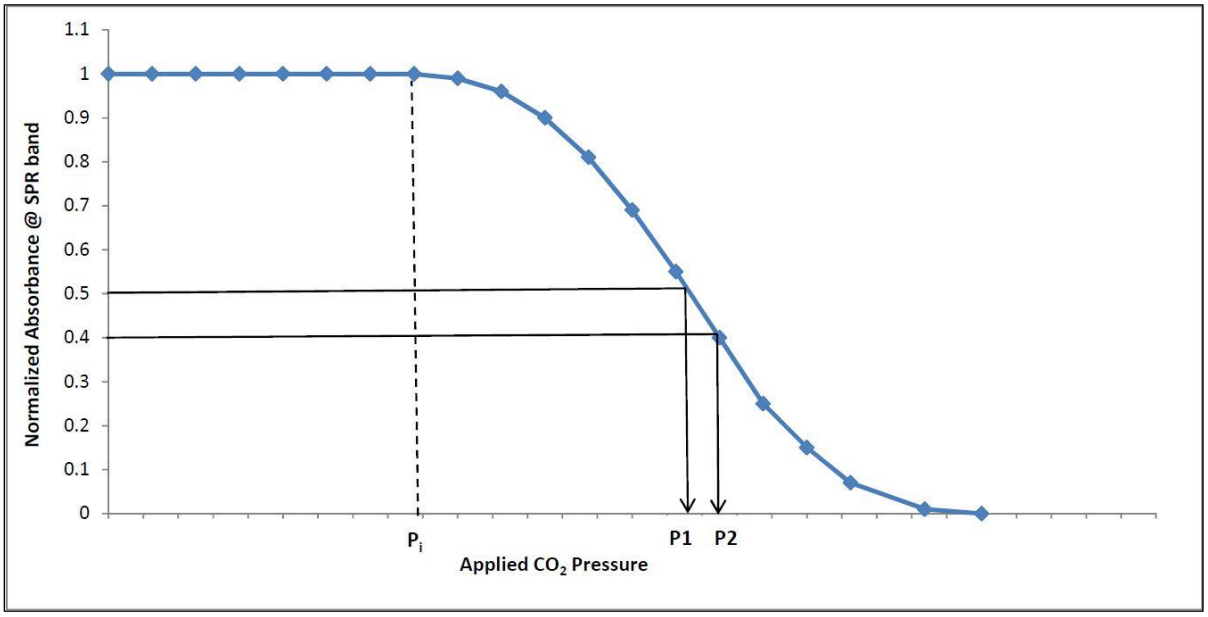

Figure 2.2 A generic representation of a nanoparticle precipitation curve where Pi corresponds to the 'pressure of incipient precipitation' and P1, P2 are the pressures employed in the GXL fractionation process, corresponding to the normalized absorbance values of 0.5 and 0.4 respectively.

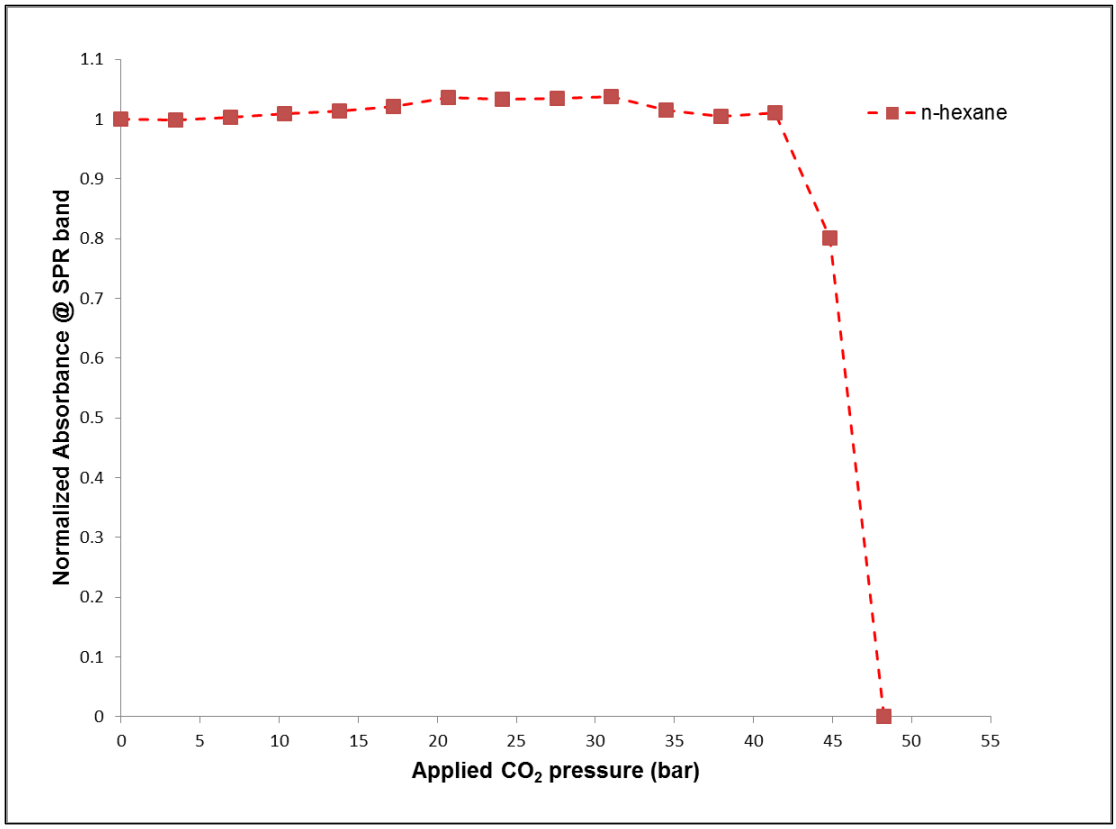

Figure 2.3 Precipitation curve for dodecanethiol coated gold nanoparticles dispersed in *n*-hexane obtained by tracking the change in intensity of normalized SPR band using *in-situ* UV-Vis spectroscopy at different pressures.

2.2.4 Determining the volume expansion of branched solvents

The decrease in the intensity of the SPR band that occurs upon increasing the degree of CO_2 pressurization is due to two phenomena occurring simultaneously. The first phenomenon is due to the dilution of the dispersion that is caused by the addition of condensed CO_2 into the solvent (so as to create a solvent + CO_2 mixture). The second phenomenon involves the decrease in nanoparticle concentration within the solvent mixture that is caused by the precipitation of the nanoparticles from the solution upon decreasing solvent strength through the addition of CO_2. The dilution effect can be corrected by using volume expansion data from experimental results obtained by visually monitoring the solvent expansion in a graduated Jerguson® site gage or by using VLE (vapor-liquid equilibrium) information determined from the Peng-Robinson equation of state (PR-EOS). The correction of intensity of the SPR band was carried out using the Beer-Lambert law assuming a negligible change in the extinction coefficient of the dispersed nanoparticles. For the *n*-hexane + CO_2 system, the experimental expansion data was verified against and found to closely match the volume expansion predicted from the PR-EOS. For the other alkanes, experimental volume expansion data was obtained using the graduated Jerguson® site gage and this data was used in correcting the intensity of the SPR band. This volume expansion data is provided in Figure 2.4.

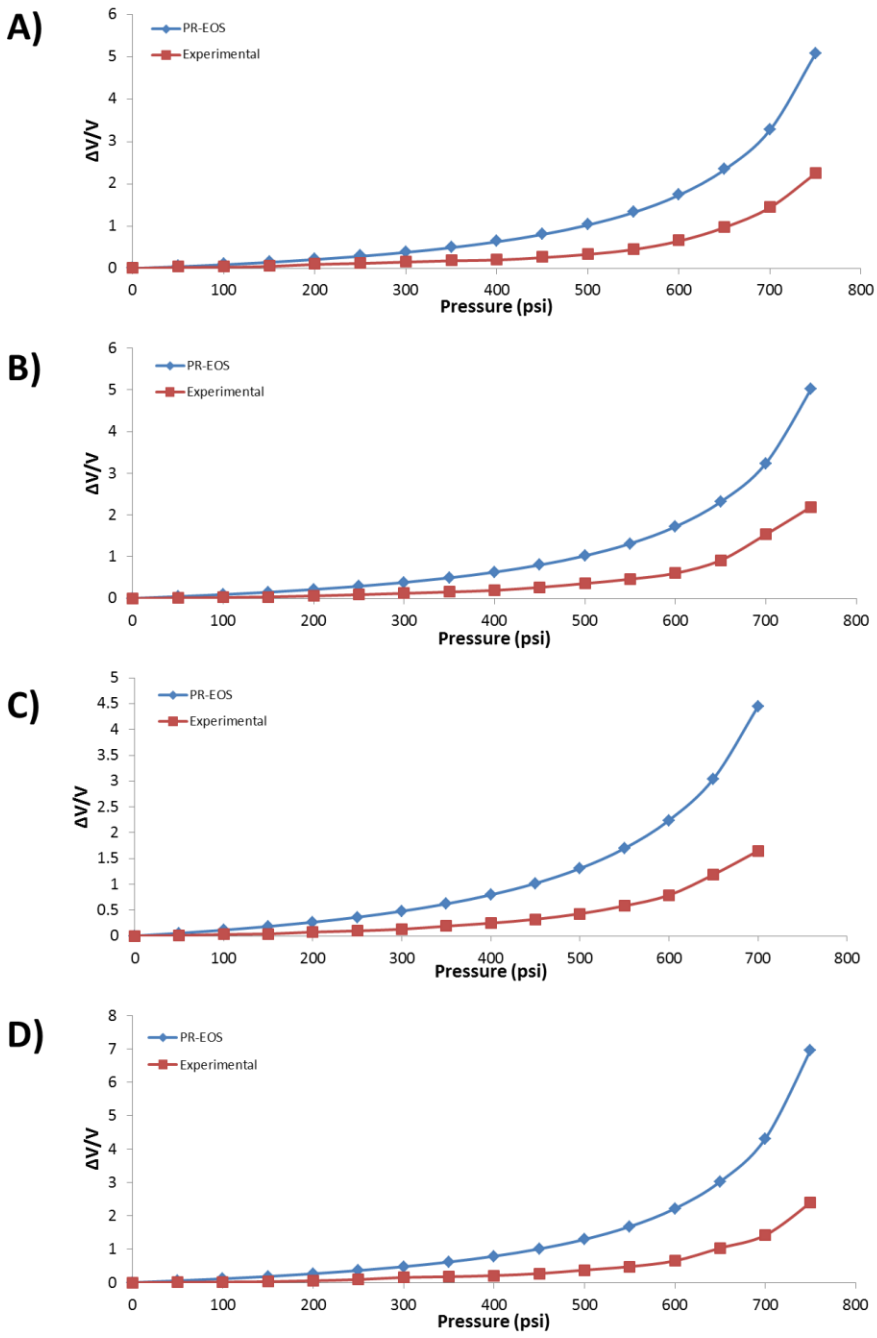

Figure 2.4 Comparison between experimental volume expansion data for various solvents and volume expansion predicted using Peng-Robinson Equation of State (PR-EOS). *(A) 2-methylpentane, (B) 3-methylpentane, (C) 2,2-dimethylbutane, (D) 2,3-dimethylbutane*

2.2.5 Size-selective fractionation process

This work employed a GXL size-selective nanoparticle separation process previously developed at Auburn University in order to obtain monodisperse nanoparticle fractions from a more polydisperse sample as described in detail elsewhere.(S R Saunders & Roberts, 2009) Specifically, this process allows for monodisperse nanoparticle samples to be separated from an initially polydisperse sample by inducing the controlled precipitation of a fraction of these nanoparticles to occur at a specific location in the apparatus through the application of elevated levels of CO_2 pressure. In short, using the apparatus shown in Figure 1.9, nanoparticles are separated based upon their size using the technique described in Section 1.2.2. Nanoparticles coated with the chosen ligand are dispersed in the solvent of choice and pressurized successively to predefined pressures of applied CO_2 to precipitate nanoparticles of increasingly smaller size with each fractionation. This entire process is repeated for each of the ligand-solvent combinations in order to examine the effects of solvent structure and ligand structure on nanoparticle precipitation, and therefore the effectiveness of this GXL nanoparticle fractionation process in light of each of these changes. Carbon-coated TEM grids of each of the collected nanoparticle fractions were then prepared via dropcasting and micrographs were acquired on a Zeiss EM 10 transmission electron microscope and sized using the ImageJ software package.

The polydispersity index (PDI) is a measure of the broadness of the size distribution which can be used to compare size distributions with dissimilar average diameters. A PDI of 1 indicates that all of the nanoparticles in a collected fraction are of exactly the same size (therefore, perfectly monodisperse), while larger values of the PDI

indicate a broader size distribution of nanoparticles. The PDI is calculated as employed elsewhere (S R Saunders & Roberts, 2009) where D_i is the size of a specific nanoparticle in a sample of 'n' nanoparticles. $\overline{D_W}$ is the diameter weighted average diameter and $\overline{D_N}$ is the number average diameter of the sample. The equations necessary for calculations are listed below.

$$PDI = \frac{\overline{D_W}}{\overline{D_N}} \quad \text{.....Equation 2-1}$$

$$\overline{D_W} = \frac{\sum_i D_i^2}{\sum_i D_i} \quad \text{.....Equation 2-2}$$

$$\overline{D_N} = \frac{1}{n}\sum_i D_i \quad \text{.....Equation 2-3}$$

2.3 Results and Discussions

The effect that different interactions between solvents and ligands have on nanoparticle precipitation from (and dispersability in) GXLs can be effectively studied using the techniques described above. The solution of dodecanethiol capped gold nanoparticles dispersed in *n*-hexane solvent was used as the control for the entire set of experiments presented in this study since *n*-hexane is a popular solvent in similar nanoparticle dispersion systems and had been researched extensively by our group previously. (S R Saunders & Roberts, 2009; Steven R. Saunders & Roberts, 2011) Also, *n*-hexane is a linear molecule whose volumetric expansion data can be accurately predicted using the unmodified Peng-Robinson Equation of State (PR-EOS). (Anand et al., 2008; Fuente et al., 2000; Mutelet et al., 2005) Volumetric expansion of *n*-hexane under varying amounts of CO_2 pressure was also measured experimentally in this work in order to verify the applicability of the PR-EOS, and it was determined that the volume expansion as predicted from the PR-EOS very closely matched the experimental data.

Dodecanethiol was chosen as the ligand for coating these gold nanoparticles in this control dispersion because it has been shown that dodecanethiol binds more strongly than other straight-chain alkanethiols and the longer thiols result in weakly bound multilayers. (Anand et al., 2005; Martin, Wilcoxon, Odinek, & Provencio, 2000) GXL nanoparticle separation experiments were performed on this control dispersion of dodecanethiol-coated gold nanoparticles in *n*-hexane solvent in order to establish the performance metrics to which the other solvent and ligand systems will be compared later in this study. The normalized absorbance of the dodecanethiol-coated gold nanoparticles dispersed in *n*-hexane (referred to herein as the dodecanethiol/*n*-hexane system) as a

function of the applied CO_2 pressure (i.e. precipitation curve) is presented in Figure 2.3. From this precipitation curve, it can be observed that the pressure of incipient precipitation (P_i) for the dodecanethiol-coated gold nanoparticles dispersed in *n*-hexane is around 41.4 bar. This relatively high P_i value can be attributed to the straight chain nature of *n*-hexane which can efficiently stabilize the straight chain ligands due to its symmetrical structure, thereby requiring higher dissolved CO_2 concentrations in order to destabilize the particles in this solvent. This result is consistent with that reported previously for the precipitation of dodecanethiol stabilized gold nanoparticles from *n*-hexane. (Anand et al., 2008; Steven R. Saunders & Roberts, 2011)

Constitutional isomers of *n*-hexane were chosen as the other solvents in this study in order to test the effect of their steric nature on the precipitation and size-selective fractionation of nanoparticles. The use of the constitutional isomers of *n*-hexane allows the steric nature of the solvent to be systematically adjusted in the different experiments in this study while also allowing the number of carbons in the solvent to be held constant. The same principle of selection was followed for the choice of ligands in this study. The popular and previously studied ligand dodecanethiol (Anand et al., 2008; McLeod, Anand, et al., 2005) and its isomer of *tert*-dodecanethiol were used so as to keep the number of carbons in the alkyl chain constant while affording very different steric structures. The structures of the solvents and ligands are shown in Figure 2.5. It should be noted that *tert*-dodecanethiol is only available commercially as a mixture of its positional isomers and a small variation in results due to this variation in steric nature is expected.

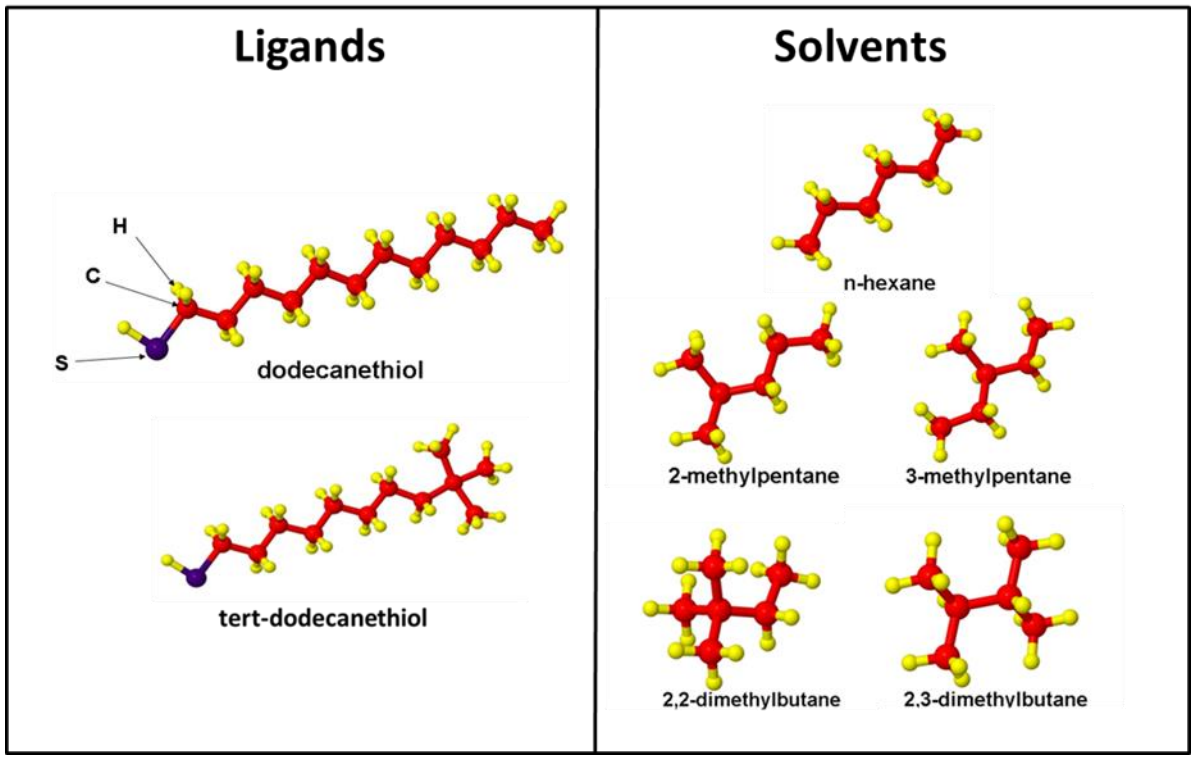

Figure 2.5 Structures of solvents and ligands used for the experiments carried out in this study

2.3.1 Straight chain ligand (dodecanethiol) with different solvents (isomers of *n*-hexane)

The next set of experiments involved varying the structure of the solvent employed, while keeping the ligand (dodecanethiol) structure consistent. These experiments aim to examine the effect that the steric nature of the solvent (i.e. the branched isomers of *n*-hexane) has on gold nanoparticle precipitation, while using particles coated with a straight chain ligand (dodecanethiol).

2.3.1.1 *Effect of steric nature of the solvent on P_i values with dodecanethiol as the capping ligand*

From the precipitation curves shown in Figure 2.6, where each of the methylpentanes were used as the solvent, it can be deduced that there is not a significant difference between the precipitation curve for 2-methylpentane/dodecanethiol and 3-methylpentane/dodecanethiol systems. The P_i for both the 2-methylpentane/dodecanethiol and 3-methylpentane/dodecanethiol systems is found to be approximately 41 bar. This similarity in P_i values can be explained from the fact that both these molecules have similar and relatively symmetric structures which should have good interactions with and effectively stabilize the straight-chain ligands. These favorable interactions result in relatively high P_i values being observed. It could be expected that the 3-methylpentane would have a slightly higher P_i value due to its more symmetric nature, but, given the 50 psig pressure intervals used during this experimental process, it is not possible to delineate the differences in these precipitation thresholds with any further certainty.

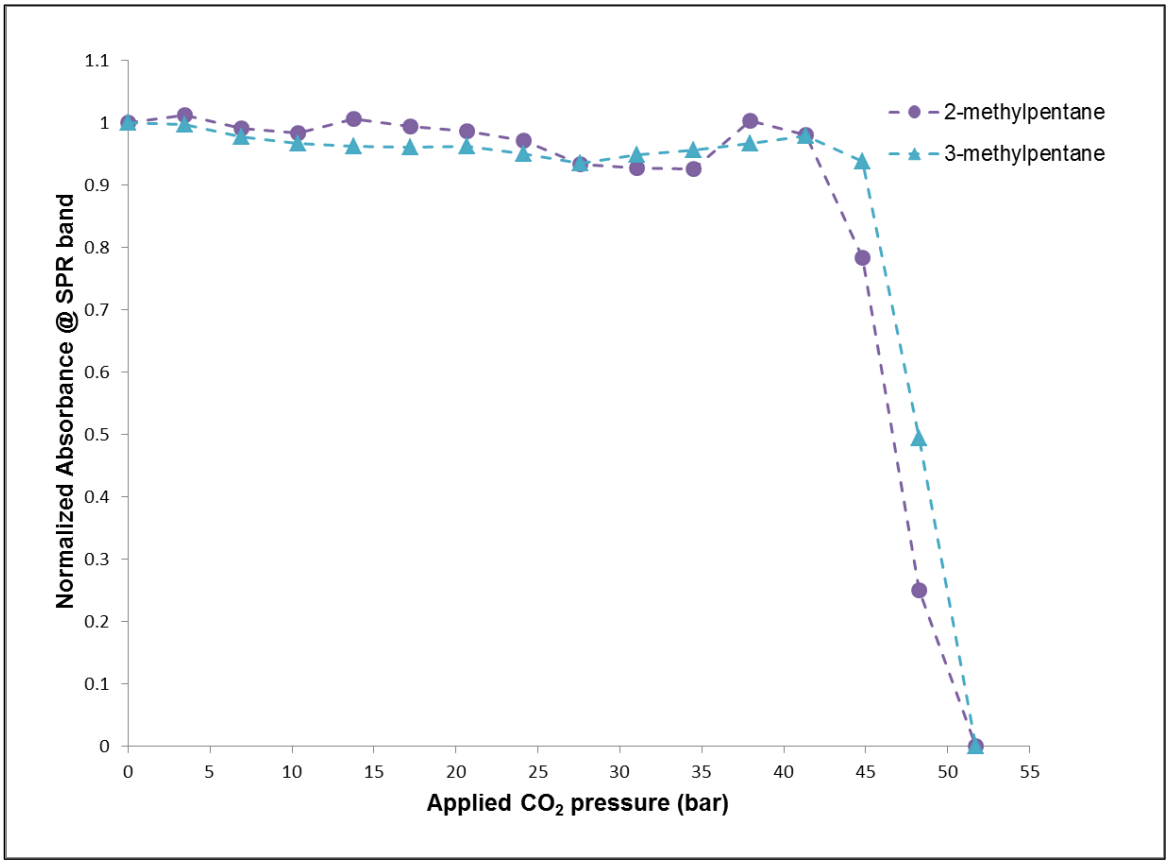

Figure 2.6 Precipitation curves for dodecanethiol coated gold nanoparticles dispersed in methylpentanes obtained by tracking the change in intensity of normalized SPR band using *in-situ* UV-Vis spectroscopy at different pressures.

As such, the performance of experiments with even smaller pressure intervals would be required to further ascertain the differences in the performance of these slightly different isomers. However, the precipitation curves that were obtained when using the different dimethylbutanes as solvent (as shown in Figure 2.7) illustrate more distinct differences in the precipitation curves for 2,2-dimethylbutane/dodecanethiol system and 2,3-dimethylbutane/dodecanethiol systems, with P_i values of approximately 38 bar and 41 bar, respectively. This difference in P_i values can be attributed to the fact that 2,2-dimethylbutane has a very bulky and branched structure compared to 2,3-dimethylbutane which has a very symmetric structure. It is expected that the more bulky and/or branched solvents will interact less favorably with the alkyl ligands than simple straight chain alkane solvents. In this case, the two extra terminal methyl groups that are on the butane chain within the 2,2-dimethylbutane result in increased steric hindrance, thereby resulting in poorer solvent-ligand interactions. This is reinforced by the fact that highly-branched alkanes have negligibly small surface energy compared to straight-chain alkanes. (Fowkes, 1980; Tancrède, Patterson, & Bothorel, 1977) This, in turn, results in an ability to destabilize the nanoparticle dispersion at lower CO_2 concentrations. This is supported by the principle that underlies the difference in boiling points of isomers which arise due to their sterically hindered nature. (W. H. Brown, Foote, Iverson, Anslyn, & Novak, 2011; Kelter, Michael, & Scott, 2008) The solvent-ligand interactions, if considered on the basis of dispersion forces, will scale with the surface area of the molecules. Based on this, the branched chain solvents are more compact than their straight-chain counterparts and we would expect them to have a lower surface area. This should result in weaker dispersion forces and hence weaker solvent-ligand interactions in

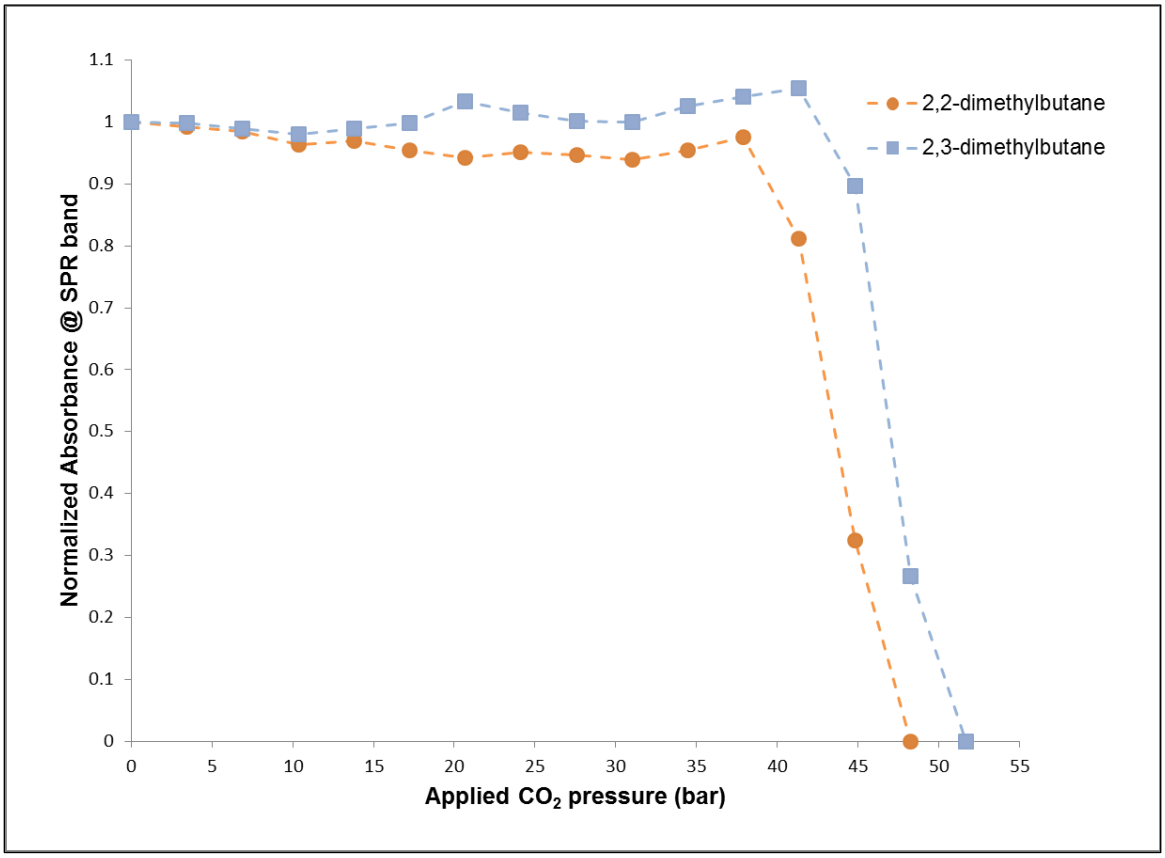

Figure 2.7 Precipitation curves for dodecanethiol coated gold nanoparticles dispersed in dimethylbutanes obtained by tracking the change in intensity of normalized SPR band using *in-situ* UV-Vis spectroscopy at different pressures.

the system.(W. H. Brown et al., 2011; Fowkes, 1980; Paulini, Frankamp, & Rotello, 2002) As such, these weakened interactions should allow us to precipitate nanoparticles from the branched chain solvent system at lower dissolved CO_2 concentrations, i.e. at a lower overall pressure, than their straight chain solvent counterparts.

2.3.1.2 *Effect of steric nature of the solvent on GXL fractionation process with dodecanethiol as the capping ligand*

A series of experiments were performed in order to examine the effectiveness of the GXL fractionation process when utilizing solvents of different steric nature. In order to have a constant frame of reference in all of these experiments, the initial pressure employed in the second stage of the process (P1) and the final pressure employed in the second stage of the process (P2) were determined from the "precipitation curves" for each respective solvent/ligand system. Specifically, P1 was assigned as the pressure that corresponded to the normalized absorbance value of 0.5 in the precipitation curve and P2 was assigned as the pressure that corresponded to the absorbance value of 0.4 in the same precipitation curves (as illustrated in Figure 2.2). This method of selecting the P1 and P2 values was based on the premise that particles of approximately the same size and composition should precipitate from each of the solvents within these absorbance values in each of the different sets of experiments. (Amendola & Meneghetti, 2009; Haiss et al., 2007; S R Saunders & Roberts, 2009; Steven R Saunders & Roberts, 2012; Steven R. Saunders & Roberts, 2011)

Monodisperse nanoparticle fractions by definition, means nanoparticles with standard deviation, σ, of diameter less than 5 % to 10 %.(Murray, Norris, & Bawendi, 1993) The nanoparticle fractions in this study however do not strictly fit this definition and are only relatively monodisperse compared to the original samples. The reason for this deviation is the method of basing the selection of P1 and P2 on specific absorbance values, which will allow for particle fractions of similar particle size to be obtained in each of the experiments (i.e. with the different solvents/ligands), but does not necessarily optimize the effectiveness of the fractionation process based on other parameters (such as yield of particles in the different fractions, monodispersity or the use of constant pressure intervals when collecting each fraction).

Nonetheless, it was important in this set of experiments to be able to compare the effectiveness of obtaining particles of similar size in each of the fractions when using the different solvent/ligand systems. With this said, it should also be noted that the original nanoparticle dispersions (prior to GXL fractionation) employed in all of these experiments contained particles of virtually identical size and size distribution. The P1 and P2 values for the control system of *n*-hexane/dodecanethiol were determined from the precipitation curve presented in Figure 2.3 using the method described above (and illustrated in Figure 2.2) where the absorbance value of 0.5 corresponded to a P1 value of 46.2 bar and the absorbance value of 0.4 corresponded to a P2 value of 46.5 bar. The P1 and P2 values for the other solvent-ligand combinations were determined similarly (corresponding the same absorbance values of 0.5 and 0.4, respectively) and are listed in Table 2.1. The pressure difference between two successive fractions is defined as ΔP where $\Delta P = P2 - P1$.

For the 2-methylpentane/dodecanethiol and the 3-methylpentane/dodecanethiol systems there is not a significant difference in the size distribution of the particles that constitute the first and second fractions which can be seen from the PDI values listed in Table 2.1. It is noted that these two systems yield nearly identical precipitation curves (Figure 2.6) stemming from the fact that they have only slightly different solvent structure. This similarity in solvent structure causes nanoparticles of comparable size and size-distribution to destabilize and precipitate from solution at generally the same pressure conditions. However, the first fractions that were obtained from the methylpentane systems (i.e. 2-methylpentane/dodecanethiol and the 3-methylpentane/dodecanethiol) had were more monodisperse (PDI of 1.03) than the first fraction that was obtained from the *n*-hexane/dodecanethiol control system (PDI of 1.06). This difference in polydispersity can be attributed to the fact that the particles precipitate from solution over a wider pressure range (ΔP) in the case of the methylpentane solvents compared to the smaller pressure range over which precipitation occurs in the *n*-hexane system. The *n*-hexane solvent system results in a relatively steep precipitation curve (Figure 2.3) that requires that the nanoparticles be precipitated from solution over a smaller pressure gradient (ΔP), thereby affording less resolution in their size-selective separation.(S R Saunders & Roberts, 2009; Steven R. Saunders & Roberts, 2011) CO_2 induced nanoparticle precipitation over a small pressure range is very sensitive to pressure variations and other environmental conditions which can result in greater polydispersity of the particles precipitating from solution, as is illustrated in the results presented in Table 2.1.

Table 2.1 Statistical summary of size-selective fractionation of gold nanoparticles using CO2 as GXL

experiment no.	ligand	solvent	P_i [a] (bar)	fraction	fractionation pressure (bar)	ΔP for 2nd fraction (bar)	mean diameter (nm)	standard deviation (nm)	PDI[b]
1	dodecanethiol	*n*-hexane	≈ 41.4	Original	-		4.8	1.2	1.06
				1st Fraction	0 - 46.19†		5.0	1.1	1.06
				2nd Fraction	46.19† - 46.54‡	0.35	4.6	1.0	1.05
				3rd Fraction	46.54‡ and above		3.8	0.8	1.05
2	dodecanethiol	2-methylpentane	≈ 41.4	Original	-		4.8	1.0	1.04
				1st Fraction	0 - 46.88†		5.4	1.0	1.03
				2nd Fraction	46.88† - 47.50‡	0.62	4.4	1.0	1.05
				3rd Fraction	47.50‡ and above		3.0	0.9	1.09
3	dodecanethiol	3-methylpentane	≈ 41.4	Original	-		4.6	1.0	1.05
				1st Fraction	0 - 48.60†		4.8	0.9	1.03
				2nd Fraction	48.60† - 49.30‡	0.70	3.8	0.8	1.05
				3rd Fraction	49.30‡ and above		2.8	1.0	1.13
4	dodecanethiol	2,2-dimethylbutane	≈ 37.9	Original	-		4.6	1.0	1.06
				1st Fraction	0 - 43.78†		5.2	0.9	1.03
				2nd Fraction	43.78† - 44.47‡	0.69	4.0	0.7	1.03
				3rd Fraction	44.47‡ and above		3.0	0.8	1.07
5	dodecanethiol	2,3-dimethylbutane	≈ 41.4	Original	-		4.8	1.1	1.06
				1st Fraction	0 - 46.88†		4.7	0.8	1.03
				2nd Fraction	46.88† - 47.57‡	0.69	3.9	1.1	1.08
				3rd Fraction	47.57‡ and above		3.0	1.0	1.10
6	*tert*-dodecanethiol	*n*-hexane	≈ 17.2	Original	-		3.6	1.1	1.10
				1st Fraction	0 - 34.47†		4.1	0.7	1.03
				2nd Fraction	34.47† - 36.54‡	2.07	3.6	0.7	1.04
				3rd Fraction	36.54‡ and above		3.1	0.8	1.06
7	*tert*-dodecanethiol	2,2-dimethylbutane	≈ 6.9	Original	-		3.4	1.0	1.09
				1st Fraction	0 - 26.13†		4.4	1.0	1.05
				2nd Fraction	26.13† - 28.96‡	2.83	4.0	0.8	1.04
				3rd Fraction	28.96‡ and above		3.4	0.8	1.06

[a] P_i = pressure of incipient precipitation

[b] PDI = polydispersity index

† = P1

‡ = P2

Table 2.1 also presents the experimental fractionation results for the 2,2-dimethylbutane/dodecanethiol and 2,3-dimethylbutane/dodecanethiol systems, where there are differences in the polydispersity values (i.e. PDI values) obtained from one system compared to the other. It is noted that the first fraction from both of the dimethylbutane systems (the 2,2-dimethylbutane/dodecanethiol and 2,3-dimethylbutane/dodecanethiol) has the same PDI value of 1.03. However, the second and third fractions obtained from the 2,2-dimethylbutane/dodecanethiol system exhibit lower PDI values than the respective fractions obtained from the 2,3-dimethylbutane/dodecanethiol system. This difference in polydispersity between these two systems can be attributed to the fact that the 2,2-dimethylbutane/dodecanethiol system has a lower P_i value and a less steep precipitation curve compared to the one for 2,3-dimethylbutane/dodecanethiol system. This results into the ability to have particles precipitate more gradually over a wider pressure range thereby providing a slightly higher resolution to the fractionation process as a function of the applied CO_2 pressure. This, in turn, results in the ability to have particles of more uniform size precipitate from solution over a given pressure range, thereby resulting in lower PDI values for the 2,2-dimethylbutane/dodecanethiol system. Furthermore, Figure 2.8 presents a visual comparison of the results obtained from the 2,2-dimethylbutane/dodecanethiol system to those obtained for the control system of *n*-hexane/dodecanethiol, where each of the three fractions were collected at the conditions noted in Table 2.1. Due to the wider pressure range over which precipitation occurs in the 2,2-dimethylbutane/dodecanethiol system (i.e. less steep precipitation curve), this system yielded narrower size-fractions when compared to the *n*-hexane/dodecanethiol system despite the fact that larger ΔP values

were employed in collecting each of the three fractions. 2,2-dimethylbutane provided the lowest P_i value amongst each of the solvents (*n*-hexane, 2-methylpentane, 3-methylpentane, 2,2-dimethylbutane, and 2,3-dimethylbutane) that were examined with this straight-chain ligand (i.e. dodecanethiol capped nanoparticles). Because of this, 2,2-dimethylbutane was used as a solvent in subsequent investigations into the effect that a branched ligand (*tert*-dodecanethiol) has on nanoparticle precipitation and fractionation in GXL systems.

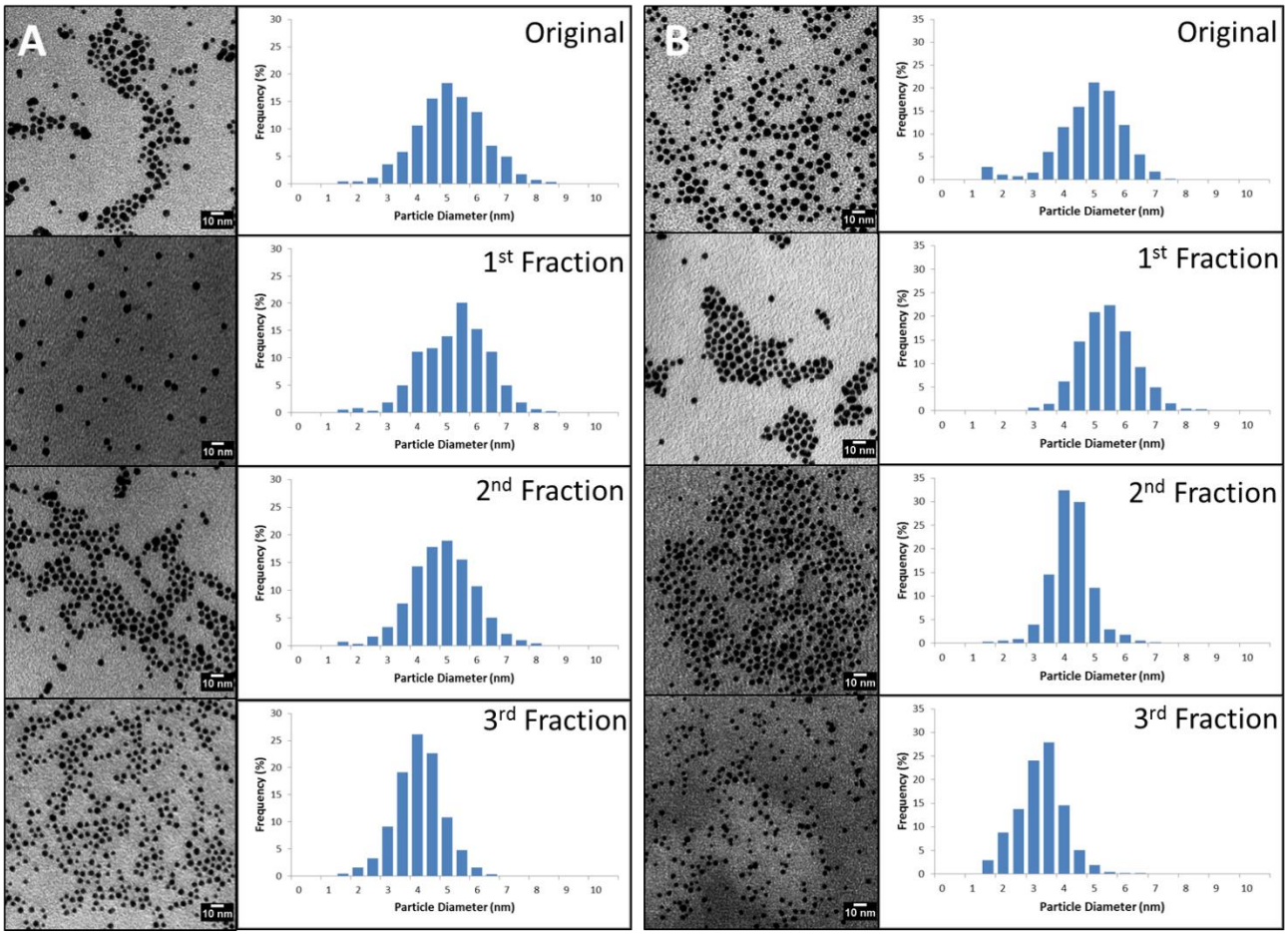

Figure 2.8 TEM micrographs and size distribution of dodecanethiol stabilized gold nanoparticles dispersed in *n*-hexane (A) and 2,2-dimethylbutane (B) fractionated into three distinct size-fractions using a CO_2 GXL. The pressures used for each of the fractions are listed in Table 1.

2.3.2 Branched chain ligand (*tert*-dodecanethiol) and various solvents (*n*-hexane & 2,2-dimethylbutane)

This set of experiments also involved varying the structure of the solvent employed while keeping the ligand structure consistent. However, a branched-chain stabilizing ligand (*tert*-dodecanethiol) was used instead of the straight-chain ligand (dodecanethiol) in examining the effect that the steric nature of the ligand has on gold nanoparticle precipitation. These experiments were performed using two different solvents. The first experiment involved using *tert*-dodecanethiol stabilized gold particles that were dispersed in 2,2-dimethylbutane solvent, and the second experiment involved using the same *tert*-dodecanethiol stabilized gold particles dispersed in *n*-hexane solvent (the control solvent). Recall that the 2,2-dimethylbutane was chosen as one of the solvents in this set of experiments because it provided the lowest P_i value among all of the solvents employed when investigating the straight chain ligand systems.

2.3.2.1 *Effect of the steric nature of the solvent on P_i values with tert-dodecanethiol as the capping ligand*

Figure 2.9 presents the precipitation curves for the *n*-hexane/*tert*-dodecanethiol system and the 2,2-dimethylbutane/*tert*-dodecanethiol system, where it is clearly demonstrated that *tert*-dodecanethiol capped particles precipitate at lower overall pressures in the 2,2-dimethylbutane solvent compared to the *n*-hexane solvent. The P_i for *n*-hexane/*tert*-dodecanethiol system is approximately 17 bar and that for the 2,2-dimethylbutane/*tert*-dodecanethiol system is roughly 7 bar. It is noted that the normalized absorbance for the 2,2-dimethylbutane/*tert*-dodecanethiol system begins to fall slightly below 1.0 even at very low applied CO_2 pressures such that the P_i value may actually be

lower than the approximated 7 bar listed here. In comparing the results in Figure 2.9 for the *tert*-dodecanethiol systems with the results in Figure 2.6 & Figure 2.7 for the dodecanethiol system, it is observed that the branched-chain ligand gives significantly lower P_i values compared to its straight-chain counterpart in each of the solvents. The P_i values of ~17 bar and ~7 bar that were obtained from the *n*-hexane/*tert*-dodecanethiol and 2,2-dimethylbutane/*tert*-dodecanethiol systems, respectively, are radically different from the P_i values of ~41 bar and ~38 bar that were obtained from the *n*-hexane/dodecanethiol and 2,2-dimethylbutane/dodecanethiol systems, respectively.

The combination of a sterically hindered solvent (2,2-dimethylbutane) with a sterically hindered ligand (*tert*-dodecanethiol) results in further deteriorated of the strength of the solvent-ligand interactions when compared to the use of the straight-chain solvent (*n*-hexane) and the straight-chain ligand (dodecanethiol), or even when compared to the use of the sterically hindered ligand (*tert*-dodecanethiol) with the straight-chain solvent. Obviously, the use of bulky, sterically hindered species in both capacities dramatically affects the ability of the GXL system to thermodynamically disperse nanoparticles, thereby drastically reducing the applied CO_2 pressure necessary for their removal from the CO_2 + solvent mixture. This reduction in the strength of the solvent-ligand interactions causes an almost 6 fold decrease in the P_i values for the 2,2-dimethylbutane/*tert*-dodecanethiol system (~7 bar) when compared to the *n*-hexane/dodecanethiol control system (~41 bar), stemming from a lower concentration of CO_2 being required to destabilize the nanoparticles from the solvent.

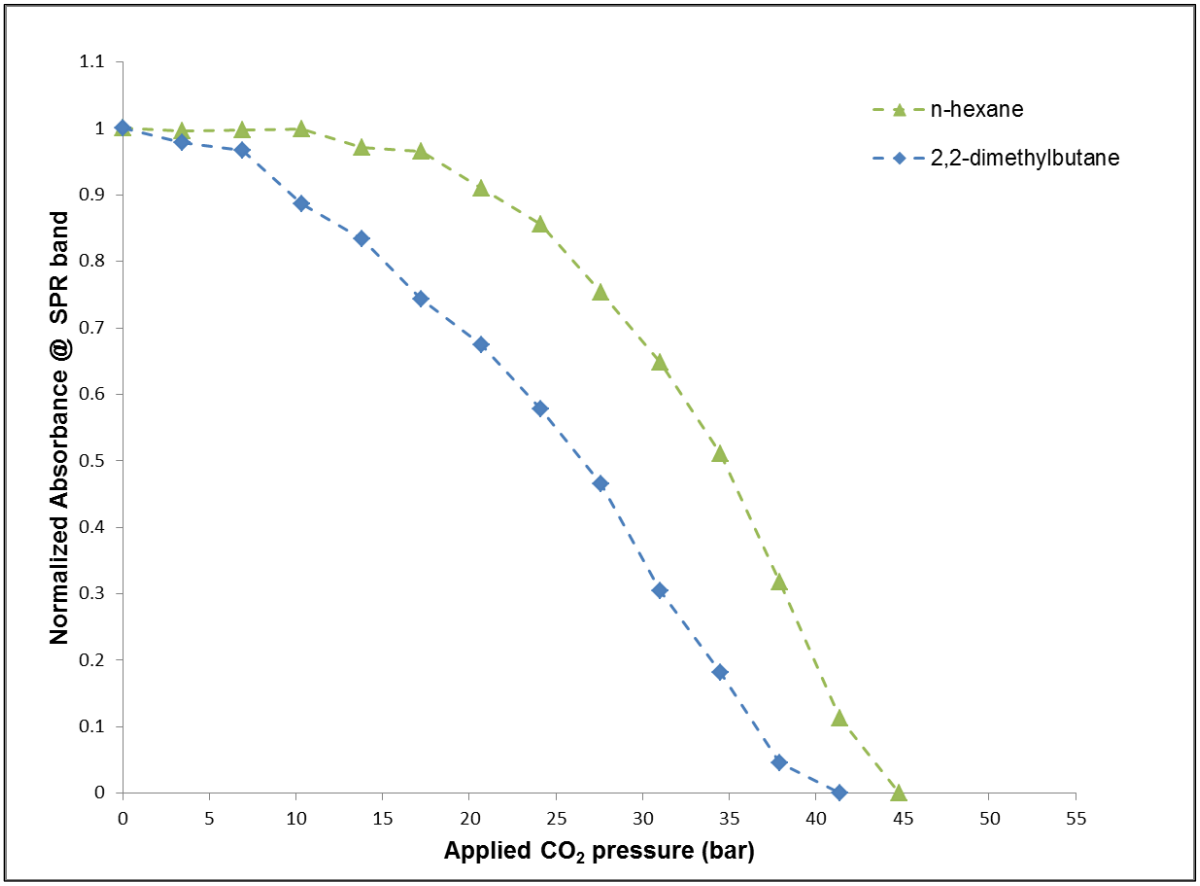

Figure 2.9 Precipitation curves for *tert*-dodecanethiol coated gold nanoparticles dispersed in *n*-hexane and 2,2-dimethylbutane obtained by tracking the change in intensity of normalized SPR band using *in-situ* UV-Vis spectroscopy at different pressures**.**

2.3.2.2 *Effect of the steric nature of the solvent on GXL fractionation process with tert-dodecanethiol capped nanoparticles (branched chain ligand)*

Figure 2.10 and Table 2.1 presents the results of the fractionation of *tert*-dodecanethiol coated gold nanoparticles dispersed in *n*-hexane and 2,2-dimethylbutane, respectively. As stated earlier in this study, the fractionation pressures (P1 and P2) that were employed in this set of experiments were determined from the precipitation curves for these systems, Figure 2.9, where P1 and P2 correspond to the normalized absorbance values of 0.5 and 0.4, respectively. The data in Table 2.1 illustrates that successful GXL fractionations were achieved using the *n*-hexane/*tert*-dodecanethiol and 2,2-dimethylbutane/*tert*-dodecanethiol systems, where distinctly different size fractions were obtained coupled with PDI values that are very comparable to those obtained from the *n*-hexane/dodecanethiol control system. It is important to note that these successful fractionations were performed using much lower applied CO_2 pressures, and higher ΔP values, than those necessary in the *n*-hexane/dodecanethiol control system. Simply based on the desire to lower the overall operating pressure in a fractionation process of this type, one might consider the combination of the 2,2-dimethylbutane solvent and the *tert*-dodecanethiol ligand capped nanoparticles to be the optimal system among those that were investigated in this study.

To further test the worthiness of the 2,2-dimethylbutane/*tert*-dodecanethiol system, fractionations were carried out over the entire precipitation range at 150 psig intervals (10.3 bar) to investigate where the particles of the highest relative monodispersity are obtained and what size nanoparticles fall out at the predetermined pressure intervals.

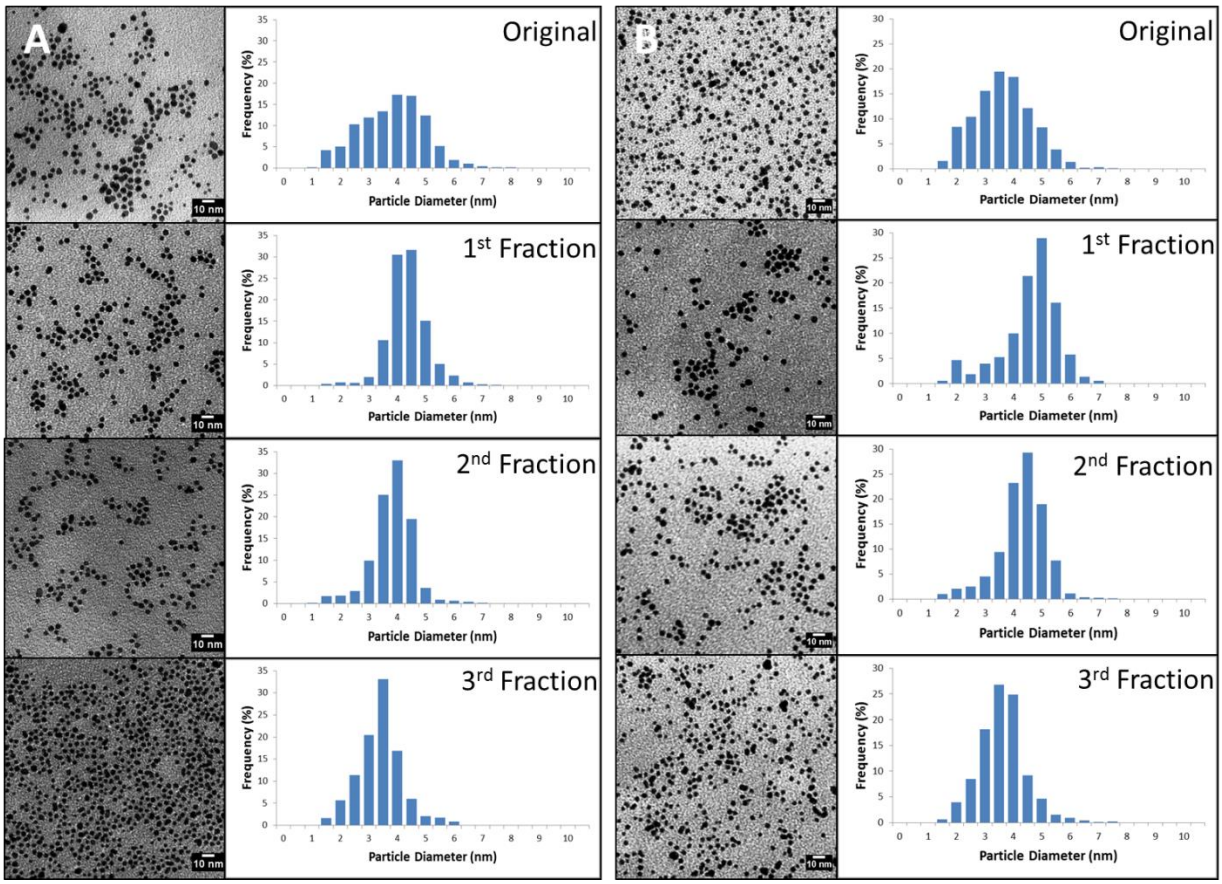

Figure 2.10 TEM micrographs and size distribution of *tert*-dodecanethiol stabilized gold nanoparticles dispersed in *n*-hexane (A) and 2,2-dimethylbutane (B) fractionated into three distinct size-fractions using a CO_2 GXL. The pressures used for each of the fractions are listed in Table 2.1.

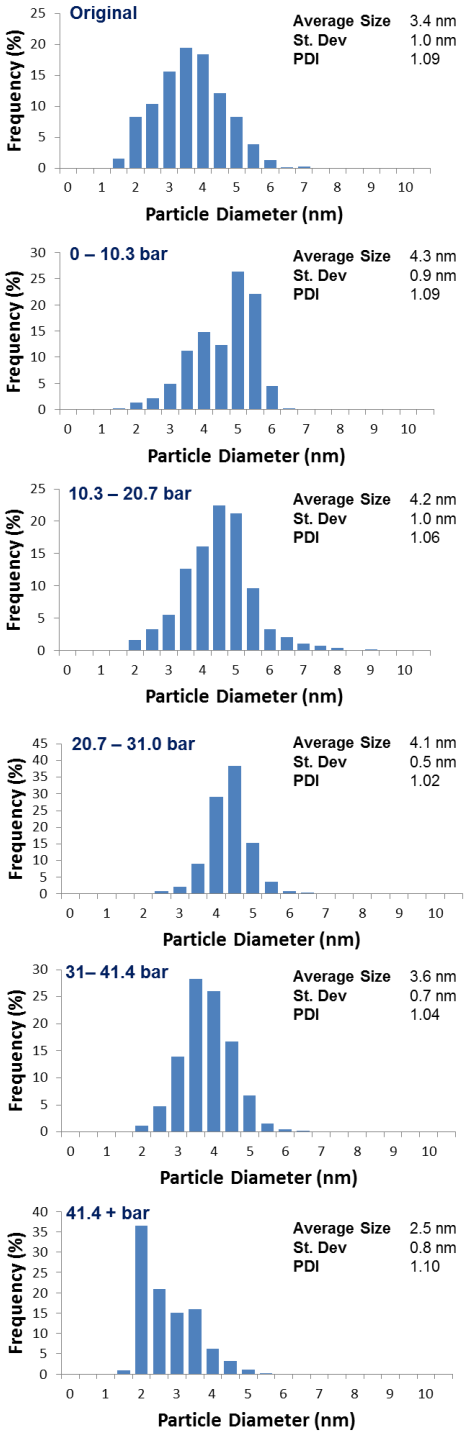

Figure 2.11 Size distribution of *tert*-dodecanethiol stabilized gold nanoparticles dispersed in 2,2-dimethylbutane fractionated into five distinct size-fractions using a CO_2 GXL. The pressures difference between each of these fractions is 150 psig (10.3 bar)

The fractionations were carried out in a recursive manner as described in previous literature.(S R Saunders & Roberts, 2009) The results of these fractionations are shown in Figure 2.11. As expected we see a decrease in average particle size as the fractionation pressure increases (Figure 2.12a) varying from 4.3 nm to 2.5 nm. By observing the change in PDI values with the fractionation pressures (Figure 2.12b), it can be deduced that at the beginning of the precipitation curve more polydisperse particles are obtained, while more monodisperse particles are obtained by carrying out fractionations around the center of the fractionation curve and around the average size of the original nanoparticle fraction. This is consistent with the results obtained for previously studied systems in the literature.(Anand et al., 2008; McLeod, Anand, et al., 2005; S R Saunders & Roberts, 2009; Steven R. Saunders & Roberts, 2011)

One important parameter that has not been discussed to this point, but is important from a process control point-of-view, is the time necessary to conduct each stage of the GXL fractionation process. In the systems where dodecanethiol was used as the stabilizing ligand of choice, approximately 20-30 mins were required to carry out each successive fractionation step, and the entire GXL fractionation process was completed in about an hour. However, for the systems in which particles were coated with *tert*-dodecanethiol, each fractionation step took around 90-120 mins and the entire process took more than 4 hours. This increase in processing time results from the fact that the *tert*-dodecanethiol ligand coated gold nanoparticles precipitate from solution at lower overall applied CO_2 pressures, and as such, they precipitate more slowly because of the

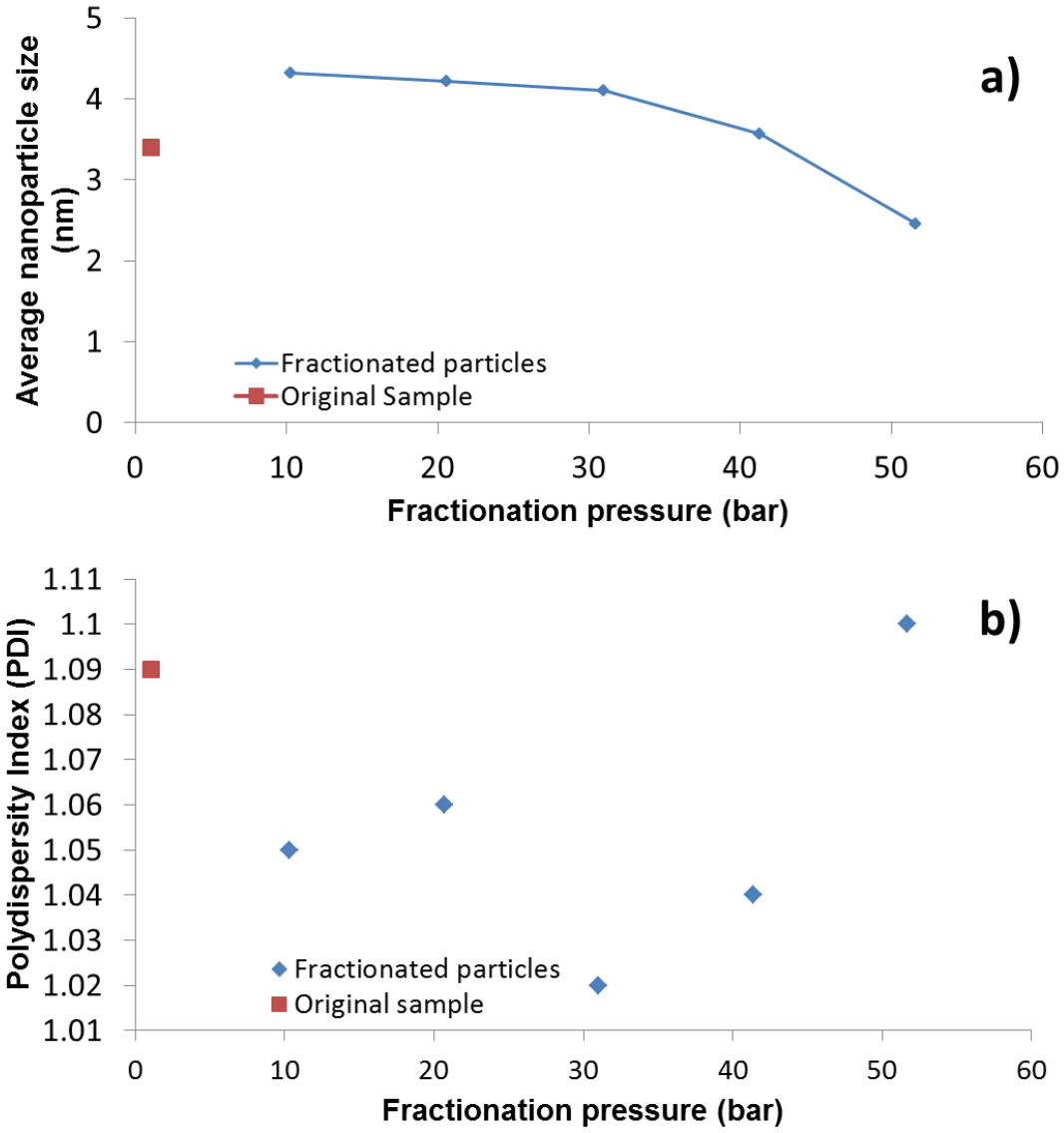

Figure 2.12 Change in average nanoparticle size (a) and polydispersity index (b) of precipitated nanoparticles with fractionation pressure for the 2,2-dimethylbutane/*tert*-dodecanethiol system using a CO_2 GXL. The pressures difference between each of these fractions is 150 psig (10.3 bar)

different thermophysical properties of the solvent mixture at those conditions. These GXL systems have higher viscosities and lower diffusion coefficients at the lower applied CO_2 pressures (i.e. lower CO_2 concentration) than they do when subjected higher CO_2 pressures (Scurto, Hutchenson, & Subramaniam, 2009).

As a result, there is an inherent trade-off between processing time and the pressures required to precipitate particles from solution in these different solvent/ligand systems, and it may not be possible to eliminate this issue completely without major process modifications.(Steven R. Saunders & Roberts, 2011) This will be an important factor to consider when scaling up the process and in determining optimum operating conditions.

2.4 Conclusion

In summary, through the simple adjustment in the solvent-ligand interactions by manipulating the steric nature of the solvent and ligand we were able to reduce the applied pressure for gold-nanoparticle precipitation from GXLs. From the various combination of solvents/ligands employed in this study to understand the influence of the steric nature of solvents/ligands on nanoparticle precipitation and fractionation, it was deduced that the 2,2-dimethylbutane/*tert*-dodecanethiol system offered the largest reduction in P_i value while retaining good fractionation characteristics. This almost six-fold reduction in P_i value from 41.4 bar (*n*-hexane/dodecanethiol system) to 6.9 bar (2,2-dimethylbutane/*tert*-dodecanethiol) can be attributed to the reduction in solvent-ligand interactions due to the steric hindrance offered by the branched ligand and branched solvent. By employing both a branched ligand and a branched solvent, successful fractionations were obtained at lower overall pressures and higher ΔP values compared to the straight chain ligand and straight chain solvent control system. This suggests that one can influence the process parameters critical to the GXL size-selective fractionation process by simply changing the physical interactions between the nanoparticles and the solvent, and this strategy can be used to effectively tune these parameters.

Chapter 3

Size-Selective Nanoparticle Fractionation of Iron Oxide Nanoparticles using a Gas-Expanded Liquid Process

3.1 Introduction

Metal-oxide nanoparticles are expected to have wide-scale applicability in the near future in various industrial fields including catalysis (J.-Y. Park et al., 2010; Zhao, Zhu, Gao, Zhai, & Ma, 2013), biomedicine (Bulte & Kraitchman, 2004; Jo, Aoki, & Tabata, 2010; Thorek, Chen, Czupryna, & Tsourkas, 2006), enhanced oil recovery (Baran Jr, Jimmie R., & Cabrera, 2006) and environmental remediation (Orbell et al., 1997; Rajeshwar & de Tacconi, 2009; W. Zhang, 2003). Iron oxide nanoparticles are especially important in this section of nanoscience because of their magnetic nature, relative safety and affordability. Nanoparticles within the size range of 1-100 nm have extremely size-dependent physicochemical properties which arise due to their dimensions being intermediate between the atomic and molecular size regimes (C. N. R. Rao et al., 2002). It is critical to harness these size-dependent properties for the effective use of nanoparticles in the applications mentioned above. There are two ways to go about harnessing these size-dependent properties of nanoparticles. The first way is to synthesize monodisperse nanoparticles using various specialized-synthesis methods and then use these nanoparticles in the targeted applications.

However, a large number of these specialized-synthesis techniques suffer from disadvantages such as requiring high temperatures (Hyeon et al., 2001; Z. Xu, Shen, Tian, Shi, & Gao, 2010; Yu, Falkner, Yavuz, & Colvin, 2004) and expensive reagents (J.-G. J. J.-H. Park et al., 2005; Yu, Chang, Sayes, Drezek, & Colvin, 2006), making large scale synthesis of these particles expensive. The other way to harness the size-dependent nanoparticle properties is to use a simple and cheap synthesis technique to generate polydisperse nanoparticles and then process them using various techniques like magnetic separation (Yavuz et al., 2006), centrifugation (Novak et al., 2001), and electrophoresis (Surugau & Urban, 2009) to obtain monodisperse particles. Most of these post-synthesis processing methods suffer from certain drawbacks such as requiring expensive equipment, having low throughputs and large solvent amounts (Bishop et al., 2009; Fletcher, 1991; S R Saunders & Roberts, 2009).

Previously, it has been shown that nanoparticle dispersions of different materials like CdSe/ZnS quantum dots and gold nanoparticles can be effectively precipitated using GXLs with CO_2 as the gaseous antisolvent (Anand et al., 2007; McLeod, Kitchens, et al., 2005; S R Saunders & Roberts, 2009). Several studies which modified the solvent-ligand combinations were also successful in tuning the pressures required to fractionate gold nanoparticles using the GXL technique (Steven R. Saunders & Roberts, 2011; P. Vengsarkar & Roberts, 2013). However, gold nanoparticles have limited use in contemporary industrial applications excluding certain biomedical roles. Iron oxide nanoparticles on the other hand have a wider applicability in current and future fields. These include use in areas such as magnetic resonance imaging (MRI) contrast agents (Andreas et al., 2012; Babes et al., 1999; Hong et al., 2008; Hu, Jia, Li, & Gao, 2011;

Kwak, 2005; R. Qiao et al., 2009), drug delivery agents (Jain et al., 2005; M. A. Morales, Jain, Labhasetwar, & Leslie-Pelecky, 2005; M. Morales et al., 2008), catalysts (Hosseinian, Rezaei, & Mahjoub, 2011; Khedr, Abdel Halim, & Soliman, 2009; J.-Y. Park et al., 2010; Torres Galvis, Bitter, Khare, et al., 2012), and for the formation of Pickering emulsions (Bernard P. Binks & Whitby, 2005; Zhou, Wang, Qiao, Binks, & Sun, 2012).

Iron oxide nanoparticles are significantly different from noble metal nanoparticles due to the oxide layer on the surface. Iron oxide nanoparticles provide a whole new set of challenges when compared to noble metal nanoparticles because iron as an element can take on multiple oxidation states (I, II and III) and hence we can get FeO, Fe_2O_3 and Fe_3O_4 as the oxidation products for it. The structure for FeO is a cubic rock salt structure while Fe_3O_4 has a cubic inverse spinel structure due to having small amounts of FeO. Fe_2O_3 on the other hand has many different polymorphs including α- Fe_2O_3 (rhombohedral) and γ- Fe_2O_3 (cubic). The presence of FeO is rare in most of the synthesis process and the polymorphs of Fe_2O_3 usually convert to α-Fe_2O_3 over time which makes Fe_3O_4, α-Fe_2O_3, and γ-Fe_2O_3 the most common forms of iron oxide present (Teja & Koh, 2009). For accurate, reproducible results we need to have the same form of iron oxide present in the system and there should be as little change as possible in the oxide structure occurring during the GXL process. The choice of iron oxide nanoparticle for various applications falls into the following general categories: namely, Fe_3O_4/α-Fe_2O_3 for catalysis, α-Fe_2O_3/γ-Fe_2O_3 for non-biomedical magnetic applications and Fe_3O_4/γ-Fe_2O_3 for biomedical applications. (Teja & Koh, 2009)

This chapter deals with the ability to extend the application of the GXL fractionation process to iron oxide nanoparticles. For the first part of this study commercially available oleic acid-coated spherical iron oxide nanoparticles of various sizes were bought and fractionated to observe if the fractionation of iron oxide nanoparticles was theoretically possible in the cascaded vessel apparatus. Detailed UV-vis studies were carried out on these iron oxide nanoparticles to determine the P_i values for these systems. A mixture having 1:1 volume ratio of these 20 nm and 5 nm iron oxide nanoparticles was then fractionated to determine the effectiveness of GXL fractionation on iron oxide nanoparticles. In the second part of this study nanoparticles were synthesized in large quantities using the coprecipitation method to study the ability to fractionate concentrated nanoparticle samples. The iron oxide nanoparticles were also coated with carboxylic acids of different chain lengths to study the effect of ligand length on nanoparticle precipitation and GXL fractionation. The study with these cheaply made concentrated samples was done so as to check the applicability of the GXL cascaded vessel apparatus in fractionating large quantities of nanoparticles necessary for application studies in subsequent chapters.

3.2 Experimental Section

3.2.1 Materials

Iron (III) chloride hexahydrate ($FeCl_3 \cdot 6H_2O$, 99.9%), iron (II) chloride tetrahydrate ($FeCl_2 \cdot 4H_2O$, 99.9%), Iron (II, III) oxide (Fe_3O_4, 99%), Iron (III) oxide (Fe_2O_3, 99%), and *n*-hexane (HPLC grade, 95%), were obtained from Alfa Aesar. Oleic acid (99%), dodecanoic acid, nonanoic acid (99 %) and octanoic (98+ %) acid were obtained from Sigma Aldric, and ammonium hydroxide (5M) was obtained from BDH. Ethanol (94.0-96.0%) was obtained from Mallinckrodt Chemicals while toluene (HPLC grade, 99.9%) and (deionized ultra-filtered) DIUF water were obtained from Fisher. Carbon dioxide (SFC/SFE grade) was obtained from Airgas. All chemicals were used as received without further purification.

Spherical oleic acid-coated Fe_3O_4 nanoparticles dispersed in toluene (average size 20 nm and 5 nm) were purchased from Sigma Aldrich. The dispersion concentration was 5 mg/mL for both the 20 nm and 5 nm nanoparticle dispersions and the dispersions contained less than 1.0% oleic acid. The iron oxide nanoparticles were dried using nitrogen and redispersed in *n*-hexane for all experiments performed in this study

3.2.2 Iron Oxide Nanoparticle Synthesis and Characterization

3.2.2.1 *Characterization of commercially bought spherical oleic acid coated Fe_3O_4 nanoparticles*

For use in the first part of this study, the 100 μL of the commercially bought nanoparticle dispersion in toluene was added to a scintillation vial followed by evaporation of the toluene using nitrogen. The solvent used for this study, *n*-hexane, was

then added (5 mL) to this vial and agitated to obtain a dispersion of the iron oxide nanoparticles in *n*-hexane. These steps were performed on both the 20 nm and 5 nm average size nanoparticle dispersions. For the sake of simplicity, these nanoparticle samples will be called 'FeNP-20' and 'FeNP-5' particles respectively throughout this study. A 1:1 mixture *by volume* was also prepared using the 20 nm (large) (50 μL) and 5 nm (small) (50 μL) particles to obtain dispersion in *n*-hexane containing both 20 nm and 5 nm iron oxide nanoparticles. This nanoparticle mixture, which will be used to check the effectiveness of the fractionation process, will be referred to as 'FeNP-mixture' throughout this study. These 5 mL dispersions of nanoparticles in *n*-hexane were then used for the all the experiments listed in this chapter. The particles were then characterized using FTIR spectroscopy and TEM. For FTIR analysis, the dispersions in *n*-hexane were added dropwise to a small amount of KBr powder, allowed to dry and then pelletized using a pellet press. A baseline for pure KBr and atmospheric correction was used for all the samples studied. Carbon-coated TEM grids of each of the nanoparticle samples were prepared via dropcasting and micrographs were acquired on a Zeiss EM 10 transmission electron microscope and sized using the ImageJ software package.

3.2.2.2 *Synthesis and characterization of fatty acid coated iron oxide nanoparticles (dispersible in organic solvent)*

Iron oxide nanoparticles coated with oleic acid (replaceable with other carboxylic acids) were synthesized based on a coprecipitation method described previously by Jain et al. (Jain et al., 2005). Initially aqueous solutions of 0.1 M Fe (III) and 0.1 M Fe (II) were prepared using DIUF water. 30 mL of Fe (III) solution was mixed with 15 mL of Fe

(II) solution in a three-necked flask with magnetic stirring. Under constant stirring and under a nitrogen atmosphere, 3 mL of 5 M ammonium hydroxide was added to this mixture to generate a black precipitate of iron oxide nanoparticles. The temperature of this system was them increased to 80 °C and maintained for 30 mins to evaporate the ammonia out of the solution. While the temperature is being increased 280μL of oleic acid was added to the mixture. The system temperature was then lowered to 60 °C and held there for 1 hour. After the end of the heating cycle the system was allowed to cool down to room temperature and washed with water to remove any excess reagents and impurities. Then 30 mL of ethanol was added and the particles were magnetically immobilized and washed with ethanol twice. The particles were then dried using nitrogen and dispersed in *n*-hexane via sonication (Fischer Scientific FS20). A similar synthesis method was used to synthesize particles coated with dodecanoic acid, nonanoic acid and octanoic acid. The particles synthesized using these methods were characterized using FTIR spectroscopy and TEM in the same way as explained in Section 3.2.2.1

3.2.3 Monitoring nanoparticle dispersability using UV-Vis spectroscopy

As shown in the previous chapter, the absorption spectra of metallic gold nanoparticles is characterized by a strong broad absorption band at around 520 nm that is absent in the bulk metal spectra (Amendola & Meneghetti, 2009; Haiss et al., 2007). However, for iron oxide nanoparticles no such absorption band is present and a relatively flat spectrum with a plateau at around 480 nm is observed as seen in for the oleic acid and dodecanoic acid capped particles in Figure 3.2. This is consistent with other results observed in literature (Kang, Lee, & Stroeve, 1998; Kebede et al., 2013; Klačanová, Fodran, & Šimon, 2013; Walt, Chown, Harris, Sosibo, & Tshikhudo, 2010). A peak for

iron oxide nanoparticles is observed in the UV range at around 215 nm (Kebede et al., 2013); however, since the light absorption is extremely high in the UV range, extremely dilute samples need to be used. Hence, this peak was not used for analysis and solutions of moderate concentration were used for analysis. The absorption value at 480 nm was selected as the point for monitoring the nanoparticle precipitation. The conditions present in an expanding GXL containing iron oxide nanoparticles can also be traced effectively by using these absorption values. The UV-vis experiments for this study were performed in the same manner as reported in Section 2.2.3. For the first set of experiments involving the spherical particles, UV-vis studies were performed on FeNP-5, FeNP-20 and FeNP-mixture samples. The UV-vis spectra for these three systems at different applied CO_2 pressure values are shown in Figure 3.1. The UV-vis spectra for the second set of experiments using the faceted iron oxide particles, synthesized using the coprecipitation method, are shown in Figure 3.2. These absorption values from these UV-vis absorption curves are then corrected in the same way as shown in Chapter 2 to obtain the precipitation curves. The precipitation curves for the as shown in Figure 3.3 and Figure 3.4.

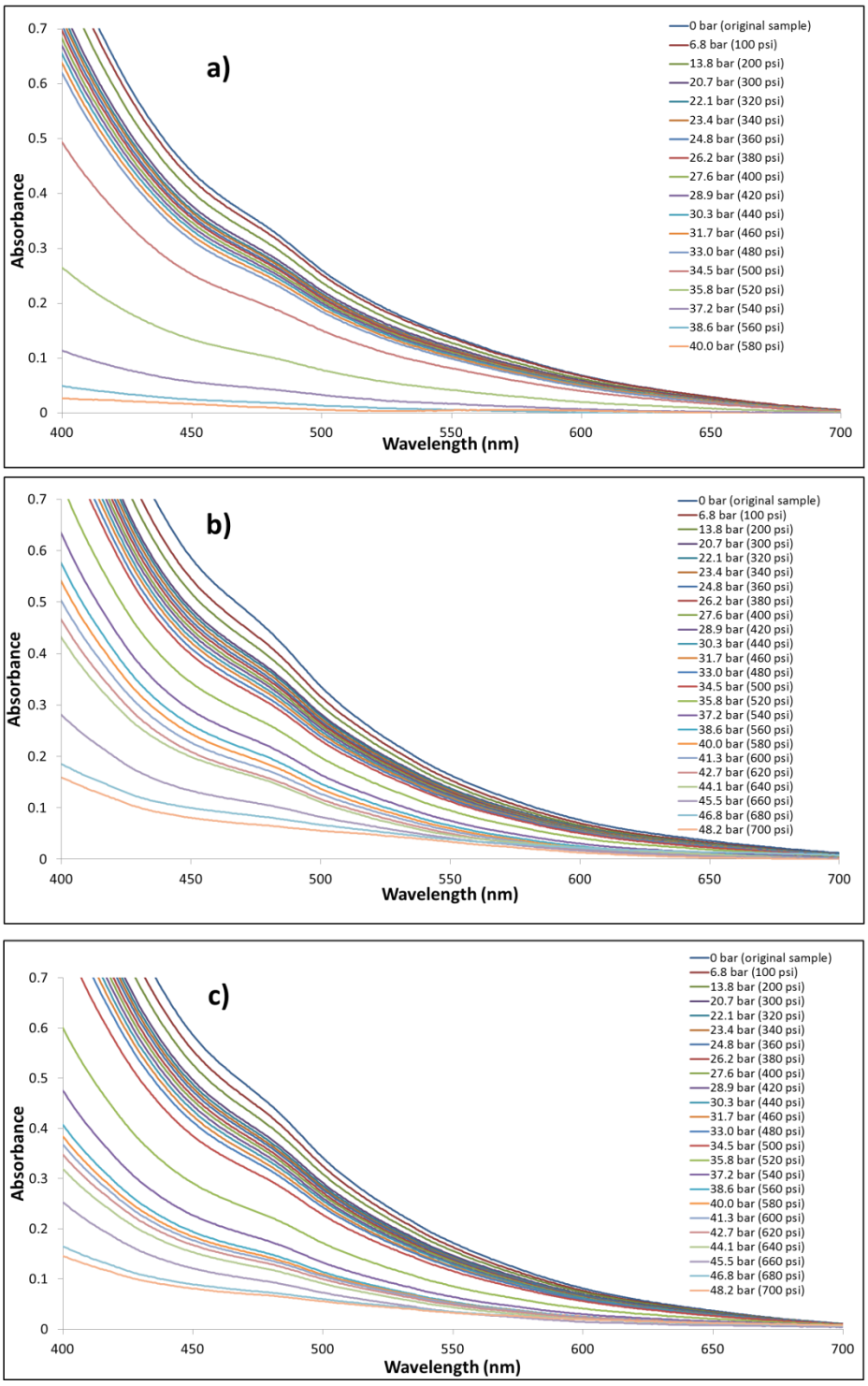

Figure 3.1 UV-Vis spectra for oleic acid coated iron oxide nanoparticles dispersed in n-hexane of 20 nm avg. size (a), 5 nm avg. size (b) and 1:1 nanoparticle mixture (c) at different applied CO_2 pressures.

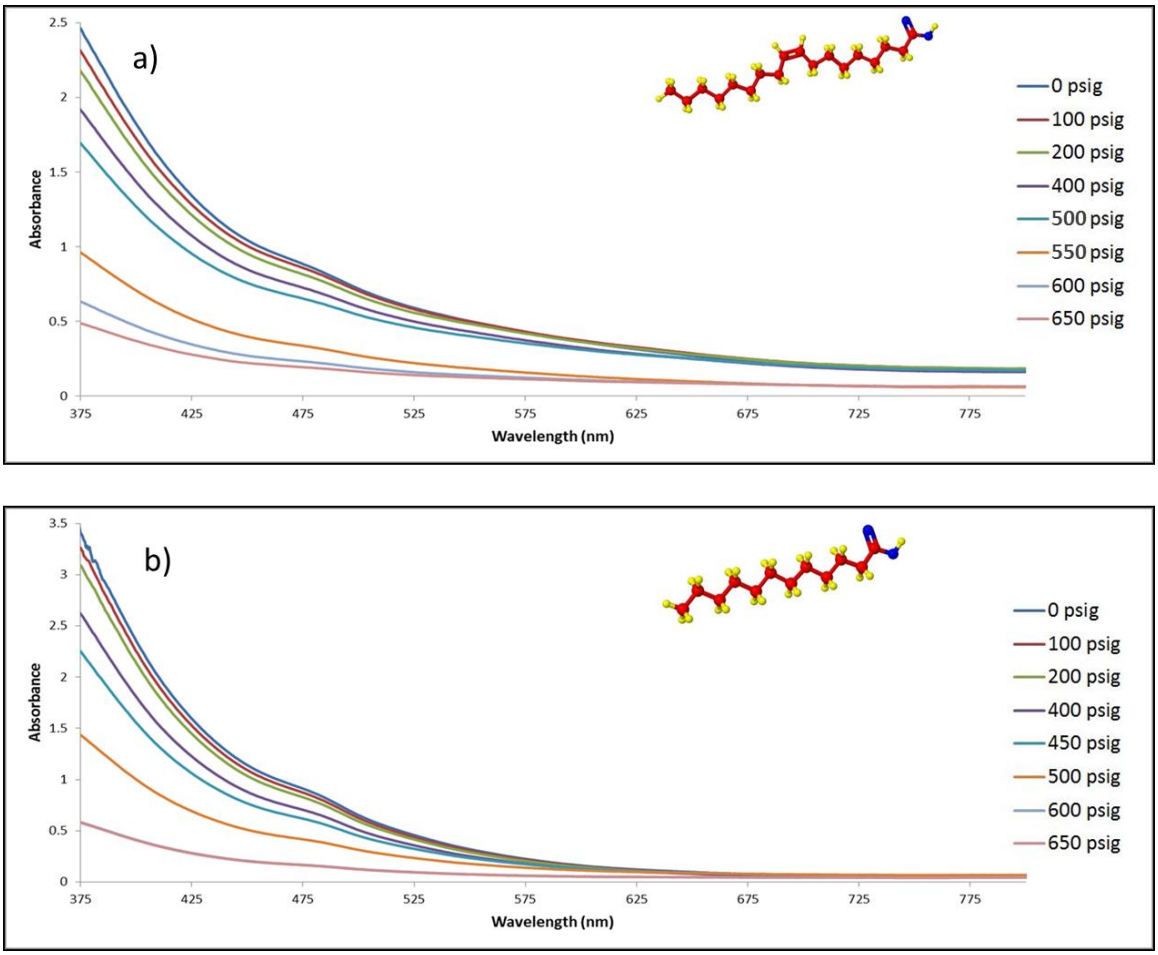

Figure 3.2 UV-Vis spectra for oleic acid (a) and dodecanoic acid (b) coated iron oxide nanoparticles dispersed in *n*-hexane at different applied CO_2 pressures. (*Inset*: Structure of stabilizing ligands)

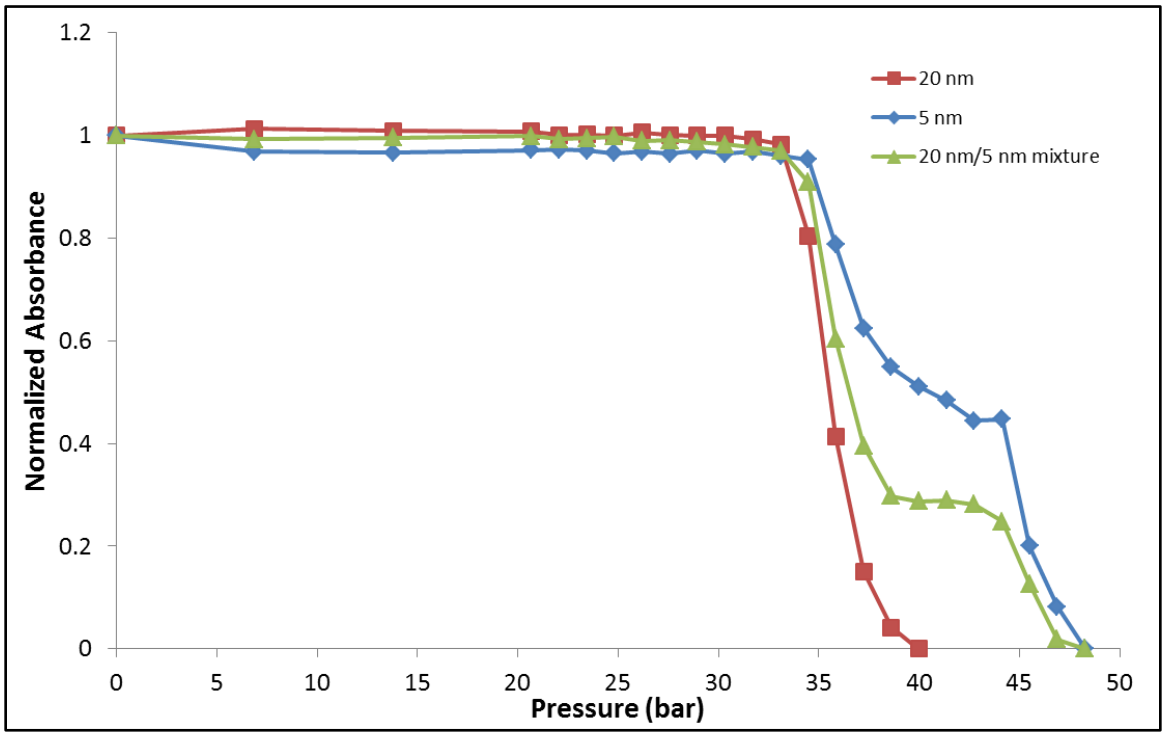

Figure 3.3 Precipitation curves for spherical oleic acid coated iron oxide nanoparticles dispersed in *n*-hexane.

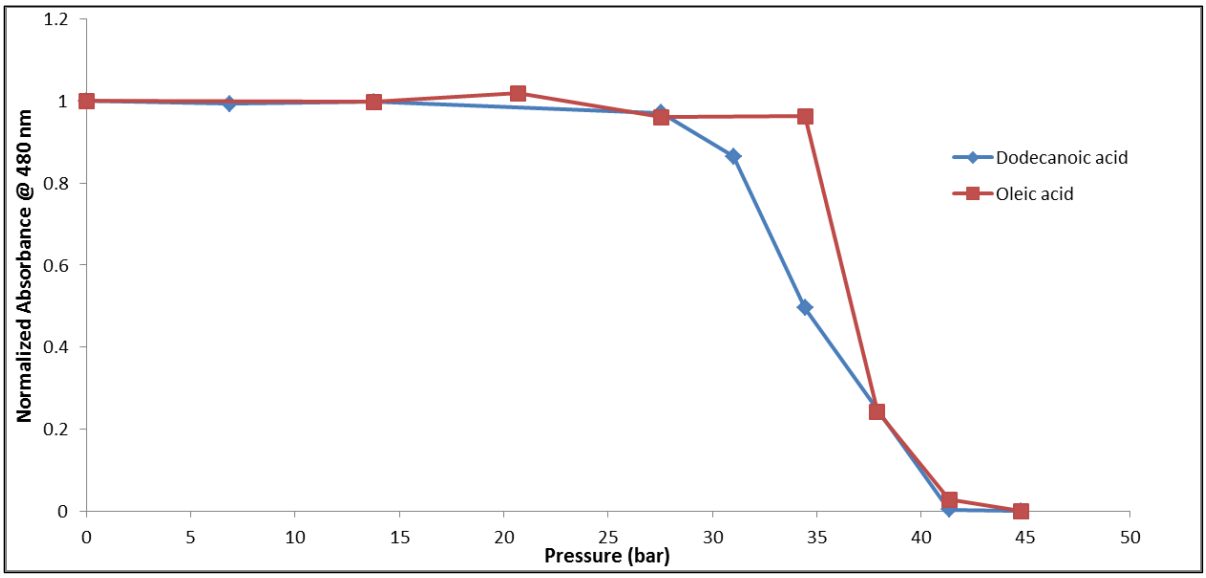

Figure 3.4 Precipitation curves for oleic acid and dodecanoic acid coated iron oxide nanoparticles dispersed in *n*-hexane.

.

3.2.4 Size-selective fractionation process

The size-selective fractionation process is carried out using the cascaded vessel apparatus, in a manner similar to that described in Section 2.2.5. For the first set of experiments the 1:1 nanoparticle mixture was fractionated at pressures determined from the precipitation curve shown in Figure 3.3. For the second set of experiments the oleic acid and dodecanoic acid coated nanoparticles were fractionated at pressures determined from the precipitation curves shown in Figure 3.4.

3.3 Results and Discussions

3.3.1 Characterization of commercially bought spherical iron-oxide nanoparticles

TEM analysis of the commercially obtained 5 nm and 20 nm avg. size iron oxide nanoparticles showed that the samples contained monodisperse spherical iron oxide nanoparticles. The sizing of these particles using the ImageJ image analysis software showed that the nanoparticle samples had an average size of 5.4 nm ± 1.2 nm and 17.0 nm ± 0.8 nm respectively, which is well within the range expected. The TEM images of these nanoparticles along with their size and size distribution are shown in Figure 3.5. FTIR analysis of these nanoparticles also confirmed the presence of oleic acid stabilizing ligands on the nanoparticle surface of both the small and large nanoparticles as shown in Figure 3.6. The two sharp peaks present in the spectra, in the range of 2800-3000 cm^{-1}, can be attributed to the $–CH_2$ stretches from the alkyl chain in oleic acid. The spectrum for the iron oxide nanoparticles shows a characteristic Fe-O stretch at approximately 590 cm^{-1} and the spectrum for pure oleic acid on the other hand shows a prominent C=O stretch at 1710 cm^{-1}. The loss of the carbonyl peak at approximately 1700 cm^{-1} hints at a ligand-core conjugation via the C-O bond in oleic acid as seen in previous studies (S.-Y.

Lee & Harris, 2006; C. Y. Wang, Hong, Chen, Zhang, & Gu, 2010; L. Zhang, He, & Gu, 2006).

3.3.2 Characterization of faceted iron-oxide nanoparticles synthesized using the coprecipitation method

Iron oxide nanoparticles which were synthesized using the co-precipitation method described in Section 3.2.2.2 were characterized using FTIR spectroscopy and TEM. From TEM analysis, it is visible that the particles synthesized were faceted and significantly polydisperse in size with the oleic acid capped nanoparticles having an average size of 7.8 nm ± 2.8 nm and the dodecanoic acid capped nanoparticles an average size of 6.6 nm ± 3.3 nm as shown in Figure 3.7. The particles coated with octanoic acid and nonanoic acid were however not stable in solution and precipitated over a period of a day and week respectively. FTIR analysis of the oleic acid and dodecanoic acid coated iron oxide nanoparticles (Figure 3.9) shows spectra similar to that observed in the commercially available particles. The loss in the C-O peak at 1700 cm^{-1} , which is present in the FTIR spectra for pure ligands (Figure 3.8) hints at a similar bidentate type of conjugation as seen in the previous commercial samples. Hence, the iron oxide nanoparticles synthesized using the coprecipitation method are functionally similar to the commercially bought iron oxide nanoparticles. The lack of control over the nucleation and growth stages of nanoparticle growth in the coprecipitation method results in the polydispersity and faceted nature of the synthesized iron oxide nanoparticles (Laurent et al., 2008).

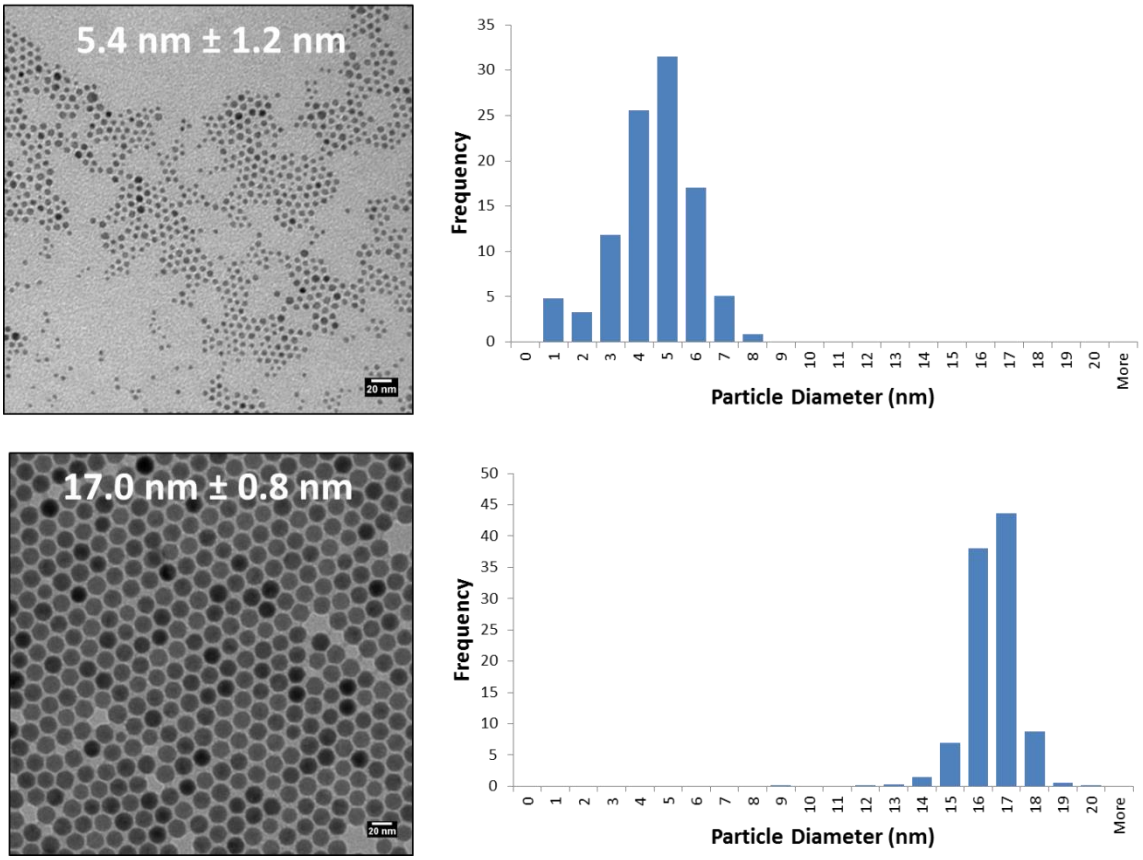

Figure 3.5 TEM images and particle size/size distribution of commercially bought oleic acid-stabilized iron oxide nanoparticles dispersed in *n*-hexane

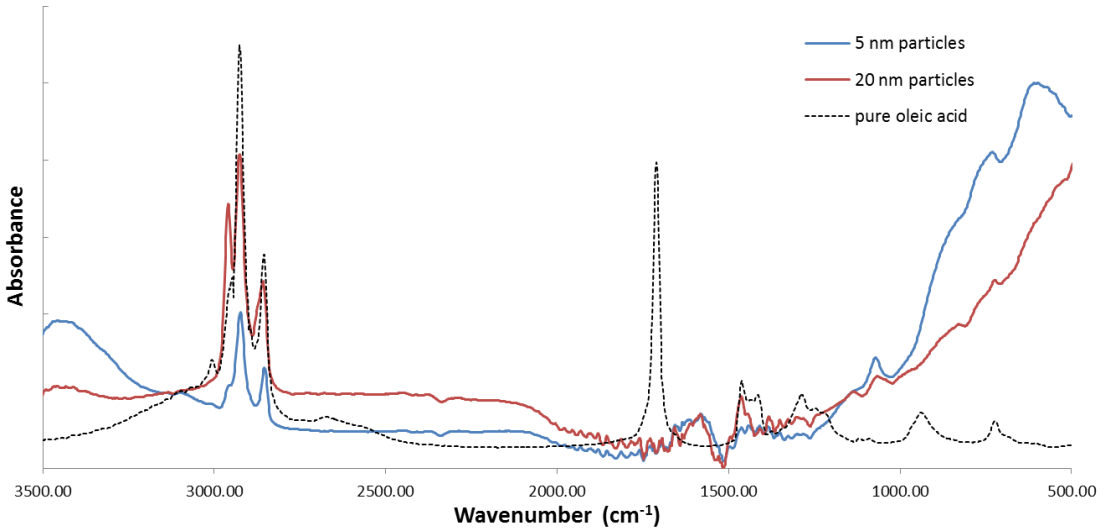

Figure 3.6 FTIR spectra of commercially bought 5 nm and 20 nm particles

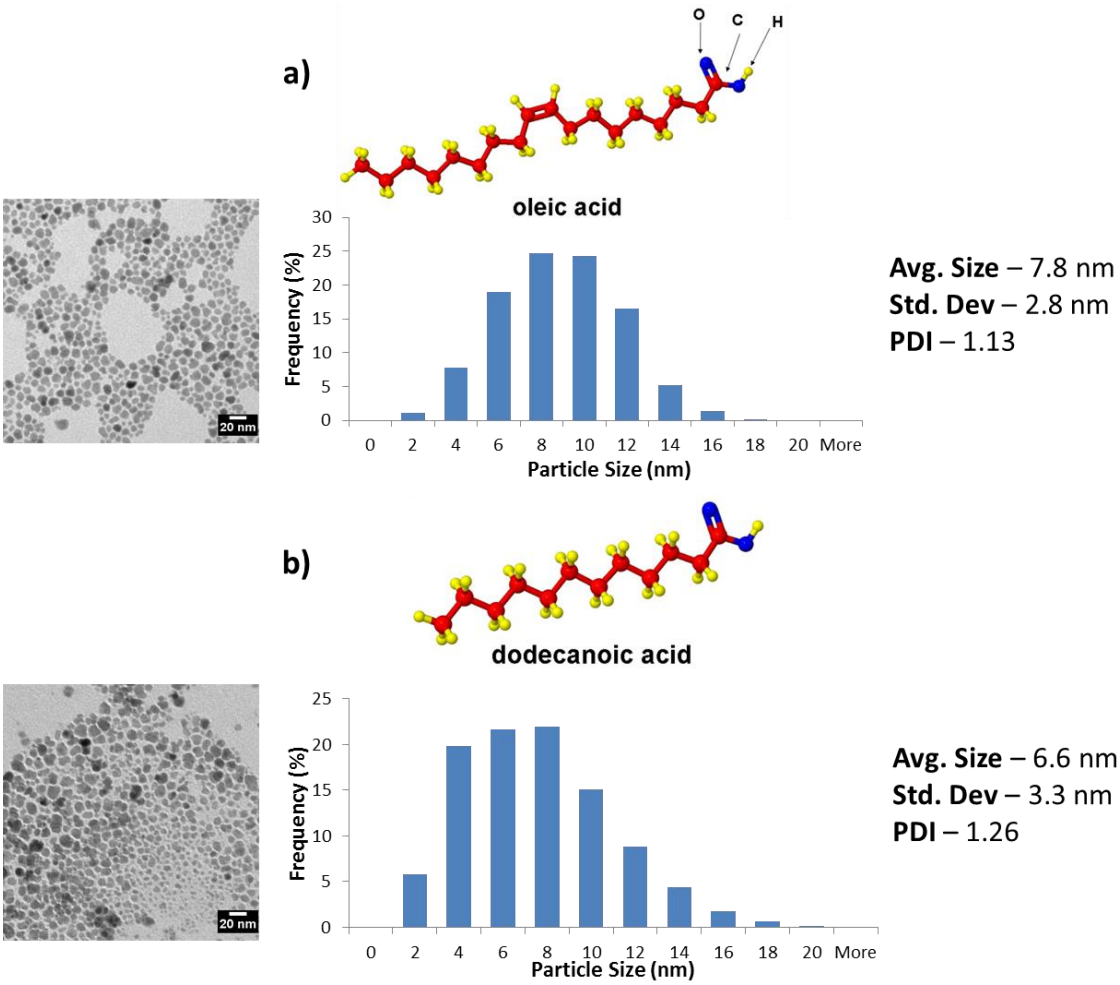

Figure 3.7 Particle size and size distribution of oleic acid (a) and dodecanoic acid (b) stabilized iron oxide nanoparticles dispersed in *n*-hexane synthesized using the coprecipiation method. (*Inset*: Structures of the stabilizing ligands)

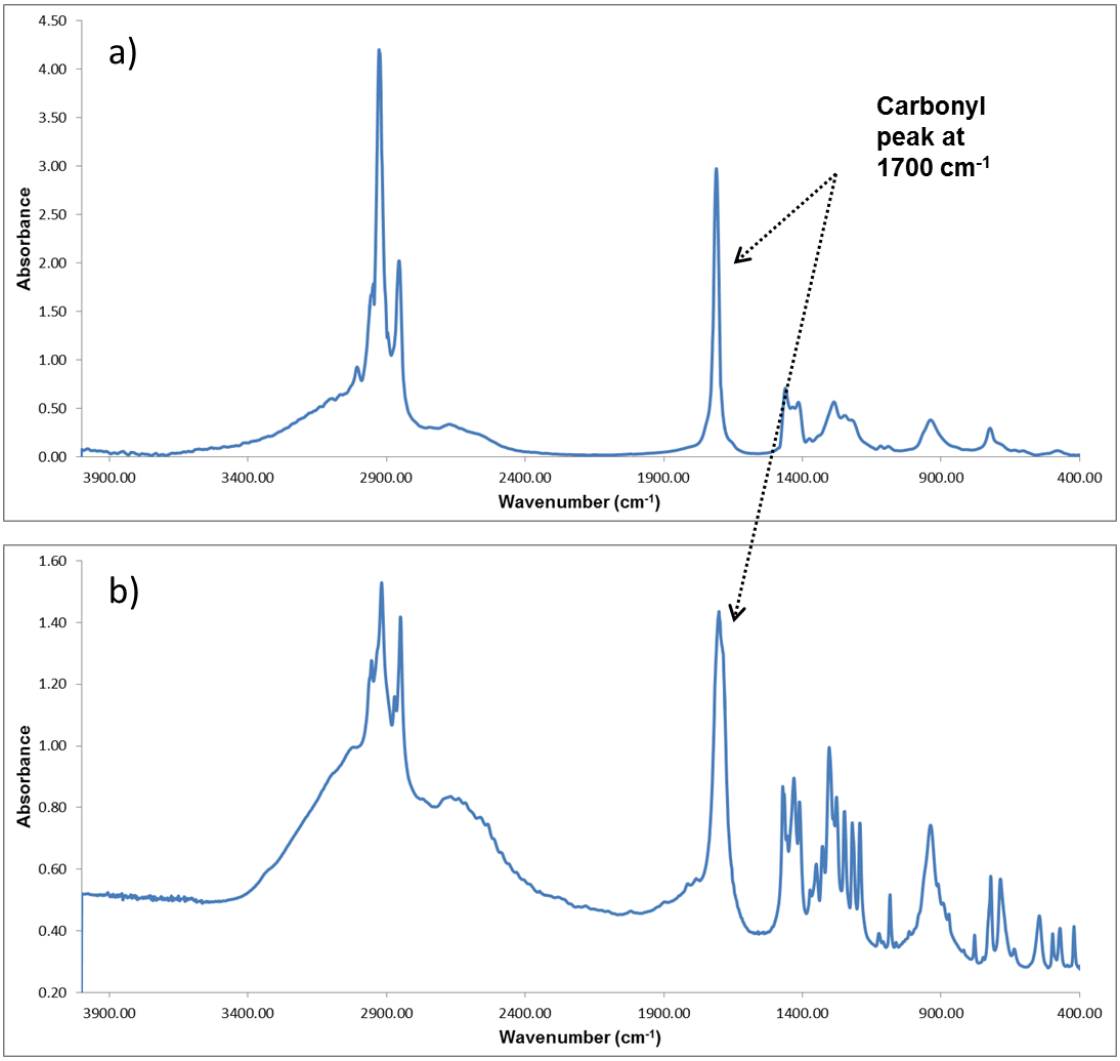

Figure 3.8 FTIR spectra of pure oleic acid (a) and pure dodecanoic acid (b) obtained by using the KBr pellet method

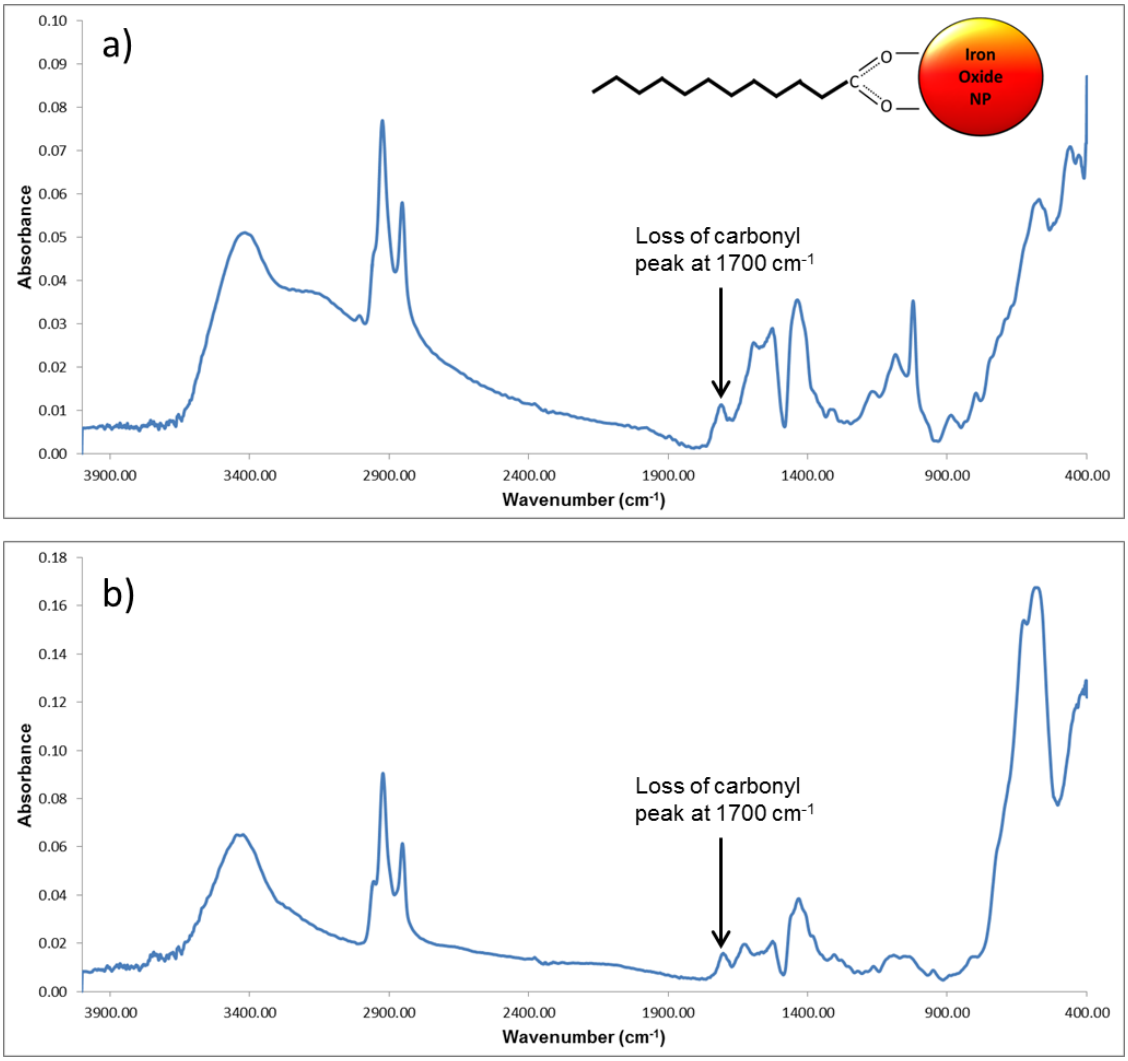

Figure 3.9 FTIR spectra of oleic acid capped iron-oxide nanoparticles (a) and dodecanoic acid capped iron-oxide nanoparticles (b) obtained by using the KBr pellet method. (*Inset image:* Bidentate bonding between ligand and iron oxide core)

3.3.3 Effect of CO_2 pressure on the precipitation of spherical iron oxide nanoparticles and nanoparticle mixtures.

The effect of CO_2 pressure on the precipitation of the spherical nanoparticles from hexane is visible from the precipitation curves shown in Figure 3.3. For the FeNP-5 sample the P_i value is approximately 34.5 bar while the FeNP-20 sample has a P_i value of approximately 33.1 bar. This variation in P_i values is expected since the smaller nanoparticles are more stable in solution and require a slightly higher CO_2 concentration in solution (i.e. higher applied CO_2 pressure) to destabilize them. The precipitation curve for the FeNP-20 samples shows that the nanoparticle precipitation is complete at a pressure of 40.0 bar. On the other hand, for the FeNP-5 sample, precipitation is complete at a much higher pressure of 48.2 bar. Hence the pressure range for nanoparticle precipitation in the FeNP-20 sample is approximately 6.9 bar while that for the FeNP-5 sample is approximately 13.7 bar. This difference in precipitation pressure range can be explained on the basis of the difference in relative polydispersity of the FeNP-20 sample and the FeNP-5 sample detailed in Figure 3.5. The FeNP-5 sample is relatively more polydisperse since it contains smaller particles with a larger standard deviation in size compared to the FeNP-20 sample. The FeNP-20 sample on the other hand is extremely monodisperse as is obvious from the images and size-distribution data shown in Figure 3.5. The FeNP-mixture sample on the other hand has nanoparticles precipitating from 33.1 bar to 48.2 bar, which as expected, is a combination of the precipitation ranges of the FeNP-20 and FeNP-5 samples.

3.3.4 Effect of CO_2 pressure on the precipitation of faceted fatty acid-coated iron-oxide nanoparticles

The effect that different interactions between ligands have on iron oxide nanoparticle precipitation from (and dispersability in) GXLs can be effectively studied using the techniques described above. Oleic acid and dodecanoic acid were chosen as the ligands of choice. Oleic acid is a popular ligand used to coat iron oxide nanoparticles and it has been investigated previously in various studies for a variety of applications including the ability to form Pickering emulsions (Ingram et al., 2010; Lan et al., 2007; M. A. Morales et al., 2005; C. Y. Wang et al., 2010; Y. Wang, Wong, Teng, Lin, & Yang, 2003; L. Zhang et al., 2006). Dodecanoic acid was chosen as the second ligand because it is similar in carbon chain length to the ligand researched previously in our studies (i.e. dodecanethiol) and it was expected that these two systems (gold nanoparticle-dodecanethiol ligand and iron oxide nanoparticle-dodecanoic acid ligand) would have similar properties and precipitation characteristics. The precipitation curves which were obtained through the use of oleic acid and dodecanoic acid capped particles are shown in Figure 3.2.

It is observed that the particles coated with oleic acid precipitate quickly over a range of 10.3 bar with a P_i of approximately 34.5 bar. On the other hand for the particles coated with dodecanoic acid the nanoparticle precipitation is relatively gradual over a range of 17.2 bar, with a P_i value of 27.6 bar. The trend in P_i values and the pressure range over which the iron oxide particles precipitate out of solution is similar to the one observed for thiol coated gold nanoparticles in previous studies, where the particles coated with the shorter thiols precipitate slowly over a longer pressure range (Steven R.

Saunders & Roberts, 2011). The lower P_i values can be explained as a result of average particle size of iron-oxide nanoparticles synthesized by the co-precipitation method being larger than the average size of gold nanoparticles synthesized by the Brust method. It can be concluded from these observations that similar to the results obtained in Chapter 2 for the gold nanoparticles, the solvent ligand interactions between the oleic acid ligand and the solvent (*n*-hexane) are stronger than the interactions between dodecanoic acid and *n*-hexane, which results in the nanoparticles precipitating from solution at higher pressure from the *n*-hexane/oleic acid system compared to the *n*-hexane/dodecanoic acid system. It should also be noted that the P_i values for the iron oxide nanoparticles are lower than the values usually observed for the gold nanoparticles as seen in Chapter 2. This phenomenon is simply due to the larger average size and size distribution obtained for the iron-oxide nanoparticles as seen in Figure 3.4. Also, the largest particles in the iron oxide systems are around 16-18 nm in diameter compared to the 8-9 nm particles of the gold system, and this disparity in size would cause the iron oxide nanoparticles to destabilize at lower CO_2 pressures and precipitate from the system at lower pressures than the gold nanoparticles.

3.3.5 Size-selective fractionation of a nanoparticle mixture containing spherical iron-oxide nanoparticles of different sizes

TEM analysis of the FeNP-mixture sample showed that the sample had a bimodal size-distribution as is shown in Figure 3.10. The modes in size-distribution of the original FeNP-mixture are not equal since the mixture is generated by mixing the FeNP-20 and FeNP-5 samples in a 1:1 ratio *by volume*. Since the FeNP-20 and FeNP-5 samples have the same initial iron oxide concentration (5 mg/mL), for equal volumes of these samples

the FeNP-5 will have a higher *number* concentration of nanoparticles than the FeNP-20 sample. The smaller nanoparticles have a lower mass (and volume) and hence there are more of them in a particular volume of the dispersion. Combining these facts with the fact that TEM analysis determines the *number* frequency of the nanoparticles, a bimodal distribution shown in Figure 3.10 is obtained for the sample studied.

The precipitation curves shown in Figure 3.3 show that the FeNP-20 sample precipitates completely by 40.0 bar while the FeNP-5 sample does so by 48.2 bar. In this fractionation study, to demonstrate the ability to remove the larger size nanoparticles from the original sample the system with the FeNP-mixture sample was first pressurized to 40.0 bar and allowed to reach equilibrium. The unprecipitated dispersion was then transferred to the second vessel followed by vessel depressurization. The nanoparticles from the second vessel were then collected and are referred to as Fraction 2 in Figure 3.10. The first vessel is then washed with hexane to recover the precipitated nanoparticles and this fraction is referred to as Fraction 1.

From observing the precipitation curve for the FeNP-mixture sample it is clear that nanoparticle precipitation is split into two sections at around 40.0 bar. Through comparison of the FeNP-20 and FeNP-mixture precipitation curves it is apparent that the pressure of 40.0 bar is equivalent to the pressure at which almost all of the larger nanoparticles (from the FeNP-20 sample) precipitate from solution. For this fractionation study since we aim to check the feasibility of fractionation iron oxide nanoparticles, a single pressure cut at 40.0 bar was chosen so as to check if the system can successfully isolate the small particles. It is to be noted that the FeNP-20 and FeNP-5 precipitation curves overlap in the pressure range of 34.5 bar and 40.0 bar. Hence, isolation of the

large nanoparticles will not be possible and minute quantities of the smaller nanoparticles from the FeNP-5 sample are expected to be present in the first fraction.

The size distribution and TEM results from this fractionation experiment on the FeNP-mixture sample are shown in Figure 3.10. From the size distribution of the nanoparticle dispersion obtained from Fraction 1 (Figure 3.10b) it is clear that the larger nanoparticles are retained in greater numbers than the smaller nanoparticles in this sample. This is also evident in the associated TEM image which clearly shows the difference in the population of large and small nanoparticles in this sample. This trend in size distribution is expected due to overlap in precipitation curves for the FeNP-5 and FeNP-20 samples as explained in the previous paragraph. In contrast to the nanoparticles recovered in Fraction 1, the nanoparticles recovered in Fraction 2 lack the larger sized nanoparticles and the sample contains only the smaller sized particles (Figure 3.10c). This clear demarcation in the size of nanoparticles obtained proves that the trends in nanoparticle precipitation expected from the precipitation curves seen in Figure 3.3 are accurate and the iron oxide-oleic acid nanoparticle system can be successfully tracked using UV-vis spectroscopy. This also shows that the iron oxide nanoparticles coated with oleic acid can be effectively fractionated using the CO_2 GXL process and through further modifications in the GXL process one can effectively fractionate polydisperse iron oxide nanoparticles samples.

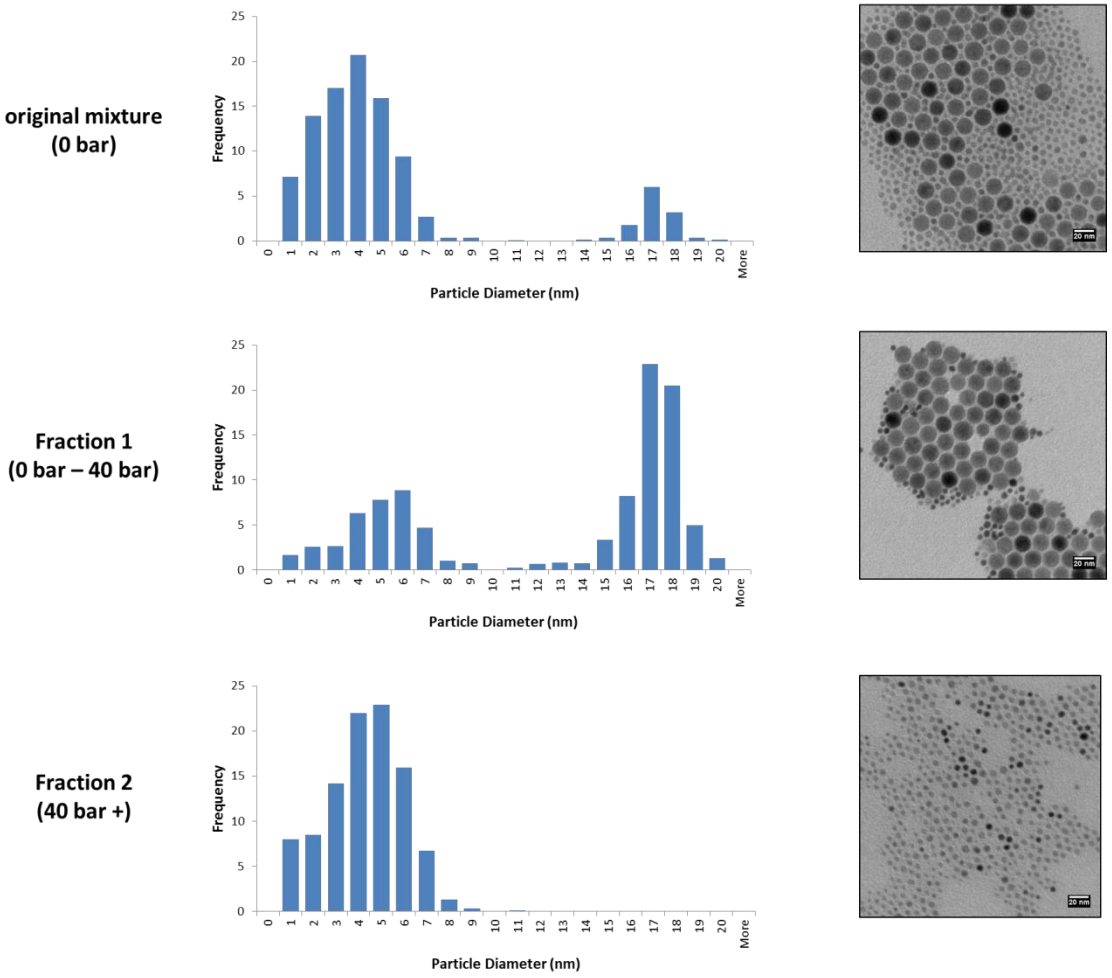

Figure 3.10 TEM micrographs and size distribution of the original FeNP-mixture and its two different size-fractions, obtained using a CO_2 GXL.

3.3.6 Size-selective fractionation of faceted iron-oxide nanoparticles synthesized using the coprecipitation method

To measure the effectiveness of the cascaded vessel apparatus on the fractionation of iron oxide nanoparticles using a GXL, particles synthesized using methods described in Section 3.2.2.2 were used along with the precipitation curve data shown in Figure 3.2 in the GXL process. To maintain a constant frame of reference across the different sets of experiments the pressures for the fractionation process were selected corresponding to 0.4 and 0.5 absorbance values of the precipitation curves on the basis that particles of approximately the same size and composition should precipitate from each of the solvents within these absorbance values in each of the different sets of experiments. Specifically, P1 was assigned as the pressure that corresponded to the normalized absorbance value of 0.5 in the precipitation curve and P2 was assigned as the pressure that corresponded to the absorbance value of 0.4 in the same precipitation curves. The pressures obtained for the *n*-hexane/oleic acid system were P1= 36.7 bar (532 psig) and P2= 37.2 bar (540 psig), while those for the *n*-hexane/dodecanoic acid system were P1= 34.3 bar (497 psig) and P2= 35.5 bar (515 psig). The fractionation results from the above two sets of experiments are shown in Figure 3.11 and Figure 3.12 respectively. It is observed from the fractionation results that the fractionation for the *n*-hexane/dodecanoic acid system is not very effective compared to the *n*-hexane/oleic acid system where the particles appear to be more normally distributed across each of the fractions.

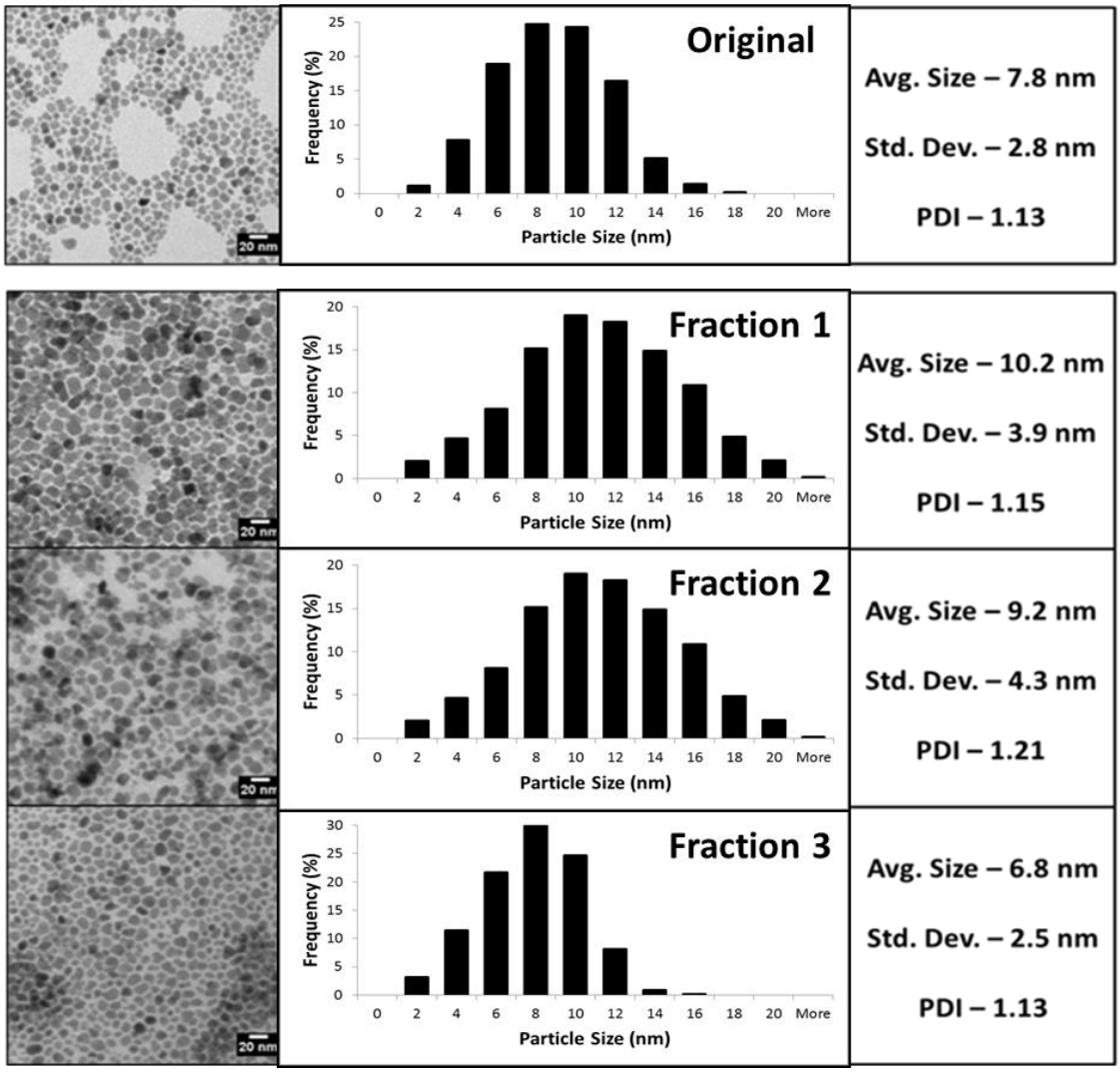

Figure 3.11 TEM micrographs and size distribution of oleic acid coated iron oxide nanoparticles fractionated into three different size-fractions using a CO_2 GXL.

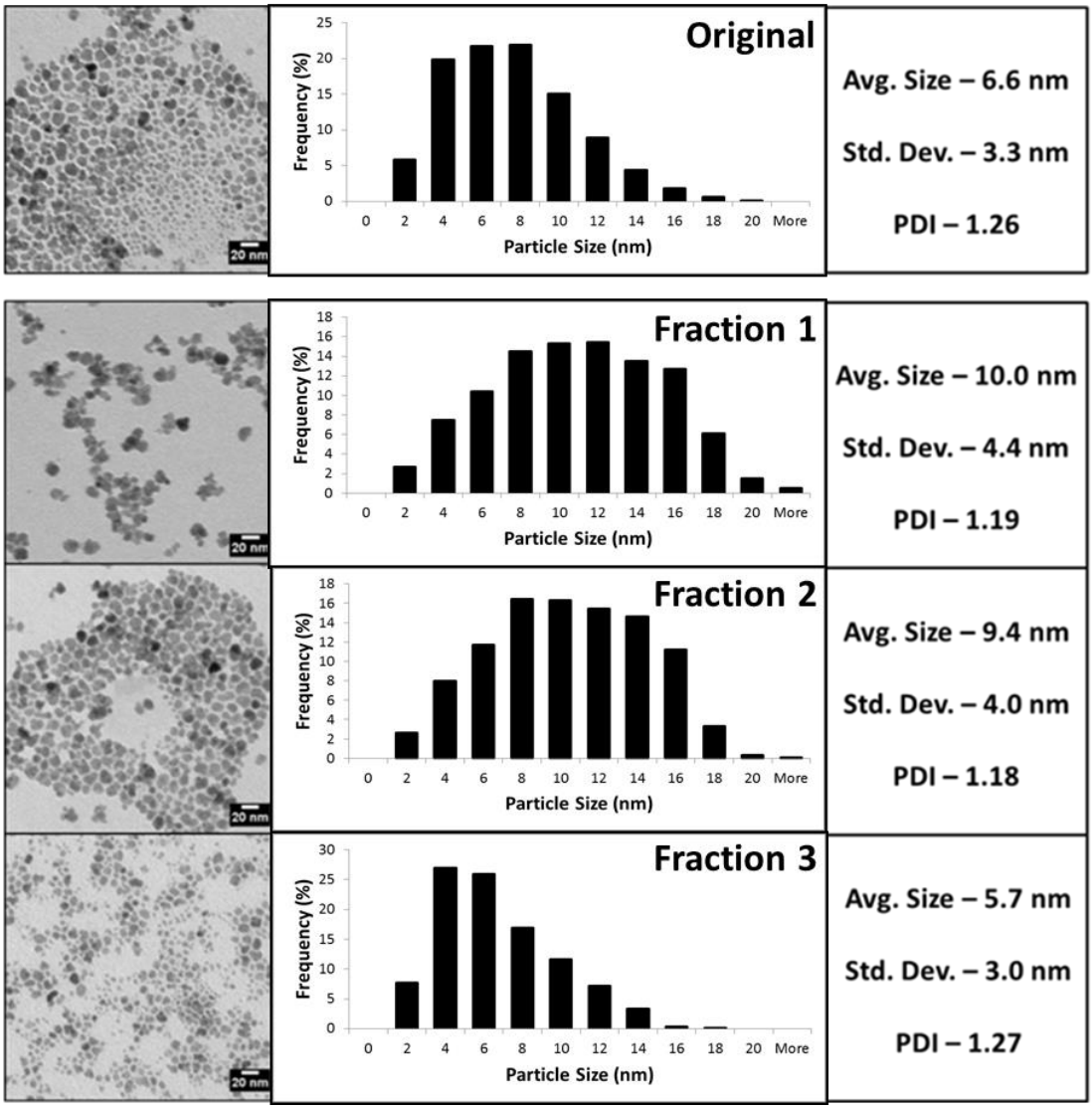

Figure 3.12 TEM micrographs and size distribution of dodecanoic acid coated iron oxide nanoparticles fractionated into three different size-fractions using a CO_2 GXL.

that observed for the gold nanoparticles presented in Chapter 2. For both these systems, the PDI for each of the fractions is more than that of the original sample and the fractions are almost equally polydisperse. In spite of the *n*-hexane/dodecanoic acid system being a lower pressure system compared to the *n*-hexane/oleic acid system the size fractions for the *n*-hexane/oleic acid system appear to be more normally distributed across each of the fractions.

The iron oxide nanoparticles also preferentially precipitated at the top of the liquid film in the cascaded vessels than uniformly precipitating across the entire surface of the glass insert as they did for the gold nanoparticles. A diagrammatical representation of the phenomenon is shown in Figure 3.13 along with actual photos of the precipitated particles in the cascaded vessel J_1. This non-uniform precipitation of the iron oxide nanoparticles can be explained on the basis of several traits of iron oxide. Firstly, the nanoparticles in the GXL process precipitate from solution due to the change in dispersability of nanoparticles as governed by van der Waals interactions, the steric interactions of the stabilizing ligands and solvent, particle nature and the physicochemical properties of the solvent.(Anand et al., 2005; Bhosale & Stretz, 2008) Now, the magnitude and range of the van der Waals interactions are closely related to the Hamaker constant (A), which in turn is dependent on the materials present in the system. The van der Waals interaction free energy (V_{vdW}) between two spheres of radius, *r* and surface separation *s* is given by Equation 3-1 (Faure, Salazar-Alvarez, & Bergström, 2011)

$$V_{vdW} = -\frac{A}{12}\frac{r}{s} \quad \text{..... Equation 3-1}$$

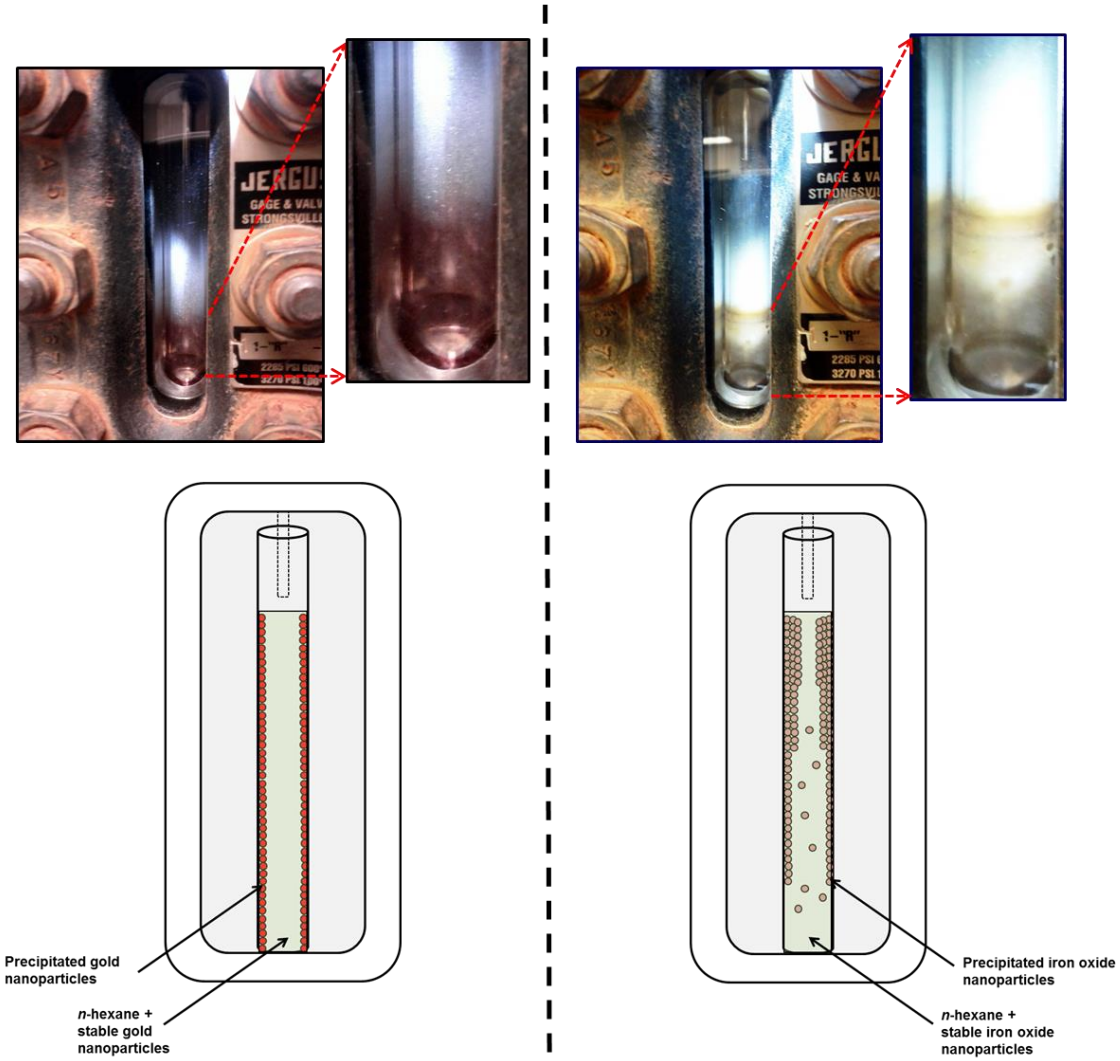

Figure 3.13 *Left*: Uniform precipitation of gold nanoparticles in cascaded vessel. *Right*: Preferential precipitation of the iron oxide nanoparticles at the top of the liquid film in the cascaded vessels

To calculate the Hamaker constant for the substrate-particle interaction across the solvent ($A_{P\text{-}Solv\text{-}S}$) in the GXL system, we use the formula shown below in Equation 3-2, where A_P, A_S and A_{Solv} are the Hamaker constants across vacuum for the particles, substrate and solvent respectively (Bhosale & Stretz, 2008).

$$A_{P-Solv-S} = (\sqrt{A_P} - \sqrt{A_{Solv}})(\sqrt{A_S} - \sqrt{A_{Solv}}) \quad \text{.....Equation 3-2}$$

The Hamaker constants used for Au, SiO_2 (glass) and Fe_3O_4 are 1.935, 0.412 and 1.31 eV respectively (Bergstrom, Meurk, Arwin, & Rowcliffe, 1996; Bhosale & Stretz, 2008; Faure et al., 2011). The Hamaker constant for the solvent mixture (*n*-hexane + CO_2) is considered to be 0.187 eV (at a pressure of 42 bar) as calculated using the Lifshiftz theory (Shah, Hanrath, Johnston, & Korgel, 2004). Applying the formula in Eqn. 5, the $A_{P\text{-}Solv\text{-}S}$ value for the gold nanoparticle GXL system is 0.201 eV while that for the iron oxide GXL system it is 0.149 eV. Thus, the fact that the substrate-particle interaction across the solvent for the iron oxide system is 0.74 times that for the gold nanoparticle system results into lower van der Waals interactions and hence a lower affinity for the particles to precipitate on the walls. This could result in iron oxide nanoparticles that would typically be expected to precipitate onto the walls of the vessel to be still dispersed in solution, and hence cause a deviation in the size of the nanoparticle fractions obtained.

Another reason for the unstable (i.e. thermodynamically unstable) nanoparticles to still remain dispersed in solution involves the inability of those particles to adhere to the glass insert wall; especially if the wall surface is already saturated with particles. From the reagent concentrations used in Section 2.2.2 and 3.2.2, it is obvious that the synthesized iron oxide nanoparticle dispersions are more concentrated than their gold

counterparts. It is possible that the surface may get saturated with iron oxide nanoparticles and making it difficult for more particles to adhere strongly to the wall. This can cause the larger nanoparticles to be transferred to the next fractionation vessel, increasing the standard deviation of the particles recovered from that vessel. Additionally, formation of a Langmuir-Blodgett type thin film (Steven R. Saunders & Roberts, 2011) (due to the lower pressures employed) can cause smaller particles to remain attached to the wall of the first vessel. A combination of all of these factors can cause an ineffective fractionation to be obtained in the iron oxide nanoparticle system.

Since previous studies by Anand et al. (Anand et al., 2005) have shown that nanoparticles can precipitate over a narrow range of pressure, the current pressurization process was carried out quickly (over a period of a couple of minutes) where the system pressure was initially raised to the P_i and then the system was further pressurized slowly over to the process pressures (P1 and P2). This method of pressurizing the system was based upon detailed studies by Bhosale and Stretz (Bhosale & Stretz, 2008) on the gold nanoparticle GXL system and hence was implemented for the iron oxide system too. However, due to the lower Hamaker constants for the iron oxide nanoparticles (as mentioned previously), it is possible that the diffusion of the particles towards the surface of the walls and the diffusion of CO_2 into the particle dispersion is slower than in the gold nanoparticle system. This would cause the nanoparticles in the solvent layer closer to the gaseous CO_2-hexane interface (top of the vessel) to precipitate first since more CO_2 would have initially diffused in that section, thereby causing the precipitation of the particles to occur near the top section of the glass insert over time. It is possible that this

phenomenon was also present in the gold nanoparticle system but was not as pronounced due to the higher Hamaker constants of the particles.

3.4 Conclusions

The main observation from these experiments is that the cascaded vessel apparatus and UV-vis spectroscopy can be used to successfully fractionate spherical, oleic acid-coated iron oxide nanoparticles. Through the use of the GXL fractionation process we were able to successfully isolate the smaller sized nanoparticles from the particle mixture and achieve an acceptable level of size separation in the spherical iron oxide nanoparticle system. However, in the case of the faceted nanoparticle system, the large nanoparticle concentrations employed combined with the fact that the samples are extremely polydisperse makes the GXL fractionation ineffective. Hence to address these issues, the apparatus which is currently being used for the GXL fractionation of nanoparticles needs to be modified for use with iron oxide nanoparticles especially at high concentrations. This new apparatus has to be designed while taking into consideration the issues associated with lower surface energy for the particles, poorer substrate-particle interactions, dampened diffusion of particles and the low available surface area inside the cascaded vessels.

Chapter 4

Enhancing and Extending the Applicability of the GXL Fractionation Technique through Process Modifications and Process Scale-up

4.1 Introduction

Metal-oxide nanoparticles are expected to have wide-scale applicability in the near future in various industrial fields including catalysis (J.-Y. Park et al., 2010; Zhao et al., 2013), biomedicine (Bulte & Kraitchman, 2004; Jo et al., 2010; Thorek et al., 2006), enhanced oil recovery (Baran Jr, Jimmie R., & Cabrera, 2006) and environmental remediation (Orbell et al., 1997; Rajeshwar & de Tacconi, 2009; W. Zhang, 2003). Iron oxide nanoparticles are especially important in this section of nanoscience because of their magnetic nature, relative safety and affordability. Nanoparticles within the size range of 1-100 nm have extremely size-dependent physicochemical properties which arise due to their dimensions being intermediate between the atomic and molecular size regimes (C. N. R. Rao et al., 2002). It is critical to harness these size-dependent properties for the effective use of nanoparticles in the applications mentioned above. There are two ways to go about harnessing these size-dependent properties of nanoparticles. The first way is to synthesize monodisperse nanoparticles using various specialized-synthesis methods and then use these nanoparticles in the targeted

applications. However, a large number of these specialized-synthesis techniques suffer from disadvantages such as requiring high temperatures (Hyeon et al., 2001; Z. Xu et al., 2010; Yu et al., 2004) and expensive reagents (J.-G. J. J.-H. Park et al., 2005; Yu et al., 2006), making large scale synthesis of these particles expensive. The other way to harness the size-dependent nanoparticle properties is to use a simple and cheap synthesis technique to generate polydisperse nanoparticles and then process them using various techniques like magnetic separation (Yavuz et al., 2006), centrifugation (Novak et al., 2001), and electrophoresis (Surugau & Urban, 2009) to obtain monodisperse particles. Most of these post-synthesis processing methods suffer from certain drawbacks such as requiring expensive equipment, having low throughputs and large solvent amounts (Bishop et al., 2009; Fletcher, 1991; S R Saunders & Roberts, 2009).

Our lab at Auburn University has previously developed a method to size-selectively separate nanoparticles using gas-expanded liquids (GXLs) (Anand et al., 2007; S R Saunders & Roberts, 2009). This process involves the controlled precipitation of nanoparticles coated with aliphatic stabilizing ligands and dispersed in an organic solvent, under applied CO_2 pressure. The technique to size-selectively fractionate nanoparticles using GXLs is a modification of the popular liquid solvent-antisolvent (LSAS) precipitation process (Murray, C.B. Kagan et al., 2000). The LSAS process usually generates large quantities of solvent waste and requires tedious steps such as centrifugation to recover the particles. In the GXL fractionation process CO_2 acts as the antisolvent for the aliphatic stabilizing ligands attached to the nanoparticles. These ligands (which are solvated in absence of any CO_2) tend to self-associate and collapse upon the addition of CO_2 in significant quantities (G Von White & Kitchens, 2010). This

ligand collapse causes the precipitation of nanoparticles out of solution and this precipitation is dictated by the amount of CO_2 dissolved in the solvent. Larger nanoparticles precipitate out of solution at lower applied CO_2 pressures (lower amounts of CO_2 dissolved) due to the larger particles having higher Van der Waals forces of attraction. Hence, by controlling the amount of CO_2 pressure applied on the system one can controllably precipitate and separate nanoparticles based upon their size from an organic solvent. The main advantage of this GXL size-selective fractionation technique is the fact that the antisolvent (CO_2) can be separated from the liquid simply by depressurization and thereby recovered and reused. Due to the decreased solvent viscosities and increased diffusivities of molecules in a GXL, the nanoparticles can also be precipitated from stable dispersions without the need for centrifugation. This makes the GXL process less energy intensive and time intensive (Steven R Saunders & Roberts, 2012). The other advantages to the use of CO_2 include its relative inertness and easy availability (Jessop & Subramaniam, 2007; P. Vengsarkar & Roberts, 2013).

Previously, it has been shown that nanoparticle dispersions of different materials like CdSe/ZnS quantum dots and gold nanoparticles can be effectively precipitated using GXLs with CO_2 as the gaseous antisolvent (Anand et al., 2007; McLeod, Kitchens, et al., 2005; S R Saunders & Roberts, 2009). Several studies which modified the solvent-ligand combinations were also successful in tuning the pressures required to fractionate gold nanoparticles using the GXL technique (Steven R. Saunders & Roberts, 2011; P. Vengsarkar & Roberts, 2013). However, gold nanoparticles have limited use in contemporary industrial applications excluding certain biomedical roles. Iron oxide nanoparticles on the other hand have a wider applicability in current and future fields.

These include use in areas such as magnetic resonance imaging (MRI) contrast agents (Andreas et al., 2012; Babes et al., 1999; Hong et al., 2008; Hu et al., 2011; Kwak, 2005; R. Qiao et al., 2009), drug delivery agents (Jain et al., 2005; M. A. Morales et al., 2005; M. Morales et al., 2008), catalysts (Hosseinian et al., 2011; Khedr et al., 2009; J.-Y. Park et al., 2010; Torres Galvis, Bitter, Khare, et al., 2012), and for the formation of Pickering emulsions (Bernard P. Binks & Whitby, 2005; Zhou et al., 2012). However, for most of applications mentioned, at least gram scale quantities of iron oxide nanoparticles are required. The first GXL fractionation apparatus which was designed was a proof-of-concept spiral tube apparatus (Anand et al., 2007) designed to fractionate approximately 700 μL of dilute nanoparticle sample. The next scaled up version of this apparatus was a cascaded vessel apparatus (S R Saunders & Roberts, 2009) which effectively fractionated dilute 20 mL samples of nanoparticles. This apparatus provided a good avenue to carry out detailed theoretical studies (Steven R. Saunders & Roberts, 2011; P. Vengsarkar & Roberts, 2013) on the GXL fractionation process, due to the ability to fine tune the process parameters and to visually observe the process. However, a major drawback of the cascaded vessel apparatus is that concentrated nanoparticle samples lead to the formation of Langmuir-Blodgett films (Steven R. Saunders & Roberts, 2011) and lower the effectiveness of the size-selective fractionation process. Also due to the small sample volume used in the apparatus, it is not possible to increase the total amount of nanoparticles being processed due solubility limitations of the solvent. These issues with the cascaded vessel apparatus make it critical to design a new system, targeted for use with iron oxide nanoparticles which are required in large quantities for any useful application.

The first part of this study aims at trying to increase the effectiveness of the cascaded vessel apparatus through the addition of various inert packing materials. This study was carried out using gold nanoparticles since they have a proven track record of being fractionated successfully in the cascaded-vessel apparatus. In the second part of the study we aim to extend the applicability of the GXL fractionation process for use with cheaply synthesized iron oxide nanoparticles at relatively high concentrations. We aim to achieve this through design of a scaled-up apparatus capable of handling high nanoparticle concentrations and large sample volumes. This study will also provide valuable insight into the size-selective fractionation of iron oxide nanoparticles using GXLs which has never been attempted before.

4.2 Experimental Section

4.2.1 Materials

Iron (III) chloride hexahydrate ($FeCl_3 \cdot 6H_2O$, 99.9%), iron (II) chloride tetrahydrate ($FeCl_2 \cdot 4H_2O$, 99.9%), and *n*-hexane (HPLC grade, 95%), were obtained from Alfa Aesar. Oleic acid (99%), was obtained from Sigma Aldric, and ammonium hydroxide (5M) was obtained from BDH. Deionized ultra-filtered (DIUF) water was obtained from Fisher. Carbon dioxide (SFC/SFE grade) was obtained from Airgas. All chemicals were used as received without further purification.

4.2.2 Nanoparticle synthesis

The concentrated gold nanoparticle dispersion was synthesized using the method developed by Brust et al.(Mathias Brust et al., 1994; Goulet & Lennox, 2010) and

described previously in Section 2.2.2. Iron oxide nanoparticles coated with oleic acid were synthesized based on a method described previously by Jain et al. (Jain et al., 2005). Initially aqueous solutions of 0.2 M Fe (III) and 0.2 M Fe (II) were prepared using DIUF water. Fe (III) solution (120 mL, 0.2 M) was mixed with the Fe (II) solution (60 mL, 0.2 M) in a three-necked flask with magnetic stirring. Under constant stirring and under a nitrogen atmosphere, 24 mL of 5M ammonium hydroxide was added to this mixture to generate a black precipitate of iron oxide nanoparticles. These reagent concentrations theoretically generate 2.78 gm of iron oxide (i.e. ~ 2.01 gm of iron).The temperature of this system was them increased to 80 °C and maintained for 30 min to evaporate the ammonia out of the solution. While the temperature is being increased 2.24 mL of oleic acid was added to the mixture. After the end of the heating cycle the system was allowed to cool down to room temperature, magnetically immobilized and washed with DIUF water to remove any excess reagents and impurities. The particles were then dried using nitrogen and dispersed in 200 mL of *n*-hexane via sonication (Fischer Scientific FS20). This 200 mL dispersion of iron oxide nanoparticles was used for each run of the GXL fractionation experiment.

4.2.3 Nanoparticle characterization

The as synthesized nanoparticles were characterized using transmission electron microscopy (TEM) to obtain their size and size-distribution. Carbon-coated TEM grids of each of the collected nanoparticle fractions were then prepared via dropcasting and micrographs were acquired on a Zeiss EM 10 transmission electron microscope and sized using the ImageJ software package (more than a 1000 nanoparticles for each sample). (HR-TEM images for gold nanoparticles shown in Appendix 2). It should be noted that

the ImageJ software uses image analysis to determine the area of a nanoparticle, and this area is then used to calculate particle diameter with the underlying assumption that the particle is perfectly spherical. Since, the iron oxide particles synthesized in this study are not perfectly spherical it is possible to get a slightly skewed size and size-distribution using the TEM analysis. Hence, dynamic light scattering (DLS) analysis was also performed on these iron oxide particles, using a Malvern Zetasizer Nano ZS, to confirm the trends obtained through TEM analysis. Fourier transform infrared spectroscopy (FTIR) was also carried out on the sample using a Nicolet Avatar 360 to investigate the nature of chemical interaction between the ligand (oleic acid) and the nanoparticle core. The solid samples were pelletized using a pellet press along with KBr for the FTIR analysis. A baseline for pure KBr and atmospheric correction was used for all the samples studied.

4.2.4 Size-selective separation process using the packed column cascaded vessel apparatus

The size-selective fractionation process is carried out using the gold nanoparticles dispersed in hexane and the cascaded vessel apparatus, in a manner similar to that described in Section 2.2.5. The P1 and P2 values in this experiment were 680 psi and 700 psi respectively for all the packing materials under study. The samples obtained at the different pressure values are then analyzed using TEM and DLS in the same way as the original synthesized nanoparticle dispersion.

The glass liner used in the experiment is filled with the glass packing material as shown in Figure 4.1. The top and bottom of the glass liner is also filled with glass wool to prevent the movement of the packing materials and to facilitate uniform dispersal of the

nanoparticle mixture. After the packing materials are loaded into the glass liner, the amount of liquid entrained in the packing material is calculated by adding a predetermined amount of hexane over the packed glass liner, draining the packed liner and noting the weight change in system. Through these simple calculations it is possible to estimate approximately how much liquid gets entrained in the packing and provides an easy way to compare the different packing materials studied. The detailed calculations for this are shown in the Appendix 3. A summary of these calculations is shown in Table 4.1. It should be noted that due to the similarity in liquid entrainment values obtained and the perceived difficulty in distinguishing between fractionation results obtained, the fractionation experiments were only carried out on the 2 mm sphere, 5 mm sphere and Raschig ring packings.

4.2.5 Size-selective separation process with the CSTR-type apparatus

The vessel (as shown in Figure 4.2) used for the bench scale size-selective separation of iron oxide nanoparticles is a modified 1L Parr-reactor Model 4571 (Parr Instruments Company, Moline, Illinois, USA). The Parr reactor is fitted with a dip tube and is also equipped with a pressure transducer and thermocouple. A removable glass liner is used inside the Parr reactor for easy cleaning and to prevent contamination of the iron oxide nanoparticle sample. The reactor system is connected to a high pressure syringe pump (ISCO 260D) which is used to control the amount of CO_2 added to the system. To initiate an experiment, 200 mL of the synthesized iron oxide nanoparticle dispersion in hexane is added to the Parr reactor. The Parr reactor is then sealed and pressure tested using CO_2 to ensure that no leaks are present in the system. The reactor system is then purged of air and pressurized to the first experimental pressure of 13.8 bar

(200 psi) by injecting CO_2 through valve V1 using the syringe pump. The system is then maintained at this pressure for a period of 4 hours (enough time for the system to reach equilibrium) using the syringe pump. This is done so as to ensure the complete dissolution of CO_2 into the hexane and the complete precipitation (if any) of the iron oxide nanoparticles. After this period of 4 hours, the valve V2 is slowly opened, while maintaining the pressure at 13.8 bar using the syringe pump. The pressure difference across valve V2 causes the nanoparticle dispersion inside the vessel to be transferred via the dip-tube into an external collection vessel where approximately 2 mL of the nanoparticle dispersion is retrieved. This sample is then transferred to a scintillation vial and the collection vessel is cleaned using pure hexane. The system pressure is then increased to the next desired pressure value (27.6 bar/400 psi), the system allowed to reach equilibrium, and the sample collection process is carried out. After this technique is repeated for each of the desired pressures, the system is then slowly depressurized to atmospheric pressure by opening valve V3. It should be noted that while only 2 mL nanoparticle dispersion samples are drawn from the system at each of the investigated pressures in this particular experiment, it is feasible to recover essentially all of the dispersed nanoparticles from the system at any given pressure by removing all of the remaining liquid dispersion from the vessel (thereby leaving only the precipitated nanoparticles in the vessel). Each of the 2 mL liquid nanoparticle dispersion samples that were retrieved from the Parr-reactor at the different system pressure values were then analyzed using TEM and DLS in the same way as the originally synthesized nanoparticle dispersion.

a)

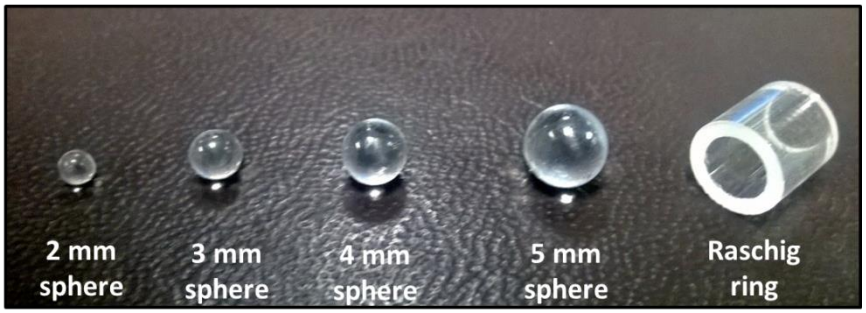

b)

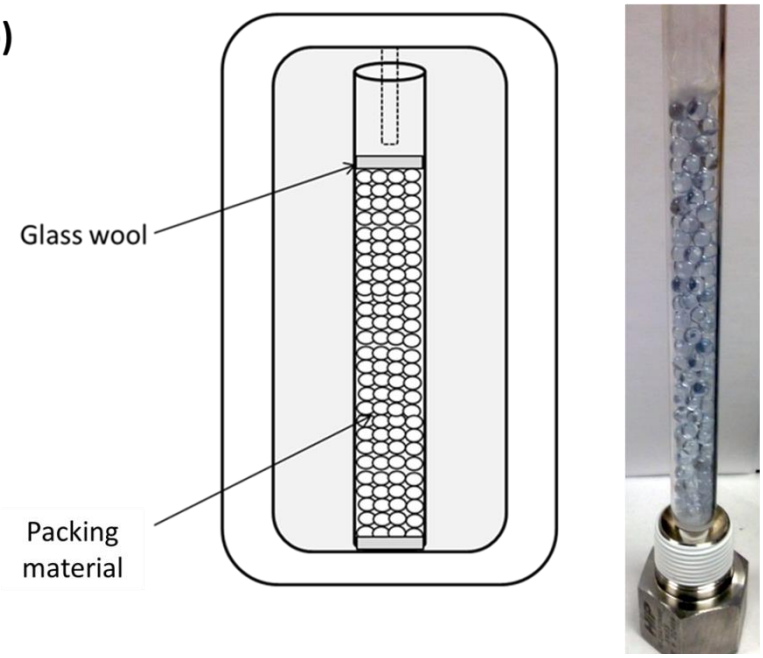

Figure 4.1 a) Types of packing materials studied in this experiment*, b) packing arrangement inside each cascaded vessel.

*Fractionation carried out using only the 2 mm sphere, 5 mm sphere and Raschig ring packings

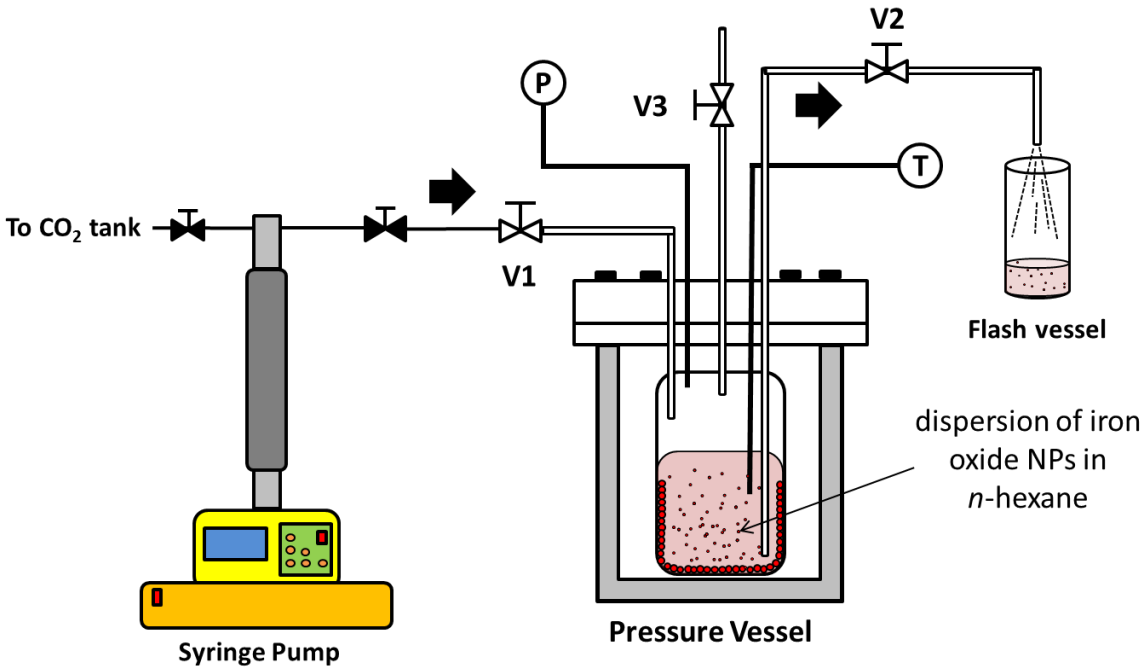

Figure 4.2 Bench scale apparatus to size-selectively separate iron oxide nanoparticles using a gas-expanded liquid system.

4.3 Results and Discussion

4.3.1 Size-selective separation process using the packed column cascaded vessel apparatus

The results from the liquid holdup experiments for the packing materials being investigated for this study are shown in Table 4.1. The surface area per packing increases with an increase in the diameter of the packing material. The Raschig rings have the highest surface area (2.04 cm^2) of all the packing material studied. The Raschig rings also occupy the lowest volume in the vessel due to their hollow cylindrical structure. The liquid entrainment experiments performed on the glass liner with various packing materials showed that in all of the spherical packing materials studied, the 2 mm spheres (the smallest packing material) had the highest amount of liquid entrainment (7.1 %). This high level of liquid entrainment is expected due to enhanced capillary action between adjacent packings in this system. Interestingly, the Raschig rings had the highest liquid entrainment value (8.9 %) compared to the other packing materials. This unusually high liquid entrainment value is due to the large quantity of liquid which gets trapped within the inner cylinder of the rings due to capillary action.

On comparing the various properties of the packing materials listed in Table 4.1, it can be noted that there is only a small and gradual variation in the properties of the 2 mm, 3 mm, 4 mm and 5 mm spherical packing materials. Hence, for the sake of simplicity the fractionation experiments were performed only on the two spherical packing materials with the largest difference in properties (i.e., 2 mm and 5 mm packing materials).

	2 mm sphere	3 mm sphere	4 mm sphere	5 mm sphere	Raschig rings
Surface area per packing (cm^2)	0.13	0.28	0.50	0.79	2.04
Surface area per unit volume (cm^{-1})	30.00	20.00	15.00	12.00	21.60
Surface area added to the system (cm^2)	240.52	159.67	130.62	99.70	51.03
Total % increase in surface area	506.59	365.11	314.29	260.16	119.29
Number of packings in reactor vessel	1915	565	260	127	25
Volume occupied by packing material (cm^3)	8.02	7.98	8.71	8.31	2.36
Liquid entrainment (% total)	7.15	6.72	5.62	5.07	8.94

Table 4.1 Properties of packing materials investigated in this study

The results from the fractionation experiments performed on the original system (with no packing materials) and the systems with packing materials (2 mm spheres, 5 mm spheres, Raschig rings) are shown in Figure 4.3. It is to be noted that the first fraction in all the samples was a control sample (with no packing being present in the first cascaded vessel) and the size distribution of this fraction is approximately the same across the various packing materials studied. From the results it is observed that the fractionation carried out using the 2 mm packing (Figure 4.3b) was the least effective due to the lack of distinct size fractions obtained in the three fractions. The 2 mm fractions were also relatively polydisperse (higher standard deviation values) compared to the other fractions. This increased polydispersity and lack of distinct size fractions could be due to the large volume occupied by the packing material and high liquid entrainment (Table 4.1) present when this packing is used. The fractionation results obtained using the 5 mm packing materials and Raschig rings (Figure 4.3c and 4.3d) are similar to the ones obtained using no packing material (Figure 4.3a). The increased surface area/packing of the Raschig rings is unable to compensate for the increased entrainment or the lower overall increase in surface area. The lower surface area/packing for the 5 mm spherical packing material combined with the large volume occupied by it in the column could be the reason behind the lack of fractionation effectiveness in this packing material. Hence, the use of various packing materials in the cascaded vessel apparatus failed to provide any conclusive increase in effectiveness in fractionation of dodecanethiol coated gold nanoparticles dispersed in *n*-hexane. To overcome the surface area limitations of the cascaded vessel apparatus and to enable the fractionation of gram-scale quantities of iron oxide nanoparticles a new system was designed and is explained in the next section.

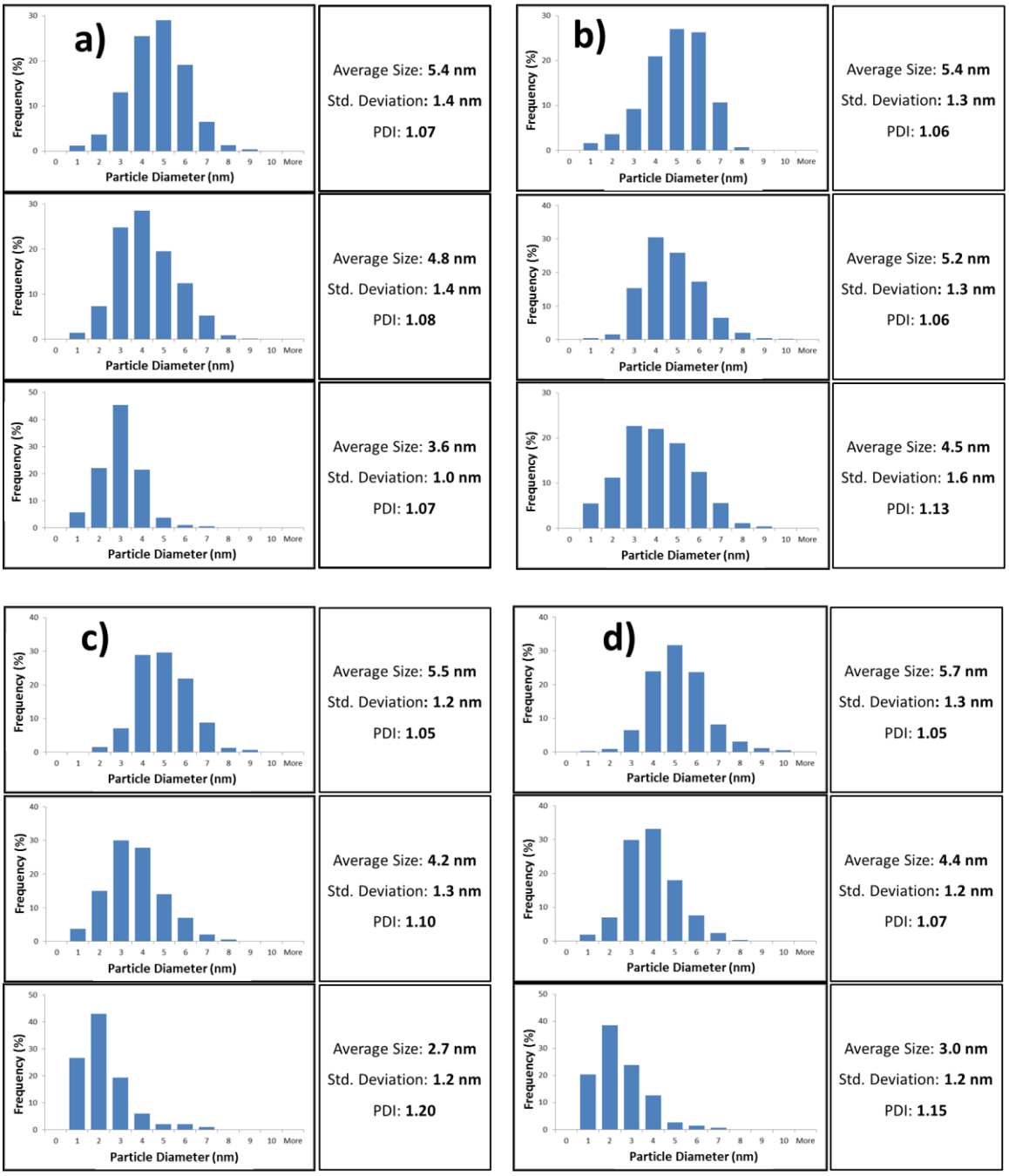

Figure 4.3 Size-distribution of the gold nanoparticle samples recovered from the GXL apparatus after fractionation at 680 and 700 psi. a) No packing, b) 2 mm glass beads, c) 5 mm glass beads and d) Raschig rings

4.3.2 Size-selective separation process with the CSTR-type apparatus

Oleic acid-coated iron oxide nanoparticles were initially synthesized using the coprecipitation method since it uses inexpensive reagents and lower reaction temperatures compared to other iron oxide nanoparticle synthesis methods.(C.-J. Chen, Lai, Lin, Wang, & Chiang, 2009; Hyeon et al., 2001; J.-G. J. J.-H. Park et al., 2005) The surface functionalization of the synthesized particles was examined using FTIR spectroscopy and the results obtained are shown in Figure 4.4 along with the spectrum for pure oleic acid. The two sharp peaks present in both spectra, in the range of 2800-3000 cm^{-1}, can be attributed to the $–CH_2$ stretches from the alkyl chain in oleic acid. The spectrum for the iron oxide nanoparticles shows a characteristic Fe-O stretch at 588 cm^{-1} and the spectrum for pure oleic acid, on the other hand, shows a prominent C=O stretch at 1710 cm^{-1}. In the spectrum of the iron oxide nanoparticles coated with oleic acid, a reduction in intensity of this C=O stretching peak is observed coupled with its splitting into two distinct peaks of lower wavenumber (1623 cm^{-1} and 1529 cm^{-1}), thereby signifying a C-O interaction. The presence of this interaction is consistent with previous observations that have been reported in the literature (S.-Y. Lee & Harris, 2006; P. S. Vengsarkar & Roberts, 2014; C. Y. Wang et al., 2010; L. Zhang et al., 2006) that indicate the presence of a ligand-core conjugation via the C-O bonds (L. Zhang et al., 2006). The size analysis obtained using TEM and DLS data indicated that the nanoparticles synthesized using the coprecipitation method were relatively polydisperse in nature. It should also be noted that some of the generated particles were not perfectly spherical in nature. which is typical for particles produced using the coprecipitation technique.(Babes et al., 1999; Maity & Agrawal, 2007; C. Y. Wang et al., 2010) The core diameter of the

iron oxide nanoparticles as determined by TEM analysis was found to be 6.4 ± 3.7 nm. The average volume-weighted hydrodynamic diameter of these same particles was determined to be 21.1 nm using DLS. DLS measures the hydrodynamic diameter of the dispersed nanoparticles consisting of the metal iron oxide core along with the solvated ligand shell Thus, DLS size analysis often yields a higher average diameter value than that obtained via TEM analysis which only provides an indication of the diameter of the metal core.(Lim, Yeap, Che, & Low, 2013)

Size-selective separation of the iron oxide nanoparticle dispersion was performed in the high pressure Parr-reactor apparatus at a series of predetermined pressures where the fractionated samples were recovered in a collection vessel, as detailed in the Experimental section. The TEM images of the nanoparticle samples obtained at each of the pressure values are shown in Figure 4.5. The reduction in nanoparticle size upon increasing system pressure is clearly visible from these images. From the size analysis of these TEM images, it is observed that there is no significant deviation of size or size-distribution of the samples drawn at 13.8 bar (200 psi) and 27.6 bar (400 psi) compared to that of the original sample (6.3 ± 3.7 nm). However, for samples recovered at even higher system pressures, a progressive decrease in average nanoparticle size and standard deviation is observed with increasing pressure. The sample collected at 34.5 bar (500 psi) has an average nanoparticle diameter that is approximately 1 nm smaller than the original nanoparticle dispersion. Further reduction in nanoparticle diameter was obtained at each of the subsequent pressures examined. The lowest nanoparticle size obtained amongst the samples studied is 2.6 ± 1.3 nm for the nanoparticle dispersion obtained at the system pressure of 48.3 bar (700 psi).

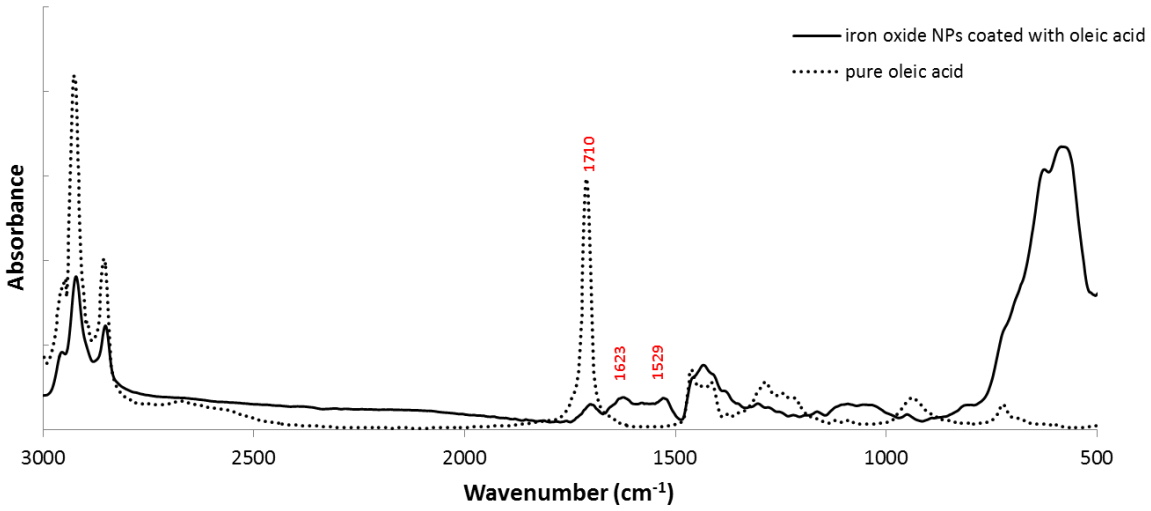

Figure 4.4 FTIR spectrum of oleic acid coated iron oxide nanoparticles synthesized using a coprecipitation technique.

The nanoparticle dispersion obtained at a highest experimental system pressure of 50 bar (725 psi) was extremely dilute and almost colorless, indicating that very few particles remained dispersed in solution at this stage. The diameter of the nanoparticles present in this particular sample could not be accurately determined given the resolution/magnification of the available TEM equipment and the small number of particles present in the system at this pressure. The reduction in the size and size distribution of nanoparticles present in the retrieved dispersions is shown in Figure 4.5b and Figure 4.6.

It can be deduced from the observed reduction in average nanoparticle size and size distribution that the iron oxide nanoparticle precipitation essentially begins at a system pressure between 27.6 bar and 34.5 bar. At sequentially higher pressure values a steady reduction in nanoparticle size and size distribution is observed (Figure 4.5b). This trend is similar to that observed previously in dodecanethiol-coated metal nanoparticle systems. (S R Saunders & Roberts, 2009; Steven R Saunders & Roberts, 2012; G Von White & Kitchens, 2010) Our hypothesis is that the increasing CO_2 pressure in the reactor system sequentially diminishes the solvent strength of the CO_2+hexane mixture, thereby reducing its ability to sufficiently solvate the oleic acid-coated iron oxide nanoparticles such that they all remain dispersed in solution. Progressively smaller nanoparticles will precipitate from solution upon worsening solvent conditions (i.e. the largest particles will precipitate first as CO_2 pressure is applied to the solution). As such, increasing the applied CO_2 pressure in the system will cause a fraction of the largest particles in the dispersion to precipitate while leaving the rest of the particles thermodynamically stabilized in solution.

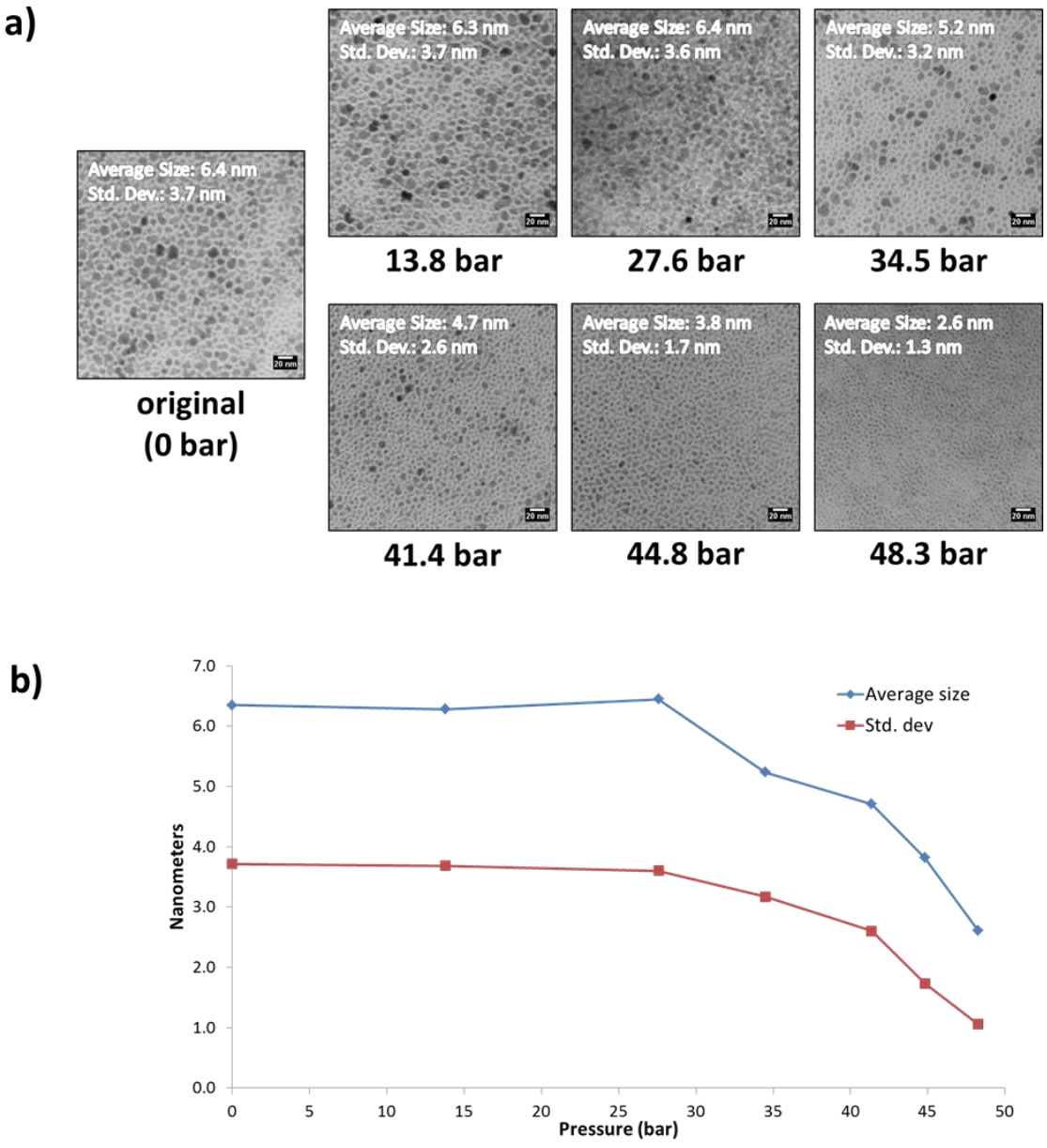

Figure 4.5 a) TEM images of the original iron oxide nanoparticle dispersion and the nanoparticle samples retrieved at the experimental pressures. b) Trends in average nanoparticle core size and standard deviation (using TEM) under different experimental pressure conditions.

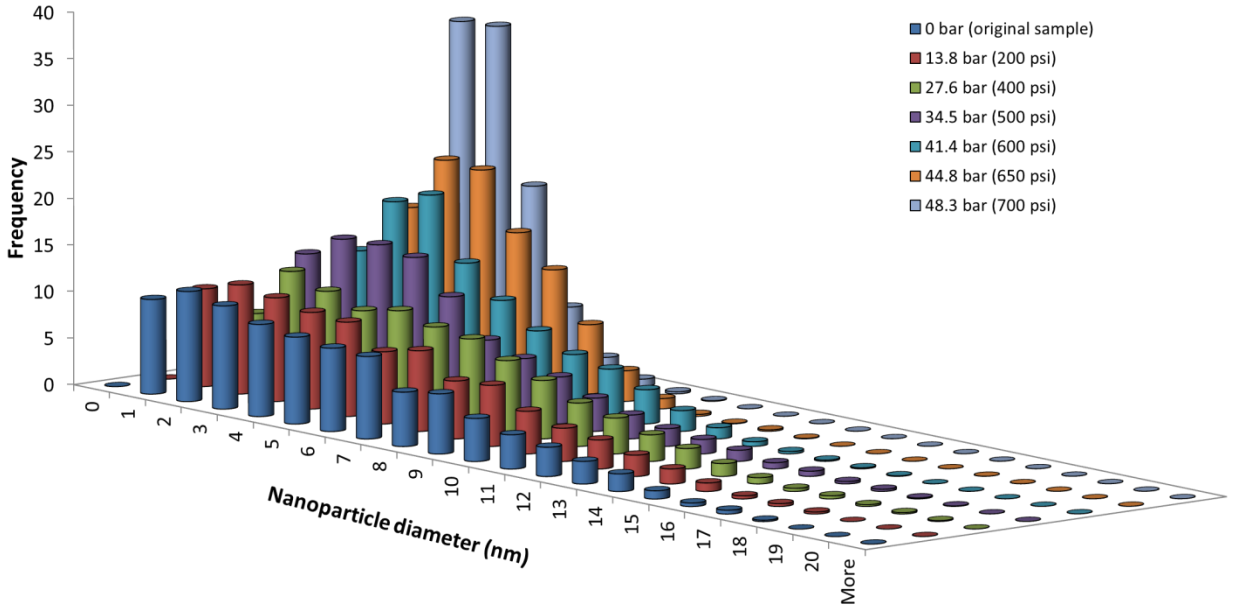

Figure 4.6 Size-distribution of the iron oxide nanoparticle samples recovered from the GXL apparatus under various pressure conditions obtained using TEM analysis

A further increase in applied CO_2 pressure will then cause the next largest fraction to precipitate where the average nanoparticle size will depend upon the pressure employed.(Anand et al., 2005, 2007; S R Saunders & Roberts, 2009)

The mechanism that underpins the precipitation of the oleic acid coated iron oxide nanoparticles is expected to be same as that attributed to the precipitation of dodecanethiol capped metal nanoparticles from a GXL solution. (Gregory Von White, Mohammed, & Kitchens, 2011; G Von White & Kitchens, 2010) Oleic acid and dodecanethiol have similar structural configurations once they are conjugated to the nanoparticle core since they both have unbranched aliphatic chains in their chemical structure. The difference in the carbon number and the double bond present in oleic acid could provide for a more densely-packed protective layer (Y. Lu, Lu, Mayers, Herricks, & Xia, 2008) on the surface thus changing the precipitation pressures in the oleic acid-iron oxide nanoparticle system when compared to the dodecanethiol-gold nanoparticle system. As mentioned previously, the largest nanoparticles precipitate first upon worsening solvent conditions (i.e. with increasing applied CO_2 pressure) due to larger van der Waals forces (Anand et al., 2007; S R Saunders & Roberts, 2009), leaving the smaller particles dispersed in the solution. These smaller unprecipitated particles are the samples which we recover from the reactor system in the flash vessel. The way the current apparatus is designed causes the nanoparticle size distribution to shift towards the left (lower nanoparticle size) upon increasing system pressure due to what is effectively a 'sieving effect' on the original nanoparticle dispersion (i.e. larger particles get held back and smaller particles pass through). In all, these TEM results confirm that progressive increases in applied CO_2 pressure causes the larger sized nanoparticles in dispersion to

successively precipitate out of solution, leaving the smaller nanoparticles dispersed in the solution and recoverable.

The results from the TEM analysis of the recovered nanoparticle samples are further supported by DLS analysis of the same samples, as shown in Figure 4.7 and Table 4.2. From the size histograms obtained using DLS, the size distributions of the samples obtained at 13.8 bar and 27.6 bar are very similar to that obtained from the original sample (average size - 16.2 nm). However, at and above system pressures of 34.5 bar, a shift towards lower nanoparticle sizes is observed. The DLS size distribution of the recovered samples also decreases as the system pressure is increased above 27.6 bar. A clear trend in average size reduction is observed at 41.4 bar (11.5 nm), 44.8 bar (8.0 nm) and 48.3 bar (4.7 nm). At 50 bar, the highest experimental pressure, DLS analysis was able to provide a size distribution for the extremely small particles (1.7 nm) present in the colorless dilute solution. By comparing these DLS results to the TEM results (Table 4.2), the reduction in the average nanoparticle size upon increasing CO_2 pressure is evident. The diameters of the nanoparticles obtained from DLS analysis are larger than the diameters obtained from TEM analysis due to the fact that DLS analysis accounts for the presence of the hydration layer and the presence of the stabilizing ligand in the measured particle. This difference in average size obtained from these two techniques matches closely that observed in literature (Lim et al., 2013). While keeping in mind the inherent differences between these characterization techniques, similar trends in size-reduction are obtained through TEM and DLS characterization of the samples.

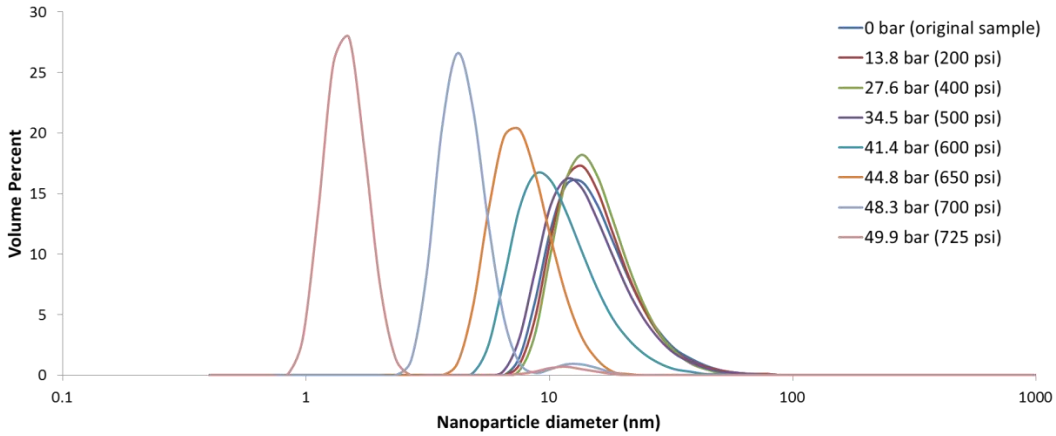

Figure 4.7 Size-distribution of the iron oxide nanoparticle samples recovered from the GXL apparatus under various pressure conditions obtained using DLS analysis.

applied CO_2 pressure (bar)	average nanoparticle diameter (TEM) (nm)	average nanoparticle diameter (DLS)* (nm)
0.0	6.3	16.2
13.8	6.3	16.3
27.6	6.4	16.4
34.5	5.2	15.3
41.4	4.7	11.5
44.8	3.8	8.0
48.3	2.6	4.7
50.0	n/a	1.7

Table 4.2 Comparison between average nanoparticle diameters obtained using TEM and DLS. **volume-weighted average*

Fractionation apparatus	spiral tube	cascaded vessel	current apparatus
primary use	proof-of-concept	fundamental studies	fundamental studies/applied studies
nanoparticle systems studied	CdSe/ZnS, Au, Ag	Au, Ag, FeO	FeO
typical processing volume	200-700 μL	5-10 mL	200-400 mL
typical metal loading	dilute (< 0.1 mg/mL)	dilute (< 0.1 mg/mL)	concentrated (>5 mg/mL)
max fractions in a single run	6	3	no limit
typical std. dev. of most monodisperse fraction	±0.5 nm	±1.0 nm	±1.5 nm
fractionation accuracy	Very High	High	Moderate*

Table 4.3 Comparison between different GXL fractionation methods

Hence, the current apparatus is very effective at separating large volumes (200 mL) of concentrated oleic-acid coated iron oxide nanoparticle solutions (~ 10 mg iron/ mL solvent) based upon their size through the use of a gas-expanded liquid. A comparison of the current fractionation device and previous apparatuses is shown in Table 4.3. This bench-scale apparatus is also easily scalable since, in structure, it is very similar to a standard continuous stirred tank reactor.

The ability of the current apparatus to collect multiple samples in a single run/loading allows one to directly determine the pressures at which precipitation occurs. By performing multiple fractionation experiments on a single nanoparticle sample, one can use the obtained experimental data to develop an empirical model to better understand the size and size-distribution of the nanoparticles that would be recovered under a given set of GXL fractionation conditions. It is noted that this is more cumbersome for the iron oxide system compared to previous studies involving metal nanoparticles where UV-vis spectroscopy and the surface plasmon resonance band of the nanoparticles could be used to directly monitor their precipitation as a function of applied CO_2 pressure (Steven R Saunders & Roberts, 2012). Saunders and Roberts demonstrated that these tools could be used to theoretically determine the size of the nanoparticles that would precipitate from solution at a given set of conditions (S R Saunders & Roberts, 2009). For example, the absorption spectrum of metallic gold nanoparticles is characterized by a strong broad absorption band around 520 nm that is absent in the bulk metal spectra (Amendola & Meneghetti, 2009; Haiss et al., 2007). However, for iron oxide nanoparticles, no such absorption band is present and a relatively flat spectrum with a plateau at around 480 nm is observed (Kang et al., 1998; Kebede et al., 2013;

Klačanová et al., 2013; Walt et al., 2010). This, unfortunately, prevents accurate *in-situ* monitoring of the precipitation of iron oxide nanoparticles in the gas-expanded liquid system. To better understand the GXL fractionation of iron oxide nanoparticles, more studies should be carried in order to develop a fundamental model that would allow one to predict the size of iron oxide nanoparticles that would precipitate at a given applied CO_2 pressure.

4.4 Conclusion

In summary, through the design of a simple high pressure reactor system, large quantities of iron oxide nanoparticles have been successfully fractionated based upon their size using a gas-expanded liquid. This GXL system is effective at separating large volumes (> 200 mL) of concentrated oleic-acid coated iron oxide nanoparticle solutions (~ 10 mg iron/ mL solvent). By successively pressurizing the GXL system to applied CO_2 pressures of up to 50 bar, the nanoparticles of core sizes varying from 6.3 ± 3.7 nm to 2.6 ± 1.6 nm were successfully fractionated from the original iron oxide nanoparticle dispersion. The monodispersity of the obtained nanoparticle fractions was observed to increase upon increasing applied CO_2 pressure. These trends in nanoparticle precipitation as a function of applied CO_2 pressure were found to be similar to those observed previously for metal nanoparticle systems. The use of this simple GXL apparatus provides a pathway to separate large quantities of inexpensively produced iron oxide nanoparticles based upon their size for subsequent use in large scale applications such as catalysis.

Chapter 5

Controlled Deposition of Iron Oxide Nanoparticles onto an Oxidic Support using A Novel Gas-Expanded Liquid Process for the Generation of a Supported Fischer-Tropsch Catalyst

5.1 Introduction

Fischer-Tropsch (FT) synthesis involves the catalytic conversion of synthesis gas ($CO + H_2$) into aliphatic hydrocarbons and has been at the forefront of gas-to-liquid technology since its discovery in the 1920s (Jacobs et al., 2002; J. Niemantsverdriet & van der Kraan, 1980; Rofer-DePoorter, 1981; Van Der Laan & Beenackers, 1999). The use of gas-to-liquid technology has been of particular contemporary interest as an alternative means of synthesizing fuels and chemicals from various carbonaceous resources such as natural gas, biomass, coal, shale gas, and others (Deklerk, 2008; Hamelinck, Faaij, Denuil, & Boerrigter, 2004; Mokrani & Scurrell, 2009; Roberts & Elbashir, 2003; Rodr & Klerk, n.d.). Fischer-Tropsch synthesis, which is a surface catalyzed polymerization process, traditionally utilizes iron or cobalt based catalyst systems depending on the composition of the syngas and the reactor configuration employed (Dry, 2002). Iron-based catalysts have certain advantages over their cobalt-based counterparts since iron disfavors the competing formation of methane and also catalyzes the water-gas shift reaction (Torres Galvis, Bitter, Khare, et al., 2012).

Iron catalysts are also relatively inexpensive and are capable of producing a wide range of hydrocarbons ranging from light olefins to wax (Zhao et al., 2013). Unsupported precipitated iron catalysts have been shown to provide commercially viable levels of conversion and selectivity in FT systems (Dry, 1996; Eilers, Posthuma, & Sie, 1990; Espinoza & Steynberg, 1999). However, the mechanical stability of bulk iron catalysts at high temperature is problematic, and carbon deposition has also been observed in such systems (D B Bukur et al., 1995). Such carbon deposition can cause plugging of the catalyst bed (i.e. in a fixed-bed reactor), as well as large pressure gradients and fouling of separation equipment (i.e. in a fluidized-bed reactor) used in the FT process (O'Brien, Xu, Bao, Raje, & Davis, 2000; Torres Galvis, Bitter, Khare, et al., 2012). An alternative to the use of a precipitated catalyst involves the use of a support material (e.g. alumina or silica) to provide a physical mechanism to disperse the iron and thereby prevent mechanical action on the catalyst (Keyvanloo & Mardkhe, 2014; Torres Galvis, Bitter, Khare, et al., 2012). Supported iron catalysts however suffer from activation limitations imposed upon them due to various factors, including reactivity with the surface of the support (D. Bukur et al., 1990; Dragomir B. Bukur & Sivaraj, 2002; J. W. Niemantsverdriet, van der Kraan, Van Dijk, & van der baan, 1980).

There are several techniques described in the literature to synthesize supported iron oxide catalysts. The impregnation method entails wetting a solid support material with a liquid solution (solvent) containing the dissolved surface oxide precursor (Regalbuto, 2006). The incipient wetness method, which is a modified version of the impregnation technique, involves the use of an impregnation liquid of volume equal to (or slightly higher than) the total pore volume of the catalyst support material(Zabidi,

2010) in order to deliver the catalyst precursor onto the support. The incipient wetness method can be used to produce nano-scale particles on the catalyst support from the dispersed precursor, but it is difficult to controllably obtain a narrow particle size distribution (R. J. White et al., 2009). Previous studies have demonstrated that the incipient wetness method can be used with various support materials to generate supported iron catalysts with high FT activity (Dragomir B. Bukur & Sivaraj, 2002; Torres Galvis, Bitter, Khare, et al., 2012; van Steen & Prinsloo, 2002). The transport of the solvent through the support material is dominated by capillary action in the incipient wetness method (Regalbuto, 2006). The transport of the solvent into the pores of the catalyst support is diffusion limited (slower than capillary action) in cases where the solvent volume is greater than the pore volume of the support (Regalbuto, 2006; Wilson & Lee, 2013). Other methods used to prepare supported catalysts include colloidal precipitation methods, which involves the precipitation of in-situ generated metal particles (via a high-temperature synthesis method) onto the support, as well as electrostatic absorption methods(Amelse, Butt, & Schwartz, 1978; van Steen & Prinsloo, 2002; Zabidi, 2010). While these methods are viable alternatives to the traditional incipient wetness method, and while it has been reported that high levels of iron dispersion can be achieved on the support material(Snel, 1989), these methods can also give rise to iron oxide crystallites of larger sizes (> 30 nm)(van Steen & Prinsloo, 2002).

Several studies in recent literature have reported that nanoparticle based FT catalysts (either iron or iron oxide) exhibit enhanced catalytic properties when compared to bulk-scale catalysts due to their high surface area to volume ratio and modified chemical potential (Dragomir B. Bukur & Sivaraj, 2002; Nakhaei Pour, Housaindokht,

Irani, & Kamali Shahri, 2014; J.-Y. Park et al., 2010; Torres Galvis, Bitter, Khare, et al., 2012). The catalytic properties of these nanoparticle based catalysts have been shown to be highly dependent on the size of the iron (or iron oxide) nanoparticles (Nakhaei Pour et al., 2013, 2014; J.-Y. Park et al., 2010). The size dependent catalytic activity have been attributed to differences in the extent of the interaction of the differently sized nanoparticles with the support material (Torres Galvis, Bitter, Khare, et al., 2012), as well as differences in the dispersion of the iron oxide (Torres Galvis, Bitter, Davidian, et al., 2012) and the activation energy of the CO adsorbed on the catalyst active sites (J.-Y. Park et al., 2010). Park et al.(J.-Y. Park et al., 2010) studied the effect of particle size of nano-sized iron oxide supported on δ-Al_2O_3, with average particle sizes ranging from 2 to 12 nm. They reported an optimum particle size of 6.1 nm for FT synthesis in terms of catalytic activity. CH_4 and hydrocarbon selectivity was found to be strongly affected by the particle size. The turn over frequency (TOF) of Fe/δ-Al_2O_3 increased with particle size from 2 to 6 nm. Further increase in the particle size from 6 to 12 nm, however, had little to no effect on TOF as reported by Park et al. (J.-Y. Park et al., 2010). Galvis et al.(Torres Galvis, Bitter, Davidian, et al., 2012) used carbon nanofibers as supporting materials to evaluate the intrinsic particle size effect (2-17 nm) on catalytic activity and selectivity under a reaction condition of Fischer Tropsch olefin synthesis, assuming that carbon nanofibers possess limited interaction toward iron nanoparticles. Their results demonstrated that for unpromoted iron carbide, low coordination sites at corners and edges are more active than sites at terraces, while similar in terms of selectivity. However, smaller iron carbide particles showed higher surface specific activities (apparent TOF), mainly due to a higher CH_4 production. Later on, Galvis et al.(Torres

Galvis, Bitter, Khare, et al., 2012) further indicated that a strong metal-support interaction inhibited the formation of catalytically active iron carbides, resulting in a low iron time yield. Iron nanoparticles dispersed on weakly interactive supports, such as α-Al_2O_3 and carbon nanofibers, also demonstrated higher selectivity towards C_2-C_4 olefins (Torres Galvis, Bitter, Khare, et al., 2012).

A common way to generate such supported catalysts with monodisperse nanoparticles is to synthesize the monodisperse nanoparticles initially and then deposit them onto the support using the previously mentioned wet chemical techniques (J.-Y. Park et al., 2010). However, common synthesis techniques used to generate monodisperse iron oxide nanoparticles require relatively high temperatures (Hyeon et al., 2001; Laurent et al., 2008; J.-Y. Park et al., 2010; Z. Xu et al., 2010; Yu et al., 2004) and expensive reagents (J.-G. J. J.-H. Park et al., 2005; Yu et al., 2006). Another alternative method would be to initially synthesize a relatively polydisperse nanoparticle population and then size selectively fractionate (i.e. separate) this nanoparticle mixture into more monodisperse fractions in order to remove the nanoparticles having undesirable sizes. Several size separation processing techniques for nanoparticles, such as magnetic separation (Yavuz et al., 2006), centrifugation (Novak et al., 2001), and electrophoresis (Surugau & Urban, 2009), exist in literature. However, these techniques can suffer from certain drawbacks including, but not limited to, the use of expensive equipment, having low throughputs, and the requirement of large quantities of solvents (Bishop et al., 2009; Fletcher, 1991; S R Saunders & Roberts, 2009).

Our lab has developed a process to overcome some of these drawbacks through the design of a novel gas-expanded liquid (GXL) technique (McLeod, Anand, et al.,

2005; McLeod, Kitchens, et al., 2005; S R Saunders & Roberts, 2009; Steven R. Saunders, Eden, & Roberts, 2011; P. Vengsarkar & Roberts, 2013). Previous studies have shown that this technique can be used to effectively separate gold, silver and CdSe nanoparticles based upon their size (Anand et al., 2007; McLeod, Anand, et al., 2005; Steven R Saunders & Roberts, 2012; P. Vengsarkar & Roberts, 2013). A GXL is generated by dissolving a compressible gas such as CO_2 into an organic phase at subcritical pressures. The dissolved CO_2 also helps increase transport properties by increasing the intrinsic diffusivity of solutes in the GXL phase (Hintermair, Leitner, & Jessop, 2010; Jessop & Subramaniam, 2007; Bala Subramaniam, 2010). Other property changes which occur in a GXL relative to the neat solvent include a reduction in viscosity, a change in solvent polarity, and a change in solubility of dissolved solids (Jessop & Subramaniam, 2007). In the GXL fractionation process, we exploit this reduction in solubility to controllably precipitate nanoparticles of progressively smaller size from solution using increasing amounts of applied CO_2 pressure. The nanoparticles used in this process are usually coated with an aliphatic ligand (e.g. dodecanethiol or oleic acid) for dispersion in an organic solvent and to ensure that they do not aggregate after precipitation (Steven R Saunders & Roberts, 2012). The CO_2, which dissolves into the solvent upon applied CO_2 pressure, is an antisolvent for these stabilizing ligands causing these ligands to collapse and induce the precipitation of the particles attached to them. It should be noted that the largest nanoparticles will precipitate first upon increasing applied CO_2 pressures due to larger van der Waals forces (Anand et al., 2007; S R Saunders & Roberts, 2009).

In this study, we have modified the GXL technique to controllably deposit iron oxide nanoparticles onto an oxidic support in order to generate a catalyst which can be used in FT synthesis. The iron oxide nanoparticles used in this study are coated with oleic acid, a popular stabilizing agent (S.-Y. Lee & Harris, 2006; C. Y. Wang et al., 2010; L. Zhang et al., 2006). Through modifications in our previously used apparatus, we aim to remove smaller sized particles from our initial dispersion, while simultaneously depositing the larger particles onto the surface of the support. This was done because previous researchers have shown that supported iron catalysts with nanoparticles of small size have lower activity due to their stronger interaction with the support surface (J.-Y. Park et al., 2010). As an added benefit, the lower viscosity and higher mass transfer coefficient in the GXL (Jessop & Subramaniam, 2007; Zeigermann & Valiullin, 2013) could enhance the diffusivity of the iron particles into the catalyst pores during deposition, resulting in a more uniform distribution of the nanoparticles (compared to traditional methods). Moreover, this study illustrates that we can apply a nanoparticle processing technology to generate more efficient and uniform FT catalysts.

5.2 Experimental Section

5.2.1 Materials

Iron (III) chloride hexahydrate ($FeCl_3 \cdot 6H_2O$, 99.9%), iron (II) chloride tetrahydrate ($FeCl_2 \cdot 4H_2O$, 99.9%), and *n*-hexane (HPLC grade, 95%), were obtained from Alfa Aesar. Oleic acid (99%), was obtained from Sigma Aldrich, and ammonium hydroxide (5M) was obtained from BDH. Deionized ultra-filtered (DIUF) water was obtained from Fisher Scientific. Activated alumina (94 - 100%, surface area > 300 m^2/g) was obtained from Labsorbents in the form of 1/16 beads. Silicon oxide (catalyst

support, 0.125 inch pellets, high surface area 250 m^2/g) was obtained from Alfa Aesar, iron nitrate was obtained from Sigma-Aldrich (99.99%). Carbon dioxide (SFC/SFE grade) was obtained from Airgas. All chemicals were used as received without further purification.

5.2.2 Synthesis of oleic acid coated iron oxide nanoparticles

Iron oxide nanoparticles coated with oleic acid were synthesized based on a method described previously by Jain et al. (Jain et al., 2005). Initially aqueous solutions of 0.2 M Fe (III) and 0.2 M Fe (II) were prepared using DIUF water. 120 mL of Fe (III) solution was mixed with 60 mL of Fe (II) solution in a three-necked flask with magnetic stirring. Under constant stirring and under a nitrogen atmosphere, 24 mL of 5M ammonium hydroxide was added to this mixture to generate a black precipitate of iron oxide nanoparticles. These reagent concentrations theoretically generate 2.78 g of iron oxide (i.e. ~2.01 g of iron). The temperature of this system was then increased to 80 °C and maintained for 30 min to evaporate the ammonia out of the solution. While the temperature is being increased, 2.24 mL of oleic acid was added to the mixture. After the end of the heating cycle, the system was allowed to cool down to room temperature. The nanoparticles were then magnetically immobilized and washed thrice with DIUF water (200 mL) to remove any excess reagents and impurities. The particles were then dried using nitrogen and dispersed in 400 mL of *n*-hexane via sonication (Fischer Scientific FS20). Half of this 400 mL dispersion of iron oxide nanoparticles (i.e. 200 mL containing ~ 1 g of iron) was used for each run of the GXL deposition process.

5.2.3 Preparation of oxidic support for nanoparticle deposition

The alumina support when obtained commercially was present in a spherical pellet form. The support was grinded down to a powder form using an IKA M20 Universal mill. The obtained powder was then sieved using mesh 45 and mesh 70 to obtain a powder of size between 212 and 355 μm. This oxidic support powder was then weighed and used for the deposition part of this study. For the silica support, the fine powder was first pelletized using a pellet press and then grinded down to a powder using an IKA M20 Universal mill. The powder was then sieved in the same way as described above to obtain a powder of uniform size (between mesh 45 and mesh 70).

5.2.4 Deposition of iron oxide nanoparticles onto the oxidic support using a GXL

A 1L Parr-reactor Model 4571 (Parr Instruments Company, Moline, Illinois, USA) fitted with a pressure transducer, thermocouple and a dip tube was used as the deposition apparatus for this study. A schematic of the reactor vessel used and the deposition process is shown in Figure 5.1. A removable glass liner is used inside the reactor for easy cleaning and to prevent contamination of the catalyst. CO_2 gas is delivered to the Parr reactor via a high pressure syringe pump (ISCO 260D) and the system pressure is monitored using the pressure gauge on the pump and an inline pressure gauge. A known quantity (8 g) of the powdered oxidic support is first added to the glass liner along with the dispersion of oleic acid-coated iron oxide nanoparticles in *n*-hexane. The glass liner is then added to the Parr reactor and the reactor is sealed. The impeller is set to a speed of 200 rpm and the reactor is purged of all air using CO_2. The pressure in the reactor is then slowly increased (over a period of one hour) by opening valve V1 and using the syringe pump until the pressure gauge reads a steady pressure of 700 psi. The

reactor is then maintained at this condition for a period of 20 hours to ensure that the *n*-hexane completely expands and that the system reaches equilibrium. After 20 hours, the impeller is stopped and the particles are allowed to settle for 30 minutes. A collection vessel is then placed at the outlet of the siphon tube and valve V2 is slowly opened under constant applied pressure via the syringe pump. The gas-expanded hexane is displaced from the reactor into the collection vessel via the siphon tube due to the pressure differential between the reactor and the collection vessel (which is maintained under atmospheric conditions). Since adiabatic expansion occurs at the location of valve V2 the hexane is removed slowly and at 2 min intervals. The system pressure usually fluctuates between 690 psi – 700 psi during this hexane removal step. The hexane removal continues until only CO_2 gas escapes the siphon tube outlet and no liquid effluent is observed. The system is then slowly depressurized (using valve V2) until the pressure in the system reaches atmospheric pressure. To remove any residual hexane left at the bottom of the glass liner, CO_2 is allowed to flow through the system from valves V1 to V2 for 15 min. The apparatus is then dismantled and the glass liner containing the catalyst precursor is removed.

The glass liner with the catalyst precursor is then placed in an oven at 100°C to evaporate any remaining hexane. The precursor of this catalyst is then removed from the glass liner and calcined at 375°C (ramp rate 5°C/min from room temperature) under the flow of air for 4 hours to remove the attached oleic acid (note: the boiling point of oleic acid is 286°C).

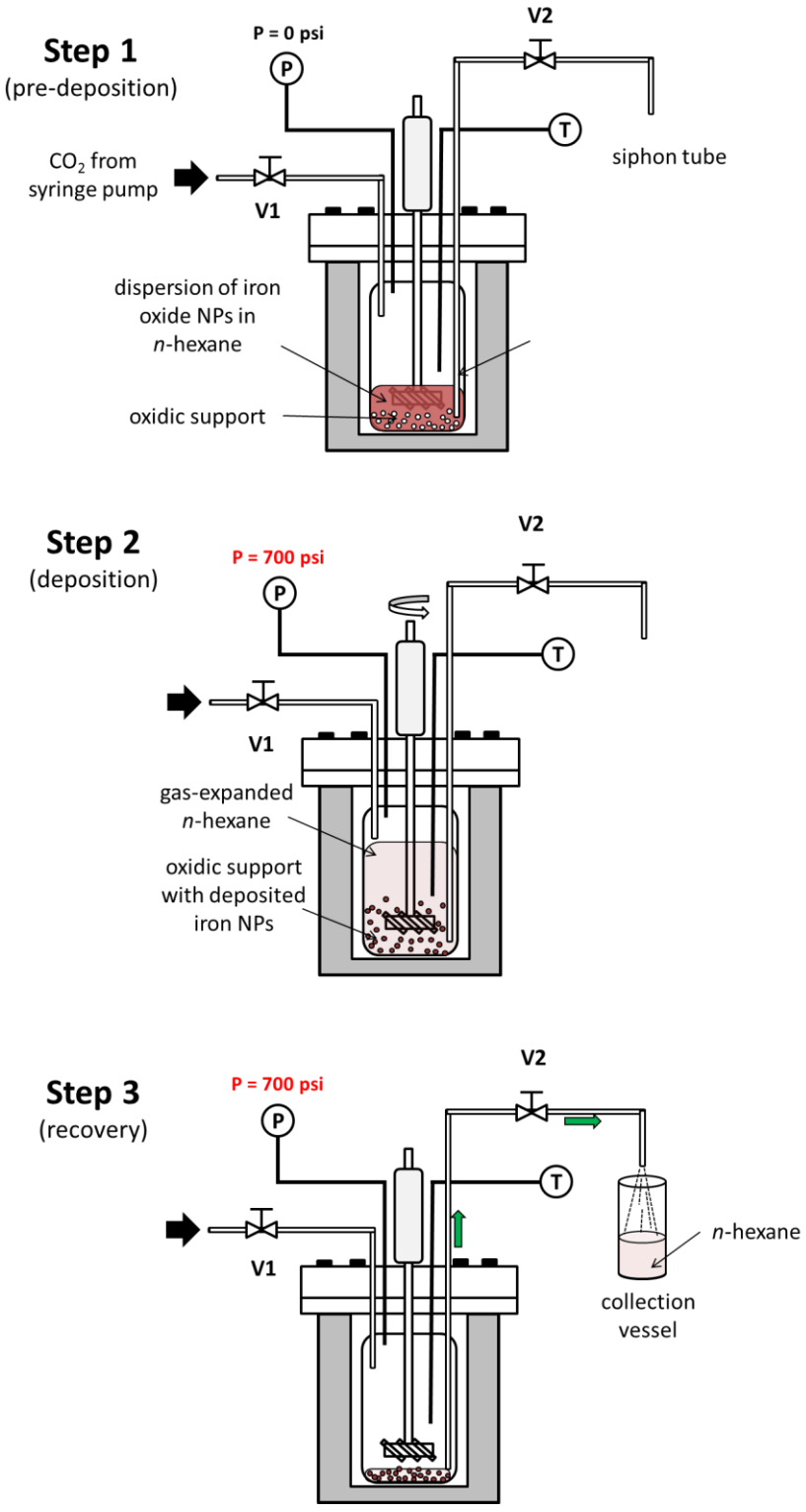

Figure 5.1 Schematic diagram of the GXL deposition apparatus and process

5.2.5 Deposition of iron onto oxidic support using incipient wetness method

In order to compare the catalytic performance of the supported nanoparticle catalysts (as described in the previous section) with the performance of a comparable FT catalyst with the same iron loading, control catalyst samples were prepared using the traditional incipient wetness method. Initially, a solution of iron nitrate was made by dissolving 7.25 g of $Fe(NO_3)_3 \cdot 9H_2O$ in 20 mL of DIUF water. This solution was then added dropwise to 10 g of pure support material until a paste was formed. This paste was then dried at 110°C for 2 hrs. This paste formation and subsequent drying process was continued until the entire 20 mL nitrate solution was expended. The final paste generated was then dried overnight followed by calcination in air. During calcination, the temperature was ramped from 25°C to 375°C at a heating rate of 5°C/min and held at 375°C for a period of 4 hrs. The generated catalysts were then used to conduct the control FT synthesis experiments. It needs to be pointed out that no structural modifiers or electronic promoters, i.e. K, Cu, have been added into the catalysts composition in order to simplify the comparison.

5.2.6 Characterization of iron oxide nanoparticles and catalysts

The synthesized iron oxide nanoparticles were characterized using transmission electron microscopy (TEM) and dynamic light scattering (DLS) in order to determine their size and size distribution. For TEM analysis, Carbon-coated TEM grids of each of the nanoparticle samples were prepared via dropcasting and micrographs were acquired on a Zeiss EM 10 transmission electron microscope and sized using the ImageJ software package. DLS was performed using a Malvern Zetasizer Nano ZS to determine the hydrodynamic diameter of the synthesized nanoparticle dispersions, as well as the

analysis of the nanoparticles that remained dispersed in the hexane solution that was recovered at the end of the GXL deposition process.

The supported iron oxide catalyst was characterized using transmission electron microscopy (TEM), Fourier transform infrared spectroscopy (FTIR), X-ray diffraction (XRD), thermogravimetric analysis (TGA), BET surface area analysis, and inductively coupled plasma emission spectrometry (ICP). Carbon-coated TEM grids of each of the catalyst samples were prepared via dropcasting using a solution of the catalyst dispersed in ethanol. These grids were then analyzed on a Zeiss EM 10 transmission electron microscope and sized using the ImageJ software package. To determine the surface functionalization of these particles, Fourier Transform Infrared (FTIR) spectroscopy was performed using a Nicolet Avatar 360 on each of the following samples: the pure ligand (oleic acid), the pure support material, the iron oxide nanoparticles, the supported iron catalyst (pre-calcination), and the supported iron catalyst (post-calcination). For FTIR analysis, a pure KBr pellet was made using a pellet press, and was used as a background for all the readings. To obtain the FTIR transmission spectra of the aforementioned samples, pellets of each were made by mixing the sample with pure KBr.

X-ray diffractometry (XRD) was used to investigate the crystallinity of the synthesized catalyst and to check for the presence of impurities. XRD data was obtained through the use of a Bruker D8 diffractometer using Cu Kα radiation operated at 40 kV and 40 mA. The sample was prepared by placing a small portion of the sample powder on a glass slide. The diffraction patterns were collected using a step size of 0.01° and 0.2 s/step count time from $5° \leq 2\theta \leq 90°$. Thermogravimetric analysis (TGA) of the supported iron catalyst was carried out using a TA Instruments (New Castle, DE) Q500

thermal gravimetric analyzer. The entire experiment was run under a constant flow of air at a flow rate of 10 mL/min. The furnace was first purged with air for 30 mins followed by taring and then the addition of a fixed quantity of sample to the platinum pan. The temperature of the system was then raised from room temperature to 110 °C at a rate of 20 °C/min and held at that temperature for 30 mins to ensure that all water from the system was removed. The temperature of the system was then increased at a ramp rate of 5 °C/min to 800 °C, and held at this temperature for 45 mins.

To reveal the reducibility of the metal species in the catalysts, TPR experiments were performed in a Micromeritics Chemisorp 2750 system attached with ChemiSoft TPx. An amount of sample (ca. 0.15g) was placed in a quartz tube in a temperature-controlled furnace and connected to a thermal conductivity detector (TCD). The sample was first purged under 50 ml/min of N_2 flow at 100 °C for 1 hour and cooled down to room temperature. Then, the carrier gas was switched to a reducing gas mixture (10% H_2 in Ar) with a flow rate of 25 mL/min and the temperature was increased to 900 °C with a constant rate of 5 °C/min. The H_2 consumption (TCD signal) was recorded automatically by a computer.

BET surface areas of the catalysts were determined by N_2 adsorption at -196°C using a Micromeritics Tristar II surface area analyzer. The pore-size distributions were calculated from the BJH desorption branch of the isotherm. Before analysis, all samples were degassed at 350 °C for 4 hours under a flow of helium. The composition of the catalyst was determined by inductively coupled plasma emission spectrometry (ICP-OES) on a Spectro Ciros ICP (SPECTRO Analytical Instruments, Kleve, Deutschland) after the sample was completely dissolved in dilute nitric acid.

CO chemisorption isotherms were recorded on an Autosorb-1(Quantachrome). A sample (0.2 g) was reduced in situ at 270 °C for 12 hours under flowing H_2, and then the sample was evacuated for 1 hour followed by cooling to 30 °C. The CO chemisorption was carried out at 30 °C in the pressure range of 80-800 mmHg. A Fe:CO stoichiometry was assumed to be 2:1.

5.2.7 Catalytic studies

The catalytic Fischer Tropsch performance was investigated using the feed gas mixture CO (36.49%), H_2 (62.02%) and N_2 (1.49%) in a single-pass tubular downflow fixed bed reactor under the reaction conditions of 230 °C, 300 psig, and 3000 $L/kg_{cat}/h$ over a period of 100 hours. The synthesis products were collected for analysis after 24 hour time on stream. The reaction set-up used in this study is as described in our previous work (R. Xu, Zhang, & Roberts, 2013). One gram of catalyst (45-70 mesh) was mixed with 2 gram glass beads (40-60 mesh) and fixed into position by packing with glass wool. Prior to reaction, the catalyst was reduced for 12 hours at 270 °C at a heating rate of 5°C/min using a gas mixture containing 5 % H_2 and 95 % N_2 and a flow rate of 100 ml/min. The effluent gas was cooled to 0 °C and separated into gas and liquid phases at a pressure of 25 psi. The liquid products were collected every 12 hours and analyzed with a Bruker 430 Gas Chromatograph equipped with a DB-5 column (DB-5, 30m × 0.53mm) and a FID detector. The gas phase products were analyzed online on a Varian CP-3380 Gas Chromatograph equipped with a Haysep-DB column and a TCD detector every 80 minutes. These catalytic experiments were repeated at least twice in order to ensure reproducibility and confirm that the results obtained were within an experimental error of 5%.

5.3 Results and Discussion

5.3.1 Nanoparticle characterization

The surface functionalization of the synthesized iron oxide nanoparticles was examined using FTIR spectroscopy where the obtained result is shown in Figure 5.2. Two sharp absorbance peaks are present in the range of 2800-3000 cm^{-1} for the spectra of both pure oleic acid (Figure 5.2a) and the oleic acid-coated iron oxide nanoparticles (Figure 5.2b). The presence of these peaks can be attributed to the $–CH_2$ stretches from the alkyl chain in oleic acid. The spectrum for the iron oxide nanoparticles (Figure 5.2b) also shows a characteristic Fe-O stretch at 588 cm^{-1}. The spectrum for the pure oleic acid exhibits a characteristic C=O peak at 1710 cm^{-1}. This carbonyl peak splits into two peaks of lower intensity at lower wavenumbers (1623 cm^{-1} and 1529 cm^{-1}) in the spectrum obtained from the oleic acid coated nanoparticles (Figure 5.2b). This observation is consistent with previous findings that have been reported in the literature (S.-Y. Lee & Harris, 2006; C. Y. Wang et al., 2010; L. Zhang et al., 2006) and indicates the presence of an oleic acid-iron oxide core conjugation via the C-O bonds (L. Zhang et al., 2006).

In addition to performing FTIR analysis on the oleic acid coated iron oxide nanoparticles, FTIR analysis was also performed on the catalyst precursor (10% Fe on alumina) that was generated by depositing these oleic acid coated iron oxide nanoparticles onto the alumina support material, as shown in Figure 5.2d. The characteristic peaks in this spectrum include the broad metal oxide peaks at wavenumbers < 1000 cm^{-1} resulting from the support (Al-O) and nanoparticles (Fe-O). These broad metal oxide peaks (from Al-O) are also visible in the spectrum for the pure alumina support (Figure 5.2c). The spectrum for the catalyst precursor also includes $–CH_2$

vibration peaks originating from oleic acid in the range of 2800-3000 cm^{-1}, confirming that the oleic acid coated iron oxide nanoparticles are present on the generated catalyst precursor. It is important to note that after calcination of this catalyst precursor at 375°C, the FTIR spectrum observed (Figure 5.2e) does not show the $–CH_2$ peaks in the 2800-3000 cm^{-1} region, suggesting that oleic acid (boiling point ≈ 286 °C) has been removed from the final catalyst. Similar trends in FTIR absorbance were observed from the studies using the 10 % Fe on SiO_2 catalysts (results not shown).

The removal of the oleic acid from the support is further confirmed by the data obtained from the TGA analysis on the catalyst precursor (10% Fe on alumina, Figure 5.3). The TGA results show that there is approximately a 20% reduction in sample weight over the entire temperature range (room temperature to 800°C) out of which around 4% can be attributed to water loss. A major fraction of the weight loss (75% of total weight loss) takes place in the range of 150°C to 400°C. This weight loss can be largely attributed to the removal of oleic acid (boiling point ≈ 286°C) from the iron oxide nanoparticle surface. The two distinct peaks seen in the derivative weight loss graph, can be attributed to the presence of a strongly adsorbed layer of oleic acid and a weakly attached quasi-second layer (Sahoo, Pizem, Fried, & Golodnitsky, 2001; L. Zhang et al., 2006). This quasi-second layer has been attributed to the interchain van der Waals interactions and hydrogen bonding between the ligand headgroups (Sahoo et al., 2001). Hence, through calcination (at a temperature of 375°C) oleic acid can be successfully removed from the catalyst precursor, leaving just the iron oxide nanoparticles on the support.

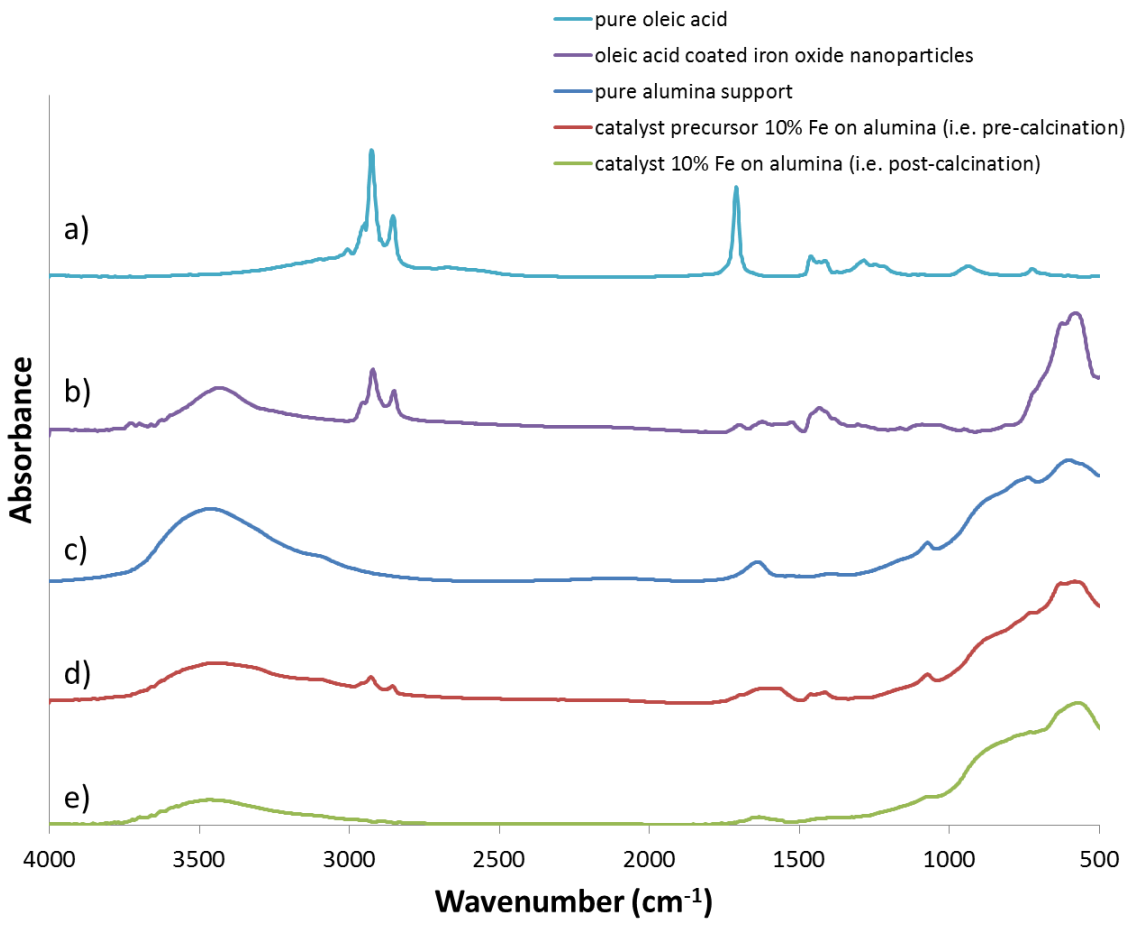

Figure 5.2 FTIR analysis of a) pure oleic acid, b) oleic acid coated iron oxide nanoparticles, c) pure alumina support, d)10% Fe on alumina catalyst precursor (pre-calcination), e) 10% Fe on alumina catalyst (post-calcination)

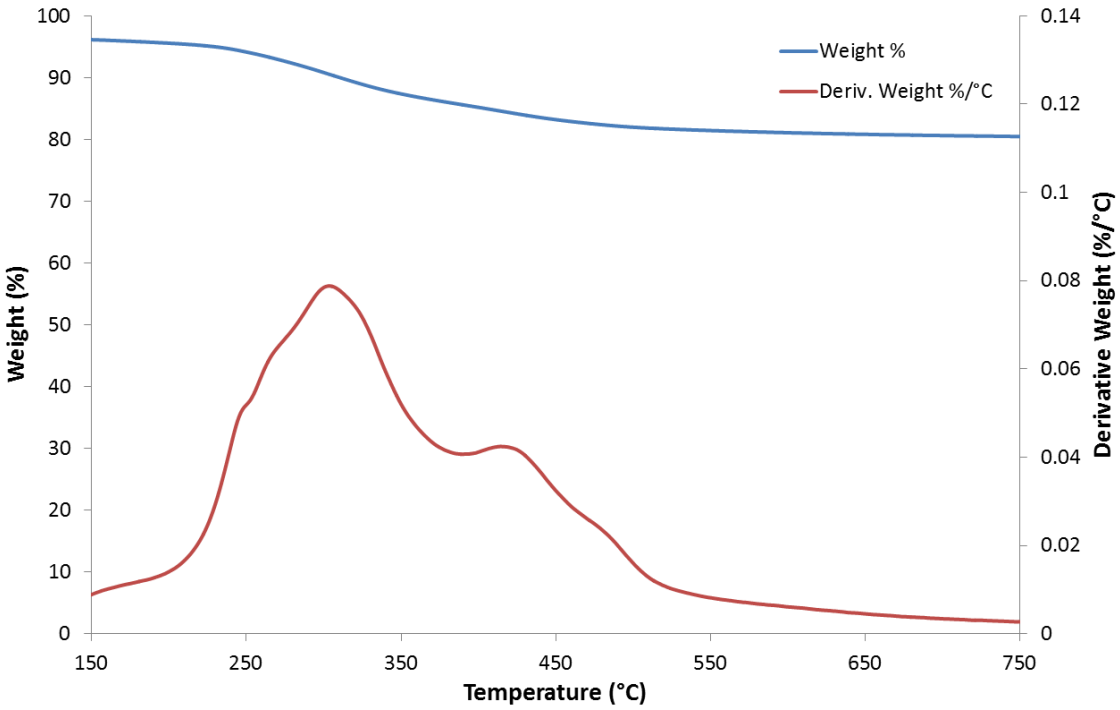

Figure 5.3 Thermogravimetric analysis results for 10% Fe on alumina catalyst

The nanoparticle size and size distribution of the initial iron oxide sample, analyzed using TEM, is shown in Figure 5.4a. The sample is polydisperse in nature with an average nanoparticle size of 12.1 nm ± 4.5 nm. This degree of polydispersity is common for particles synthesized using the synthesis method described within (A.-H. Lu, Salabas, & Schüth, 2007). This polydisperse iron oxide nanoparticle sample was then used in the GXL process to prepare the supported catalyst. It is to be noted that the largest nanoparticles in the nanoparticle dispersion will precipitate on the support first upon progressive introduction of CO_2 (i.e. larger particles precipitate first upon worsening solvent conditions) (Anand et al., 2007; McLeod, Anand, et al., 2005; S R Saunders & Roberts, 2009). Thus, not all nanoparticles in the initial dispersion will be deposited onto the support and the smaller particles will remain dispersed in the hexane+CO_2 mixture depending on the final pressure employed. TEM images of the alumina and silica supported catalysts (with 10% Fe loading) that were generated using the GXL technique are shown in Figure 5.5a and Figure 5.5b, respectively. From the TEM images of the catalysts, one can see that the iron oxide nanoparticles (darker sections) are dispersed on the support and the size of the individual particles is approximately 10-15 nm. On the other hand, TEM analysis of the control catalysts (synthesized using incipient wetness method as opposed to the GXL technique) showed large metal aggregates of sizes > 100 nm deposited on the support (Figure 5.6). Hence, the GXL deposition method employed in this study was successful in generating a supported catalyst with iron oxide nanoparticles.

A TEM image of the residual nanoparticle dispersion that was collected in the flash vessel after the deposition process was completed (i.e. those nanoparticles that

remained dispersed in hexane throughout the GXL deposition process and were not deposited onto the support material) is also shown in Figure 5.4b along with the particle size distribution results. The average nanoparticle size of this sample was around 2.7 nm ± 1.0 nm. The concentration of iron oxide nanoparticles in this recovered solution is lower than that of the initial hexane dispersion as evidenced by the change in color intensity shown in the photos in Figure 5.4. These TEM results are supported by DLS studies on the liquid samples (Figure 5.7) which show a clear difference in the particle size-histograms of the initial and residual nanoparticle dispersions in hexane. Similar trends were observed in terms of a reduction in the size of the nanoparticles that remained dispersed in solution after the GXL process versus the initial dispersion, though it is noted that there are inherent differences in these characterization techniques (i.e., TEM allows determination of particle core size while DLS measures the hydrodynamic diameter). The nanoparticles present in the residual nanoparticle dispersion recovered post-deposition are much smaller in size than the original nanoparticle dispersion, confirming our previous hypothesis that most of the larger sized nanoparticles have been deposited onto the support via the GXL deposition process.

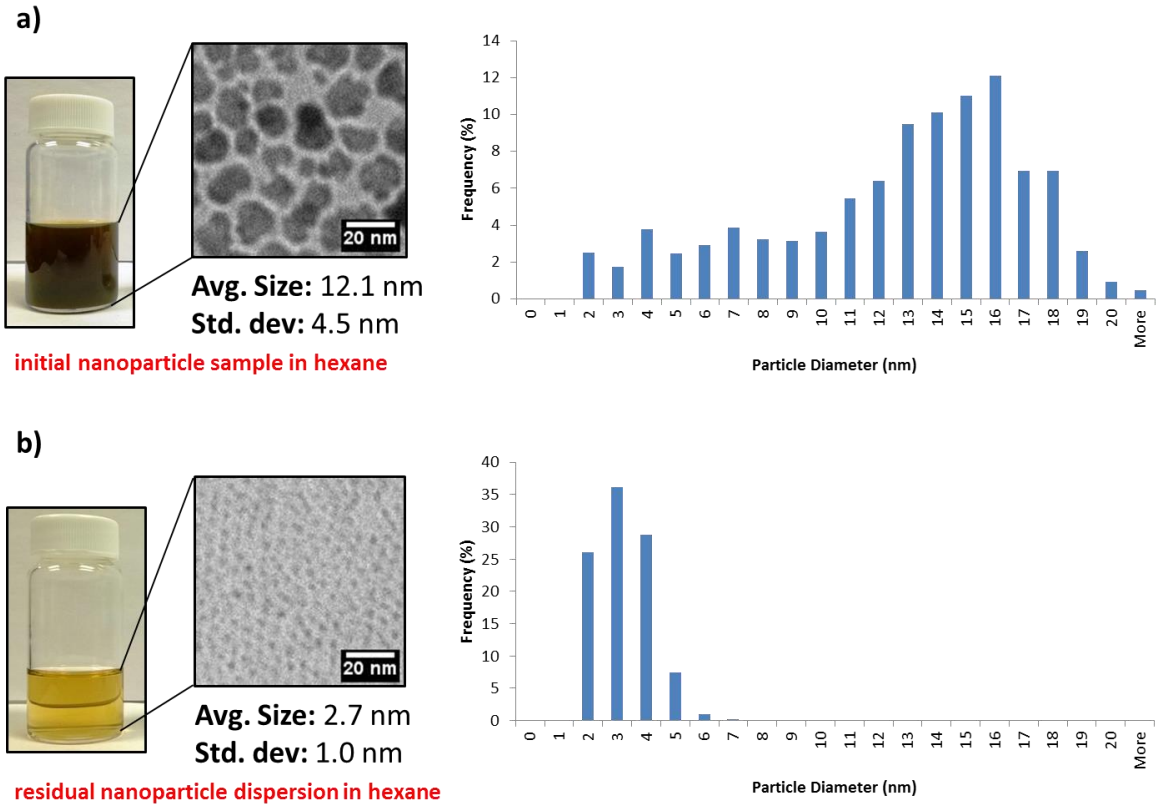

Figure 5.4 TEM analysis of a) original nanoparticle sample, b) residual nanoparticle dispersion in hexane recovered post-deposition.

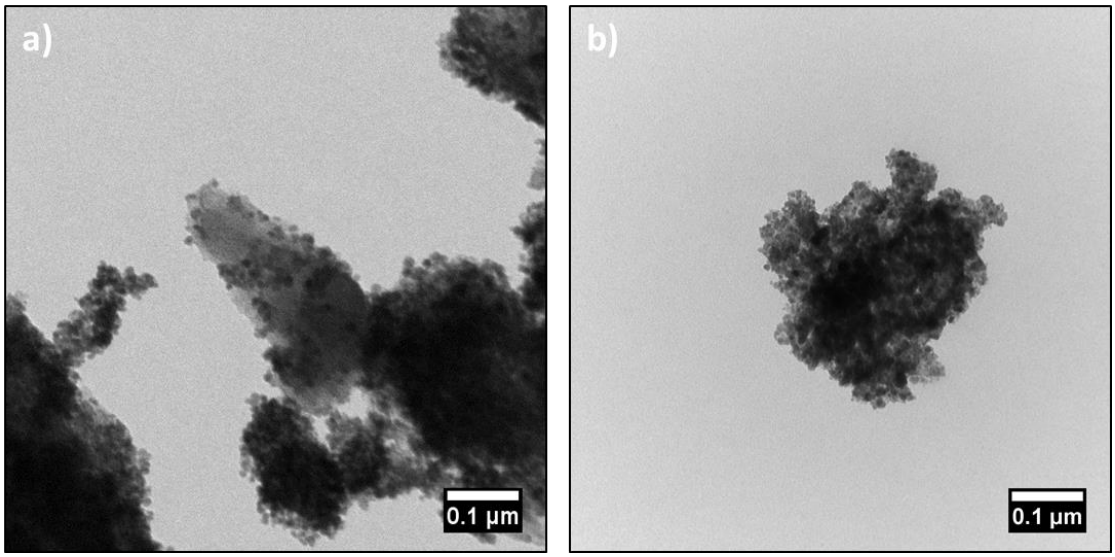

Figure 5.5 TEM images of a) sample G10Al, 10 % Fe on alumina catalyst and b) sample G10Si, 10 % Fe on silica catalyst, prepared using the GXL deposition technique

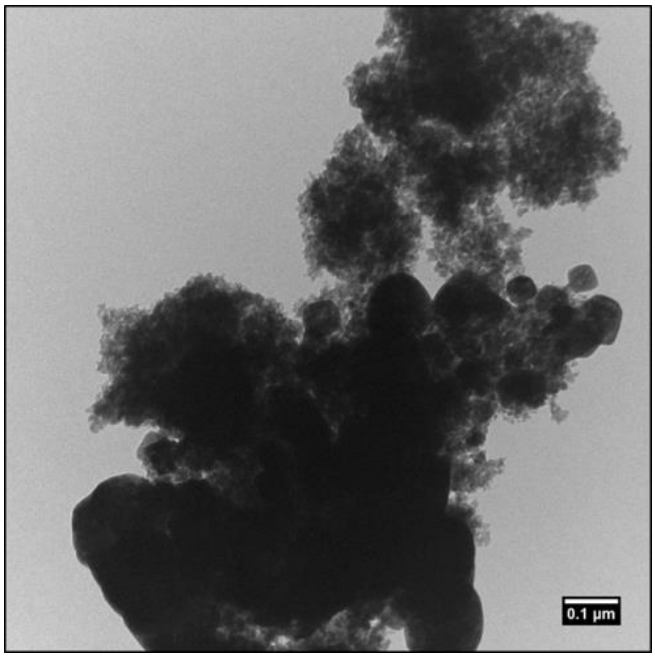

Figure 5.6 TEM image of 10% Fe on silica catalyst synthesized using the incipient wetness method

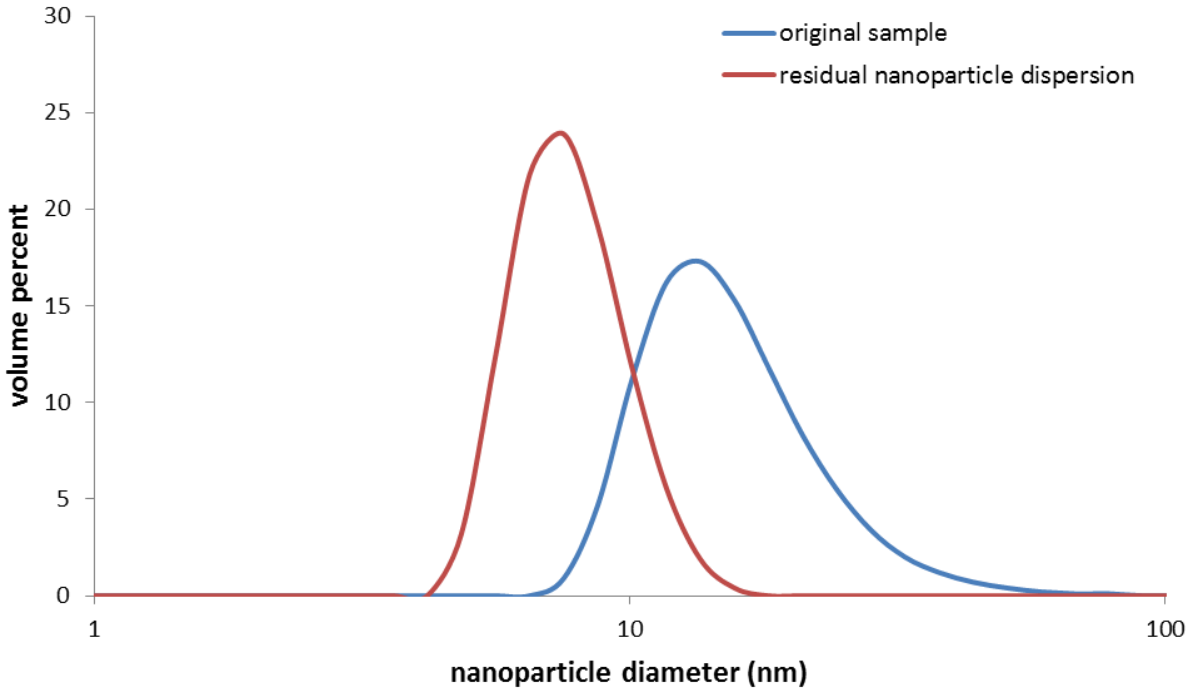

Figure 5.7 Dynamic light scattering analysis results for the original nanoparticle dispersion and the residual nanoparticle dispersion

Results from the XRD analysis of the fresh and spent catalysts generated using the GXL technique and the control catalysts are shown in Figure 5.8 and Figure 5.9, respectively. From Figure 5.8, one can see that XRD spectra of the catalysts synthesized using the GXL technique (G10Al and G10Si) show characteristic peaks for γ-Fe_2O_3 (maghemite, JCPDS 80-2186) (Cui, Liu, & Ren, 2013; X. Zhang, Niu, Meng, Li, & Zhao, 2013) at 30°, 35°, 43°, 57°, and 63°. It should be noted that the XRD peaks for γ-Fe_2O_3 match the peaks observed for Fe_3O_4 (magnetite) which is what the coprecipitation method for iron oxide nanoparticle synthesis usually yields (J. Sun, Zhou, Hou, & Yang, 2007). However, the observed change in color (black to dull reddish-brown) coupled with the fact that the samples were calcined at 375°C beforehand (Cui et al., 2013) strongly suggests that the predominant species on the sample is γ-Fe_2O_3. Compared to the GXL catalysts, the fresh control catalysts (i10Al and i10Si) (Figure 5.8) exhibit peaks at 33°, 35°, 40°, 49°, 53°, and 63° which are characteristic of α-Fe_2O_3 (hematite, JCPDS 73-8431) (Cui et al., 2013; X. Zhang et al., 2013). The control catalyst synthesized using alumina as the support (i10Al) does not show strong peaks and is more amorphous compared to its silica counterpart (i10Si). The presence of α-Fe_2O_3 in the control catalyst is expected as the presence of large quantities of α-Fe_2O_3 crystallites have been observed in supported iron catalysts prepared using the incipient wetness method in previous studies (van Steen & Prinsloo, 2002). These characteristic γ-Fe_2O_3 and α-Fe_2O_3 peaks in the fresh catalysts, however, do tend to disappear in the XRD spectra post-FT reaction (Figure 5.9). The peaks which are seen in the post-FT reaction spectra match closely to that of cubic Fe_3O_4 (JCPDS 87-0245). The dark black color of the samples hints that the sample is predominantly Fe_3O_4. The presence of Fe_3O_4 is expected since the catalysts are

reduced prior to reaction at 270°C in a H_2 environment which has been shown to form Fe_3O_4 from Fe_2O_3 particles (X. Zhang et al., 2013).

The crystallite size of the prepared catalyst was further determined by XRD analysis to estimate the size of the nanoparticles deposited on the catalyst. The crystallite size of the iron oxide nanoparticles deposited on the support is determined using the Scherrer equation and is listed in Table 5.1. From this data one can see that the average crystallite size for both the alumina and silica support catalysts is around 14 nm which is slightly larger than the original nanoparticle size of ~12 nm. This difference in size is expected due to the differences in the characterization techniques and the fact that the smaller particles are removed from the systems, hence leading to a slight increase in average particle size. Interestingly, the used GXL catalyst (i.e. post-FT reaction) revealed an approximate doubling in crystallite size compared to the initial (unused) GXL catalyst. A similar increase in nanoparticle size was observed in previous studies carried out on a spent catalyst consisting of iron nanoparticles deposited on an alumina support, and this increase in nanoparticle size was attributed to sintering (Torres Galvis, Bitter, Khare, et al., 2012). Hence, we expect sintering, along with processes such as Ostwald ripening at higher temperatures (R. M. M. Abbaslou, Tavassoli, Soltan, & Dalai, 2009), to be the cause for the increase in crystallite size in these catalysts. In contrast, while larger crystallite sizes are observed in the control silica catalyst when compared to its GXL counterpart, the control alumina catalyst is relatively amorphous in nature. This shows that the incipient wetness method can produce catalysts with variations in crystallite size depending upon the support while the GXL deposition technique generates catalysts with a relatively uniform crystallite size which is independent of the support used. It is also to

be noted that a slight increase in crystallite size is observed for the silica control catalyst (i10Si) post-FT reaction.

The BET surface areas of the catalysts prepared using the GXL method and the incipient wetness method are listed along with the catalyst pore volume and average pore radius in Table 5.1. The catalysts prepared by the GXL method exhibited an increase in the surface area (compared to the raw support) resulting from the iron particle deposition on the surface. The surface area of i10Si catalyst (207 m^2/g) was found to be lower than the surface areas of the pure SiO_2 supports (230 m^2/g). This decrease in surface area can be attributed to the particles being embedded in the pores of the support and the subsequent blocking of the mesopores during the incipient wetness process (Dragomir B. Bukur & Sivaraj, 2002), further confirmed by a decrease in the volume of pores having a radius of ca. 9 nm as observed from the pore size distribution for i10Si catalyst as shown in Figure A4.1. In general, there is no clear trend in the average pore radius for the catalysts studied. More detailed studies would be required to determine how the average pore radius is affected by the deposition method and the catalyst processing method. The CO chemisorption results are summarized in Table 5.1 as well. CO uptake results for the four catalysts used in this study show that the G10Al and G10Si catalyst prepared by GXL technique possess a greater number of CO active sites than their incipient wetness counterparts.

Figure 5.10 shows the H_2-TPR profiles of the supported Fe catalysts prepared by the GXL deposition method as well as the incipient wetness method. A profile showing two distinct reduction peaks were reported by Bukur and Sivaraj as the characteristics of the two step reduction process for Fe_2O_3 (Dragomir B. Bukur & Sivaraj, 2002). The first

peak that appears from 250 to 400 °C was attributed to the reduction of Fe_2O_3 to Fe_3O_4. The broad peak at the higher temperature (from 350 °C to 700 °C) was assigned to the subsequent transformation of Fe_3O_4 to metallic Fe (R. Abbaslou & Dalai, 2012; Jin & Datye, 2000). As shown in Figure 5.10, the onset of reduction of Fe_2O_3 on the GXL catalysts occurs around 270 °C, earlier than on the incipient wetness catalyst. This reduction process of Fe_2O_3 to Fe_3O_4 for the GXL catalysts was also more facile than on their incipient wetness counterparts, as indicated by more narrow peaks. In Figure 5.10, curve c represents the TPR profile of the i10Al sample, which was prepared using the incipient wetness method. It is observed that the broad peak at higher temperature (from 350 °C to 700 °C) for the Fe_3O_4 reduction in the i10Al sample (c) is much smaller than those obtained for the GXL catalysts (a & b) and the control i10Si sample (d), thereby indicating that it is more difficult to reduce the control Al_2O_3 catalyst that was produced by the incipient wetness method. This is consistent with previous literature which demonstrated that iron supported on alumina is harder to reduce than other supported catalysts (Dragomir B. Bukur & Sivaraj, 2002). Quantitative results from hydrogen consumption measurements during the H_2-TPR are provided in Table A4.1, demonstrating greater reduction of the GXL catalysts. The high degree of similarity in curves a and b indicates that the reducibility of the Fe_2O_3 may be independent of the support materials used for the catalysts prepared using the GXL technique.

Table 5.1 Catalyst characterization results using ICP, BET, XRD and CO chemisorption

Catalyst	Measured Composition	BET surface area (m^2/g)	Total pore volume (cc/g)	Average pore width (nm)	Crystallite size* (nm)		CO uptake (μmol/g)
					Before	After	
G10Al	9.6	284	0.37	2.4	15.2	29.4	7.7
G10Si	12.8	240	0.87	6.2	11.6	20.0	6.5
i10Al	9.6	292	0.39	2.4	NA	23.1	1.5
i10Si	8.9	207	0.76	6.5	17.9	18.6	2.0

G10Al: 10% Fe/Al_2O_3 prepared by the GXL technology
G10Si: 10% Fe/SiO_2 prepared by the GXL technology
i10Al: 10% Fe/Al_2O_3 prepared by the incipient wetness method
i10Si: 10% Fe/SiO_2 prepared by the incipient wetness method
* Crystallite size are calculated from XRD results
NA: i10Al catalyst is more like amorphous
BET surface areas for raw support- alumina: 256 m^2/g, total pore volume 0.34 cc/g, average pore width 2.4 nm
BET surface areas for raw support- silica: 230 m^2/g, total pore volume 0.88 cc/g, average pore width 6.6 nm

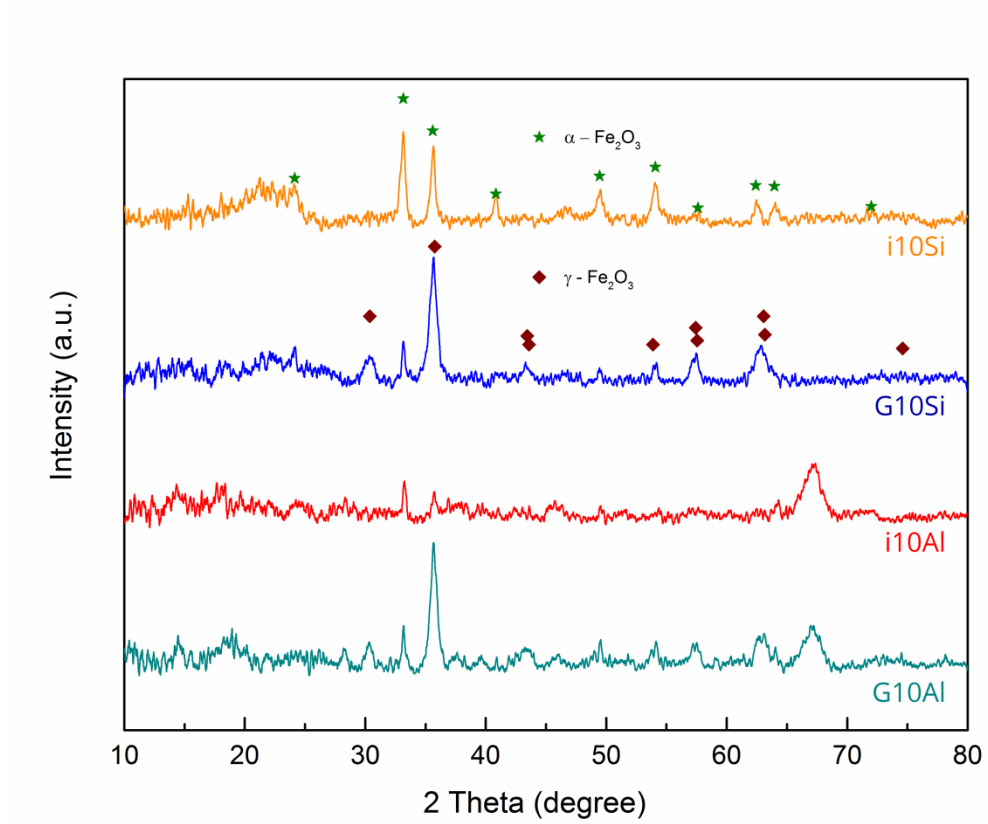

Figure 5.8 X-ray diffraction patterns of the fresh catalysts

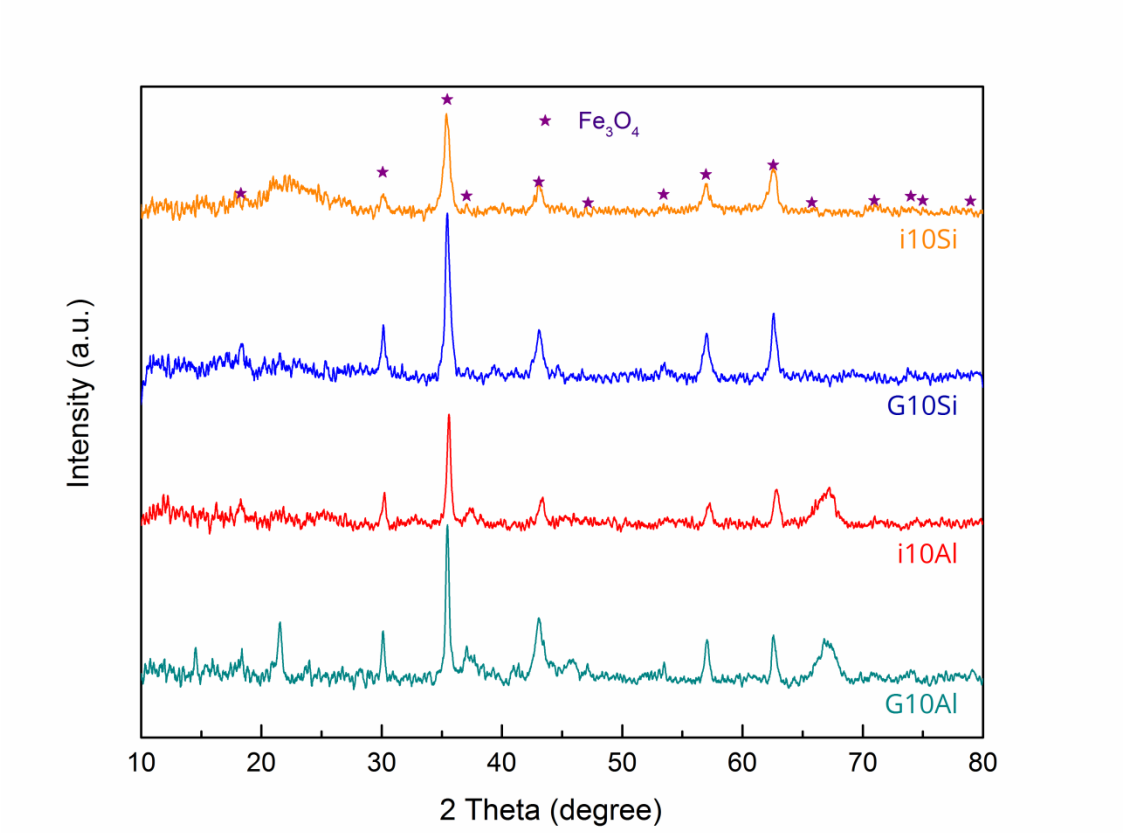

Figure 5.9 X-ray diffraction patterns of the used catalysts after 100+ hours FT operation, reaction conditions: T = 230°C, P = 2.0 MPa (20 bar), and GHSV = 3000 L/kg$_{cat}$/h

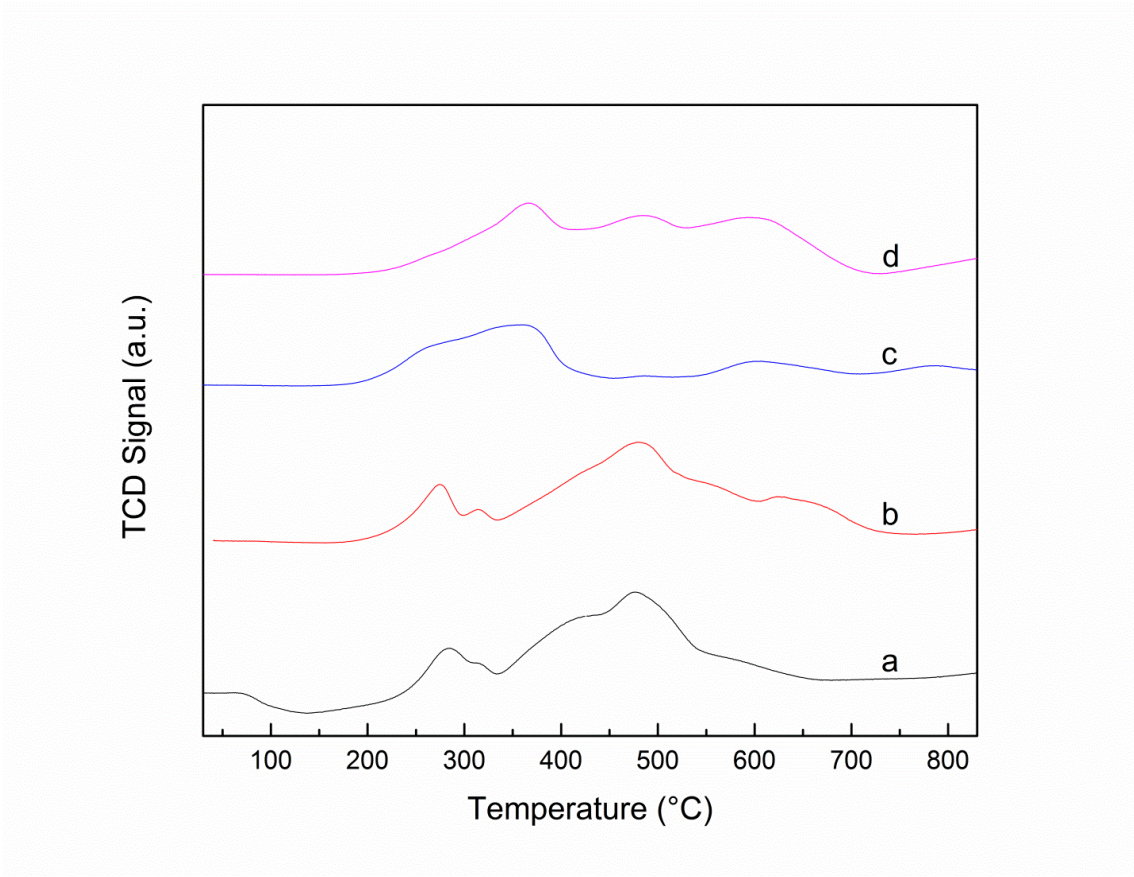

Figure 5.10 TPR Profile of the supported Fe catalysts: a) sample G10Al, 10% Fe/Al_2O_3 prepared by the GXL technique, b) sample G10Si, 10% Fe/SiO_2 prepared by the GXL technique, c) sample i10Al, 10% Fe/Al_2O_3 prepared by the incipient wetness method, d) sample i10Si, 10% Fe/SiO_2 prepared by the incipient wetness method.

5.3.2 FT Catalytic Studies

Four supported iron catalysts prepared by the incipient wetness method and the gas-expanded liquid technique described above were tested in a fixed-bed FT reactor at a reaction condition of 230 °C, 2.0 MPa (20 bar), and a GHSV of 3000 L/kg_{cat}/h. The catalytic performance results of these four catalysts are presented in Table 5.2. It should be noted that the conversion and selectivity results in Table 5.2 are the average values of at least 20 data points obtained once the reaction had reached steady state (as evidenced by stable CO conversion).

In order to compare the FT activity of the catalysts synthesized using the GXL technique to the catalysts synthesized using the incipient wetness method, the CO conversions and product distributions for these catalysts are presented in Table 5.2. It is observed that the catalysts prepared by the incipient wetness method demonstrated low CO conversions, specifically, 6.6 % for the i10Al and 13.8 % for the i10Si catalyst. The catalysts prepared by the gas expanded liquid technique showed higher CO conversions with respect to the catalyst support materials used, specifically, 12.3 % for the G10Al and 18.0 % for the G10Si. The differences in the CO conversions can be attributed to the effects of the different support materials as well as the different preparation methods used in this study. It should be noted that the conversion over the alumina catalysts is lower than the conversion over the silica catalysts irrespective of the catalyst preparation method employed. The lower activity of the alumina supported catalyst can be ascribed primarily to its lower degree of reduction as noted by Bukur and Sivaraj (Dragomir B. Bukur & Sivaraj, 2002). They also pointed out that the nature of iron phases present and the iron crystallite particle size affect the catalytic activity. Strong metal-support

interactions, which have been shown to inhibit the formation of catalytically active iron phase and lower CO conversions by Galvis et al. (Torres Galvis, Bitter, Khare, et al., 2012), could be the reason behind the lower activities obtained from the incipient wetness catalysts. Based on the H_2-TPR results, it is reasonable to attribute this increase in CO conversion to the weaker interaction between the iron oxide particles and the supporting material. More CO adsorption active sites could also be a reason for the higher conversion, as the GXL catalysts were found to possess high CO uptake in the CO chemisorption study relative to the incipient wetness catalysts. Combined, this suggests that the outstanding catalytic performance of the catalysts prepared by GXL technique is due to the GXL catalysts having the aforementioned weaker metal-support interactions.

The performance of the synthesized catalysts was also evaluated in terms of the hydrocarbon selectivity (Table 5.2), liquid product distribution (Figure 5.11) and the 1-olefin/paraffin ratio (Figure 5.12) obtained. Table 5.2 shows that the CH_4 selectivities obtained using the GXL prepared catalysts were lower than the CH_4 selectivities obtained using the catalysts that were produced by the incipient wetness method. For example, the CH_4 selectivity for the G10Al catalyst was 14.7% while the CH_4 selectivity reached 49.4% over the i10Al catalyst. High CH_4 selectivity has been commonly recognized as an indication of the presence of dissociated hydrogen on the catalyst surface (J.-Y. Park et al., 2010). Catalysts with smaller particle sizes have a higher tendency towards hydrogen adsorption rather than dissociative adsorption of CO. As a result, the population of hydrogen species increases on the surface of the small particles (J.-Y. Park et al., 2010). Since, the GXL technique allows small particles to remain in the liquid solution while

depositing the larger particles onto the support materials, the reduced CH_4 selectivity over the GXL catalysts can be attributed, in part, to the absence of these smaller particles.

The selectivity towards light hydrocarbons (C_2-C_4) does not appear to be significantly influenced by the catalyst preparation method, as shown by the data in Table 5.2. Both of the SiO_2 supported catalysts had similar selectivities toward C_2-C_4 hydrocarbons with values of approximately 40%, while the catalysts supported on Al_2O_3 exhibited C_2-C_4 hydrocarbon selectivities of nearly 30%. However, the C_{5+} hydrocarbon selectivities over the GXL catalysts were found to be much higher than the C_{5+} hydrocarbon selectivities obtained from the analogous catalysts that were prepared using the incipient wetness method, as shown in Table 5.2. Under the same catalytic conditions, the G10Al and G10Si catalysts demonstrated a selectivity of 55.3% and 69.4% respectively towards the C_{5+} hydrocarbons, while the i10Al and i10Si catalysts only achieved selectivities of 17.3% and 29.7% respectively. This increase in liquid hydrocarbon selectivity could be attributed to the higher CO/H_2 conversions in the GXL catalysts and the corresponding lower methane/CO_2 selectivities which would effectively lead to the formation of the desired, heavier hydrocarbons (C_{5+}). Zhao et al.(Zhao et al., 2013) studied the FT performance over a series of catalysts that had iron oxide nanoparticles supported on carbon materials. They found the C_{5+} selectivity changed with the nature of active components, which was governed by specific interactions between the active iron phase and the support materials.

Figure 5.11 shows the distribution of liquid products for the SiO_2 supported catalyst prepared by the GXL method. It was found that the liquid product distribution (from C_7 to C_{25}) over this catalyst obeys an ASF (Anderson-Schulz-Flory) plot (Laan &

Beenackers, 1999) with a carbon chain growth propagation factor (α) of 0.72. This alpha value is very comparable to the one (ca. 0.72) obtained over the supported SiO_2 catalyst prepared by the incipient wetness method, as shown in Table 5.2. It should be pointed out that hexane solvent was used to dilute the FT liquid products, and as such, the calculation of the alpha value is based on the weight fraction of the products with carbon numbers varying from 7 to 25. Figure 5.12 demonstrates the changes in 1-olefin/paraffin ratio as a function of carbon number for each of the four catalysts used in this study. While no method or support specific trends were seen, an exponential decrease in the 1-olefin/paraffin ratio as a function of carbon chain length (with the exception of C_2) was observed. This exponential decrease in the 1-olefin/paraffin ratio with increasing carbon number has been reported previously and was attributed to diffusional limitations (Iglesia, Reyes, & Madon, 1991; Iglesia, 1997), preferential physisorption (E. Kuipers, 1995), and an increase in the solubility of longer olefins in liquid products with carbon chain length (E. W. Kuipers, Scheper, Wilson, Vinkenburg, & Oosterbeek, 1996; Shi & Davis, 2005). The deviation of ethene/ethane ratio from this trend can be explained by the fact that ethene is 10-25 times more reactive than all other olefins (Claeys & van Steen, 2004). Hence, in summary, from the FT catalytic results we were able to determine that the catalysts generated by the GXL technique had enhanced CO conversion, lower CO_2 and CH_4 selectivity, and higher selectivity towards liquid hydrocarbons (C_{5+}), compared to their incipient wetness counterparts.

Table 5.2 CO conversion and product selectivity of the iron catalysts prepared by GXL and incipient wetness method (2.0 MPa, 230 °C, $H_2/CO = 1.70$)

Sample	CO conversion (%)	H_2 conversion (%)	H_2/CO usage ratio	CO_2 selectivity (%)	Hydrocarbon selectivity (%)			α value*
					CH_4	C_2-C_4	C_{5+}	
G10Al	12.3	16.5	2.3	6.8	14.6	30.1	55.3	0.78
G10Si	18.0	17.7	1.7	5.4	9.2	21.5	69.4	0.72
i10Al	6.6	8.7	2.2	21.7	49.4	33.3	17.3	0.76
i10Si	13.8	14.3	1.7	19.5	29.4	40.9	29.7	0.72

G10Al: 10% Fe/Al_2O_3 prepared by GXL technology
G10Si: 10% Fe/SiO_2 prepared by GXL technology
i10Al: 10% Fe/Al_2O_3 prepared by incipient wetness method
i10Si: 10% Fe/SiO_2 prepared by incipient wetness method
* α value for the G10Si catalyst was obtained from the plot of ln(wn/n) as a function of carbon number n, $7 \leq n \leq 25$, α values for the other three catalysts were obtained from the plot of ln(wn/n) as a function of carbon number n, $15 \leq n \leq 25$, in order to keep a strict linear relationship.

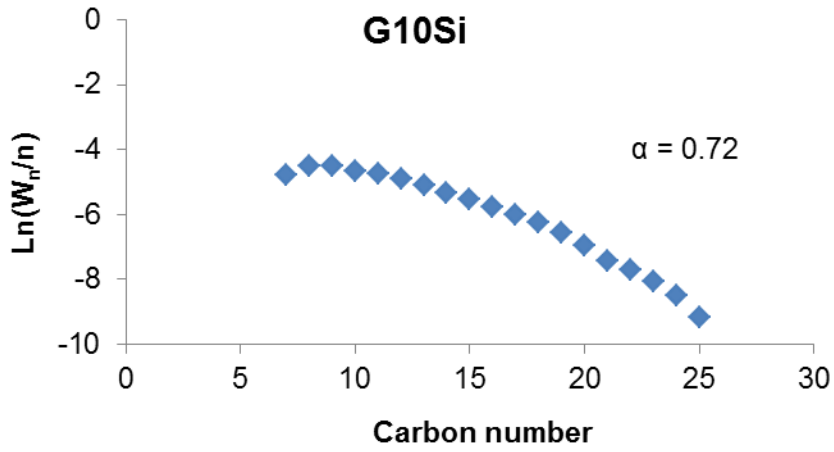

Figure 5.11 Anderson-Schulz-Flory plots for the liquid product distribution over the G10Si catalyst at 230 °C, 2.0 MPa (20 bar) and H_2/CO ratio of 1.70. W_n is the weight fraction of the products with n number of carbon atoms, α is the chain growth probability factor

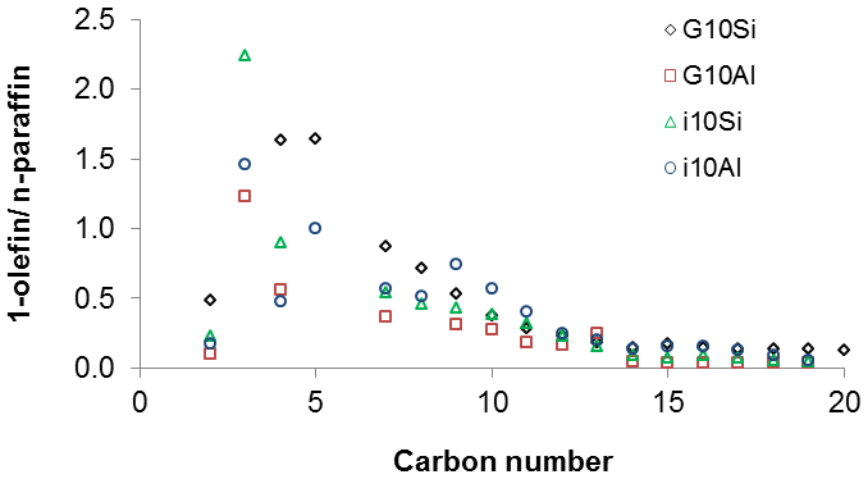

Figure 5.12 1-olefin/*n*-paraffin ratios as a function of carbon number, reaction conditions: T = 230°C, P = 2.0 MPa (20 bar), and GHSV = 3000 L/kg_{cat}/h

5.4 Conclusion

In this work, a method has been developed to produce active supported iron Fischer Tropsch synthesis catalysts using a gas expanded liquid technique. This method provided a way to effectively disperse pre-synthesized iron oxide nanoparticles onto oxidic support materials (i.e. silica and alumina) in such a manner that the nanoparticles smaller than 5 nm were controllably excluded from the final composition of the catalysts. The iron oxide on SiO_2 supported GXL catalyst resulted in the best overall performance of the four catalysts studied, and this catalyst was demonstrated to exhibit higher CO conversion and lower methane selectivity compared to its counterpart that was prepared using the traditional incipient wetness method. The C_{5+} hydrocarbon selectivity for the GXL catalysts was found to be significantly higher than their incipient wetness counterparts. The carbon chain growth probability factor was found to be primarily affected by the type of support material, while not being influenced by the catalyst preparation method employed. In addition, it was determined that the catalysts prepared by the GXL technique exhibit a weaker interaction between iron oxide nanoparticles and the support material. This ability to affect the metal-support interactions through this GXL nanoparticle deposition process offers a new means to influence the activity and selectivity of iron based FTS catalysts.

Chapter 6

Synthesis and Processing of Metal Oxide Nanoparticles for Pickering Emulsion Applications

6.1 Introduction

Iron oxide nanoparticles are an integral part of contemporary nanoparticle research due to their unique physicochemical properties and wide applicability. These applications include their use as magnetic resonance imaging (MRI) contrast agents(Andreas et al., 2012; Babes et al., 1999; Hong et al., 2008; Hu et al., 2011; Kwak, 2005; R. Qiao et al., 2009), drug delivery agents (Avdeev et al., 2010; Jain et al., 2005; M. A. Morales et al., 2005; M. Morales et al., 2008), catalysts (Hosseinian et al., 2011; Khedr et al., 2009; J.-Y. Park et al., 2010; Torres Galvis, Bitter, Khare, et al., 2012), and for the formation of Pickering emulsions (Bernard P. Binks & Whitby, 2005; Zhou et al., 2012). The ability to produce monodisperse nanoparticles that are dispersible in various solvents (aqueous and organic) is necessary for their use in the applications listed above. In addition to this, the interfacial properties of the iron oxide nanoparticles can be tuned, using different stabilizing ligands, to ensure the applicability of the nanoparticles in their respective applications. The interfacial properties of the iron oxide nanoparticles are especially critical in applications which involve surface based phenomena like catalysis, micro-electro-mechanical devices and emulsion stabilization.

In an emulsion, droplets of one liquid are dispersed in another immiscible liquid, and these droplets are usually stabilized by an emulsifier. An emulsifier is a molecule (usually a surface active amphiphile) which adsorbs at the oil-water interface and forms a protective film to resist droplet coalescence and phase separation. (X. Qiao, Zhou, Binks, Gong, & Sun, 2012) In 1907, Pickering observed that colloidal particles which were located at the oil-water interface can also be used to stabilize emulsions of oil and water (Melle et al., 2005). An illustration of the solid stabilized emulsion phenomenon is shown in Figure 6.1. These Pickering emulsions have remarkable stability due, in part, to the extremely high energies of attachment for particles held at liquid-liquid interfaces (B. P. Binks & Lumsdon, 2001). Previous studies have shown that extremely effective Pickering emulsions can be formed using nanoparticles of various materials like latex, (B. P. Binks & Lumsdon, 2001) carbonyl iron, (Melle et al., 2005) fatty acid-coated iron oxide, (Ingram et al., 2010; Lan et al., 2007) silica, (Bernard P. Binks & Whitby, 2005; He & Yu, 2007) titanium dioxide, (T. Chen, Colver, & Bon, 2007) and zinc oxide (W. Chen, Liu, Liu, & Kim, 2010). Pickering emulsions have various application especially in the biomedical field where they have been investigated in the controlled release of drugs like ibuprofen (K. Zhang, Wu, Guo, Chen, & Zhang, 2009). They also have various applications in areas like heavy oil transportation, oil recovery and emulsion polymerization (Jian Li & Stöver, 2008). Pickering emulsions generated through the use of nanoparticles are also being investigated for use as alternative or supplementary dispersants for oil-spill remediation applications. (Katepalli et al., 2013; Saha, Nikova, Venkataraman, John, & Bose, 2013; Sullivan & Kilpatrick, 2002) Magnetic nanoparticles can also be used to form these Pickering emulsions, which add magnetism as another

controlling factor to tune the emulsion forming capacity of the particles and the stability of the generated emulsions (P. Brown et al., 2012; Melle et al., 2005; Orbell, Dao, Ngeh, & Bigger, 2007; Orbell et al., 1997). Lan et al.(Lan et al., 2007) and Ingram et al.(Ingram et al., 2010) have shown through previous studies that surface-modified iron oxide nanoparticles at low concentrations (1% and 0.14%, respectively) are capable of stabilizing oil-in-water Pickering emulsions. The particles used in both these studies were coated with oleic acid, which is a popular stabilizing ligand for iron oxide nanoparticles (C. Y. Wang et al., 2010; L. Zhang et al., 2006). Zhou et al. (X. Qiao et al., 2012; Zhou et al., 2012) has also reported the stabilization of Pickering emulsions using iron oxide nanoparticles coated with silane coupling agents and a variety of carboxylic acids.

The aim of this particular chapter was initially to use magnetic nanoparticles of different sizes (obtained using GXL fractionation) and coated with various surface active agents to generate relatively stable Pickering emulsions. Synthesis of various types of ligand stabilized iron oxide nanoparticles for their use in fractionation and in stabilizing oil-in-water emulsions was supposed to be tested in this chapter. Besides synthesis, the effects of the aqueous dispersion pH and ion strength on the phase inversion and stability of Pickering emulsions prepared through the use of ligand coated Fe_3O_4 nanoparticles were also to be investigated. However, due to the inability of the oleic acid monolayer coated nanoparticles to generate O/W emulsions (as shown later in this chapter) another study using sodium stearoyl lactylate (SSL) as a coating was performed instead to generate more effective Pickering emulsions.

In this study, by carefully varying the amount of SSL added to the reaction system, it was aimed to controllably synthesize monolayer and bilayer coated iron oxide

nanoparticles. After analyzing these particles using various particle characterization methods to determine the surface functionalization of the iron oxide core, these surface modified particles were then investigated for their capacity to stabilize oil-in-water Pickering emulsions. The generated Pickering emulsions were also tested for their pH and salinity responsiveness so as to assess the stability and practical applicability of the emulsions. In this study, by carefully varying the amount of SSL added to the reaction system it was aimed to controllably synthesize monolayer and bilayer coated iron oxide nanoparticles. After analyzing these particles using various particle characterization methods to determine the surface functionalization of the iron oxide core, these surface modified particles were then investigated for their capacity to stabilize oil-in-water Pickering emulsions. The generated Pickering emulsions were also tested for their pH and salinity responsiveness so as to assess the stability and practical applicability of the emulsions.

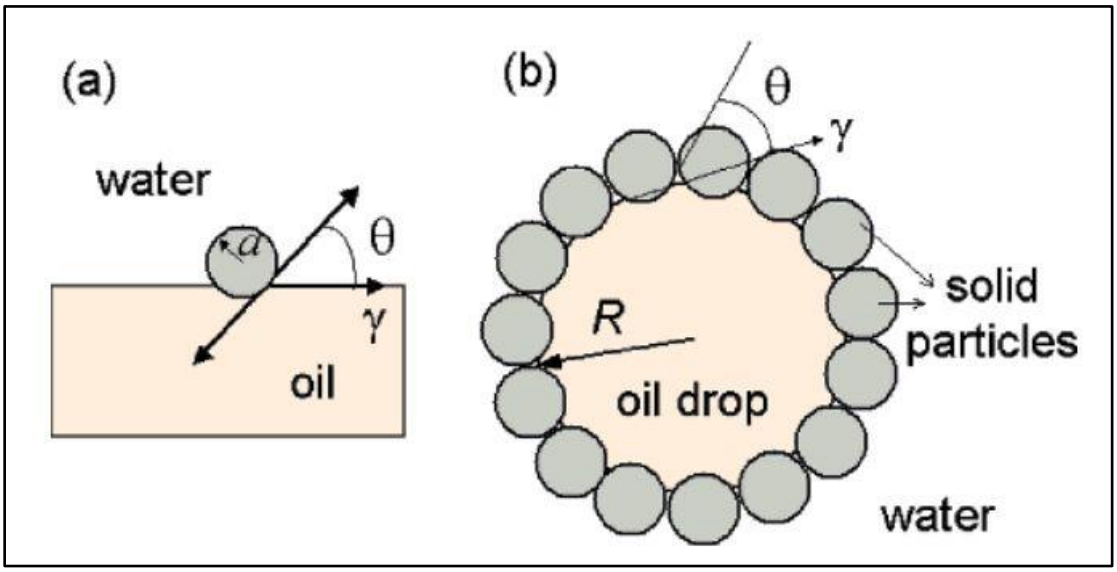

Figure 6.1 (a) Position of a spherical particle at a planar oil-water interface for a contact angle (measured through the aqueous phase) less than 90°. (b) Corresponding position of those particles at a droplet interface giving a solid-stabilized oil-in-water emulsion (Melle et al., 2005).

6.2 Experimental Section

6.2.1 Materials

Iron (III) chloride hexahydrate ($FeCl_3 \cdot 6H_2O$, 99.9%), iron (II) chloride tetrahydrate ($FeCl_2 \cdot 4H_2O$, 99.9%), Tetramethylammonium hydroxide (TMAOH, 1.0 M solution, ACS grade), n-dodecane (99 + %) and n-hexane (HPLC grade, 95%), were obtained from Alfa Aesar, USA. Ammonium hydroxide (5N, reagent grade) was obtained from BDH Chemicals, USA and sodium stearoyl lactylate (SSL) (acid value 60-80) was obtained from Spectrum Chemicals, USA. Oleic acid (99%), citric acid, dodecanoic acid, nonanoic acid (99 %) and octanoic (98+ %) acid were obtained from Sigma Aldric. Ethanol (94.0-96.0%) was obtained from Mallinckrodt Chemicals while toluene (HPLC grade, 99.9%) and (deionized ultra-filtered) DIUF water were obtained from Fisher. Acid Blue 9 ($C_{37}H_{34}N_2Na_2O_9S_3$) water soluble dye was obtained from TCI America. All chemicals were used as received without further purification.

6.2.2 Preliminary experiments

6.2.2.1 *Synthesis of fatty acid coated iron oxide nanoparticles (dispersible in organic solvent)*

Iron oxide nanoparticles coated with oleic acid (replaceable with other carboxylic acids) were synthesized based on a method described previously by Jain et al. (Jain et al., 2005). Initially aqueous solutions of 0.1 M Fe (III) and 0.1 M Fe (II) were prepared using DIUF water. 30mL of Fe (III) solution was mixed with 15mL of Fe (II) solution in a three-necked flask with magnetic stirring. Under constant stirring and under a nitrogen atmosphere, 3 mL of 5M ammonium hydroxide was added to this mixture to generate a

black precipitate of iron oxide nanoparticles. The temperature of this system was them increased to 80 °C and maintained for 30 mins to evaporate the ammonia out of the solution. While the temperature is being increased 280μL of oleic acid was added to the mixture. The system temperature was then lowered to 60 °C and held there for 1 hour. After the end of the heating cycle the system was allowed to cool down to room temperature and washed with water to remove any excess reagents and impurities. Then 30mL of ethanol was added and the particles were magnetically immobilized and washed with ethanol twice. The particles were then dried using nitrogen and dispersed in *n*-hexane via sonication (Fischer Scientific FS20). A similar synthesis method was used to synthesize particles coated with dodecanoic acid, nonanoic acid and octanoic acid.

6.2.2.2 *Synthesis of fatty acid coated iron oxide nanoparticles (dispersible in aqueous solvent)*

Iron oxide nanoparticles dispersed in water were synthesized using a modification of the method described by Maity and Agrawal (Maity & Agrawal, 2007). Initially, a solution of 10% (w/v) ammonium salt of oleic acid (pH=10) is prepared separately by mixing 30mL of water, 3mL oleic acid and 30-40 drops of ammonium hydroxide. The synthesis procedure was kept similar to the one used to generate fatty acid particles dispersed in organic solvents, except for the fact that after the addition of oleic acid and after heating the solution at 80 °C for 30 mins to remove all the ammonia, the ammonium salt of oleic acid solution is added dropwise to this solution of single-layer oleic-acid coated iron oxide nanoparticles till a stable dispersion is formed. Stability is checked by exposing the dispersion to a permanent magnet for 15 mins.

6.2.2.3 *Synthesis of iron oxide nanoparticles coated with other ligands (dispersible in aqueous solvent)*

Iron oxide nanoparticles coated with other hydrophilic ligands were synthesized based on a method described previously by Jain et al. (Jain et al., 2005). These ligands included sodium stearoyl lactylate (SSL, a FDA approved emulsifier), carboxymethyl cellulose (CMC) and citric acid and particles synthesized using these ligands were all soluble in water. CMC and citric acid coated particles were unstable in solution and precipitated over a period of two days and hence were not used for any further studies.

The particles synthesized using these methods were characterized using FTIR spectroscopy and TEM. The solid samples were pelletized using a pellet press along with KBr for the FTIR analysis. A baseline for pure KBr and atmospheric correction was used for all the samples studied. Carbon-coated TEM grids of each of the nanoparticle samples were prepared via dropcasting and micrographs were acquired on a Zeiss EM 10 transmission electron microscope and sized using the ImageJ software package. To understand the capacity of the iron-oxide nanoparticles in stabilizing oil-in-water emulsions, experiments were carried out using *n*-dodecane as the oil-phase and by using TMAOH to adjust the pH of the aqueous phase. The volume fraction of the oil phase was maintained at 0.3 for all sets of experiments. 5mL of the *n*-dodecane was initially combined with 5mL of the aqueous solution (of a predetermined pH) in a 20mL scintillation vial such that a two-phase mixture was formed. The iron oxide nanoparticle solution was then slowly added dropwise to this mixture. The scintillation vial was then gently shaken and the Pickering emulsion was formed using a sonication bath for 15 mins. The iron-oxide nanoparticle concentration was measured by a simple mass balance.

For the preliminary experiments, the stability of the emulsions was checked through optical microscopy and visual observation of phase separation in the emulsions.

6.2.3 SL coated iron oxide nanoparticle synthesis

The results from the preliminary experiments are explained in detail later in Section 6.3.1, however, to summarize, the SSL bilayer iron oxide nanoparticle system exhibited interesting properties and enhanced emulsion formation effectiveness which merited further detailed analysis. Iron oxide nanoparticles coated with sodium stearoyl lactylate were synthesized using a technique based upon the coprecipitation method described previously by Jain et al. (Jain et al. 2005). In this method Fe (III) and Fe (II) salts are mixed in stoichiometric amounts in a basic solution to yield iron oxide nanoparticles. Initially aqueous solutions of 0.1 M Fe (III) and 0.1 M Fe (II) were prepared using DIUF water and the iron chloride salts. 30 mL of Fe (III) solution was mixed with 15 mL of Fe (II) solution in a three-necked flask with vigorous magnetic stirring. Under constant stirring and under a nitrogen atmosphere, 3 mL of 5M ammonium hydroxide was added to this mixture to generate a black precipitate of iron oxide nanoparticles. The temperature of this system was then increased to 80 °C and maintained for 30 mins to evaporate the ammonia out of the solution. While the temperature was being increased, a predetermined amount of SSL (powder) (25 mg to 800 mg) was added to the mixture. The SSL powder was added slowly, under constant stirring to ensure complete dissolution. The system temperature was then lowered to 60 °C and held there for 1 hour. The system was then allowed to cool down to room temperature. Depending upon the amount of SSL used during synthesis, the nanoparticles either precipitated out of the aqueous solution or remained dispersed in the water post-

synthesis. Since the sodium counter-ion in SSL will be present in solution and not attached to the particles, the particles will be henceforth referred to as stearoyl lactylate (SL) coated iron oxide nanoparticles. For the particles which precipitated out of the aqueous solution, separation using magnetic decantation was carried out followed by washing with DIUF water and dispersal in an organic solvent (hexane/dodecane). For the particles which remained dispersed in the aqueous solution, purification of the particles was performed by first dialyzing 10mL batches of the solution using multiple disposable dialyzers (Spectrum Labs Float-A-Lyzer® G2) for 12 hours in DIUF water. The solution obtained post dialysis was then centrifuged in 10 mL batches with a Pall Macrosep® Advance Centrifugal device to remove any salt impurities. During these purification steps, DIUF water was added where necessary to recover the particles from the membrane surfaces.

6.2.4 Characterization of SL coated iron oxide nanoparticles

The core size and size distribution of the synthesized nanoparticles was determined through the use of transmission electron microscopy (TEM). Carbon-coated TEM grids of the nanoparticles (obtained post-purification) were then prepared via dropcasting and micrographs were acquired on a Zeiss EM 10 transmission electron microscope. The images obtained from the TEM were sized using the ImageJ software package. Hydrodynamic diameter of the coated particles was also measured through the use of dynamic light scattering (DLS) using a NICOMP^{TM} 380 Submicron Particle Sizer. The stability of the particles in an organic solvent or water was determined through visual observation. The aqueous nanoparticle systems were studied for stability under various pH values by adjusting the pH of the system using tetramethylammonium hydroxide

(TMAOH) and HCl. Zeta-potential analysis (Smoluchowski model) was also performed on all these samples using a Malvern Zetasizer Nano ZS to quantify the stability of the nanoparticle system under different pH conditions.

To determine the surface functionalization of these particles, powder samples of the nanoparticles were obtained through lyophilization of the aqueous dispersions (Labconco FreeZone 4.5), and using nitrogen–drying for the organic nanoparticle dispersions. Fourier Transform Infrared (FTIR) spectroscopy was performed using a Nicolet Avatar 360 to investigate the nature of chemical interaction between SSL and the nanoparticle core. A pure KBr pellet was made using a pellet press, and was used as a background for all the readings. To obtain the FTIR transmission spectra, pellets made by mixing the solid nanoparticles with pure KBr were used in the FTIR apparatus. X-ray diffractometry (XRD) was used to investigate the crystallinity of the synthesize nanoparticles and to check for the presence of impurities. XRD data was obtained through the use of a Bruker D8 diffractometer operated at 40 kV and 40 mA. The sample was prepared by placing a small portion of the iron oxide nanoparticle powder on a glass slide. The diffraction patterns were collected using a step size of 0.01° and 0.1 s/step count time from $10° \leq 2\theta \leq 80°$. The obtained peaks were compared to available spectra for known compounds using the International Center for Diffraction Data (ICDD) database to determine the species present.

Thermogravimetric analysis (TGA) of the pure ligand (SSL) and the iron oxide nanoparticles was carried out using a TA Instruments (New Castle, DE) Q500 thermal gravimetric analyzer. The entire experiment was run under a constant flow of argon at a flow rate of 10mL per min. The furnace was first purged with argon for 30 mins followed

by taring and by then adding a fixed quantity of sample to the platinum pan. The temperature of the system was then raised from room temperature to 110 °C and held at that temperature for 30 mins to ensure that all water from the system was removed. The temperature of the system was then increased slowly at a ramp rate of 5 °C/min to 600 °C, and held at this temperature for 30 mins.

6.2.5 Emulsion formation and stability experiments

For the emulsion stability studies, dodecane was used as the oil phase while water, with its pH adjusted using TMAOH and HCl, was used as the aqueous phase. The emulsions were generated by mixing the two phase systems using a Tissue Master homogenizer at 8000 rpm for 15 secs. A 1:1 volume ratio (i.e. volume fraction of oil phase 'Φ' was 0.5) of organic phase to aqueous phase was also maintained for all the experiments. To determine the type of Pickering emulsions (O/W or W/O) generated using the water-soluble and oil-soluble nanoparticles, a preliminary emulsion test was initially performed. For this experiment the pH of the aqueous phase was adjusted to 10 using TMAOH and the concentration of the nanoparticle solutions was adjusted to 0.1 wt. % using TGA analysis. Nanoparticle solutions of a known volume and weight were first added to a platinum TGA pan which was then loaded into the TGA device. The system was then heated to 600 °C under a steady flow of argon. The residual weight on the pan determined the amount of iron oxide present in solution (since the solvent and ligands would be completely removed at 600 °C). These emulsions were then colored using Acid Blue 9 dye, which preferentially colors the aqueous phase, and optical microscopy images of the emulsions formed using the oil-soluble and water-soluble particles were obtained using a National 163 optical microscope fitted with a custom digital imaging

apparatus. The two phase mixtures were mixed using the homogenizer for 15 secs after which 100 μL samples were immediately drawn using a micropipette. These samples were added on top of a sterile glass slide and covered with a glass cover slip to obtain optical microscopy images.

Studies for pH and salinity responsiveness of the dodecane-in-water emulsions were also carried out at the same conditions ($\Phi = 0.5$). TMAOH/HCl was used to adjust the pH and pure NaCl was used to adjust the salinity of the samples. The pH of the system was varied from 6-12 and the salinity was varied from 0.1 wt. % to 3.5 wt. % NaCl. Optical microscopy was carried out on the samples immediately after mixing, as well as 10 days after mixing, to determine the reduction in emulsion stability over time. To understand the influence of surfactant and iron oxide nanoparticles independently on emulsion stability, a simple experiment using the emulsions and a permanent magnet was carried out. The emulsion systems at the different pH values were generated using the SL coated particles and were kept undisturbed for 10 days after mixing using the homogenizer in the same way as performed for the pH-responsiveness study. These emulsion systems were then exposed to a strong permanent magnet and were kept in contact with the magnet for 24 hours. This drove the magnetic iron oxide nanoparticles to the bottom of the vial and removed some of the nanoparticles which were influencing emulsion stability. The emulsion stability at this reduced concentration of iron oxide nanoparticles was then noted visually and photographic evidence was obtained for the same.

6.3 Results and discussion

6.3.1 Results from preliminary experiments using fatty acid coated iron oxide nanoparticles

Experiments were performed to test the applicability of monolayer and bilayer coated iron oxide nanoparticles in forming Pickering emulsions. These were preliminary experiments aimed at understanding the Pickering emulsion formation phenomenon and to determine whether the GXL process could be employed to improve our fundamental understanding of Pickering emulsion behavior using precisely sized nanoparticles. The GXL process requires the use of solvents that expand significantly upon pressurization with CO_2 and these solvents are usually organic in nature (e.g., hexane). The organic nature of these solvents requires the nanoparticles to be stabilized with hydrophobic ligands. Ligands like oleic acid conjugate with the iron oxide core via a carbonyl bond and cause the alkyl chains to be extended into the solvent when a ligand monolayer is present (Figure 6.3). These alkyl chains then help to stabilize the nanoparticles in an organic solvent which help stabilize W/O (water-in-oil) emulsions due to their nature (Horozov & Binks, 2006; Melle et al., 2005). However, in bilayer coated nanoparticles, the alkyl chains on the monolayer coated-particles conjugate with other alkyl chains from free (unattached) ligand molecules to give hydrophilic structures as shown in Figure 6.4. This gives rise to effective O/W (oil-in-water) emulsions as shown in previous studies (Ingram et al., 2010; Melle et al., 2005). In this study we are primarily concerned with the formation of O/W emulsions as the final goal of this funded project is connected to the dispersability of crude oil in seawater, which is an O/W type of emulsion.

The preliminary experiments which were performed using methods described in Section 6.2, were intended to verify the applicability of monolayer/bilayer coated nanoparticles in the formation of O/W emulsions. A basic aqueous solution (pH = 10) was used to check the emulsion forming capacity of these nanoparticles since basic aqueous solutions have a tendency to create more stable Pickering emulsions than solutions with a lower pH (Ingram et al., 2010; Lan et al., 2007). Optical microscope images were acquired with and without the use of a water soluble dye (Acid Blue 9) which preferentially colored the aqueous phase within the emulsions as illustrated in Figure 6.2 and Figure 6.3/Figure 6.4 respectively. The optical microscope images with the Acid Blue 9 dye confirm the presence of oil-in-water emulsions and it is obvious from the images that water is the continuous phase. The water-soluble dye was not used for the other images since its effect on the interfacial tension, pH, droplet size and the stabilizing ligands is unknown.

The aim of these preliminary Pickering emulsion stability experiments is to examine if it is feasible to create stable Pickering emulsions using monolayer or bilayer fatty acid-coated iron oxide particles. For the dispersion of nanoparticles in an organic solvent, the nanoparticles must be coated with a hydrophobic (lipophilic) stabilizing ligand. Fatty acids like oleic acid, when present as a monolayer on the surface of the iron oxide core (Figure 6.3) have their alkyl chains extend into the solvent. This makes it easier for these monolayer systems to dissolve in an organic solvent due to the hydrophobic nature of the chains. In presence of fatty acid bilayers the alkyl chains of the two layers interact with each other, leaving the hydrophilic group (− OH) at the surface (Figure 6.4). This causes these bilayer particles to disperse easily in an aqueous solution

due to the hydrogen bonding between the OH groups and the water molecules. If it is possible for the monolayer particles (soluble in an organic gas-expandable solvent) to create effective Pickering emulsions, only then attempts will be made to fractionate nanoparticles in an organic solvent and to use those particles to check the effect of nanoparticle size on the stability of O/W emulsions.

Upon addition of 100μL of the aqueous bilayer dispersion of oleic acid-coated iron oxide nanoparticles to the two phase solution of *n*-dodecane and water (pH 10) it was observed that the particles were instantly attracted to the oil-water interface. These particles stayed at the interface until external energy was provided (via sonication). Post-sonication, a whitish-brown emulsion was formed which was confirmed to be an O/W emulsion through the use of optical microscopy. This emulsion remained stable for about 24 hours before it started creaming (migration of the dispersed phase due to buoyancy), and after 3 days a stable state, consisting of an emulsified organic phase and an aqueous phase, was observed. These results match those from other studies which have shown that the bilayer layer particles are extremely responsive to pH of the system and at a pH of 10, yield relatively stable O/W Pickering emulsions (Lan et al., 2007). For the monolayer coated particles, they were initially dispersed in a small amount of dodecane and then 100μL of that solution was added to the two-phase mixture of dodecane and water. Upon addition, the solution instantly dispersed in the organic phase and stayed there until the mixture was sonicated. The emulsion that was formed post-sonication was very unstable and separated out into dark organic phase and a turbid aqueous phase. From optical microscopy it was shown that the organic phase contained small quantities of the aqueous phase dispersed due to the monolayer coated particles (W/O emulsions). This result

though never shown experimentally before for fatty acid-coated iron oxide nanoparticles, was expected, since the monolayer particles should have a contact angle >90° due to their lipophilic nature (Melle et al., 2005). At contact angles >90°, a larger fraction of the particle surface will reside in oil than in water and hence W/O emulsions are expected to form due the presence of such particles (Horozov & Binks, 2006; Lan et al., 2007) which are observed in the aqueous phase in Figure 6.3.

As explained previously in the experimental methods Section 6.2.2, the nonanoic acid, octanoic acid, citric acid and CMC coatings failed to deliver nanoparticles stable enough for testing. The iron oxide nanoparticles coated with sodium stearoyl lactylate (SSL) were water soluble and emulsion stability studies on these particles delivered an emulsion system similar to the bilayer oleic acid system. However, the SSL system delivered O/W emulsions which stayed stable for a longer time (7 days) than the oleic acid bilayer system and was resistant to creaming. Since SSL is a good emulsifier by itself we decided to investigate this system further, as is shown in Section 6.3.2.

From these preliminary experiments we have deduced that only fatty acid bilayer coated iron oxide nanoparticles can effectively produce O/W Pickering emulsions and the monolayer coated particles are unable to produce a stable emulsion at the conditions studied. This shows us that there is a fundamental difference in the properties required for a) iron oxide nanoparticles to be dispersed in an expandable organic solvent and b) iron oxide nanoparticles to produce stable Pickering emulsions. The monolayer coated iron oxide nanoparticles, which are dispersible in gas expandable solvents, are poor choices to prepare O/W Pickering emulsions due to their inherent lipophilicity. On the other hand, the bilayer coated iron oxide nanoparticles, dispersible in water, cannot be used in the

GXL fractionation process due to poor gas expansion characteristics of water (Class I GXL)(Jessop & Subramaniam, 2007). The result of this is that we will not be able to synthesize fatty acid-coated iron oxide nanoparticles which can be fractionated using the GXL system and use those particles to understand the effect of size on Pickering emulsion stability. This will not be possible until a ligand-solvent combination is found for the iron oxide nanoparticles, where the solvent is expandable in the GXL system and the ligand can assist in the formation of stable Pickering emulsions. In the meantime, we will examine a system encompassing a better stabilizing agent for iron oxide nanoparticles and try to determine which conditions are ideal for that system to be used in the formation of Pickering emulsions.

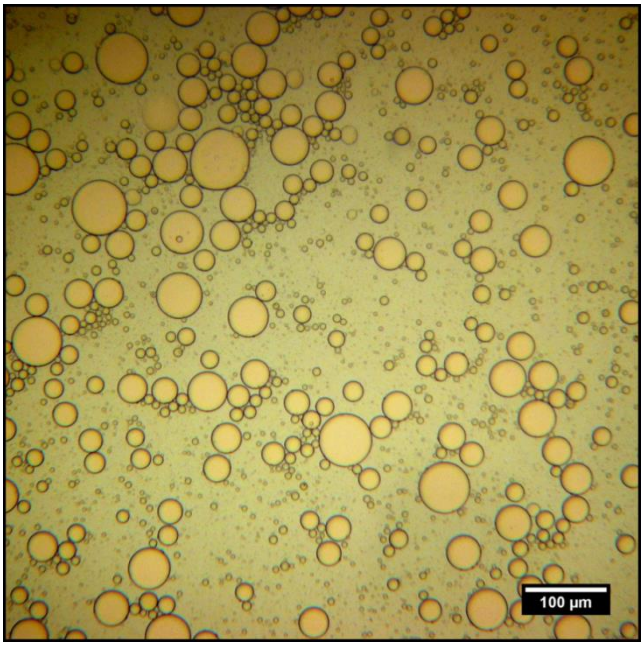

Figure 6.2 Optical microscopy image of O/W Pickering emulsions, obtained by using oleic acid bilayer capped iron oxide nanoparticles. The aqueous phase is dyed using Acid Blue 9.

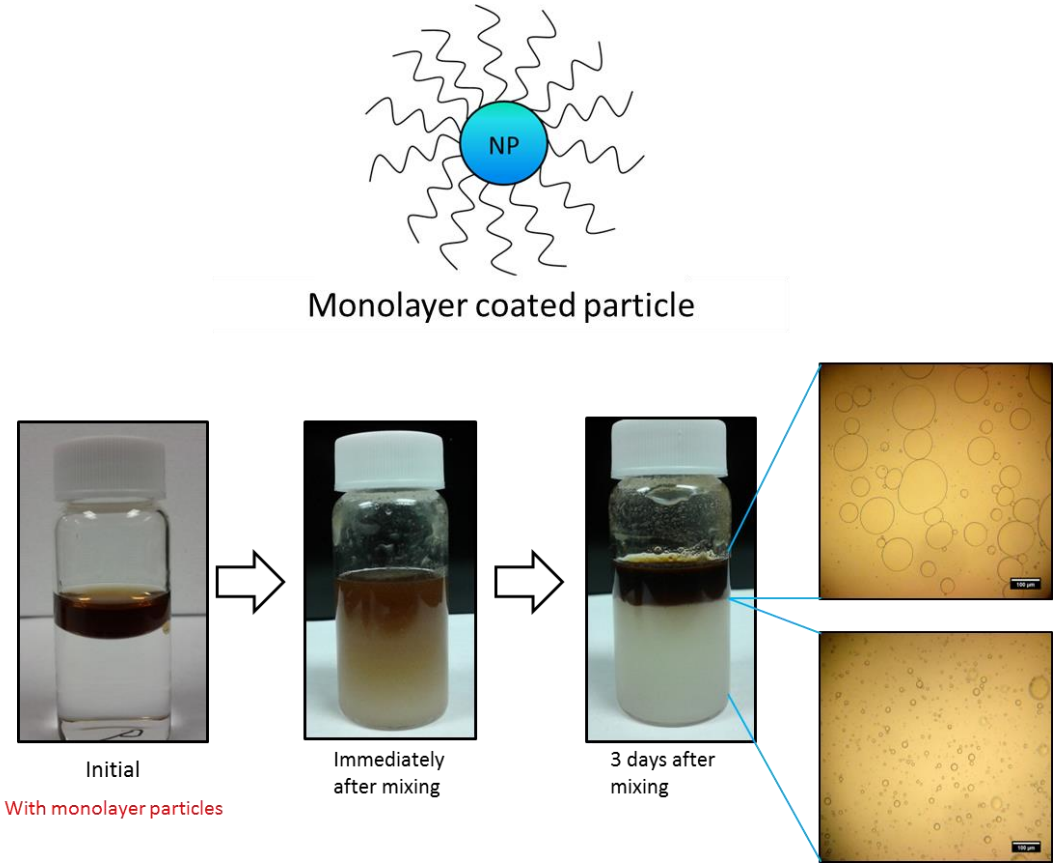

Figure 6.3 Preliminary experiments testing the applicability of oleic acid monolayer-coated iron oxide nanoparticles in Pickering emulsion formation

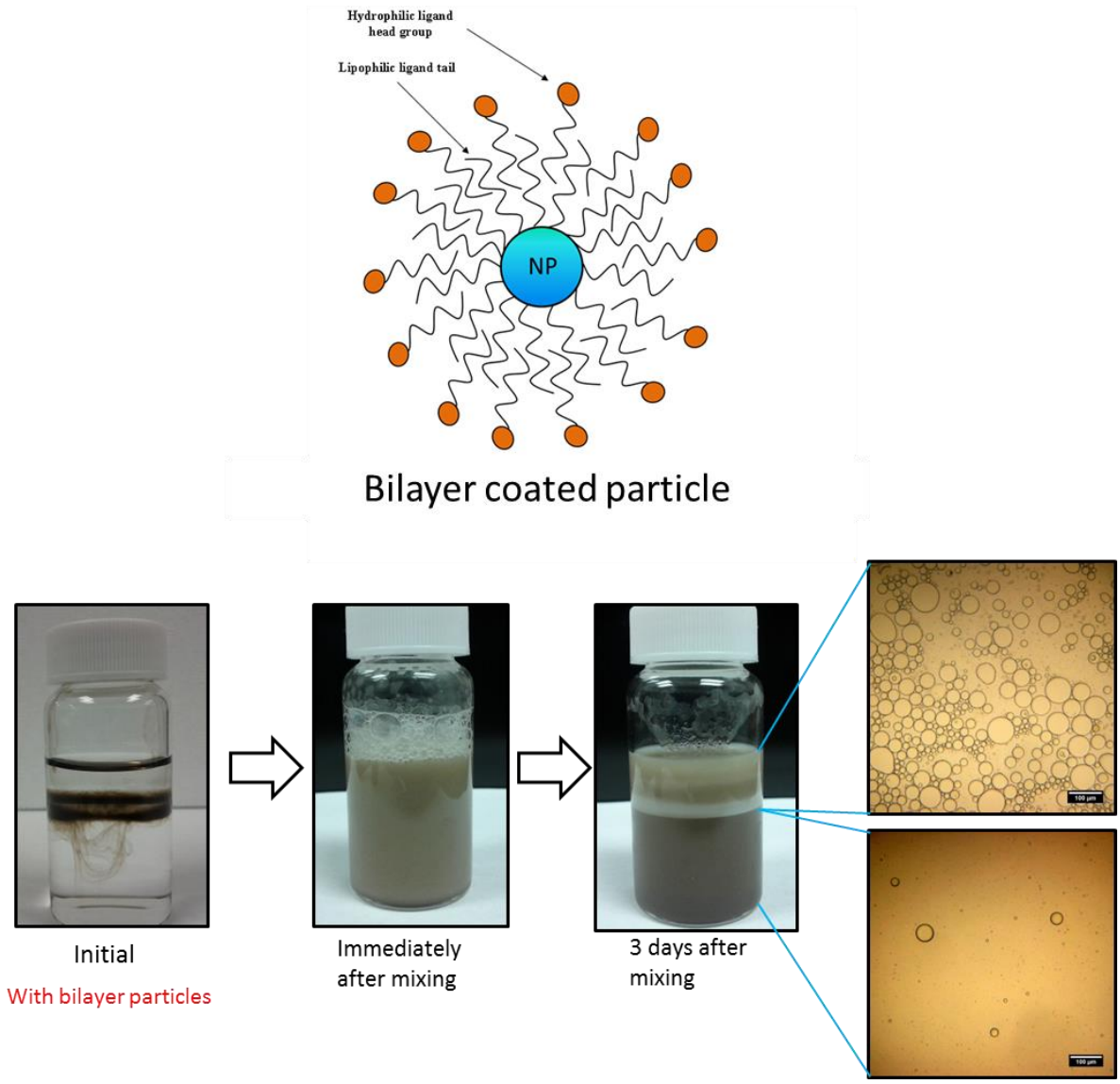

Figure 6.4 Preliminary experiments testing the applicability of oleic acid bilayer-coated iron oxide nanoparticles in Pickering emulsion formation.

6.3.2 Results from experiments using stearoyl lactylate coated iron oxide nanoparticles

6.3.2.1 *Preparation and characterization of SL coated iron oxide nanoparticles*

The aim of this particular study is to controllably synthesize magnetic iron oxide nanoparticles coated with a relatively benign stabilizing ligand (i.e. sodium stearoyl lactylate) and to test the pH and salinity responsiveness of Pickering emulsions generated through the use of these particles. Sodium stearoyl lactylate (SSL) is a biodegradable, FDA approved, food-additive which is primarily used as a dough-strengthener and processing aid in baked products (European Food Safety Authority, 2013; Flores, Giner, Fiszman, Salvador, & Flores, 2007; Lamb et al., 2010) and toxicity studies on SSL using rats have shown no statistically significant health effects (Lamb et al., 2010). Industrial grade SSL is manufactured through the esterification of commercial grade lactic and stearic acid, followed by neutralization. It should be noted that since lactic acid contains a hydroxyl as well as a carboxyl group, the stearic acid can be esterified to a single lactic acid or lactic acid polymer in commercially available SSL. This results into the presence of multiple species of lactylate esters (eg. stearoyl-2-lactylate, stearoyl-3-lactylate), along with unreacted lactic acid in commercially available SSL.(Whitehurst, 2008) The high emulsifying efficiency of SSL is countered by the fact that it is poorly soluble in aqueous and organic solutions,(Grigoriev, Leser, Michel, & Miller, 2007) which reduces its applicability outside the food industry. SSL is an anionic emulsifier and is useful in the generation of oil-in-water (O/W) emulsions due to its high hydrophilic-lipophilic balance and excellent bilayer-forming capacity. (Kokelaar, Garritsen, & Prins, 1995; Kurukji, Pichot, Spyropoulos, & Norton, 2013) The capacity of SSL to stabilize emulsions is based on the amphiphilic nature of the SSL molecule, consisting of a hydrophilic charged

head and a long hydrophobic hydrocarbon tail. (Sovilj, Milanovic, & Petrovic, 2013) The presence of multiple carbonyl functionalities also gives a chance for one or two of the carbonyl groups to coordinate with the metal oxide surface. (Lodhia et al., 2010) Previous studies have shown that SSL, by itself, can be used as an emulsifier for O/W emulsions,(Kurukji et al., 2013) or it can be used with other surface active agents like chitosan (Zinoviadou, Moschakis, Kiosseoglou, & Biliaderis, 2011) or carrageenan (Flores et al., 2007) to give emulsions with increased stability to coalescence and creaming.

The coprecipitation method is a popular choice for researchers to easily synthesize iron oxide nanoparticles due to the low cost of precursors and relatively low reaction temperatures required. It is easy to achieve gram scale quantities of nanoparticles by using the coprecipitation method even though the synthesized samples are usually polydisperse in nature. Iron oxide nanoparticles synthesized using the coprecipiation method have been surface functionalized with agents like oleic acid, dextrin, etc. for use in various specialized applications.(Babes et al., 1999; D.K. Kim et al., 2001; Predoi, 2007) Upon synthesis of SL coated iron oxide nanoparticles with varying amounts of SSL, it was observed that at lower SSL concentrations (ligand : iron oxide ratio by weight < 0.5) the synthesized particles are readily dispersible in an organic solvent like hexane, while at higher concentrations (ligand : iron oxide ratio by weight > 1.0) the particles are dispersible in water. At intermediate concentrations (0.5 – 1.0), while some of the particles are dispersible in hexane or water, there are also a significant number of particles which are unstable and precipitate from solution. This leads us to conclude that at lower concentrations of SSL there is just enough of the ligand to coat the iron oxide

core with a monolayer, leaving the hydrophobic alkyl tails/chains extended into the solvent, making the particles dispersible in organic solvents. At higher concentrations, there is enough SSL in solution for the hydrophobic tails of the free ligand in solution to interact with the hydrophobic tails of the attached ligand to form a bilayer structure, as shown in Figure 6.6. This would leave the polar head group of SSL (Figure 1) to be extended in solution, leading to the solubility of these nanoparticles in water. At the intermediate concentrations, there is enough SSL to create a monolayer but not enough SSL to form bilayers which could cause the particles to aggregate into large unstable structures which precipitate from solution. Only the particles synthesized using 400 mg SSL were used for the emulsion studies in this section. These particles were selected because it is not desirable to have excess SSL in solution since we want the emulsions to be particle stabilized and not SSL stabilized. The presence of excess SSL in solution could also lead to the formation of micelles within the solution (CMC of SSL ≈ 0.1 wt. %) (Kurukji et al., 2013; Meshram & Jadhav, 2012) which would be undesirable.

Through TEM imaging of the monolayer and bilayer particles it was shown that the iron oxide nanoparticle core size was approximately 10 nm for both the monolayer and bilayer coated particles. TEM images of the monolayer and bilayer particles are shown in Figure 6.5. The core diameters determined via TEM are listed in the Table 6.1. Table 6.1 illustrates that the particles are relatively polydisperse in nature. Dynamic light scattering studies show that the hydrodynamic diameter of the monolayer particles is approximately 25 nm while that of the bilayer particles is around 37 nm. Due to the high polydispersity of the samples being studied and the difference in the

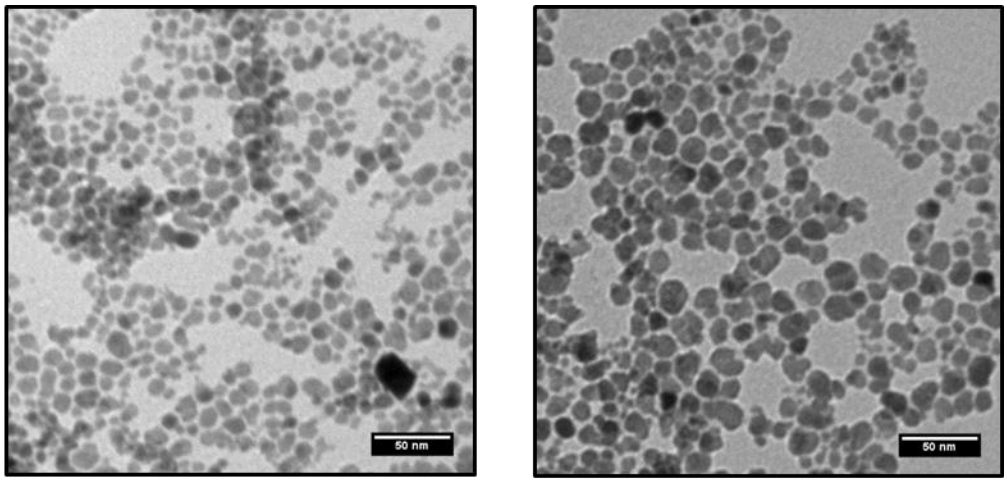

Figure 6.5 TEM images of SL monolayer/bilayer coated iron oxide nanoparticles.

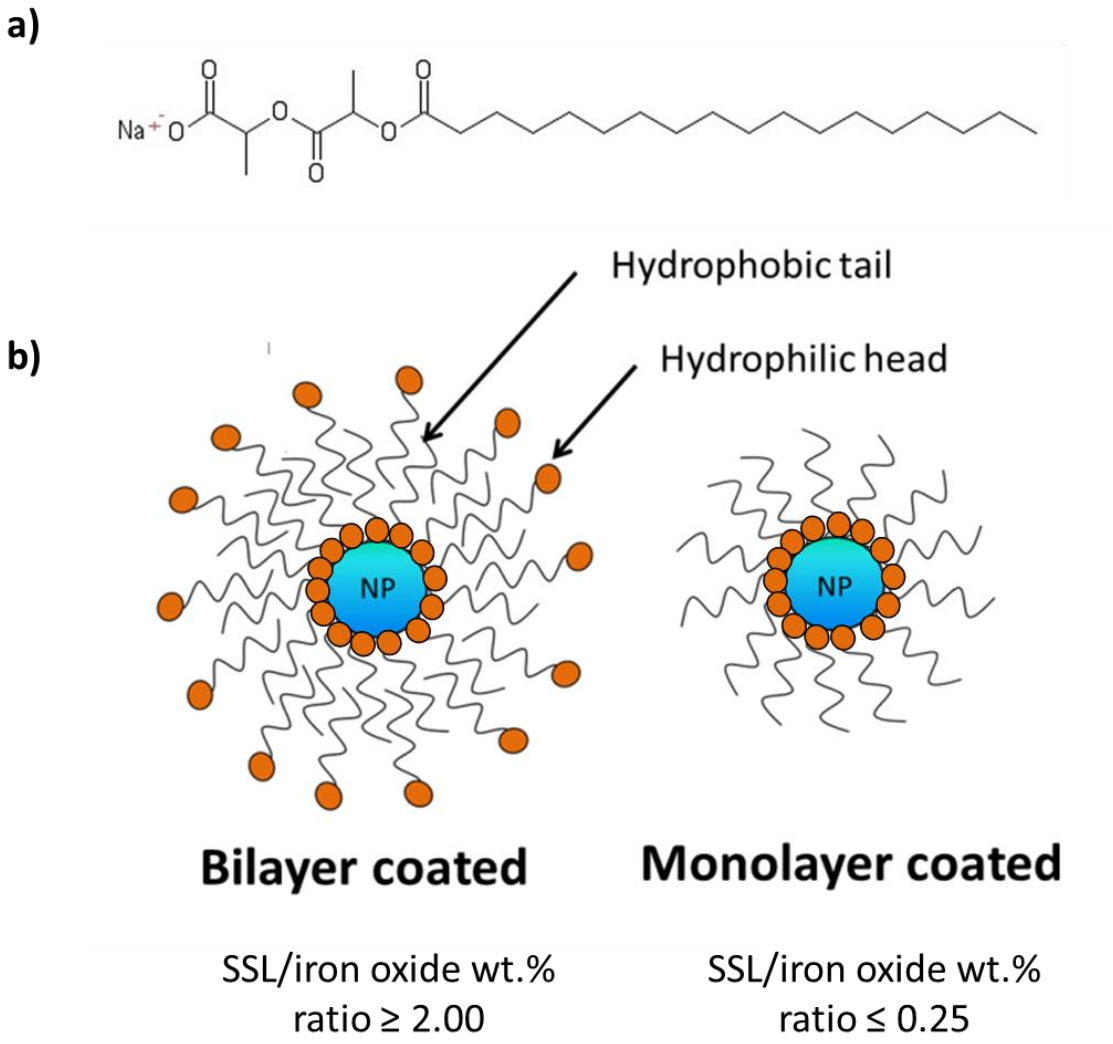

Figure 6.6 a) Chemical structure of sodium stearoyl lactylate (SSL), b) Generation of monolayer and bilayer coated SSL particles depending upon the amount of SSL added to the reaction system.

Table 6.1 Stability, solubility and particle size results for iron oxide nanoparticles synthesized in the presence of varying amounts of SSL.

**At these SSL concentrations some particles were stable in hexane but a majority of the particles precipitated out of solution.*

SSL Amount	**Wt. of ligand/ Wt. of iron oxide**	**Solubility** (hexane/water)	**Stability**	**Zeta potential (mV)**	**Nanoparticle core size (nm) TEM**	**Hydrodynamic diameter (nm) DLS** *(Volume weighted)*
25 mg	0.125	hexane	**Stable**	-14.5	8.8 ± 4.2	23.7 ± 9.3
50 mg	0.250	hexane	**Stable**	-2.5	10.8 ± 4.2	27.2 ± 7.4
100 mg	0.500	N/A*	**Unstable**	N/A	N/A	N/A
200 mg	1.00	N/A*	**Unstable**	N/A	N/A	N/A
400 mg	2.00	water	**Stable**	-58.5	9.9 ± 4.9	39.1 ± 23.5
600 mg	3.00	water	**Stable**	-45.7	7.8 ± 4.4	35.1 ± 24.8
800 mg	4.00	water	**Stable**	-43.1	9.8 ± 5.4	38.0 ± 27.7

associated hydration shell inherent to a DLS measurement, (Prakash et al., 2009) the difference in the hydrodynamic diameters cannot be conclusively attributed to factors such as the larger thickness of the bilayer (due to interpenetration of the SL molecules) (K. Yang, Peng, Wen, & Li, 2010).

The FTIR spectra obtained for the pure SSL, the SL monolayer coated particles and the SL bilayer particles are shown in Figure 6.7. A detailed analysis of the FTIR spectra is also shown in Table 6.2. The FTIR spectrum of pure SSL shows characteristic CH_2 bands (from the alkyl group in SSL) (Nakamoto, 1997a) at 2918 and 2850 cm^{-1}. Similar bands are also seen in the spectra for the SL monolayer and bilayer coated iron oxide nanoparticles. The spectra for pure SSL and the SL monolayer particles also have a CH_3 umbrella mode peak (Wu et al., 2004) at 1411 cm^{-1}. The FTIR spectrum of the SL monolayer coated particles was compared to the FTIR spectrum of pure SSL so as to analyze how the SSL attaches to the iron oxide core. By analyzing the C=O ester peak (Larkin, 2011) (1739 cm^{-1}) present in the pure SSL spectrum and comparing it to the conjugated C=O peak in the SL monolayer coated particle spectra it is possible to determine how the C=O groups conjugate with the iron oxide surface. (Nakamoto, 1997b) The splitting of the 1739 cm^{-1} C=O stretch in pure SSL into two peaks at 1718 cm^{-1} and 1614 cm^{-1} (Δ or difference in the wavelengths after splitting = 104 cm^{-1}) in the SL monolayer spectrum hints at a bidentate type of bridging being present in the system (J. Liu et al., 2008; Nakamoto, 1997b). Such type of attachment of surfactants to nanoparticles has been shown before in other studies (N. Shukla, Liu, Jones, & Weller, 2003).

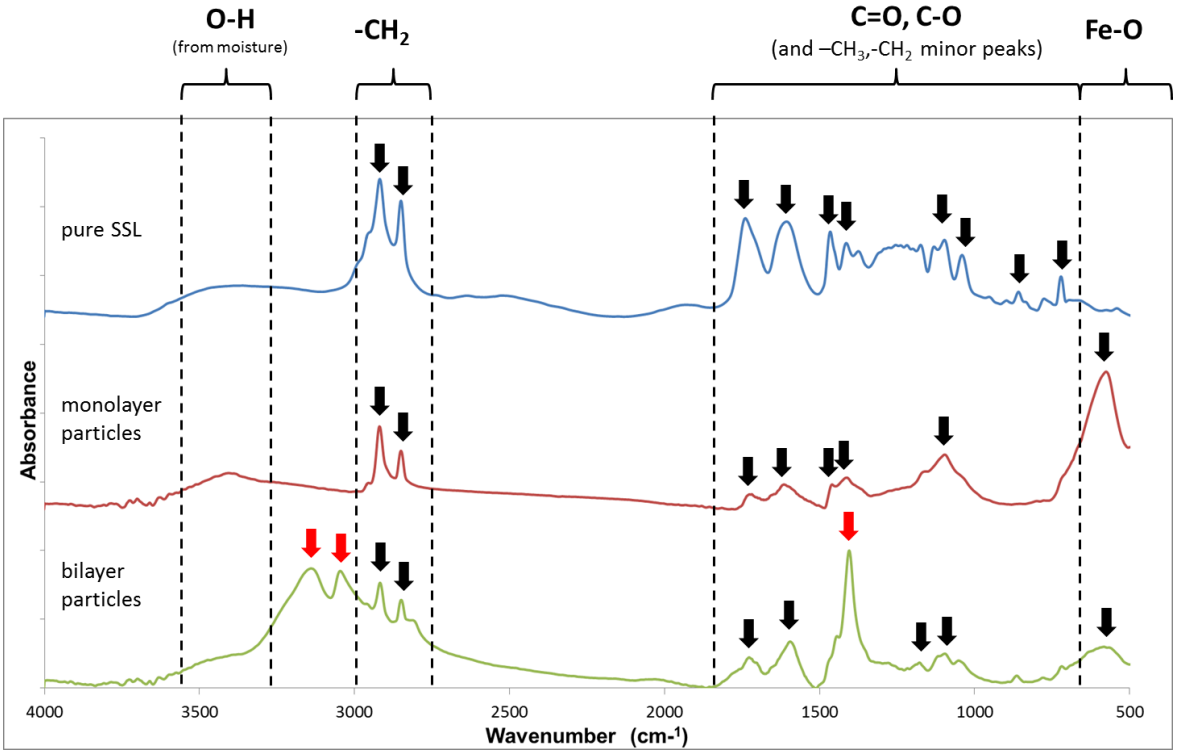

Figure 6.7 FTIR spectra for pure SSL, SL monolayer iron oxide particles and SL bilayer iron oxide particles. (black arrows - analyzed peaks, red arrows - impurity peaks)

Table 6.2 Details for FTIR peaks of pure SSL, SL monolayer iron oxide particles and SL bilayer iron oxide particles.

Species	**Peak position (cm^{-1})**	**Interaction**(Larkin, 2011; Nakamoto, 1997a, 1997b; Smith, 1998; Wu et al., 2004)
Pure SSL	2918	(-CH_2 stretch) *symmetric*
	2850	(-CH_2 stretch) *asymmetric*
	1739	(C=O stretch) from R-CO-O-R
	1605	(C=O stretch) from R-CO_2^-
	1465	(-CH_2 bend)
	1411	(-CH_3 umbrella mode)
	1095	(C-O stretch) from R-CO-O-R
	1037	(C-O stretch) from R-CO-O-R
	721	(-CH_2 rocking)
SL monolayer nanoparticles	2919	(-CH_2 stretch) *symmetric*
	2850	(-CH_2 stretch) *asymmetric*
	1718	(C=O stretch) *conjugated*
	1614	(C-O stretch) *conjugated*
	1461	(-CH_2 bend)
	1411	(-CH_3 umbrella mode)
	1096	(C-O stretch) from R-CO-O-R
	575	(Fe-O stretch)
SL bilayer nanoparticles	3140	(NH_4 stretch) *asymmetric*
	3046	(NH_4 stretch) *symmetric*
	2917	(-CH_2 stretch) *symmetric*
	2849	(-CH_2 stretch) *asymmetric*
	1727	(C=O stretch) *conjugated*
	1594	(C-O stretch) from R-CO_2^-
	1404	(NH_4 bend)
	1177	(C-O stretch) from R-CO-O-R
	1095	(C-O stretch) from R-CO-O-R
	582	(Fe-O stretch)

However, due to the sheer number of C=O and C-O interactions present in the SSL molecule it is not possible to definitively determine which of the carbonyl carbons interacts with the iron oxide surface. It is interesting to note that the FTIR spectrum for the SL bilayer coated nanoparticles shows the presence of NH_4^+ impurities present in the bilayer coated nanoparticle system (Figure 2, red arrows). The ammonium ion peaks (3140, 3046 and 1404 cm^{-1}) (Larkin, 2011) are possibly a result of NH_4Cl being generated in the system during synthesis. Usually during the coprecipitation method, the ammonium hydroxide will be converted to ammonia due to the relatively high temperature and high pH of the system. The ammonia vapors are then removed by the nitrogen flowing over the system. However, commercial grade SSL contains free lactic acid which can cause localized reductions in pH in the reaction vessel. This will shift the ammonia formation reaction equilibrium towards the reactants, thereby releasing ammonium ions in solution. (Yeh, Pennline, Resnik, & Rygle, 2005) These ammonium ions can then combine with the free chloride ions from the iron salts and generate water soluble ammonium chloride. XRD analysis of the lyophilized water soluble particles (Figure 6.8) shows that the particles are primarily Fe_3O_4 and also confirms the presence of these ammonium chloride impurities. The purification processes of dialysis and centrifugal ultrafiltration are successful in removing most of the ammonium chloride, but a small amount of ammonium chloride impurities do remain in the system and are visible in the FTIR and XRD results due to the high sensitivity of these techniques.

Even though the solubility results and FTIR results suggest the presence of a bilayer on the particles synthesized with higher amounts of SSL, thermogravimetric analysis (TGA) was also performed on the particles to confirm the presence of a bilayer.

The TGA curves shown in Figure 6.9 shows that the release of molecules upon increase in temperature is split into two bands or sections, namely Section 1: where any free lactic acid (boiling point: 122°C) and SSL (flash point: 221°C) are removed from the particles and Section 2: where the layer of surfactant molecules attached to the iron oxide core is released. It is also important to note that the position of Section 2 is around 376°C which is the boiling point of stearic acid and most of the weight loss in this section can be attributed to the removal of attached surfactant (which should be similar to stearic acid due to the conjugated C=O groups) from the iron oxide core. Also, since the decomposition sublimation of ammonium chloride starts at around 338°C and an increased reduction in weight is not observed after that point, one can safely say that a significant quantity of ammonium chloride is not present in the system.

From the TGA results in Figure 6.9, it is evident that the water-soluble particles synthesized at higher concentrations of SSL (400 mg) have a much higher % weight loss in section 1 (≈ 50 %) compared to the hexane-soluble particles synthesized at lower concentrations of SSL (25 mg) (≈ 10 %). The TGA results for the other concentrations of SSL follow the trends listed above and are shown in Figure 6.10. Hence, we can deduce that the particles synthesized at higher concentrations of SSL have relatively more SSL molecules loosely associated to the nanoparticle (i.e. held via ligand-ligand/ligand-solvent interactions) compared to the particles synthesized at lower concentrations of SSL, which have a higher fraction of ligand molecules attached to the iron oxide core.

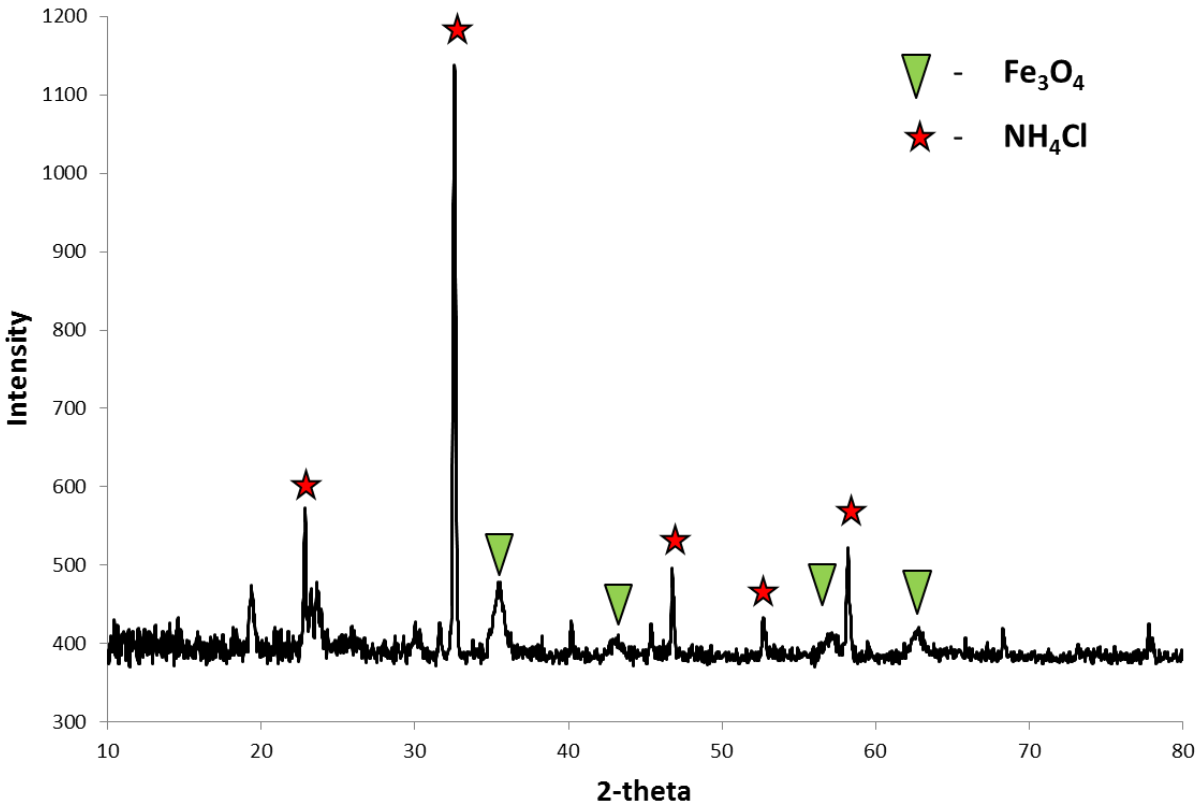

Figure 6.8 XRD spectra for SL bilayer coated iron oxide nanoparticles.

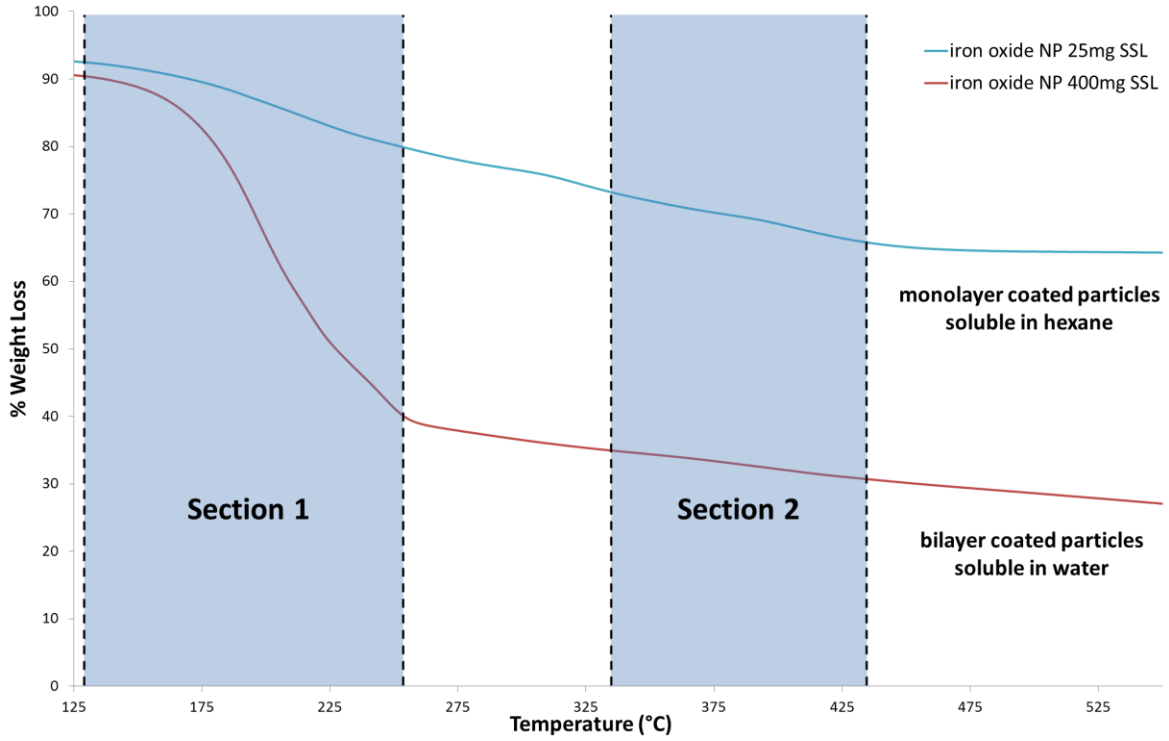

Figure 6.9 TGA curves of SL monolayer/bilayer coated iron oxide nanoparticles.

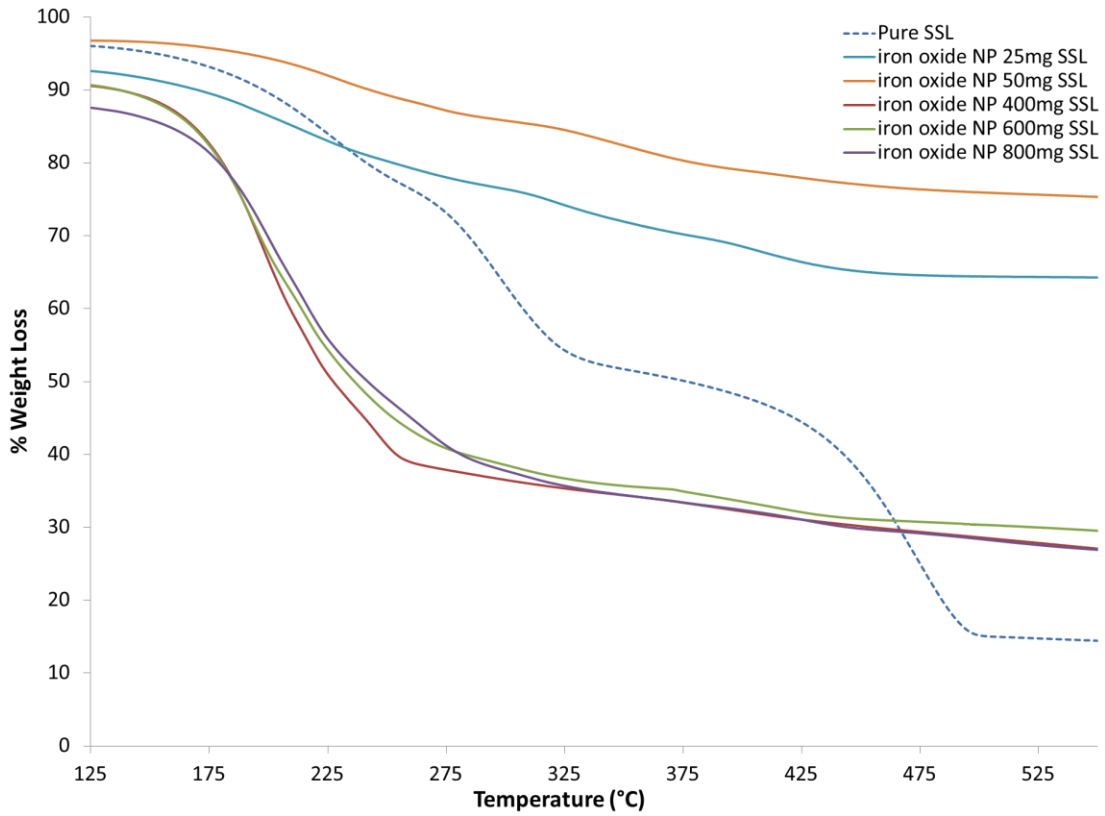

Figure 6.10 TGA curves of Pure SSL and SL monolayer/bilayer coated iron oxide nanoparticles at different reactant (SSL) concentrations

This adds more evidence to our analysis that at higher SSL concentrations, bilayers are present in the system. It should be noted that even though most of the SSL should be associated with the nanoparticle in the aqueous dispersions, the presence of a small amount of SSL micelles in solution is inevitable. The presence of these SSL micelles in solution could slightly improve the emulsion forming capacity of the iron oxide system under investigation since a very small fraction of the overall emulsion could be stabilized by these micelles themselves.

6.3.2.2 *Application of SL coated iron oxide nanoparticles in Pickering emulsions*

The results from the preliminary emulsion formation experiments carried out using the SL monolayer and bilayer coated particles are shown in Figure 6.11. For the SL monolayer coated nanoparticles (dispersible in organic phase) it was observed (Figure 6.11a) post-mixing that an extremely unstable emulsion was generated. This emulsion separated into two phases over a period of 30 mins. Before complete phase separation was achieved, we were able to obtain optical microscopy images using Acid Blue 9 water soluble dye to determine the type of emulsion formed. From the presence of water droplets (blue) dispersed in the organic phase (brown) in the optical microscopy image (Figure 6.11a) one can see that these monolayer coated particles generate extremely unstable water-in-oil (W/O) emulsions. Note that since the emulsion is extremely unstable with droplets coalescing frequently, it is difficult to get clear optical microscopy images. In contrast, a relatively stable emulsion was obtained post-mixing, for the SL bilayer coated nanoparticles (dispersible in aqueous phase), as is seen in Figure 6.11b. Upon optical microscopy analysis of this emulsion in the presence of Acid Blue 9 dye, the presence of dodecane droplets (brown) dispersed in water (blue) is clearly visible in

Figure 6.11b. This indicates the successful formation of oil-in-water (O/W) Pickering emulsions through the use of SL bilayer coated iron oxide nanoparticles. These findings match those expected from following the Bancroft rule (i.e. the phase in which the stabilizing agent is more soluble will be the continuous phase) (Davies, 1957) and directs us towards using the SL bilayer coated nanoparticles in our next set of Pickering emulsion studies.

Zeta-potential analysis of the 400mg SL coated iron oxide nanoparticles dispersed in water at different pH values (adjusted using TMAOH) showed an increase in zeta-potential from pH 6 to pH 10 (Figure 6.12). The fact that the particles are stable at a pH of 7, which is approximately the isoelectric point for uncoated iron oxide nanoparticles, is further proof for the presence of a charged bilayer being present on the particle core (Ingram et al., 2010). Upon further increase in pH (pH > 10) however, a drop in zeta-potential was observed. This trend in zeta-potential is similar to that observed by Lan et al. (Lan et al., 2007) for oleic acid bilayer coated iron oxide nanoparticles where a drop in zeta-potential was observed for a pH value of 12.5, and this behavior was attributed to the desorption of the secondary oleic acid layer. Hence, due to the similarity between the stabilizing agent conjugation and structure (oleic acid and SSL), the reduction in zeta-potential (at a pH > 10), can also be attributed to the possible desorption of the outer SSL layer in this case of SL bilayer coated nanoparticles. This desorption occurs due to the strong hydration of the hydrophilic head groups and weakening van der Waals forces (between the interacting hydrophobic tail groups) in an alkaline environment. (Fu, Dravid, & Johnson, 2001; Lan et al., 2007; Shen, Laibinis, & Hatton, 1999; Zhou et al., 2012)

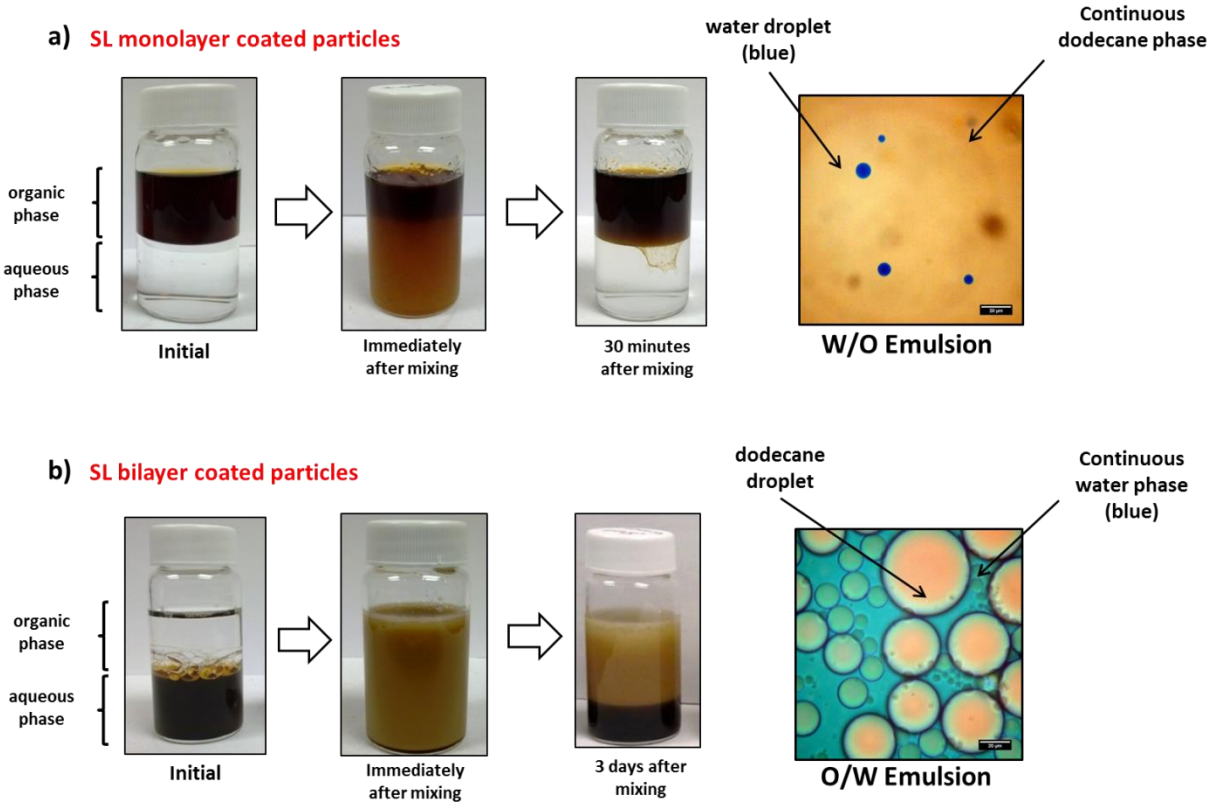

Figure 6.11 Preliminary Pickering emulsion experiments using a) SL monolayer and b) SL bilayer coated iron oxide nanoparticles. (pH of aqueous phase = 10 and iron oxide nanoparticle concentration = 0.1 wt. %)

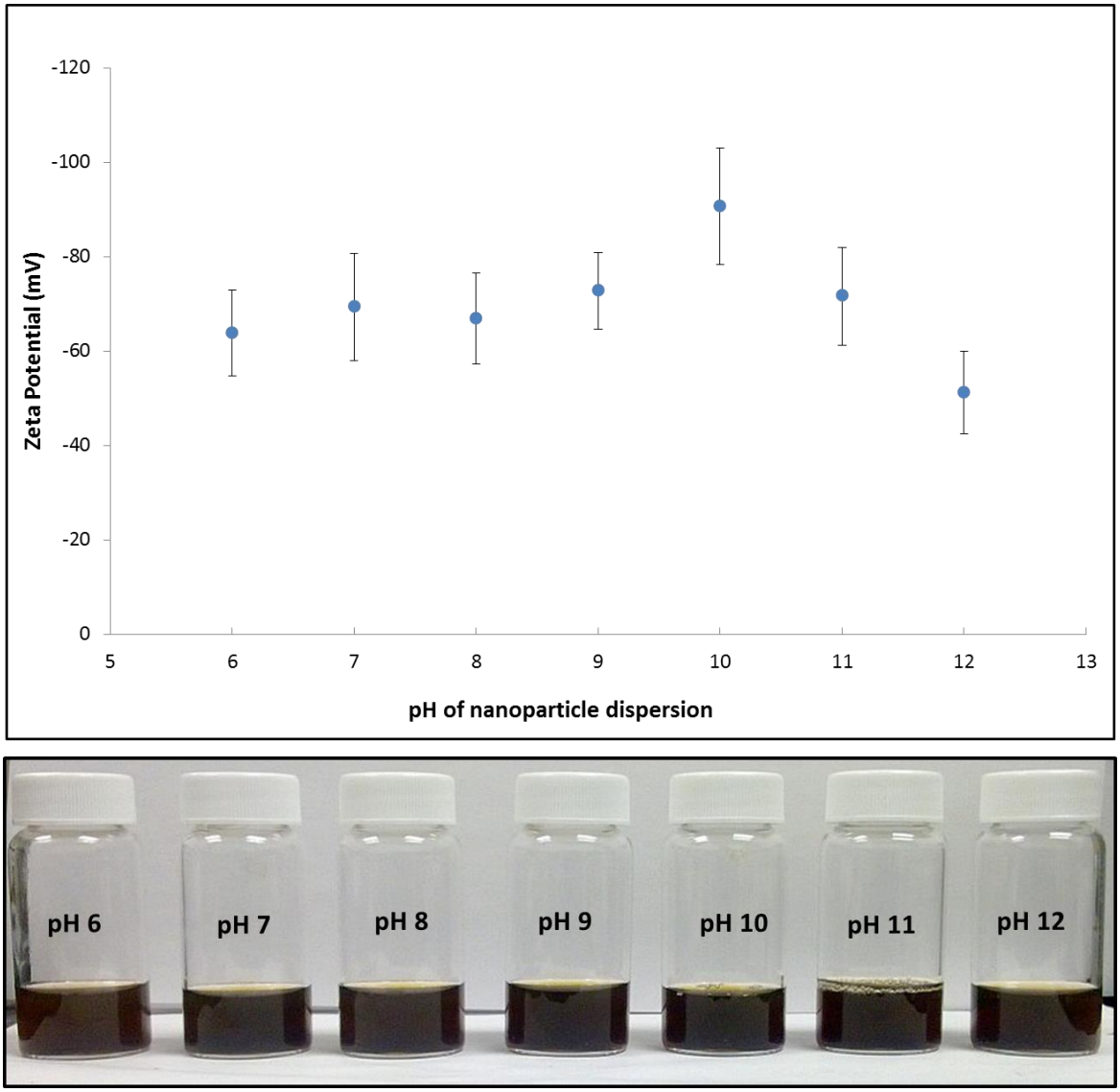

Figure 6.12 Stability analysis using zeta-potential of SL bilayer coated iron oxide nanoparticles at various pH values

The results obtained from the pH-responsiveness experiment on Pickering emulsions stabilized using the SL bilayer coated particles are shown in Figure 6.13. As mentioned before, the iron oxide concentration in the aqueous phase was maintained at 0.1 wt. % using TGA analysis for the samples in this experiment. Immediately upon mixing, emulsions were formed with the SL bilayer particles at all of the seven pH values studied. Optical microscopy of these emulsions shows that at the higher pH values ($pH \geq 9$) the oil droplet size in the O/W emulsions is approximately 20 μm while at lower pH values ($pH \leq 8$) the droplet size is slightly larger at around 35 μm. The visibly larger droplets (formed due to due to rapid coalescence after mixing) for the samples at the lower pH values are proof that the emulsions at the lower pH values are not being stabilized to a large extent (compared to the samples at high pH values). By observing the samples and their optical microscopy images after an extended period of time (10 days), a clear trend in stability is observed over the range of pH values studied. At the acidic and neutral pH values the carboxylate groups are protonated resulting in a reduction in interfacial activity for the particles. (Ingram et al., 2010) The emulsions at pH 6 and pH 7 almost completely separate into the original oil and water phases, while the emulsion at pH 8 has an abundance of larger sized droplets. Creaming is also observed at the pH values where stable emulsions are obtained ($pH \geq 8$). This is also confirmed by the increased density of droplets visualized in the optical microscopy images. The stable emulsion volume fraction is around 50 % which is common for similar systems with O/W ratios of 1:1. (Lan et al., 2007) The color of iron oxide nanoparticles in the emulsions also confirmed their role in emulsion stability. This trend in stability is very similar to that obtained by other studies (Ingram et al., 2010; Lan et al., 2007) on oleic acid bilayer

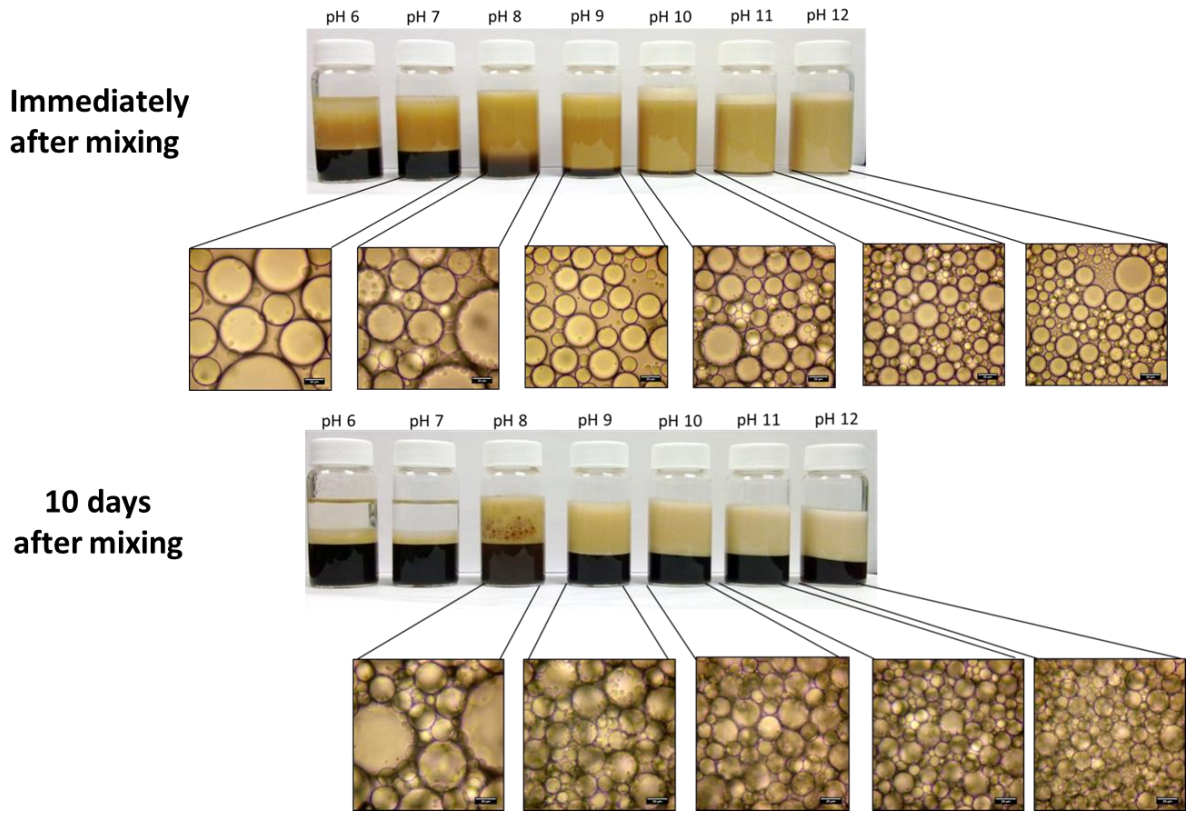

Figure 6.13 pH-responsiveness studies on oil-in-water Pickering emulsions generated using SL bilayer coated iron oxide nanoparticles

coated iron oxide nanoparticles. From the zeta-potential analysis results and the pH-responsiveness study, one can hypothesize that while the particles stabilize the emulsions at neutral and borderline basic pH, at higher pH values the emulsions are possibly stabilized by both the particles and the free surfactant (SSL). At neutral and acidic pH (pH 6 and 7), the protonation of the carboxylic groups combined with the lack of free SSL results into the destabilization seen in Figure 6.13. At pH values of 8, 9, and 10, the O/W emulsions could be stabilized by the bilayer coated nanoparticles, but at the higher pH values of 11 and 12, it is possible that the desorbed surfactant can be stabilizing the emulsions along with the nanoparticles. This type of synergistic stabilization of O/W emulsions by nanoparticles and surfactants has been seen previously in other nanoparticle-surfactant systems (Eskandar et al., 2007; Zou, Yang, Liu, & Wang, 2013) and has been hypothesized to occur due to competitive adsorption of particles and desorbed surfactant molecules in bilayer systems (Lan et al., 2007).

The simple test using a permanent magnet (Figure 6.14) shows us that the emulsions at the pH values studied respond differently under the influence of a magnetic field. For the sample at pH 8, the emulsion is destabilized (due to removal of the magnetic iron oxide nanoparticles) and the oil droplets coalesce to give a distinct oil phase and water phase. For the emulsion sample at pH of 9, a few oil droplets in the emulsion phase coalesce and form a distinct layer of dodecane at the top of the emulsion phase. However, there is still an emulsion phase present in the system. The emulsion sample at pH 10 remains relatively stable under the influence of the magnetic field and no visual evidence of dodecane droplet coalescence in the emulsion phase is observed.

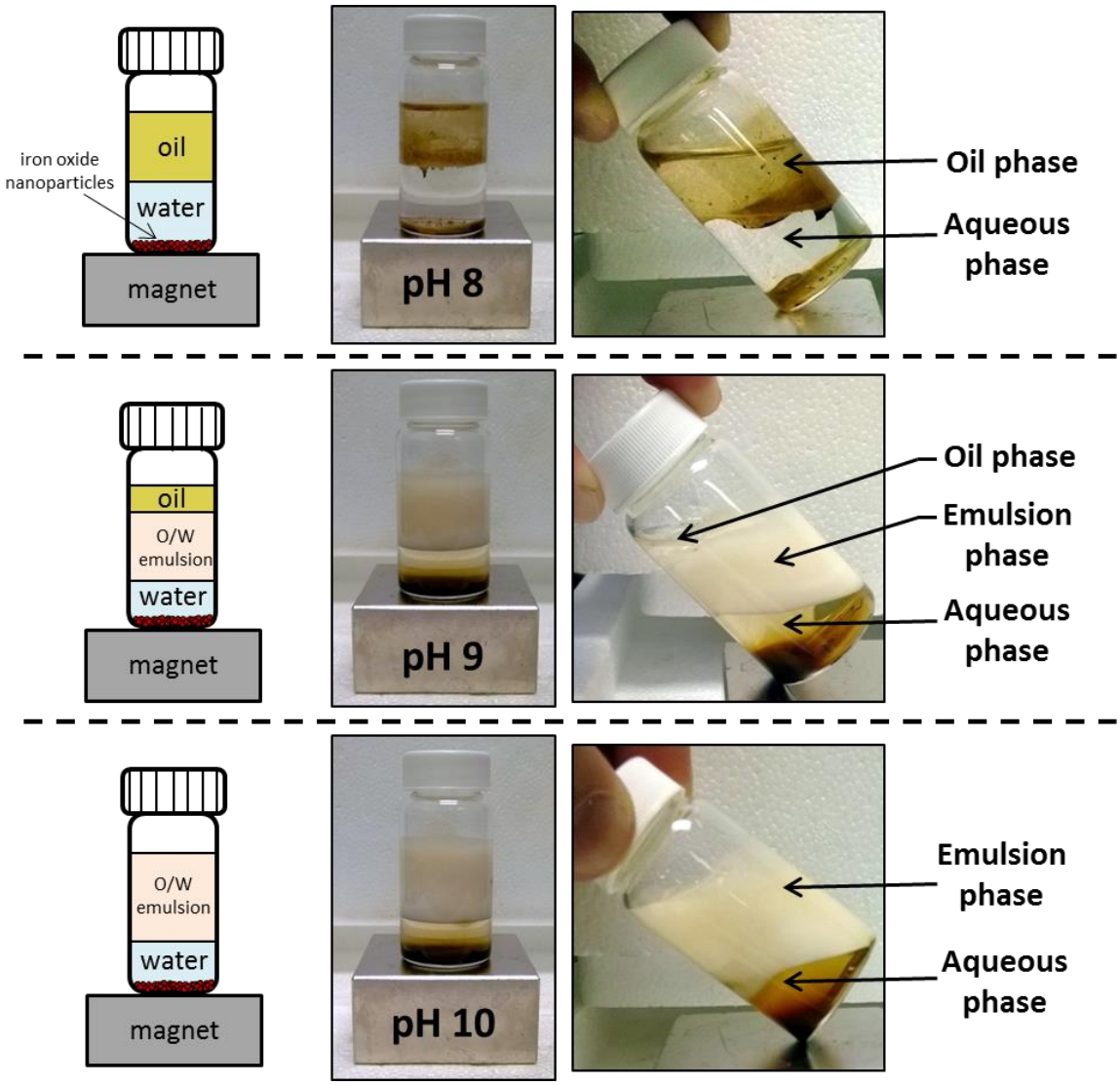

Figure 6.14 Effect of a permanent magnet on emulsion stability at various pH values

At higher pH values, the magnet has an effect on emulsion stability similar to that observed at pH 10 (i.e. no visual evidence of a distinct oil phase). This lends credence to our previous hypothesis that at higher pH values the emulsion may be co-stabilized by the nanoparticles and the surfactant (SSL). It is important to note that the smaller iron oxide nanoparticles will not be influenced by the magnetic field and will still remain dispersed in the emulsion/organic phase (as is visible from the brownish iron oxide color of the emulsion in Figure 6.14). While it is difficult to reach a definitive conclusion without the aid of detailed interfacial studies on these systems, the magnetic effect on emulsion stability does indicate surfactant/nanoparticle co-stabilization at higher pH values.

Salinity studies carried out using salt concentrations from 0.1 wt. % to 3.5 wt. % are shown in Figure 6.15. From visual observation it is clear that the emulsions are stable at all of the salt concentrations studied. Over a period of 10 days, creaming is observed in all the samples and the stable emulsion volume fraction is around 50 %, similar to that witnessed in the previous pH-responsiveness studies. A small degree of coalescence is, however, observed for the samples with the salt concentration above 0.1 wt. %. Optical microscopy on these samples revealed a significant quantity of larger sized droplets (droplet size > 50 μm). At higher salt concentrations, the presence of Na^+ ions in solution has a similar effect to the presence of H^+ ions in an acidic solution and causes the carboxylate groups to associate with the ions, hence decreasing double layer thickness. This combined with competitive adsorption of particles and desorbed surfactant molecules results in a change in the wettability of the particles. (Bernard P Binks, Murakami, Armes, & Fujii, 2006; Ingram et al., 2010; Lan et al., 2007) This results in the larger droplet size being present, thereby aiding emulsion destabilization.

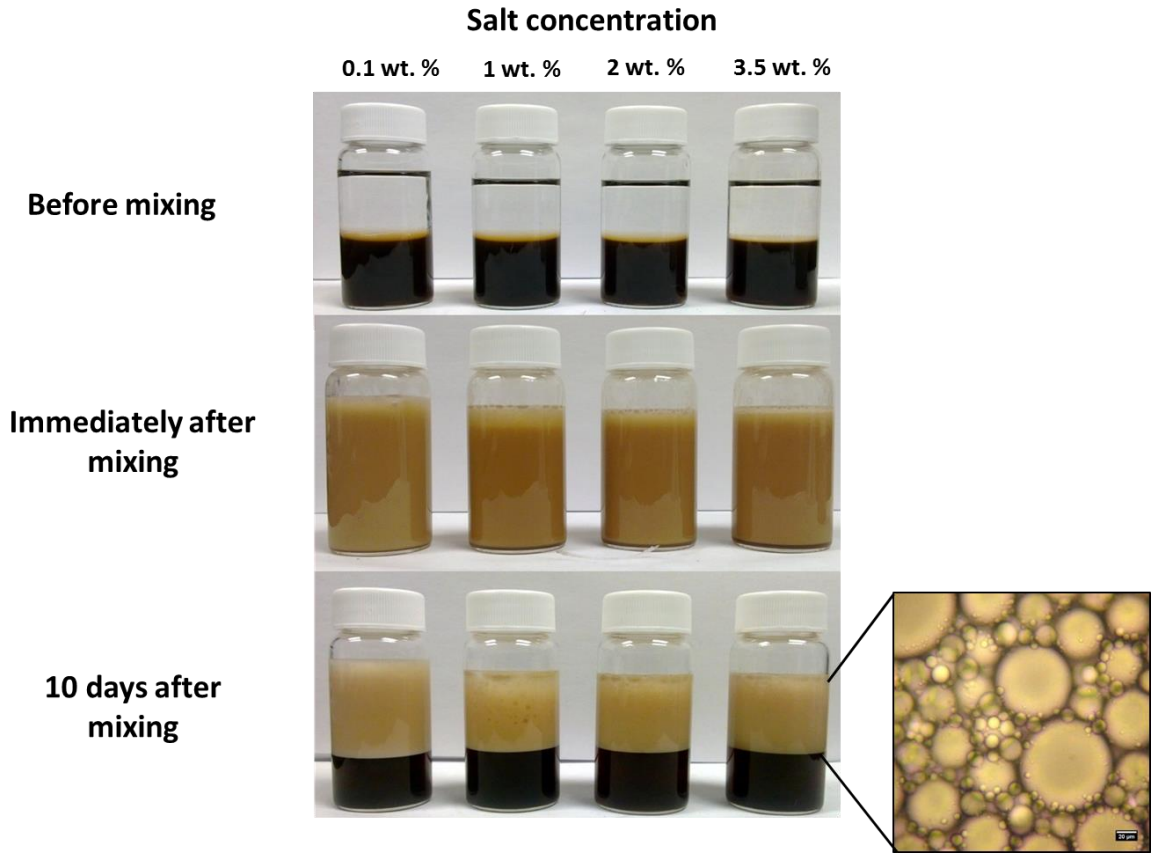

Figure 6.15 Salinity studies on oil-in-water Pickering emulsions generated using SL bilayer coated iron oxide nanoparticles (pH of aqueous phase *before* salt addition = 7.5 and iron oxide nanoparticle concentration = 0.1 wt. %)

There is a possibility that the destabilizing effect of the salt is being countered by the fact that stearoyl lactylate (SL) in presence of a sodium counter ion (i.e. SSL) has been shown to have a better interfacial tension reduction capacity. This phenomenon has been attributed in literature to the difference in micellar aggregation behavior of SL and SSL.(Meshram & Jadhav, 2012) This proposed micellar aggregation behavior could explain relatively high stability (compared to oleic acid bilayer particles) (Ingram et al., 2010) of the Pickering emulsions generated using SL bilayer coated nanoparticles in the presence of significant salt concentrations.

6.4 Conclusion

Iron oxide nanoparticles were synthesized using a co-precipitation technique and their surfaces were successfully functionalized with monolayers and bilayers of various stabilizing agents including oleic acid and sodium stearoyl lactylate (SSL). From preliminary experiments we have deduced that only fatty acid bilayer coated iron oxide nanoparticles can effectively produce O/W Pickering emulsions and the monolayer coated particles are unable to produce a stable emulsion at the conditions studied. Hence, using the currently investigated fatty acid ligands and through the use of a GXL based system we were unable to separate iron oxide nanoparticles based upon their size to test the size effects on emulsion formation. To carry out size-effect studies on the stability of Pickering emulsion stabilized using iron oxide nanoparticles it would be simpler to use synthesis procedures to obtain monodisperse nanoparticles of different sizes such as those described by Chen et al. (C.-J. Chen et al., 2009). While methods like these are expensive and tedious, they would provide one with significant quantities of monodisperse

nanoparticles which could then be coated with a surfactant bilayer and tested for their emulsion forming effectiveness.

During our preliminary studies we did however stumble upon a bilayer based system using sodium stearoyl lactylate (SSL) which delivered O/W emulsions with remarkable stability. The presence of a monolayer or bilayer was dependent upon the amount of the surfactant SSL introduced into the system during synthesis. Characterization using various analytical techniques confirmed that the particles were primarily Fe_3O_4 iron oxide nanoparticles with the SL molecules attached to the nanoparticle core via a bidentate type chelating complex. Small quantities of ammonium chloride impurities are present in the synthesized particles which are reduced in concentration via various purification methods. Preliminary studies showed that the SL monolayer coated particles generated unstable W/O emulsions, while the SL bilayer coated particles generated relatively stable O/W emulsions. Dispersions of the synthesized SL bilayer coated nanoparticles in water were stable over an extended period of time at pH values varying from 6 to 12. O/W Pickering emulsions were also successfully generated using the SL bilayer coated iron oxide nanoparticles at extremely low iron oxide concentrations (0.1 wt. %). The pH-responsiveness studies on emulsions systems stabilized by these particles showed that these particles were successful at stabilizing O/W emulsions at pH values from 8 and 12. At acidic and neutral pH values the emulsions coalesced into distinct oil and water phases due to protonation of bilayers on the particles. These trends in pH-responsiveness are comparable to those reported previously by other researchers in similar bilayer systems.(Ingram et al., 2010; Lan et al., 2007) The trends in emulsion stability combined with zeta-potential analysis on the

nanoparticle dispersions and the simple magnetic test, hint to a co-stabilization of the emulsions by the nanoparticle and the desorbed surfactant at various pH values. Salinity studies also showed that emulsions stabilized using the bilayer coated particles were stable over an extended period of time at salt concentrations ranging from 0.1 wt. % to 3.5 wt. %. Thus from this study, we have demonstrated the capacity to functionalize iron oxide nanoparticles with a benign surfactant and tested its effectiveness in stabilizing O/W Pickering emulsions at various pH and salinity conditions. This study provides fundamental insights into the capacity to multi-functionalize nanoparticles and Pickering emulsions generated using such particles could be used in the future for applications like oil-spill cleanup.

Chapter 7

Conclusions and Avenues for Future Work

7.1 Summary and Conclusions

The primary goal of this work was to improve our understanding of the fundamental physical/chemical phenomena which influence the gas-expanded liquid nanoparticle fractionation process. Our aim was then to use the lessons learned from these fundamental studies to improve the GXL nanoparticle process and to apply the process in various relevant applications. The GXL fractionation process has some inherent advantages over other nanoparticle processing techniques including enhanced transport properties, relatively low cost and reusability of solvents used. However, there have been disadvantages to the process, including the relatively high operating pressures required and the lack of scalability. The GXL nanoparticle systems in spite of these advantages and disadvantages have not been used in many relevant applications. Hence, this dissertation looks into studying the GXL nanoparticle processing technique and improving it to make it more scalable, more versatile and capable of operating at lower pressures. Also, included in this dissertation is research pertaining to the application of the GXL system and iron oxide nanoparticles in two relevant applications of catalysis and environmental remediation. The iron oxide nanoparticles are used to make supported

catalysts for the Fischer-Tropsch synthesis process and for make particle emulsifiers to stabilize oil-in-water emulsions.

In Chapter 2, a study aimed at reducing the operating pressures in the GXL nanoparticle fractionation system through various modifications in ligand and solvent structure is presented. In this study gold nanoparticles coated with a straight-chain ligand (dodecanethiol) and its branched isomer (*tert*-dodecanethiol) were dispersed in *n*-hexane and its isomers to determine if the solvent/ligand structures affect nanoparticle precipitation in a GXL system. It was expected that the stearically hindered solvents and ligand would interact poorly resulting into lower CO_2 pressures required to destabilize and precipitate the nanoparticles out of solution. After carrying out UV-vis studies on various solvent-ligand systems it was determined that the system employing gold nanoparticles coated with *tert*-dodecanethiol (branched ligand) and dispersed in 2,2-dimethylbutane (branched solvent) gave us the lowest incipient nanoparticle precipitation pressure (P_i) for the GXL fractionation process. The reduction in the P_i value was almost six-fold compared to the control system of dodecanethiol (straight-chain ligand) and *n*-hexane (straight-chain solvent). Successful fractionations were also obtained at lower overall operating pressures and higher ΔP values compared to the straight chain ligand and straight chain solvent control system. This suggests that one can manipulate the process parameters critical to the GXL size-selective fractionation process and improve the process by simply changing the physical interactions between the nanoparticles and the solvent.

In Chapter 3, experiments aimed at increasing the versatility of the GXL nanoparticle fractionation process by extending it to iron oxide nanoparticles are detailed.

The iron oxide nanoparticles used in this study are primarily of two types: a) perfectly spherical monodisperse iron oxide nanoparticles purchased commercially, and b) faceted polydisperse iron oxide nanoparticles synthesized by the coprecipitation method. The precipitation of the iron oxide nanoparticles is studied using *in-situ* UV-vis spectroscopy and it was determined that iron oxide nanoparticles have similar precipitation profiles to gold nanoparticles, albeit at lower pressures due to their larger size. Unlike the monodisperse spherical iron oxide nanoparticle system, the faceted nanoparticle system gave poor GXL fractionation results. The large nanoparticle concentrations employed and the fact that the synthesized faceted iron oxide nanoparticle samples are extremely polydisperse made the GXL fractionation ineffective. The interactions between the glass substrate and the iron oxide nanoparticles were also poor resulting into the relatively poor results. Our attempts to try and overcome some of these difficulties along with their solutions are detailed in Chapter 4. Hence, through the use of the cascaded vessel GXL fractionation apparatus we were able to successfully isolate the smaller sized iron oxide nanoparticles from a particle mixture and achieve an acceptable level of size separation for a spherical iron oxide nanoparticle system. This proves that the GXL nanoparticle fractionation process can be effectively extended to various other metal and metal oxide nanoparticle systems.

Based on the findings from Chapter 3, it was first attempted to convert the cascaded vessel apparatus into a packed column like apparatus to see if increasing the surface area would increase the effectiveness of the GXL fractionation process. However, after testing various packing materials in the cascaded vessel apparatus using dodecanethiol-coated gold nanoparticles dispersed in *n*-hexane, no observable

improvement in GXL fractionation was reported. In fact, liquid holdup in the packings caused a reduction in GXL fractionation effectiveness for some of the packing materials studied. Hence, to overcome the limitations of the cascaded vessel apparatus a new apparatus was designed using a Parr-reactor. This is reactor design a marked improvement over the previous GXL fractionation systems like the cascaded-vessel apparatus which would be cumbersome and expensive to scale-up. This reactor system delivered a marked reduction in nanoparticle size in the fractionated samples retrieved from the high-pressure apparatus. The fractionation of gram-scale quantities of iron oxide nanoparticles was also performed successfully for the first time using a GXL technique. The design and use of a scalable GXL apparatus capable of separating large quantities of cheaply made iron oxide nanoparticles based upon their size, demonstrated in this chapter, could pave the way forward in the field of nanoparticle processing for industrial applications.

In Chapter 5, we applied the scalable apparatus designed in Chapter 4 to the field of catalysis. The GXL nanoparticle processing system was modified so as to deposit iron oxide nanoparticles onto oxidic supports for use in Fischer-Tropsch catalysis. Polydisperse iron oxide nanoparticles were synthesized using the coprecipitation method and were then deposited onto silica and alumina supports using the GXL apparatus designed in Chapter 4. Through the use of the GXL nanoparticle processing technique, smaller sized nanoparticles, which have lower catalytic activity, were prevented from being deposited on the support material. Supported catalysts were also synthesized using the traditional incipient wetness technique and their performance was compared to the GXL synthesized materials. The iron oxide on silica supported GXL catalyst resulted in

the best overall performance of the catalysts studied, and this catalyst was demonstrated to exhibit much higher CO conversion and lower methane selectivity compared to its incipient wetness counterpart. Through various catalyst characterization techniques, it was determined that the catalysts prepared by the GXL technique exhibit a weaker interaction between iron oxide nanoparticles and the support material. This ability to affect the metal-support interactions through this GXL nanoparticle deposition technique combined with the capacity to control the size of the nanoparticles being deposited, offers a new way to influence the activity and selectivity of iron based Fischer-Tropsch catalysts.

Another application for which the GXL nanoparticle fractionation was intended to be used was the study of nanoparticle size on the stability of oil-in-water (O/W) Pickering emulsions and the results from this endeavor shown in Chapter 6. This study would enable us to gain a fundamental understanding into the phenomenon of solid-stabilized emulsions which are useful in many applications including environmental remediation. However, through preliminary studies into the type of nanoparticles required to form stable O/W emulsions it was determined that the bilayer coated nanoparticles required to form stable O/W emulsions would be incompatible with the GXL fractionation process due to their inability to dissolve in organic solvents. However, through our investigation into various ligands for the iron oxide nanoparticles, it was determined that iron oxide nanoparticles synthesized with sodium stearoyl lactylate (SSL), a FDA approved emulsifier, exhibited interesting properties and demonstrated O/W emulsification at low concentrations. Hence, a study was carried out to determine and quantify the effectiveness of the stearoyl lactylate (SL) coated nanoparticles in stabilizing O/W

emulsions. O/W Pickering emulsions were successfully generated using the SL bilayer coated iron oxide nanoparticles at extremely low iron oxide concentrations (0.1 wt. %). The pH-responsiveness studies on emulsions systems stabilized by these particles showed that these particles were successful at stabilizing O/W emulsions at pH values from 8 and 12 and at salinity values up to 3.5%. The trends in emulsion stability hint to a co-stabilization of the emulsions by the nanoparticle and the desorbed surfactant at the various pH and salinity values. Hence, we have demonstrated the capacity to functionalize iron oxide nanoparticles with a benign surfactant and tested its effectiveness in stabilizing O/W Pickering emulsions at extremely low concentrations. Lessons learned from this study could be used in the future for applications like oil-spill cleanup to reduce the amount of dispersant applied and to enhance the effectiveness of the dispersants used.

7.2 Avenues for Future Work

Similar to the goal of the work published previously in this document the future directions suggested below are primarily targeted at a) providing further fundamental insights into the GXL nanoparticle processing process for improving it and b) to extend the applicability of the GXL nanoparticle processing technique to various applications. Some of the future avenues for which the research in this document can be used is shown henceforth.

7.2.1 Modelling the GXL precipitation of iron oxide nanoparticles under various conditions and onto various surfaces

Research highlighted in this document has shown that one can successfully precipitate and fractionate iron oxide nanoparticles using the GXL nanoparticle process. The successfully precipitation of iron oxide nanoparticles out of an expanded solvent

occurs due to van der Waals forces overcoming the inherent repulsive forces between the stabilizing ligands. The degree of solvent ligand-interaction can affect the size and pressures at which the nanoparticles precipitate out of solution. This effect was exploited previously in Chapter 2 to reduce the operating pressures in a system of gold nanoparticles coated with various solvents and ligands.

Previous studies (Anand et al., 2008; Steven R. Saunders et al., 2011) have shown that through the use of the fundamental properties of the GXL system mentioned above one can effectively model the precipitation of a gold nanoparticle system. These previous modelling attempts used total interaction energy calculations to determine which would be the most energetically favorable state at various pressures conditions to determine what would be average diameter of nanoparticles precipitating out of the expanded solvent. A schematic of the three phenomenological models used to estimate the threshold particles size for the precipitation of gold nanoparticles in an expanded solvent is shown in Figure 7.1. However, currently other than trial and error techniques there is no way to model/predict the precipitation of iron oxide nanoparticles out of expanded solvents.

An important factor which would need to be considered for modelling the particle-particle interactions in an iron oxide nanoparticle system is the magnetic nature of the nanoparticles. This factor could be added to the total interaction energy model in the form of a magnetic interaction energy term (ϕ_{mag}) to the total interaction energy term (ϕ_{total}) as described in the article by Anand et al. (Anand et al., 2008). The contents of this magnetic interaction term could be designed in a way so as to accommodate the change in magnetism due to change in particle size and shape. Several previous studies in

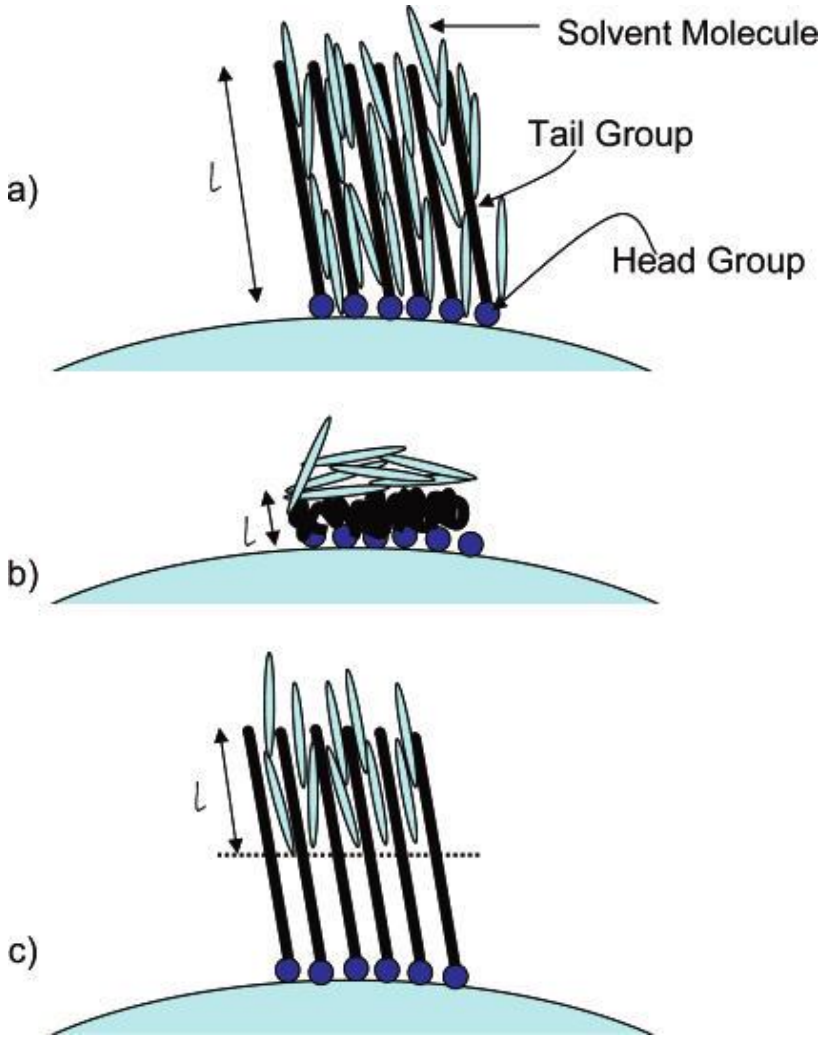

Figure 7.1 A schematic of the three phenomenological models used to estimate the threshold particles size for the precipitation of gold nanoparticles in an expanded solvent. a) extended ligand length solvation model (ELLSM), b) condensed phase model (CPM) and c) limited ligand length solvation model (LLLSM)(Anand et al., 2008)

literature have approached the modelling of interacting magnetic particles using various approaches including first order reversal curves (FORC) (Pike, Roberts, & Verosub, 1999) and Monte Carlo simulations (El-Hilo, Chantrell, & O'Grady, 1998). However, with regard to the total interaction energy model used previously by us, the best approach would be the one used by Shen et al. (Shen, Stachowiak, Fateen, Laibinis, & Hatton, 2001) using SANS studies. The equation used to estimate the interaction between magnetic particles (ϕ_{mag}) by Shen et al. has been used by other researchers to successfully model the aggregation of magnetite nanoparticles modified with poly (ethylene glycol) (Barrera, Herrera, & Rinaldi, 2009). By adapting this equation to our GXL nanoparticle system we should be able to obtain a more accurate estimate of the threshold nanoparticle sizes precipitating out of the expanded solvent at the operating pressures employed. Hence, by carrying out these studies in the future we would be able to obtain a deeper understanding of the fundamental phenomenon dominant in the GXL fractionation of magnetic particles and this understanding would be critical to improve the overall process.

7.2.2 Coating hydrophilic materials with hydrophobic nanoparticles using the GXL process to generate particulate emulsifiers

For particulate emulsifiers to stabilize O/W emulsions the particles must be able to aggregate at the oil-water interface and stabilize the oil droplet in water. From Chapter 6 we have seen that to stabilize oil droplets in water the synthesized system has to have a certain hydrophilic-lipophilic balance (HLB) and the emulsion type is determined by the nanoparticles wettability in a particular phase. Another way to develop such nanomaterials is through the surface modification of hydrophilic materials with

hydrophobic molecules to give functional nanomaterials with a HLB suitable for forming O/W emulsions. Previous studies have shown that oxidic materials like TiO_2 can be surface modified to give stable O/W Pickering emulsions (Stiller et al., 2004). The stability of the emulsions generated and their properties depended upon the combination of inorganic and organic materials used for the surface modification. Similar surface modification studies were also performed using materials such as montmorillonite clay (Voorn, Ming, & Herk, 2006) and halloysite nanotubes (Z. Wei, Wang, Liu, Zou, & Tong, 2012) to give effective particulate agents to generate Pickering emulsions.

From Chapters 4 and 5 we were able to successfully show that the GXL nanoparticle processing technique can be used to successfully deposit iron oxide nanoparticles onto an oxidic support. Through the use of the same technique we can deposit hydrophobic iron oxide nanoparticles onto various hydrophilic nanoclays to generate nanomaterials which would have a partially hydrophobic and a partially hydrophilic nature. An additional benefit of this approach would be that the generated nanomaterials will be magnetic in nature, adding another parameter which can be used to monitor the effectiveness of the emulsifying action of the particles. Such magnetically responsive Pickering emulsifiers have already been developed using materials such as graphene oxide (Lin, Yang, Petit, & Lee, 2015) for biomedical applications. By using inexpensive/non-toxic materials like nanoclays and combining them with inexpensive/non-toxic and functional nanoparticles we can expect the resulting composite nanomaterials to have extremely interesting interfacial properties which would be extremely useful for emulsification applications.

7.2.3 Deposition studies on supporting materials using cobalt nanoparticles and promoters to generate a more effective FTS catalyst

In Chapter 5, we have shown that the GXL nanoparticles deposition process was successful in generating supported iron catalysts for Fischer-Tropsch (FT) synthesis process. However, the experiments performed in this chapter were preliminary experiments designed to highlight the applicability of the GXL process in the synthesis of FT catalysts. While iron catalysts are inexpensive than other FT catalysts, cobalt catalysts are more active and can be important for the synthesis of high molecular weight paraffinic waxes.

Cobalt nanoparticles coated with fatty acid monolayers (Wu et al., 2004) would be susceptible to precipitation under CO_2 pressure and can be used in the GXL deposition process to generate effective supported FT catalysts. It has been shown in literature that the support material, the metal loading and promoters used have a significant effect on the FT products obtained using such a supported cobalt catalyst (Jacobs et al., 2002). The effect of promoters such as B, Zr and K on the activity and productivity of these supported cobalt catalysts (synthesized using the GXL technique) would also have to be investigated to gain a fundamental understanding into the effect of the GXL technique on the catalyst. Studies on various support materials like TiO_2 and ZrO_2 would also expand our understanding of the metal-support interactions in the FT process and help one select an optimum support for the desired product range. Through such a study we would be able to determine if the GXL deposition process is versatile enough to be extended to other nanoparticle systems and hence capable enough to be used to generate other catalytic materials.

References

Abbaslou, R., & Dalai, A. (2012). Promoted iron catalysts supported on carbon nanotubes for fischer-tropsch synthesis. *US Patent App. 13/667,333*. Retrieved from http://www.google.com/patents/US20130116350

Abbaslou, R. M. M., Tavassoli, A., Soltan, J., & Dalai, A. K. (2009). Iron catalysts supported on carbon nanotubes for Fischer–Tropsch synthesis: Effect of catalytic site position. *Applied Catalysis A: General, 367*(1-2), 47–52. doi:10.1016/j.apcata.2009.07.025

Aida, T., Aizawa, T., Kanakubo, M., & Nanjo, H. (2010). Dependence of volume expansion on alkyl chain length and the existence of branched methyl group of CO2-expanded ketone systems at 40°C. *The Journal of Supercritical Fluids, 55*(1), 71–76. doi:10.1016/j.supflu.2010.05.025

Al-Somali, A. M., Krueger, K. M., Falkner, J. C., & Colvin, V. L. (2004). Recycling size exclusion chromatography for the analysis and separation of nanocrystalline gold. *Analytical Chemistry, 76*(19), 5903–10. doi:10.1021/ac049355h

Alvarez, M. M., Khoury, J. T., Schaaff, T. G., Shafigullin, M. N., Vezmar, I., & Whetten, R. L. (1997). Optical absorption spectra of nanocrystal gold molecules. *The Journal of Physical Chemistry B, 101*(19), 3706–3712. Retrieved from http://pubs.acs.org/doi/abs/10.1021/jp962922n

Amelse, J., Butt, J., & Schwartz, L. (1978). Carburization of supported iron synthesis catalysts. *The Journal of Physical …*, *82*(5). Retrieved from http://pubs.acs.org/doi/pdf/10.1021/j100494a012

Amendola, V., & Meneghetti, M. (2009). Size Evaluation of Gold Nanoparticles by UV−vis Spectroscopy. *The Journal of Physical Chemistry C, 113*(11), 4277–4285. doi:10.1021/jp8082425

Anand, M., McLeod, M. C., Bell, P. W., & Roberts, C. B. (2005). Tunable solvation effects on the size-selective fractionation of metal nanoparticles in CO2 gas-expanded solvents. *The Journal of Physical Chemistry B, 109*(48), 22852–9. doi:10.1021/jp0547008

Anand, M., Odom, L. A., & Roberts, C. B. (2007). Finely controlled size-selective precipitation and separation of CdSe/ZnS semiconductor nanocrystals using CO2-

gas-expanded liquids. *Langmuir : The ACS Journal of Surfaces and Colloids*, *23*(13), 7338–43. doi:10.1021/la700325z

Anand, M., You, S.-S., Hurst, K. M., Saunders, S. R., Kitchens, C. L., Ashurst, W. R., & Roberts, C. B. (2008). Thermodynamic Analysis of Nanoparticle Size Selective Fractionation Using Gas-Expanded Liquids. *Industrial & Engineering Chemistry Research*, *47*(3), 553–559. doi:10.1021/ie070981p

Andreas, K., Georgieva, R., Ladwig, M., Mueller, S., Notter, M., Sittinger, M., & Ringe, J. (2012). Highly efficient magnetic stem cell labeling with citrate-coated superparamagnetic iron oxide nanoparticles for MRI tracking. *Biomaterials*, *33*(18), 4515–25. doi:10.1016/j.biomaterials.2012.02.064

Arnold, M. S., Stupp, S. I., & Hersam, M. C. (2005). Enrichment of single-walled carbon nanotubes by diameter in density gradients. *Nano Letters*, *5*(4), 713–8. doi:10.1021/nl050133o

Avdeev, M. V, Mucha, B., Lamszus, K., Vékás, L., Garamus, V. M., Feoktystov, A. V, … Willumeit, R. (2010). Structure and in vitro biological testing of water-based ferrofluids stabilized by monocarboxylic acids. *Langmuir : The ACS Journal of Surfaces and Colloids*, *26*(11), 8503–9. doi:10.1021/la904471f

Babes, L., Denizot, B., Tanguy, G., Le Jeune JJ, & Jallet, P. (1999). Synthesis of Iron Oxide Nanoparticles Used as MRI Contrast Agents: A Parametric Study. *Journal of Colloid and Interface Science*, *212*(2), 474–482. doi:10.1006/jcis.1998.6053

Baran Jr, Jimmie R., & Cabrera, O. J. (2006). Use of surface-modified nanoparticles for oil recovery. Washington, DC: U.S. Patent and Trademark Office.

Barrera, C., Herrera, A. P., & Rinaldi, C. (2009). Colloidal dispersions of monodisperse magnetite nanoparticles modified with poly(ethylene glycol). *Journal of Colloid and Interface Science*, *329*(1), 107–13. doi:10.1016/j.jcis.2008.09.071

Bee, A. (1995). Synthesis of very fine maghemite particles. *Journal of Magnetism and Magnetic Materials*, *149*(1-2), 6–9. doi:10.1016/0304-8853(95)00317-7

Belloni, J. (1996). Metal nanocolloids. *Current Opinion in Colloid & Interface Science*, *1*(2), 184–196. doi:10.1016/S1359-0294(96)80003-3

Bergstrom, L., Meurk, A., Arwin, H., & Rowcliffe, D. J. (1996). Estimation of Hamaker constants of ceramic materials from optical data using Lifshitz theory. *Journal of the American Ceramic Society*, *79*(2), 339–348. doi:10.1111/j.1151-2916.1996.tb08126.x

Bezemer, G. L., Falke, U., van Dillen, a J., & de Jong, K. P. (2005). Cobalt on carbon nanofiber catalysts: auspicious system for study of manganese promotion in Fischer-

Tropsch catalysis. *Chemical Communications (Cambridge, England)*, (6), 731–3. doi:10.1039/b414788j

Bhosale, P. S., & Stretz, H. a. (2008). Gold nanoparticle deposition using CO2 expanded liquids: effect of pressure oscillation and surface-particle interactions. *Langmuir : The ACS Journal of Surfaces and Colloids*, *24*(21), 12241–6. doi:10.1021/la801618m

Binks, B. P., & Lumsdon, S. O. (2001). Pickering Emulsions Stabilized by Monodisperse Latex Particles: Effects of Particle Size. *Langmuir*, *17*(15), 4540–4547. doi:10.1021/la0103822

Binks, B. P., Murakami, R., Armes, S. P., & Fujii, S. (2006). Effects of pH and salt concentration on oil-in-water emulsions stabilized solely by nanocomposite microgel particles. *Langmuir : The ACS Journal of Surfaces and Colloids*, *22*(5), 2050–7. doi:10.1021/la053017+

Binks, B. P., & Whitby, C. P. (2005). Nanoparticle silica-stabilised oil-in-water emulsions: improving emulsion stability. *Colloids and Surfaces A: Physicochemical and Engineering Aspects*, *253*(1-3), 105–115. doi:10.1016/j.colsurfa.2004.10.116

Bishop, K. J. M., Wilmer, C. E., Soh, S., & Grzybowski, B. a. (2009). Nanoscale forces and their uses in self-assembly. *Small*, *5*(14), 1600–30. doi:10.1002/smll.200900358

Bréchignac, C., Houdy, P., & Lahmani, M. (2008). *Nanomaterials and nanochemistry*. Retrieved from http://books.google.com/books?hl=en&lr=&id=yKOtuRjNRoYC&oi=fnd&pg=PA3&dq=Nanomaterials+and+Nanochemistry&ots=6DLIVSRd5y&sig=iogPHCXIFJ_J2VG5teVb_QnAuf4

Brown, K. R., Walter, D. G., & Natan, M. J. (2000). Seeding of Colloidal Au Nanoparticle Solutions. 2. Improved Control of Particle Size and Shape. *Chemistry of Materials*, *12*(2), 306–313. doi:10.1021/cm980065p

Brown, P., Bushmelev, A., Butts, C. P., Cheng, J., Eastoe, J., Grillo, I., … Schmidt, A. M. (2012). Magnetic control over liquid surface properties with responsive surfactants. *Angewandte Chemie (International Ed. in English)*, *51*(10), 2414–6. doi:10.1002/anie.201108010

Brown, W. H., Foote, C. S., Iverson, B. L., Anslyn, E. V., & Novak, B. M. (2011). *Organic Chemistry*. Cengage Learning.

Brust, M., Fink, J., Bethell, D., Schiffrin, D. J., & Kiely, C. (1995). Synthesis and reactions of functionalised gold nanoparticles. *Journal of the Chemical Society, Chemical Communications*, (16), 1655. doi:10.1039/c39950001655

Brust, M., Walker, M., Bethell, D., Schiffrin, D. J., & Whyman, R. (1994). Synthesis of thiol-derivatised gold nanoparticles in a two-phase liquid system. *Journal of the Chemical Society, Chemical Communications*, (7), 801. doi:10.1039/c39940000801

Bukur, D. B., Okabe, K., Rosynek, M. P., Li, C. P., Wang, D. J., Rao, K. R. P. M., & Huffman, G. P. (1995). Activation Studies with a Precipitated Iron Catalyst for Fischer-Tropsch Synthesis .1. Characterization Studies. *Journal of Catalysis*, *155*(2), 353–365.

Bukur, D. B., & Sivaraj, C. (2002). Supported iron catalysts for slurry phase Fischer–Tropsch synthesis. *Applied Catalysis A: General*, *231*(1-2), 201–214. doi:10.1016/S0926-860X(02)00053-4

Bukur, D., Lang, X., Doble, M., Zimmerman, W., Rosynek, M., & Li, C. (1990). Binder/support effects on the activity and selectivity of iron catalysts in the Fischer-Tropsch synthesis. *Industrial & Engineering Chemistry Research*, *29*(8), 1588–1599. Retrieved from http://pubs.acs.org/doi/abs/10.1021/ie00104a003

Bulte, J. W. M., & Kraitchman, D. L. (2004). Iron oxide MR contrast agents for molecular and cellular imaging. *NMR in Biomedicine*, *17*(7), 484–99. doi:10.1002/nbm.924

Byrappa, K., Ohara, S., & Adschiri, T. (2008). Nanoparticles synthesis using supercritical fluid technology - towards biomedical applications. *Advanced Drug Delivery Reviews*, *60*(3), 299–327. doi:10.1016/j.addr.2007.09.001

Cao, G. (2004). *Nanostructures & nanomaterials: synthesis, properties & applications*. Imperial College Press.

Chen, C.-J., Lai, H.-Y., Lin, C.-C., Wang, J.-S., & Chiang, R.-K. (2009). Preparation of Monodisperse Iron Oxide Nanoparticles via the Synthesis and Decomposition of Iron Fatty Acid Complexes. *Nanoscale Research Letters*, *4*(11), 1343–50. doi:10.1007/s11671-009-9403-x

Chen, F., Xu, G.-Q., & Hor, T. S. A. (2003). Preparation and assembly of colloidal gold nanoparticles in CTAB-stabilized reverse microemulsion. *Materials Letters*, *57*(21), 3282–3286. doi:10.1016/S0167-577X(03)00048-X

Chen, T., Colver, P. J., & Bon, S. a. F. (2007). Organic–Inorganic Hybrid Hollow Spheres Prepared from TiO2-Stabilized Pickering Emulsion Polymerization. *Advanced Materials*, *19*(17), 2286–2289. doi:10.1002/adma.200602447

Chen, W., Liu, X., Liu, Y., & Kim, H.-I. (2010). Synthesis of microcapsules with polystyrene/ZnO hybrid shell by Pickering emulsion polymerization. *Colloid and Polymer Science*, *288*(14-15), 1393–1399. doi:10.1007/s00396-010-2277-8

Chou, L. Y. T., Ming, K., & Chan, W. C. W. (2010). Strategies for the intracellular delivery of nanoparticles. *Chemical Society Reviews*, *40*(1), 233–45. doi:10.1039/c0cs00003e

Chow, M., & Zukoski, C. (1994). Gold sol formation mechanisms: role of colloidal stability. *Journal of Colloid and Interface Science*. Retrieved from http://www.sciencedirect.com/science/article/pii/S0021979784712100

Claeys, M., & van Steen, E. (2004). *Fischer-Tropsch Technology*. *Studies in Surface Science and Catalysis* (Vol. 152). Elsevier. doi:10.1016/S0167-2991(04)80465-8

Clarke, N. Z., Waters, C., Johnson, K. a., Satherley, J., & Schiffrin, D. J. (2001). Size-Dependent Solubility of Thiol-Derivatized Gold Nanoparticles in Supercritical Ethane. *Langmuir*, *17*(20), 6048–6050. doi:10.1021/la010794a

Coccia, M., Finardi, U., & Margon, D. (2011). Current trends in nanotechnology research across worldwide geo-economic players. *The Journal of Technology Transfer*, *37*(5), 777–787. doi:10.1007/s10961-011-9219-6

Creighton, J. A. J. J. A., & Eadon, D. G. D. D. G. (1991). Ultraviolet–visible absorption spectra of the colloidal metallic elements. *Journal of the Chemical Society, Faraday Transactions*, *87*(24), 3881. doi:10.1039/ft9918703881

Cui, H., Liu, Y., & Ren, W. (2013). Structure switch between α-Fe2O3, γ-Fe2O3 and Fe3O4 during the large scale and low temperature sol–gel synthesis of nearly monodispersed iron oxide nanoparticles. *Advanced Powder Technology*, *24*(1), 93–97. doi:10.1016/j.apt.2012.03.001

Dalvi, S. V., & Mukhopadhyay, M. (2009). Use of Subcritical CO 2 for Production of Ultrafine Particles by Pressure Reduction of Gas-Expanded Organic Liquids. *Industrial & Engineering Chemistry Research*, *48*(12), 5696–5707. doi:10.1021/ie900132r

Daniel, M.-C., & Astruc, D. (2004). Gold nanoparticles: assembly, supramolecular chemistry, quantum-size-related properties, and applications toward biology, catalysis, and nanotechnology. *Chemical Reviews*, *104*(1), 293–346. doi:10.1021/cr030698+

Davies, J. (1957). A quantitative kinetic theory of emulsion type, I. Physical chemistry of the emulsifying agent. *Proceedings of the Second International Congress of Surface Activity*, *London*, 426–438. Retrieved from http://www.firp.ula.ve/archivos/historicos/57_Chap_Davies.pdf

Deklerk, a. (2008). Hydroprocessing peculiarities of Fischer–Tropsch syncrude. *Catalysis Today*, *130*(2-4), 439–445. doi:10.1016/j.cattod.2007.10.006

Deng, H., Li, X., Peng, Q., Wang, X., Chen, J., & Li, Y. (2005). Monodisperse Magnetic Single-Crystal Ferrite Microspheres. *Angewandte Chemie*, *117*(18), 2842–2845. doi:10.1002/ange.200462551

Dry, M. E. (1996). Practical and theoretical aspects of the catalytic Fischer-Tropsch process. *Applied Catalysis A: General*, *138*(2), 319–344. doi:10.1016/0926-860X(95)00306-1

Dry, M. E. (2002). The Fischer – Tropsch process : 1950 – 2000. *Catalysis Today*, *71*, 227–241.

Du, M., Guo, B., & Jia, D. (2010). Newly emerging applications of halloysite nanotubes: a review. *Polymer International*, (June 2009), n/a–n/a. doi:10.1002/pi.2754

Eilers, J., Posthuma, S. A., & Sie, S. T. (1990). The shell middle distillate synthesis process (SMDS). *Catalysis Letters*, *7*(March 1990), 253–270.

El-Hilo, M., Chantrell, R. W., & O'Grady, K. (1998). A model of interaction effects in granular magnetic solids. *Journal of Applied Physics*, *84*(9), 5114. doi:10.1063/1.368761

El-Sayed, M. A. (2004). Small is different: shape-, size-, and composition-dependent properties of some colloidal semiconductor nanocrystals. *Accounts of Chemical Research*, *37*(5), 326–33. doi:10.1021/ar020204f

Elvassore, N., Bertucco, A., & Di Noto, V. (2002). On-line monitoring of volume expansion in gas-antisolvent processes by UV-vis spectroscopy. *Journal of Chemical & Engineering Data*, *47*(2), 223–227. Retrieved from http://pubs.acs.org/doi/abs/10.1021/je010189%2B

Eskandar, N., Simovic, S., & Prestidge, C. (2007). Synergistic effect of silica nanoparticles and charged surfactants in the formation and stability of submicron oil-in-water emulsions. *Physical Chemistry Chemical …*, *9*(48), 6313–8. doi:10.1039/b705094a

Espinoza, R. L., & Steynberg, A. P. (1999). Low temperature Fischer–Tropsch synthesis from a Sasol perspective. *Applied Catalysis A: …*, *186*(1-2), 13–26. doi:10.1016/S0926-860X(99)00161-1

European Food Safety Authority. (2013). EFSA ANS Panel (EFSA Panel on Food Additives and Nutrient Sources added to food), 2013: Scientific Opinion on the re-evaluation of sodium stearoyl-2-lactylate (E 481) and calcium stearoyl-2-lactylate (E 482) as food additives. *EFSA Journal*, *11*(5), 1–35. doi:10.2903/j.efsa.2013.3144

Eustis, S., & el-Sayed, M. a. (2006). Why gold nanoparticles are more precious than pretty gold: noble metal surface plasmon resonance and its enhancement of the

radiative and nonradiative properties of nanocrystals of different shapes. *Chemical Society Reviews*, *35*(3), 209–17. doi:10.1039/b514191e

Eustis, S., Hsu, H.-Y., & El-Sayed, M. a. (2005). Gold nanoparticle formation from photochemical reduction of Au3+ by continuous excitation in colloidal solutions. A proposed molecular mechanism. *The Journal of Physical Chemistry. B*, *109*(11), 4811–5. doi:10.1021/jp0441588

Faure, B., Salazar-Alvarez, G., & Bergström, L. (2011). Hamaker constants of iron oxide nanoparticles. *Langmuir : The ACS Journal of Surfaces and Colloids*, *27*(14), 8659–64. doi:10.1021/la201387d

Fedlheim, D., & Foss, C. (2001). *Metal nanoparticles: synthesis, characterization, and applications*. Retrieved from http://books.google.com/books?hl=en&lr=&id=-u9tVYWfRcMC&oi=fnd&pg=PR3&dq=Metal+Nanoparticles:+Synthesis,+Characterization,+and+Applications&ots=4DDIFVT-jT&sig=pB8p0WDrDKBOe9dWlkdTDrqX1A4

Fletcher, D. (1991). Fine particle high gradient magnetic entrapment. *IEEE Transactions on Magnetics*, *27*(4), 3655–3677. doi:10.1109/20.102936

Flores, M., Giner, E., Fiszman, S. M., Salvador, a, & Flores, J. (2007). Effect of a new emulsifier containing sodium stearoyl-2-lactylate and carrageenan on the functionality of meat emulsion systems. *Meat Science*, *76*(1), 9–18. doi:10.1016/j.meatsci.2006.06.032

Fowkes, F. (1980). Surface effects of anisotropic London dispersion forces in n-alkanes. *The Journal of Physical Chemistry*, 510–512. Retrieved from http://pubs.acs.org/doi/abs/10.1021/j100442a011

Freestone, I., Meeks, N., Sax, M., & Higgitt, C. (2007). The Lycurgus cup—a roman nanotechnology. *Gold Bulletin*, *40*(4). Retrieved from http://link.springer.com/article/10.1007/BF03215599

Frens, G. (1973). Controlled nucleation for the regulation of the particle size in monodisperse gold suspensions. *Nature*. Retrieved from http://www.nature.com/nature-physci/journal/v241/n105/abs/physci241020a0.html

Fu, L., Dravid, V. P., & Johnson, D. L. (2001). Self-assembled (SA) bilayer molecular coating on magnetic nanoparticles. *Applied Surface Science*, *181*(1-2), 173–178. doi:10.1016/S0169-4332(01)00388-9

Fuente, J. C. De, Peters, C. J., & Arons, J. D. S. (2000). Volume expansion in relation to the gas – antisolvent process. *Science*, *17*, 13–23.

Gonzales, M., & Krishnan, K. M. (2005). Synthesis of magnetoliposomes with monodisperse iron oxide nanocrystal cores for hyperthermia. *Journal of Magnetism and Magnetic Materials*, *293*(1), 265–270. doi:10.1016/j.jmmm.2005.02.020

Goulet, P. J. G., & Lennox, R. B. (2010). New insights into Brust-Schiffrin metal nanoparticle synthesis. *Journal of the American Chemical Society*, *132*(28), 9582–4. doi:10.1021/ja104011b

Grigoriev, D. O., Leser, M. E., Michel, M., & Miller, R. (2007). Mixed micelles as delivery systems for enhanced emulsifier adsorption at the air/water interface: Sodium stearoyl lactylate (SSL)/Tween80 solutions. *Colloids and Surfaces A: Physicochemical and Engineering Aspects*, *301*(1-3), 158–165. doi:10.1016/j.colsurfa.2006.12.048

Guzmán, M. G., Dille, J., & Godet, S. (2008). Synthesis of silver nanoparticles by chemical reduction method and their antibacterial activity. *Engineering and Technology*, 357–364.

Haiss, W., Thanh, N. T. K., Aveyard, J., & Fernig, D. G. (2007). Determination of size and concentration of gold nanoparticles from UV-vis spectra. *Analytical Chemistry*, *79*(11), 4215–21. doi:10.1021/ac0702084

Hallett, J. P., Ford, J. W., Jones, R. S., Pollet, P., Thomas, C. a., Liotta, C. L., & Eckert, C. a. (2008). Hydroformylation Catalyst Recycle with Gas-Expanded Liquids. *Industrial & Engineering Chemistry Research*, *47*(8), 2585–2589. doi:10.1021/ie0714091

Hamelinck, C., Faaij, a, Denuil, H., & Boerrigter, H. (2004). Production of FT transportation fuels from biomass; technical options, process analysis and optimisation, and development potential. *Energy*, *29*(11), 1743–1771. doi:10.1016/j.energy.2004.01.002

Hanauer, M., Pierrat, S., Zins, I., Lotz, A., & Sönnichsen, C. (2007). Separation of nanoparticles by gel electrophoresis according to size and shape. *Nano Letters*, *7*(9), 2881–5. doi:10.1021/nl071615y

Haruta, M., & Daté, M. (2001). Advances in the catalysis of Au nanoparticles. *Applied Catalysis A: General*, *222*(1-2), 427–437. doi:10.1016/S0926-860X(01)00847-X

He, Y., & Yu, X. (2007). Preparation of silica nanoparticle-armored polyaniline microspheres in a Pickering emulsion. *Materials Letters*, *61*(10), 2071–2074. doi:10.1016/j.matlet.2006.08.018

Henglein, A. (1989). Small-particle research: physicochemical properties of extremely small colloidal metal and semiconductor particles. *Chemical Reviews*. Retrieved from http://pubs.acs.org/doi/abs/10.1021/cr00098a010

Henglein, A. (1993). Physicochemical properties of small metal particles in solution:“ microelectrode” reactions, chemisorption, composite metal particles, and the atom-to-metal transition. *The Journal of Physical Chemistry*. Retrieved from http://pubs.acs.org/doi/abs/10.1021/j100123a004

Henglein, A. (1998). Colloidal silver nanoparticles: photochemical preparation and interaction with O2, CCl4, and some metal ions. *Chemistry of Materials*, *2*(1), 444–450. Retrieved from http://pubs.acs.org/doi/abs/10.1021/cm970613j

Hintermair, U., Leitner, W., & Jessop, P. (2010). Expanded Liquid Phases in Catalysis: Gas-expanded Liquids and Liquid–Supercritical Fluid Biphasic Systems. *Wiley Online Library*, *4*. Retrieved from http://onlinelibrary.wiley.com/doi/10.1002/9783527628698.hgc037/full

Hong, R. Y., Feng, B., Chen, L. L., Liu, G. H., Li, H. Z., Zheng, Y., & Wei, D. G. (2008). Synthesis, characterization and MRI application of dextran-coated Fe3O4 magnetic nanoparticles. *Biochemical Engineering Journal*, *42*(3), 290–300. doi:10.1016/j.bej.2008.07.009

Horozov, T. S., & Binks, B. P. (2006). Particle-stabilized emulsions: a bilayer or a bridging monolayer? *Angewandte Chemie*, *45*(5), 787–790. doi:10.1002/ange.200503131

Hosseinian, A., Rezaei, H., & Mahjoub, A. (2011). Preparation of Nanosized Iron Oxide and their Photocatalytic Properties for Congo Red. *World Acedemy of Science, Engineering and Technology*, *52*, 736–739. Retrieved from http://waset.org/journals/waset/v52/v52-144.pdf

http://www.nano.gov/about-nni/what/funding. (n.d.). ,NNI Budget,. *Last accessed 7/22/2013*. Retrieved from http://www.nano.gov/about-nni/what/funding

Hu, F., Jia, Q., Li, Y., & Gao, M. (2011). Facile synthesis of ultrasmall PEGylated iron oxide nanoparticles for dual-contrast T(1)- and T(2)-weighted magnetic resonance imaging. *Nanotechnology*, *22*(24), 245604. doi:10.1088/0957-4484/22/24/245604

Hurst, K., & Ansari, N. (2011). Self-assembled monolayer-immobilized gold nanoparticles as durable, anti-stiction coatings for MEMS. *… Systems, Journal of*, *20*(2), 424–435. Retrieved from http://ieeexplore.ieee.org/xpls/abs_all.jsp?arnumber=5721757

Hurst, K. M., Roberts, C. B., & Ashurst, W. R. (2011). Characterization of gas-expanded liquid-deposited gold nanoparticle films on substrates of varying surface energy. *Langmuir : The ACS Journal of Surfaces and Colloids*, *27*(2), 651–5. doi:10.1021/la1041629

Hyeon, T., Lee, S. S., Park, J., Chung, Y., & Na, H. B. (2001). Synthesis of highly crystalline and monodisperse maghemite nanocrystallites without a size-selection process. *Journal of the American Chemical Society*, *123*(51), 12798–801. Retrieved from http://www.ncbi.nlm.nih.gov/pubmed/22754999

Iglesia, E. (1997). Design, synthesis, and use of cobalt-based Fischer-Tropsch synthesis catalysts. *Applied Catalysis A: General*, *161*(1-2), 59–78. doi:10.1016/S0926-860X(97)00186-5

Iglesia, E., Reyes, S. C., & Madon, R. J. (1991). Transport-Enhanced a-Olefin Readsorption Pathways in Ru-Catalyzed Hydrocarbon Synthesis, *6*, 238–256.

Iida, H., Nakanishi, T., Takada, H., & Osaka, T. (2006). Preparation of magnetic iron-oxide nanoparticles by successive reduction–oxidation in reverse micelles: Effects of reducing agent and atmosphere. *Electrochimica Acta*, *52*(1), 292–296. doi:10.1016/j.electacta.2006.05.007

Ingram, D. R., Kotsmar, C., Yoon, K. Y., Shao, S., Huh, C., Bryant, S. L., … Johnston, K. P. (2010). Superparamagnetic nanoclusters coated with oleic acid bilayers for stabilization of emulsions of water and oil at low concentration. *Journal of Colloid and Interface Science*, *351*(1), 225–32. doi:10.1016/j.jcis.2010.06.048

Jacobs, G., Das, T. K., Zhang, Y., Li, J., Racoillet, G., & Davis, B. H. (2002). Fischer–Tropsch synthesis: support, loading, and promoter effects on the reducibility of cobalt catalysts. *Applied Catalysis A: General*, *233*(1-2), 263–281. doi:10.1016/S0926-860X(02)00195-3

Jain, T. K., Morales, M. a, Sahoo, S. K., Leslie-Pelecky, D. L., & Labhasetwar, V. (2005). Iron oxide nanoparticles for sustained delivery of anticancer agents. *Molecular Pharmaceutics*, *2*(3), 194–205. doi:10.1021/mp0500014

Jana, N., Gearheart, L., & Murphy, C. (2001). Evidence for seed-mediated nucleation in the chemical reduction of gold salts to gold nanoparticles. *Chemistry of Materials*, (26), 2313–2322. Retrieved from http://pubs.acs.org/doi/abs/10.1021/cm000662n

Jana, N. R., Gearheart, L., & Murphy, C. J. (2001). Seeding Growth for Size Control of 5−40 nm Diameter Gold Nanoparticles. *Langmuir*, *17*(22), 6782–6786. doi:10.1021/la0104323

Jana, N. R., Gearheart, L., & Murphy, C. J. (2001). Seed-Mediated Growth Approach for Shape-Controlled Synthesis of Spheroidal and Rod-like Gold Nanoparticles Using a Surfactant Template. *Advanced Materials*, *13*(18), 1389–1393. doi:10.1002/1521-4095(200109)13:18<1389::AID-ADMA1389>3.0.CO;2-F

Jessop, P. G., & Subramaniam, B. (2007). Gas-expanded liquids. *Chemical Reviews*, *107*(6), 2666–94. doi:10.1021/cr040199o

Jin, Y., & Datye, A. (2000). Phase transformations in iron Fischer–Tropsch catalysts during temperature-programmed reduction. *Journal of Catalysis*, *196*(1), 8–17. doi:10.1006/jcat.2000.3024

Jo, J., Aoki, I., & Tabata, Y. (2010). Design of iron oxide nanoparticles with different sizes and surface charges for simple and efficient labeling of mesenchymal stem cells. *Journal of Controlled Release : Official Journal of the Controlled Release Society*, *142*(3), 465–73. doi:10.1016/j.jconrel.2009.11.014

Ju-Nam, Y., & Lead, J. R. (2008). Manufactured nanoparticles: an overview of their chemistry, interactions and potential environmental implications. *The Science of the Total Environment*, *400*(1-3), 396–414. doi:10.1016/j.scitotenv.2008.06.042

Kang, Y., Lee, D., & Stroeve, P. (1998). FTIR and UV-vis spectroscopy studies of Langmuir–Blodgett films of stearic acid/ γ-Fe 2 O 3 nanoparticles. *Thin Solid Films*, *329*, 541–544. Retrieved from http://www.sciencedirect.com/science/article/pii/S0040609098007081

Katepalli, H., John, V. T., & Bose, A. (2013). The response of carbon black stabilized oil-in-water emulsions to the addition of surfactant solutions. *Langmuir : The ACS Journal of Surfaces and Colloids*, *29*(23), 6790–7. doi:10.1021/la400037c

Kebede, A., Singh, A. K., Rai, P. K., Giri, N. K., Rai, A. K., Watal, G., & Gholap, a V. (2013). Controlled synthesis, characterization, and application of iron oxide nanoparticles for oral delivery of insulin. *Lasers in Medical Science*, *28*(2), 579–87. doi:10.1007/s10103-012-1106-3

Kéki, S., Török, J., Deák, G., Daróczi, L., & Zsuga, M. (2000). Silver Nanoparticles by PAMAM-Assisted Photochemical Reduction of Ag(+). *Journal of Colloid and Interface Science*, *229*(2), 550–553. doi:10.1006/jcis.2000.7011

Kelly, K., & Coronado, E. (2003). The optical properties of metal nanoparticles: the influence of size, shape, and dielectric environment. *The Journal of Physical …*, 668–677. Retrieved from http://pubs.acs.org/doi/abs/10.1021/jp026731y

Kelter, P., Michael, M., & Scott, A. (2008). *Chemistry: The Practical Science, Volume 10*. Cengage Learning.

Keyvanloo, K., & Mardkhe, M. (2014). Supported Iron Fischer–Tropsch Catalyst: Superior Activity and Stability Using a Thermally Stable Silica-Doped Alumina Support. *ACS Catalysis*. Retrieved from http://pubs.acs.org/doi/abs/10.1021/cs401242d

Khedr, M. H., Abdel Halim, K. S., & Soliman, N. K. (2009). Synthesis and photocatalytic activity of nano-sized iron oxides. *Materials Letters*, *63*(6-7), 598–601. doi:10.1016/j.matlet.2008.11.050

Kim, D. K., Mikhaylova, M., Zhang, Y., & Muhammed, M. (2003). Protective Coating of Superparamagnetic Iron Oxide Nanoparticles. *Chemistry of Materials*, *15*(8), 1617–1627. doi:10.1021/cm021349j

Kim, D. K., Zhang, Y., Voit, W., Rao, K. V., & Muhammed, M. (2001). Synthesis and characterization of surfactant-coated superparamagnetic monodispersed iron oxide nanoparticles. *Journal of Magnetism and Magnetic Materials*, *225*(1-2), 30–36. doi:10.1016/S0304-8853(00)01224-5

Kimling, J., Maier, M., Okenve, B., Kotaidis, V., Ballot, H., & Plech, a. (2006). Turkevich method for gold nanoparticle synthesis revisited. *The Journal of Physical Chemistry. B*, *110*(32), 15700–7. doi:10.1021/jp061667w

Kittel, C. (1946). Theory of the structure of ferromagnetic domains in films and small particles. *Physical Review*, *70*(1932). Retrieved from http://prola.aps.org/abstract/PR/v70/i11-12/p965_1

Klačanová, K., Fodran, P., & Šimon, P. (2013). Formation of Fe (0)-Nanoparticles via Reduction of Fe (II) Compounds by Amino Acids and Their Subsequent Oxidation to Iron Oxides. *Journal of Chemistry*, *2013*. doi:10.1155/2013/961629

Kodama, R. (1999). Magnetic nanoparticles. *Journal of Magnetism and Magnetic Materials*, *200*(1-3), 359–372. doi:10.1016/S0304-8853(99)00347-9

Kokelaar, J., Garritsen, J., & Prins, A. (1995). Surface rheological properties of sodium stearoyl-2-lactylate (SSL) and diacetyl tartaric esters of mono (and di) glyceride (DATEM) surfactants after a mechanical surface treatment in relation to their bread improving abilities. *Colloids and Surfaces A: Physicochemical and Engineering Aspects*, *95*(1), 69–77. Retrieved from http://www.sciencedirect.com/science/article/pii/092777579403009O

Kowalczyk, B., Lagzi, I., & Grzybowski, B. a. (2011). Nanoseparations: Strategies for size and/or shape-selective purification of nanoparticles. *Current Opinion in Colloid & Interface Science*, *16*(2), 135–148. doi:10.1016/j.cocis.2011.01.004

Kuipers, E. (1995). Chain Length Dependence of α-Olefin Readsorption in Fischer-Tropsch Synthesis. *Journal of Catalysis*, *152*(1), 137–146. doi:10.1006/jcat.1995.1068

Kuipers, E. W., Scheper, C., Wilson, J. H., Vinkenburg, I. H., & Oosterbeek, H. (1996). Non-ASF Product Distributions Due to Secondary Reactions during Fischer – Tropsch Synthesis, *300*(158), 288–300.

Kurukji, D., Pichot, R., Spyropoulos, F., & Norton, I. T. (2013). Interfacial behaviour of sodium stearoyllactylate (SSL) as an oil-in-water pickering emulsion stabiliser.

Journal of Colloid and Interface Science, *409*, 88–97. doi:10.1016/j.jcis.2013.07.016

Kwak, B. (2005). Synthesis of MRI contrast agent by coating superparamagnetic iron oxide with chitosan. *IEEE Transactions on Magnetics*, *41*(10), 4102–4104. doi:10.1109/TMAG.2005.855338

Laan, G. P. Van Der, & Beenackers, A. A. C. M. (1999). Kinetics and Selectivity of the Fischer – Tropsch Synthesis : A Literature Review, (731844027). doi:10.1081/CR-100101170

Lamb, J., Hentz, K., Schmitt, D., Tran, N., Jonker, D., & Junker, K. (2010). A one-year oral toxicity study of sodium stearoyl lactylate (SSL) in rats. *Food and Chemical Toxicology : An International Journal Published for the British Industrial Biological Research Association*, *48*(10), 2663–9. doi:10.1016/j.fct.2010.06.037

Lan, Q., Liu, C., Yang, F., Liu, S., Xu, J., & Sun, D. (2007). Synthesis of bilayer oleic acid-coated Fe3O4 nanoparticles and their application in pH-responsive Pickering emulsions. *Journal of Colloid and Interface Science*, *310*(1), 260–9. doi:10.1016/j.jcis.2007.01.081

Larkin, P. (2011). *Infrared and Raman spectroscopy; principles and spectral interpretation*. Elsevier. Retrieved from http://books.google.com/books?hl=en&lr=&id=KPyV1DRMRbwC&oi=fnd&pg=PP2&dq=Infrared+and+Raman+Spectroscopy%3B+Principles+and+Spectral+Interpretation&ots=cAfKBEYGN6&sig=QRAMBq97Ysl0HJTi_jbgGwbt9ZE

Latham, A. H., Freitas, R. S., Schiffer, P., & Williams, M. E. (2005). Capillary magnetic field flow fractionation and analysis of magnetic nanoparticles. *Analytical Chemistry*, *77*(15), 5055–62. doi:10.1021/ac050611f

Laurent, S., Forge, D., Port, M., Roch, A., Robic, C., Vander Elst, L., & Muller, R. N. (2008). Magnetic iron oxide nanoparticles: synthesis, stabilization, vectorization, physicochemical characterizations, and biological applications. *Chemical Reviews*, *108*(6), 2064–110. doi:10.1021/cr068445e

Lee, H.-J., Ghanta, M., Busch, D. H., & Subramaniam, B. (2010). Toward a CO2-free ethylene oxide process: Homogeneous ethylene oxide in gas-expanded liquids. *Chemical Engineering Science*, *65*(1), 128–134. doi:10.1016/j.ces.2009.02.008

Lee, S.-Y., & Harris, M. T. (2006). Surface modification of magnetic nanoparticles capped by oleic acids: characterization and colloidal stability in polar solvents. *Journal of Colloid and Interface Science*, *293*(2), 401–8. doi:10.1016/j.jcis.2005.06.062

Lee, Y., Lee, J., Bae, C. J., Park, J.-G., Noh, H.-J., Park, J.-H., & Hyeon, T. (2005). Large-Scale Synthesis of Uniform and Crystalline Magnetite Nanoparticles Using Reverse Micelles as Nanoreactors under Reflux Conditions. *Advanced Functional Materials*, *15*(3), 503–509. doi:10.1002/adfm.200400187

Leitner, W. (2002). Supercritical carbon dioxide as a green reaction medium for catalysis. *Accounts of Chemical Research*, *35*(9), 746–56. Retrieved from http://www.ncbi.nlm.nih.gov/pubmed/12234204

Li, J., Rodrigues, M., Matos, H. a., & Gomes de Azevedo, E. (2005). VLE of Carbon Dioxide/Ethanol/Water: Applications to Volume Expansion Evaluation and Water Removal Efficiency. *Industrial & Engineering Chemistry Research*, *44*(17), 6751–6759. doi:10.1021/ie050075h

Li, J., & Stöver, H. D. H. (2008). Doubly pH-responsive pickering emulsion. *Langmuir : The ACS Journal of Surfaces and Colloids*, *24*(23), 13237–40. doi:10.1021/la802619m

Li, J., Wu, J., Zhang, X., Liu, Y., Zhou, D., Sun, H., … Yang, B. (2011). Controllable Synthesis of Stable Urchin-like Gold Nanoparticles Using Hydroquinone to Tune the Reactivity of Gold Chloride. *The Journal of Physical Chemistry C*, *115*(9), 3630–3637. doi:10.1021/jp1119074

Lim, J., Yeap, S. P., Che, H. X., & Low, S. C. (2013). Characterization of magnetic nanoparticle by dynamic light scattering. *Nanoscale Research Letters*, *8*(1), 381. doi:10.1186/1556-276X-8-381

Lin, K.-Y. A., Yang, H., Petit, C., & Lee, W. (2015). Magnetically controllable Pickering emulsion prepared by a reduced graphene oxide-iron oxide composite. *Journal of Colloid and Interface Science*, *438*, 296–305. doi:10.1016/j.jcis.2014.10.015

Liu, F., & Tang, C.-H. (2013). Soy protein nanoparticle aggregates as pickering stabilizers for oil-in-water emulsions. *Journal of Agricultural and Food Chemistry*, *61*(37), 8888–98. doi:10.1021/jf401859y

Liu, F., & Wei, G. (2004). Effect of mobile-phase additives on separation of gold nanoparticles by size-exclusion chromatography. *Chromatographia*, 115–119. doi:10.1365/s10337-003-0135-2

Liu, J., Duggan, J. N., Morgan, J., & Roberts, C. B. (2012). Seed-mediated growth and manipulation of Au nanorods via size-controlled synthesis of Au seeds. *Journal of Nanoparticle Research*, *14*(12), 1289. doi:10.1007/s11051-012-1289-3

Liu, J., He, F., Durham, E., Zhao, D., & Roberts, C. B. (2008). Polysugar-stabilized Pd nanoparticles exhibiting high catalytic activities for hydrodechlorination of

environmentally deleterious trichloroethylene. *Langmuir : The ACS Journal of Surfaces and Colloids*, *24*(1), 328–36. doi:10.1021/la702731h

Liu, J., He, F., Gunn, T. M., Zhao, D., & Roberts, C. B. (2009). Precise seed-mediated growth and size-controlled synthesis of palladium nanoparticles using a green chemistry approach. *Langmuir : The ACS Journal of Surfaces and Colloids*, *25*(12), 7116–28. doi:10.1021/la900228d

Lodhia, J., Mandarano, G., Ferris, N., Eu, P., & Cowell, S. (2010). Development and use of iron oxide nanoparticles (Part 1): Synthesis of iron oxide nanoparticles for MRI. *Biomedical Imaging and Intervention Journal*, *6*(2). doi:10.2349/biij.6.2.e12

Lu, A.-H., Salabas, E. L., & Schüth, F. (2007). Magnetic nanoparticles: synthesis, protection, functionalization, and application. *Angewandte Chemie (International Ed. in English)*, *46*(8), 1222–44. doi:10.1002/anie.200602866

Lu, Y., Lu, X., Mayers, B. T., Herricks, T., & Xia, Y. (2008). Synthesis and characterization of magnetic Co nanoparticles: A comparison study of three different capping surfactants. *Journal of Solid State Chemistry*, *181*(7), 1530–1538. doi:10.1016/j.jssc.2008.02.016

Mahajan, D., Gütlich, P., & Ensling, J. (2003). Evaluation of nanosized iron in slurry-phase Fischer-Tropsch synthesis. *Energy & Fuels*, *17*, 1210–1221. Retrieved from http://pubs.acs.org/doi/abs/10.1021/ef0300343

Maity, D., & Agrawal, D. C. (2007). Synthesis of iron oxide nanoparticles under oxidizing environment and their stabilization in aqueous and non-aqueous media. *Journal of Magnetism and Magnetic Materials*, *308*(1), 46–55. doi:10.1016/j.jmmm.2006.05.001

Manna, A., Chen, P.-L., Akiyama, H., Wei, T.-X., Tamada, K., & Knoll, W. (2003). Optimized Photoisomerization on Gold Nanoparticles Capped by Unsymmetrical Azobenzene Disulfides. *Chemistry of Materials*, *15*(1), 20–28. doi:10.1021/cm0207696

Manna, A., Imae, T., Yogo, T., Aoi, K., & Okazaki, M. (2002). Synthesis of Gold Nanoparticles in a Winsor II Type Microemulsion and Their Characterization. *Journal of Colloid and Interface Science*, *256*(2), 297–303. doi:10.1006/jcis.2002.8691

Martin, J. E., Wilcoxon, J. P., Odinek, J., & Provencio, P. (2000). Control of the Interparticle Spacing in Gold Nanoparticle Superlattices. *The Journal of Physical Chemistry B*, *104*(40), 9475–9486. doi:10.1021/jp001292t

Mayo, J. T., Yavuz, C., Yean, S., Cong, L., Shipley, H., Yu, W., … Colvin, V. L. (2007). The effect of nanocrystalline magnetite size on arsenic removal. *Science and Technology of Advanced Materials*, *8*(1-2), 71–75. doi:10.1016/j.stam.2006.10.005

McLeod, M. C., Anand, M., Kitchens, C. L., & Roberts, C. B. (2005). Precise and rapid size selection and targeted deposition of nanoparticle populations using CO2 gas expanded liquids. *Nano Letters*, *5*(3), 461–5. doi:10.1021/nl047966j

McLeod, M. C., Kitchens, C. L., & Roberts, C. B. (2005). CO2-expanded liquid deposition of ligand-stabilized nanoparticles as uniform, wide-area nanoparticle films. *Langmuir : The ACS Journal of Surfaces and Colloids*, *21*(6), 2414–8. doi:10.1021/la047576c

Melle, S., Lask, M., & Fuller, G. G. (2005). Pickering emulsions with controllable stability. *Langmuir : The ACS Journal of Surfaces and Colloids*, *21*(6), 2158–62. doi:10.1021/la047691n

Meshram, P., & Jadhav, S. (2012). Preparation and Properties of Lactic Acid-based Modified Carboxylic Surfactant. *Journal of Surface Science and Technology*, *28*(3), 149–161. Retrieved from http://issstindian.org/pubpdf/voiume28/art-5.pdf

Moeser, G. D., Roach, K. a., Green, W. H., Alan Hatton, T., & Laibinis, P. E. (2004). High-gradient magnetic separation of coated magnetic nanoparticles. *AIChE Journal*, *50*(11), 2835–2848. doi:10.1002/aic.10270

Mokrani, T., & Scurrell, M. (2009). *Gas Conversion to Liquid Fuels and Chemicals: The Methanol Route Catalysis and Processes Development*. *Catalysis Reviews* (Vol. 51). doi:10.1080/01614940802477524

Morales, M. A., Jain, T. K., Labhasetwar, V., & Leslie-Pelecky, D. L. (2005). Magnetic studies of iron oxide nanoparticles coated with oleic acid and Pluronic® block copolymer. *Journal of Applied Physics*, *97*(10), 10Q905. doi:10.1063/1.1850855

Morales, M., Finotelli, P., Coaquira, J., Rochaleao, M., Diazaguila, C., Baggiosaitovitch, E., & Rossi, a. (2008). In situ synthesis and magnetic studies of iron oxide nanoparticles in calcium-alginate matrix for biomedical applications. *Materials Science and Engineering: C*, *28*(2), 253–257. doi:10.1016/j.msec.2006.12.016

Murray, C., Norris, D., & Bawendi, M. (1993). Synthesis and characterization of nearly monodisperse CdE (E= sulfur, selenium, tellurium) semiconductor nanocrystallites. *Journal of the American …*, (4), 8706–8715. Retrieved from http://pubs.acs.org/doi/abs/10.1021/ja00072a025

Murray, C.B. Kagan, C. R., Bawendi, M. G., & Murray, C. (2000). Synthesis and characterization of monodisperse nanocrystals and close-packed nanocrystal

assemblies. *Annual Review of Materials …*, 545–610. Retrieved from http://www.annualreviews.org/doi/pdf/10.1146/annurev.matsci.30.1.545

Mutelet, F., Sup, E. N., Chimiques, I., Polyphas, M., Grandville, R., Vitu, S., … Jaubert, J.-N. (2005). Solubility of CO2 in branched alkanes in order to extend the PPR78 model (predictive 1978, Peng–Robinson EOS with temperature-dependent kij calculated through a group contribution method) to such systems. *Fluid Phase Equilibria*, *238*(2), 157–168. doi:10.1016/j.fluid.2005.10.001

Nagarajan, R., & Hatton, T. (2008). *Nanoparticles: synthesis, stabilization, passivation, and functionalization*. Retrieved from http://scholar.google.com/scholar?hl=en&btnG=Search&q=intitle:Nanoparticles:+synthesis,+stabilization,+passivation,+and+functionalization#0

Nakamoto, K. (1997a). *Infrared and Raman Spectra of Inorganic and Coordination Compounds: Part A: Theory and Applications in Inorganic Chemistry* (Fifth Edit.). John Wiley & Sons.

Nakamoto, K. (1997b). *Infrared and Raman Spectra of Inorganic and Coordination Compounds: Part B: Applications in Coordination, Organometallic, and Bioinorganic Chemistry* (Fifth Edit.). John Wiley & Sons.

Nakhaei Pour, A., Housaindokht, M. R., Behroozsarand, A., & Khodagholi, M. A. (2013). Thermodynamic analysis of nanoparticle size effect on kinetics in Fischer–Tropsch synthesis by lanthanum promoted iron catalyst. *Applied Physics A*. doi:10.1007/s00339-013-8156-7

Nakhaei Pour, A., Housaindokht, M. R., Irani, M., & Kamali Shahri, S. M. (2014). Size-dependent studies of Fischer–Tropsch synthesis on iron based catalyst: New kinetic model. *Fuel*, *116*, 787–793. doi:10.1016/j.fuel.2013.08.080

Nativo, P., Prior, I. a, & Brust, M. (2008). Uptake and intracellular fate of surface-modified gold nanoparticles. *ACS Nano*, *2*(8), 1639–44. doi:10.1021/nn800330a

Niemantsverdriet, J., & van der Kraan, A. M. (1980). Behaviour of catalysts during Fischer-Tropsch synthesis studied with Moessbauer spectroscopy, x-ray diffraction, carbon content determination, and reaction kinetic measurements. *The Journal of Physical Chemistry*, *84*(25), 3363–3370. Retrieved from http://pubs.acs.org/doi/abs/10.1021/j100462a011

Niemantsverdriet, J. W., van der Kraan, A. M., Van Dijk, W. L., & van der baan, H. S. (1980). Behaviour of catalysts during Fischer-Tropsch synthesis studied with Mossbauer spectroscopy, x-ray diffraction, carbon content determination, and reaction kinetic measurements. *The Journal of Physical Chemistry*, *84*(25), 3363–3370.

Novak, J. P., Nickerson, C., Franzen, S., & Feldheim, D. L. (2001). Purification of molecularly bridged metal nanoparticle arrays by centrifugation and size exclusion chromatography. *Analytical Chemistry*, *73*(23), 5758–5761. Retrieved from http://pubs.acs.org/doi/abs/10.1021/ac010812t

Noyori, R. (1999). Supercritical Fluids: Introduction. *Chemical Reviews*, *99*(2), 353–354. Retrieved from http://www.ncbi.nlm.nih.gov/pubmed/19354029

O'Brien, R. J., Xu, L., Bao, S., Raje, A., & Davis, B. H. (2000). Activity, selectivity and attrition characteristics of supported iron Fischer–Tropsch catalysts. *Applied Catalysis A: General*, *196*(2), 173–178. doi:10.1016/S0926-860X(99)00462-7

Orbell, J. D., Dao, H. V., Ngeh, L. N., & Bigger, S. W. (2007). Magnetic particle technology in environmental remediation and wildlife rehabilitation. *The Environmentalist*, *27*(1), 175–182. doi:10.1007/s10669-007-9026-7

Orbell, J. D., Godhino, L., Bigger, S. W., Nguyen, T. M., & Ngeh, L. N. (1997). Oil Spill Remediation Using Magnetic Particles: An Experiment in Environmental Technology. *Journal of Chemical Education*, *74*(12), 1446. doi:10.1021/ed074p1446

Oszwałdowski, S., Zawistowska-Gibuła, K., & Roberts, K. P. (2011). Capillary electrophoretic separation of nanoparticles. *Analytical and Bioanalytical Chemistry*, *399*(8), 2831–42. doi:10.1007/s00216-011-4650-y

Palmer, M. V., & Ting, S. S. T. (1995). Applications for supercritical fluid technology in food processing. *Food Chemistry*, *52*(4), 345–352. doi:10.1016/0308-8146(95)93280-5

Pankhurst, Q. A., Connolly, J., Jones, S. K., & Dobson, J. (2003). Applications of magnetic nanoparticles in biomedicine. *Journal of Physics D: Applied Physics*, *36*(13), R167. doi:10.1088/0022-3727/36/13/201

Park, J.-G. J. J.-H., Lee, E., Hwang, N.-M., Kang, M., Kim, S. C., Hwang, Y., … Hyeon, T. (2005). One-Nanometer-Scale Size-Controlled Synthesis of Monodisperse Magnetic Iron Oxide Nanoparticles. *Angewandte Chemie*, *117*(19), 2932–2937. doi:10.1002/ange.200461665

Park, J.-Y., Lee, Y.-J., Khanna, P. K., Jun, K.-W., Bae, J. W., & Kim, Y. H. (2010). Alumina-supported iron oxide nanoparticles as Fischer–Tropsch catalysts: Effect of particle size of iron oxide. *Journal of Molecular Catalysis A: Chemical*, *323*(1-2), 84–90. doi:10.1016/j.molcata.2010.03.025

Paulini, R., Frankamp, B., & Rotello, V. (2002). Effects of branched ligands on the structure and stability of monolayers on gold nanoparticles. *Langmuir*, (13), 2368–2373. Retrieved from http://pubs.acs.org/doi/abs/10.1021/la0155395

Pike, C. R., Roberts, A. P., & Verosub, K. L. (1999). Characterizing interactions in fine magnetic particle systems using first order reversal curves. *Journal of Applied Physics*, *85*(9), 6660. doi:10.1063/1.370176

Poole Jr., C. P., & Owens, F. (2003). *Introduction to Nanotechnology*. Hoboken, NJ: Wiley- Interscience: Retrieved from http://books.google.com/books?hl=en&lr=&id=XfzgEoY9SNkC&oi=fnd&pg=PR11&dq=Introduction+to+Nanotechnology&ots=rM-0sejdwj&sig=FVtoPDwGy-SOMBd4HT77KjNwt2U

Prakash, A., Zhu, H., Jones, C. J., Benoit, D. N., Ellsworth, A. Z., Bryant, E. L., & Colvin, V. L. (2009). Bilayers as phase transfer agents for nanocrystals prepared in nonpolar solvents. *ACS Nano*, *3*(8), 2139–46. doi:10.1021/nn900373b

Predoi, D. (2007). A study on iron oxide nanoparticles coated with dextrin obtained by coprecipitation. *Dig J Nanomater Biostruct*, *2*(1), 169–173. Retrieved from http://www.chalcogen.ro/Predoi-DJNB2.pdf

Qiao, R., Yang, C., & Gao, M. (2009). Superparamagnetic iron oxide nanoparticles: from preparations to in vivo MRI applications. *Journal of Materials Chemistry*, *19*(35), 6274. doi:10.1039/b902394a

Qiao, X., Zhou, J., Binks, B. P., Gong, X., & Sun, K. (2012). Magnetorheological behavior of Pickering emulsions stabilized by surface-modified Fe3O4 nanoparticles. *Colloids and Surfaces A: Physicochemical and Engineering Aspects*, *412*, 20–28. doi:10.1016/j.colsurfa.2012.06.026

Rajeshwar, K., & de Tacconi, N. R. (2009). Solution combustion synthesis of oxide semiconductors for solar energy conversion and environmental remediation. *Chemical Society Reviews*, *38*(7), 1984–98. doi:10.1039/b811238j

Rao, C., Müller, A., & Cheetham, A. (2006). *The Chemistry of Nanomaterials: Synthesis, Properties and Applications*. John Wiley & Sons.

Rao, C. N. R., Kulkarni, G. U., Thomas, P. J., & Edwards, P. P. (2002). Size-dependent chemistry: properties of nanocrystals. *Chemistry (Weinheim an Der Bergstrasse, Germany)*, *8*(1), 28–35. Retrieved from http://www.ncbi.nlm.nih.gov/pubmed/11826864

Regalbuto, J. (Ed.). (2006). *Catalyst preparation: science and engineering*. CRC Press.

Rheinländer, T., & Kötitz, R. (2000). Different methods for the fractionation of magnetic fluids. *Colloid & Polymer …*, *263*, 259–263. Retrieved from http://www.springerlink.com/index/8YY20MM232YHHP41.pdf

Roberts, C. B., & Elbashir, N. O. (2003). An overview to "Advances in C1 chemistry in the year 2002." *Fuel Processing Technology*, *83*(1-3), 1–9. doi:10.1016/S0378-3820(03)00081-X

Rodr, D. F., & Klerk, A. De. (n.d.). Improving the Interface between Fischer − Tropsch Synthesis and Re fi ning, (Figure 1).

Rofer-DePoorter, C. (1981). A comprehensive mechanism for the Fischer-Tropsch synthesis. *Chemical Reviews*, 447–474. Retrieved from http://pubs.acs.org/doi/pdf/10.1021/cr00045a002

Rotello, V. (2004). *Nanoparticles: Building Blocks for Nanotechnology*. Springer.

Saha, A., Nikova, A., Venkataraman, P., John, V. T., & Bose, A. (2013). Oil Emulsification Using Surface-Tunable Carbon Black Particles. *ACS Applied Materials & Interfaces*, *5*(8), 3094–3100. Retrieved from http://pubs.acs.org/doi/full/10.1021/am3032844

Sahoo, Y., Pizem, H., Fried, T., & Golodnitsky, D. (2001). Alkyl phosphonate/phosphate coating on magnetite nanoparticles: a comparison with fatty acids. *Langmuir*, (23), 7907–7911. Retrieved from http://pubs.acs.org/doi/abs/10.1021/la010703+

Sassiat, P. R., Mourier, P., Caude, M. H., & Rosset, R. H. (1987). Measurement of diffusion coefficients in supercritical carbon dioxide and correlation with the equation of Wilke and Chang. *Analytical Chemistry*, *59*(8), 1164–1170. doi:10.1021/ac00135a020

Saunders, S. R., Eden, M. R., & Roberts, C. B. (2011). Modeling the Precipitation of Polydisperse Nanoparticles Using a Total Interaction Energy Model. *The Journal of Physical Chemistry C*, *115*(11), 4603–4610. doi:10.1021/jp200116a

Saunders, S. R., & Roberts, C. B. (2009). Size-selective fractionation of nanoparticles at an application scale using CO2 gas-expanded liquids. *Nanotechnology*, *20*(47), 475605. doi:10.1088/0957-4484/20/47/475605

Saunders, S. R., & Roberts, C. B. (2011). Tuning the Precipitation and Fractionation of Nanoparticles in Gas-Expanded Liquid Mixtures. *The Journal of Physical Chemistry C*, *115*(20), 9984–9992. doi:10.1021/jp2019878

Saunders, S. R., & Roberts, C. B. (2012). Nanoparticle separation and deposition processing using gas expanded liquid technology. *Current Opinion in Chemical Engineering*, *1*, 1–11. doi:10.1016/j.coche.2011.12.004

Scurto, A. M., Hutchenson, K., & Subramaniam, B. (2009). Gas-Expanded Liquids: Fundamentals and Applications. *Symposium A Quarterly Journal In Modern*

Foreign Literatures, 3–37. Retrieved from http://pubs.acs.org/doi/abs/10.1021/bk-2009-1006.ch001

Selin, C. (2007). Expectations and the Emergence of Nanotechnology. *Science, Technology & Human Values*, *32*(2), 196–220. Retrieved from http://sth.sagepub.com/content/32/2/196.short

Shah, P. S., Hanrath, T., Johnston, K. P., & Korgel, B. a. (2004). Nanocrystal and Nanowire Synthesis and Dispersibility in Supercritical Fluids. *The Journal of Physical Chemistry B*, *108*(28), 9574–9587. doi:10.1021/jp049827w

Shah, P. S., Holmes, J. D., Johnston, K. P., & Korgel, B. a. (2002). Size-Selective Dispersion of Dodecanethiol-Coated Nanocrystals in Liquid and Supercritical Ethane by Density Tuning. *The Journal of Physical Chemistry B*, *106*(10), 2545–2551. doi:10.1021/jp013931l

Shen, L., Laibinis, P. E. P., & Hatton, T. A. T. (1999). Bilayer Surfactant Stabilized Magnetic Fluids: Synthesis and Interactions at Interfaces. *Langmuir*, *15*(11), 447–453. doi:10.1021/la9807661

Shen, L., Stachowiak, A., Fateen, S.-E. K., Laibinis, P. E., & Hatton, T. A. (2001). Structure of Alkanoic Acid Stabilized Magnetic Fluids. A Small-Angle Neutron and Light Scattering Analysis. *Langmuir*, *17*(2), 288–299. doi:10.1021/la9916732

Shi, B., & Davis, B. H. (2005). Fischer–Tropsch synthesis: The paraffin to olefin ratio as a function of carbon number. *Catalysis Today*, *106*(1-4), 129–131. doi:10.1016/j.cattod.2005.07.159

Shukla, C., & Hallett, J. (2006). Molecular dynamics simulation of the cybotactic region in gas-expanded methanol-carbon dioxide and acetone-carbon dioxide mixtures. *The Journal of …*, *110*(47), 24101–11. doi:10.1021/jp0648947

Shukla, N., Liu, C., Jones, P. M., & Weller, D. (2003). FTIR study of surfactant bonding to FePt nanoparticles. *Journal of Magnetism and Magnetic Materials*, *266*(1-2), 178–184. doi:10.1016/S0304-8853(03)00469-4

Siebrands, T., Giersig, M., Mulvaney, P., & Fischer, C. H. (1993). Steric exclusion chromatography of nanometer-sized gold particles. *Langmuir*, *9*(9), 2297–2300. doi:10.1021/la00033a009

Sigman, M. B., Saunders, A. E., & Korgel, B. A. (2004). Metal nanocrystal superlattice nucleation and growth. *Langmuir*, *20*(3), 978–983. doi:Doi 10.1021/La035405m

Sih, R., Armenti, M., Mammucari, R., Dehghani, F., & Foster, N. R. (2008). Viscosity measurements on saturated gas-expanded liquid systems—Ethanol and carbon

dioxide. *The Journal of Supercritical Fluids*, *43*(3), 460–468. doi:10.1016/j.supflu.2007.08.001

Sih, R., Dehghani, F., & Foster, N. R. (2007). Viscosity measurements on gas expanded liquid systems—Methanol and carbon dioxide. *The Journal of Supercritical Fluids*, *41*(1), 148–157. doi:10.1016/j.supflu.2006.09.002

Smith, B. (1998). *Infrared spectral interpretation: a systematic approach*. CRC Press. Retrieved from http://books.google.com/books?hl=en&lr=&id=Ywzf4GyoUaoC&oi=fnd&pg=PA1&dq=Infrared+Spectral+Interpretation:+A+Systematic+Approach&ots=C3WKG61FGd&sig=zW1m0waWpA1it3A_9Y040WwQSNY

Snel, R. (1989). Supported iron catalysts in Fischer-Tropsch synthesis: influence of the preparation method. *Industrial & Engineering Chemistry Research*, 654–659. Retrieved from http://pubs.acs.org/doi/pdf/10.1021/ie00090a002

Song, I., Spuller, M., Levitin, G., & Hess, D. W. (2006). Photoresist and Residue Removal Using Gas-Expanded Liquids. *Journal of The Electrochemical Society*, *153*(4), G314. doi:10.1149/1.2171824

Sovilj, V., Milanovic, J., & Petrovic, L. (2013). Influence of gelatin–sodium stearoyl lactylate interaction on the rheological properties of gelatin gels. *Colloids and Surfaces A: Physicochemical and Engineering Aspects*, *417*, 211–216. doi:10.1016/j.colsurfa.2012.11.009

Spatz, J., Mößmer, S., & Möller, M. (2006). Mineralization of gold nanoparticles in a block copolymer microemulsion. *Chemistry-A European Journal*, (731), 1552–1555. Retrieved from http://onlinelibrary.wiley.com/doi/10.1002/chem.19960021213/abstract

Stiller, S., Gers-Barlag, H., Lergenmueller, M., Pflücker, F., Schulz, J., Wittern, K. P., & Daniels, R. (2004). Investigation of the stability in emulsions stabilized with different surface modified titanium dioxides. *Colloids and Surfaces A: Physicochemical and Engineering Aspects*, *232*(2-3), 261–267. doi:10.1016/j.colsurfa.2003.11.003

Subramaniam, B. (2010). Gas-expanded liquids for sustainable catalysis and novel materials: Recent advances. *Coordination Chemistry Reviews*, *254*(15-16), 1843–1853. doi:10.1016/j.ccr.2009.12.009

Subramaniam, B., Rajewski, R. a, & Snavely, K. (1997). Pharmaceutical processing with supercritical carbon dioxide. *Journal of Pharmaceutical Sciences*, *86*(8), 885–90. doi:10.1021/js9700661

Sullivan, A. P., & Kilpatrick, P. K. (2002). The Effects of Inorganic Solid Particles on Water and Crude Oil Emulsion Stability. *Industrial & Engineering Chemistry Research*, *41*(14), 3389–3404. doi:10.1021/ie010927n

Sun, J., Zhou, S., Hou, P., & Yang, Y. (2007). Synthesis and characterization of biocompatible Fe3O4 nanoparticles. *Journal of Biomedical …*, 2–10. doi:10.1002/jbm.a

Sun, S. (2000). Monodisperse FePt Nanoparticles and Ferromagnetic FePt Nanocrystal Superlattices. *Science*, *287*(5460), 1989–1992. doi:10.1126/science.287.5460.1989

Sun, S., & Zeng, H. (2002). Size-Controlled Synthesis of Magnetite Nanoparticles. *Journal of the American Chemical Society*, *124*(28), 8204–8205. doi:10.1021/ja026501x

Sun, X., Tabakman, S. M., Seo, W.-S., Zhang, L., Zhang, G., Sherlock, S., … Dai, H. (2009). Separation of nanoparticles in a density gradient: FeCo@C and gold nanocrystals. *Angewandte Chemie (International Ed. in English)*, *48*(5), 939–42. doi:10.1002/anie.200805047

Sun, Y., & Xia, Y. (2002). Shape-controlled synthesis of gold and silver nanoparticles. *Science*, *298*(5601), 2176–9. doi:10.1126/science.1077229

Sun, Y.-P., Li, X., Cao, J., Zhang, W., & Wang, H. P. (2006). Characterization of zero-valent iron nanoparticles. *Advances in Colloid and Interface Science*, *120*(1-3), 47–56. doi:10.1016/j.cis.2006.03.001

Surugau, N., & Urban, P. L. (2009). Electrophoretic methods for separation of nanoparticles. *Journal of Separation Science*, *32*(11), 1889–906. doi:10.1002/jssc.200900071

Tancrède, P., Patterson, D., & Bothorel, P. (1977). Interactions in alkane systems by depolarized Rayleigh scattering and calorimetry. Part 2.-Orientational order in systems containing hexadecane isomers of different. *J. Chem. Soc., Faraday Trans.*, *2*(1), 29–39. Retrieved from http://pubs.rsc.org/en/content/articlepdf/1977/f2/f29777300029

Tartaj, P., Morales, M. a D. P., Veintemillas-Verdaguer, S., Gonz lez-Carre o, T., & Serna, C. J. (2003). The preparation of magnetic nanoparticles for applications in biomedicine. *Journal of Physics D: Applied Physics*, *36*(13), R182–R197. doi:10.1088/0022-3727/36/13/202

Tassa, C., Shaw, S. Y., & Weissleder, R. (2011). Dextran-Coated Iron Oxide Nanoparticles: A Versatile Platform for Targeted Molecular Imaging, Molecular Diagnostics, and Therapy. *Accounts of Chemical Research*, *XXX*(Xx). doi:10.1021/ar200084x

Tegart, G. (2004). Nanotechnology: the technology for the twenty-first century. *Foresight*, *6*(6), 364–370. doi:10.1108/14636680410569948

Teja, A. S., & Koh, P.-Y. (2009). Synthesis, properties, and applications of magnetic iron oxide nanoparticles. *Progress in Crystal Growth and Characterization of Materials*, *55*(1-2), 22–45. doi:10.1016/j.pcrysgrow.2008.08.003

Thorat, A. a., & Dalvi, S. V. (2012). Liquid antisolvent precipitation and stabilization of nanoparticles of poorly water soluble drugs in aqueous suspensions: Recent developments and future perspective. *Chemical Engineering Journal*, *181-182*, 1–34. doi:10.1016/j.cej.2011.12.044

Thorek, D. L. J., Chen, A. K., Czupryna, J., & Tsourkas, A. (2006). Superparamagnetic iron oxide nanoparticle probes for molecular imaging. *Annals of Biomedical Engineering*, *34*(1), 23–38. doi:10.1007/s10439-005-9002-7

Torres Galvis, H. M., Bitter, J. H., Davidian, T., Ruitenbeek, M., Dugulan, A. I., & De Jong, K. P. (2012). Iron particle size effects for direct production of lower olefins from synthesis gas. *Journal of the American Chemical Society*, *134*(39), 16207–16215. doi:10.1021/ja304958u

Torres Galvis, H. M., Bitter, J. H., Khare, C. B., Ruitenbeek, M., Dugulan, a I., & de Jong, K. P. (2012). Supported iron nanoparticles as catalysts for sustainable production of lower olefins. *Science (New York, N.Y.)*, *335*(6070), 835–8. doi:10.1126/science.1215614

Tuchscherer, a, Schaarschmidt, D., Schulze, S., Hietschold, M., & Lang, H. (2012). Gold nanoparticles generated by thermolysis of "all-in-one" gold(I) carboxylate complexes. *Dalton Transactions (Cambridge, England : 2003)*, *41*(9), 2738–46. doi:10.1039/c2dt11748g

Turkevich, J., Stevenson, P., & Hillier, J. (1951). A study of the nucleation and growth processes in the synthesis of colloidal gold. *Discuss. Faraday Soc.*, *55*(c). Retrieved from http://pubs.rsc.org/en/content/articlepdf/1951/df10.1039/df9511100055

Van Der Laan, G. P., & Beenackers, a. a. C. M. (1999). Kinetics and Selectivity of the Fischer–Tropsch Synthesis: A Literature Review. *Catalysis Reviews*, *41*(3-4), 255–318. doi:10.1081/CR-100101170

Van Steen, E., & Prinsloo, F. F. (2002). Comparison of preparation methods for carbon nanotubes supported iron Fischer–Tropsch catalysts. *Catalysis Today*, *71*(3-4), 327–334. doi:10.1016/S0920-5861(01)00459-X

Varadan, V., Chen, L., & Xie, J. (2008). *Nanomedicine: design and applications of magnetic nanomaterials, nanosensors and nanosystems*. John Wiley & Sons. Retrieved from

http://books.google.com/books?hl=en&lr=&id=gKogq_dseX8C&oi=fnd&pg=PR5&dq=Nanomedicine:+Design+and+Applications+of+Magnetic+Nanomaterials,+Nanosensors+and+Nanosystems&ots=lMX2ZjY5Zk&sig=QhXKgvo7_2Lu4rT-6fX8SAzpOek

Vatta, L., Sanderson, R., & Koch, K. (2006). Magnetic nanoparticles: Properties and potential applications. *Pure and Applied Chemistry*, *78*(9), 1793–1801. doi:10.1351/pac200678091801

Vengsarkar, P., & Roberts, C. (2013). Effect of Ligand and Solvent Structure on Size-Selective Nanoparticle Dispersability and Fractionation in Gas Expanded Liquid (GXL) Systems. *The Journal of Physical Chemistry C*, *117*(27), 14362–14373. Retrieved from http://pubs.acs.org/doi/abs/10.1021/jp403670w

Vengsarkar, P. S., & Roberts, C. B. (2014). Solid-stabilized emulsion formation using stearoyl lactylate coated iron oxide nanoparticles. *Journal of Nanoparticle Research*, *16*(10), 2627. doi:10.1007/s11051-014-2627-4

Von White, G., Mohammed, F. S., & Kitchens, C. L. (2011). Small-Angle Neutron Scattering Investigation of Gold Nanoparticle Clustering and Ligand Structure Under Antisolvent Conditions. *The Journal of Physical Chemistry C*, *115*(38), 18397–18405. doi:10.1021/jp112020r

Voorn, D., Ming, W., & Herk, A. Van. (2006). Polymer-clay nanocomposite latex particles by inverse pickering emulsion polymerization stabilized with hydrophobic montmorillonite platelets. *Macromolecules*, 2137–2143. Retrieved from http://pubs.acs.org/doi/abs/10.1021/ma052539t

Walt, H. Van Der, Chown, L., Harris, R., Sosibo, N., & Tshikhudo, R. (2010). Fe3O4 and Fe3O4@ Au Nanoparticles: Synthesis and Functionalisation for Biomolecular Attachment. *World Acedemy of Science, Engineering and Technology*, *4*, 1048–1052. Retrieved from http://waset.org/journals/waset/v44/v44-174.pdf

Wang, C. Y., Hong, J. M., Chen, G., Zhang, Y., & Gu, N. (2010). Facile method to synthesize oleic acid-capped magnetite nanoparticles. *Chinese Chemical Letters*, *21*(2), 179–182. doi:10.1016/j.cclet.2009.10.024

Wang, J., & Shapira, P. (2009). Partnering with universities: a good choice for nanotechnology start-up firms? *Small Business Economics*, *38*(2), 197–215. doi:10.1007/s11187-009-9248-9

Wang, Y., Wong, J. F., Teng, X., Lin, X. Z., & Yang, H. (2003). "Pulling" Nanoparticles into Water: Phase Transfer of Oleic Acid Stabilized Monodisperse Nanoparticles into Aqueous Solutions of α-Cyclodextrin. *Nano Letters*, *3*(11), 1555–1559. doi:10.1021/nl034731j

Wei, G. T., Liu, F. K., & Wang, C. R. (1999). Shape separation of nanometer gold particles by size-exclusion chromatography. *Analytical Chemistry*, *71*(11), 2085–91. doi:10.1021/ac990044u

Wei, Z., Wang, C., Liu, H., Zou, S., & Tong, Z. (2012). Halloysite nanotubes as particulate emulsifier: Preparation of biocompatible drug-carrying PLGA microspheres based on pickering emulsion. *Journal of Applied Polymer Science*, *125*(S1), E358–E368. doi:10.1002/app.36456

White, R. J., Luque, R., Budarin, V. L., Clark, J. H., & Macquarrie, D. J. (2009). Supported metal nanoparticles on porous materials. Methods and applications. *Chemical Society Reviews*, *38*(2), 481–94. doi:10.1039/b802654h

White, G. Von, & Kitchens, C. (2010). Small-angle neutron scattering of silver nanoparticles in gas-expanded hexane. *The Journal of Physical Chemistry C*, 16285–16291. Retrieved from http://pubs.acs.org/doi/abs/10.1021/jp1058808

Whitehurst, R. (Ed.). (2008). *Emulsifiers in Food Technology*. John Wiley & Sons.

Wilson, K., & Lee, A. (2013). *Heterogeneous Catalysts for Clean Technology: Spectroscopy, Design, and Monitoring*. John Wiley & Sons.

Wu, N., Fu, L., Su, M., Aslam, M., Wong, K. C., & Dravid, V. P. (2004). Interaction of Fatty Acid Monolayers with Cobalt Nanoparticles. *Nano Letters*, *4*(2), 383–386. doi:10.1021/nl035139x

Wyatt, V. T., Bush, D., Lu, J., Hallett, J. P., Liotta, C. L., & Eckert, C. a. (2005). Determination of solvatochromic solvent parameters for the characterization of gas-expanded liquids. *The Journal of Supercritical Fluids*, *36*(1), 16–22. doi:10.1016/j.supflu.2005.03.009

Xia, L., Lenaghan, S. C., Zhang, M., Zhang, Z., & Li, Q. (2010). Naturally occurring nanoparticles from English ivy: an alternative to metal-based nanoparticles for UV protection. *Journal of Nanobiotechnology*, *8*, 12. doi:10.1186/1477-3155-8-12

Xie, X., Liotta, C., & Eckert, C. (2004). CO2-catalyzed acetal formation in CO2-expanded methanol and ethylene glycol. *Industrial & Engineering Chemistry …*, (Scheme 2), 2605–2609. Retrieved from http://pubs.acs.org/doi/abs/10.1021/ie034103c

Xu, R., Zhang, S., & Roberts, C. (2013). Mixed Alcohol Synthesis over a K Promoted Cu/ZnO/Al2O3 Catalyst in Supercritical Hexanes. *Industrial & Engineering Chemistry …*. doi:10.1021/ie3024017

Xu, Z., Shen, C., Tian, Y., Shi, X., & Gao, H.-J. (2010). Organic phase synthesis of monodisperse iron oxide nanocrystals using iron chloride as precursor. *Nanoscale*, *2*(6), 1027–32. doi:10.1039/b9nr00400a

Yamamoto, M. (2009). Size-controlled Synthesis of Gold Nanoparticles by Thermolysis of a Gold (I)-Sulfide Complex in the Presence of Alkylamines. *... Für Naturforschung. B, A ...*, (I), 8553. Retrieved from http://znaturforsch.com/rb/s64b1305.pdf

Yang, J., Lee, J., Deivaraj, T., & Too, H. (2004). An improved Brust's procedure for preparing alkylamine stabilized Pt, Ru nanoparticles. *Colloids and Surfaces A: Physicochemical and Engineering Aspects*, *240*(1-3), 131–134. doi:10.1016/j.colsurfa.2004.03.019

Yang, K., Peng, H., Wen, Y., & Li, N. (2010). Re-examination of characteristic FTIR spectrum of secondary layer in bilayer oleic acid-coated Fe3O4 nanoparticles. *Applied Surface Science*, *256*(10), 3093–3097. doi:10.1016/j.apsusc.2009.11.079

Yavuz, C. T., Mayo, J. T., Yu, W. W., Prakash, A., Falkner, J. C., Yean, S., … Colvin, V. L. (2006). Low-field magnetic separation of monodisperse Fe3O4 nanocrystals. *Science (New York, N.Y.)*, *314*(5801), 964–7. doi:10.1126/science.1131475

Yeh, J. T., Pennline, H. W., Resnik, K. P., & Rygle, K. (2005). Semi-batch absorption and regeneration studies for CO2 capture by aqueous ammonia. *Fuel Processing Technology*, *86*(14-15), 1533–1546. doi:10.1016/j.fuproc.2005.01.015

Yu, W. W., Chang, E., Sayes, C. M., Drezek, R., & Colvin, V. L. (2006). Aqueous dispersion of monodisperse magnetic iron oxide nanocrystals through phase transfer. *Nanotechnology*, *17*(17), 4483–4487. doi:10.1088/0957-4484/17/17/033

Yu, W. W., Falkner, J. C., Yavuz, C. T., & Colvin, V. L. (2004). Synthesis of monodisperse iron oxide nanocrystals by thermal decomposition of iron carboxylate salts. *Chemical Communications (Cambridge, England)*, (20), 2306–7. doi:10.1039/b409601k

Zabidi, N. (2010). Synthesis of Nanocatalysts via Reverse Microemulsion Route for Fischer-Tropsch Reactions. *Cdn.intechopen.com*, *2*(2). Retrieved from http://cdn.intechopen.com/pdfs/32558.pdf

Zeigermann, P., & Valiullin, R. (2013). Transport properties of gas-expanded liquids in bulk and under confinement. *The Journal of Supercritical Fluids*, *75*, 43–47. doi:10.1016/j.supflu.2012.12.011

Zhang, J., Han, B., Liu, J., Zhang, X., Liu, Z., & He, J. (2001). A new method to recover the nanoparticles from reverse micelles: recovery of ZnS nanoparticles synthesized

in reverse micelles by compressed CO2. *Chem. Commun.*, (24), 2724–2725. doi:10.1039/b109802k

Zhang, K., Wu, W., Guo, K., Chen, J.-F., & Zhang, P.-Y. (2009). Magnetic polymer enhanced hybrid capsules prepared from a novel Pickering emulsion polymerization and their application in controlled drug release. *Colloids and Surfaces A: Physicochemical and Engineering Aspects*, *349*(1-3), 110–116. doi:10.1016/j.colsurfa.2009.08.005

Zhang, L., He, R., & Gu, H. (2006). Oleic acid coating on the monodisperse magnetite nanoparticles. *Applied Surface Science*, *253*(5), 2611–2617. doi:10.1016/j.apsusc.2006.05.023

Zhang, W. (2003). Nanoscale iron particles for environmental remediation: an overview. *Journal of Nanoparticle Research*, 323–332. Retrieved from http://link.springer.com/article/10.1023/A:1025520116015

Zhang, X., Niu, Y., Meng, X., Li, Y., & Zhao, J. (2013). Evolution and characteristics of the phase transformations between α-Fe2O3, Fe3O4 and γ-Fe2O3 nanoparticles under reducing and oxidizing atmospheres. *CrystEngComm*, *15*, 8166–8172. Retrieved from http://pubs.rsc.org/EN/content/articlehtml/2013/ce/c3ce41269e

Zhao, H., Zhu, Q., Gao, Y., Zhai, P., & Ma, D. (2013). Iron oxide nanoparticles supported on pyrolytic graphene oxide as model catalysts for Fischer Tropsch synthesis. *Applied Catalysis A: General*, *456*, 233–239. doi:10.1016/j.apcata.2013.03.006

Zhou, J., Wang, L., Qiao, X., Binks, B. P., & Sun, K. (2012). Pickering emulsions stabilized by surface-modified Fe3O4 nanoparticles. *Journal of Colloid and Interface Science*, *367*(1), 213–24. doi:10.1016/j.jcis.2011.11.001

Zinoviadou, K. G., Moschakis, T., Kiosseoglou, V., & Biliaderis, C. G. (2011). Impact of emulsifier-polysaccharide interactions on the stability and rheology of stabilised oil-in-water emulsions. *Procedia Food Science*, *1*(Icef 11), 57–61. doi:10.1016/j.profoo.2011.09.010

Zou, S., Yang, Y., Liu, H., & Wang, C. (2013). Synergistic stabilization and tunable structures of Pickering high internal phase emulsions by nanoparticles and surfactants. *Colloids and Surfaces A: Physicochemical and Engineering Aspects*, *436*, 1–9. doi:10.1016/j.colsurfa.2013.06.013

Appendix 1

A1. Correcting UV-Vis data to obtain nanoparticle precipitation curves

Step 1: Retrieve vapor liquid equilibrium data (VLE) *(pressure vs liquid fraction of solvent)* from Aspen at the temperatures employed. Peng-Robinson equation of state (PR-EOS) is applicable for most straight chain alkane solvent. For branched chain alkanes and other solvent molecules, experimental studies or more complex equations of state may be required.

Step 2: Using a curve fitting technique (spline fitting used here) extend the obtained VLE data to the system pressures under investigation.

Step 3: Plot the surface plasmon peak absorbance value against the system pressure to obtain the uncorrected precipitation curve.

Step 4: Assume that 1 mole of solvent is present in the system. ($m_s = 1$)

Step 5: Using molecular weight data for the solvent (M_s) and its density (ρ_s), calculate molar volume of the solvent (V_s) and hence V_s is amount of solvent is present in the system. ($Vs = Ms/\rho_s$)

Step 6: Since at zero pressure 1 mole of solvent is present (assumption), liquid fraction of solvent (X_s) at P=0 is 1. (X_s =1). The remaining values of X_s are obtained from the VLE data.

Step 7: $X_{co2}= (1-X_s)$. X_{co2} is the mole fraction of CO_2 dissolved in the GXL.

Step 8: $m_{co2}= (1/X_s) \times X_{co2.}$ m_{co2} is the moles of CO_2 dissolved in the GXL.

Step 9: If V_{sys} is the volume of the GXL mixture (CO_2 + solvent), at P=0, $V_{sys}=V_s$ since only 1 mole of solvent is present and we assume that no CO_2 is dissolved.

Step 10: At all the other pressure values V_{sys} can be calculate using the following formula

$V_{sys}= V_s + m_{co2} \times M_{co2} \times (1/ \rho_{co2})$, where M_{co2}, ρ_{co2} are the molecular weight and the density of *liquid* CO_2 respectively at the temperatures employed.

Step 11: $\Delta V_{sys}/V_{sys} = (V_{sys@Px} - V_{sys@P0)/} V_{sys,}$ where $V_{sys@Px}$ is the GXL mixture volume at pressure x and $V_{sys@P0}$ is the GXL mixture volume at pressure P=0

Step 12: Using Beer-Lamberts law,

$$\text{Corrected absorbance} = \text{initial uncorrected absorbance} \times (1 + \Delta V_{sys}/V_{sys})$$

Step 13: Normalize the corrected absorbance such that the initial values (lowest P) is 1 and the final value (highest P) is 0, so that it is easier to compare datasets. See example image below in Figure A1.1 to get an idea on how the precipitation curves correction turn out.

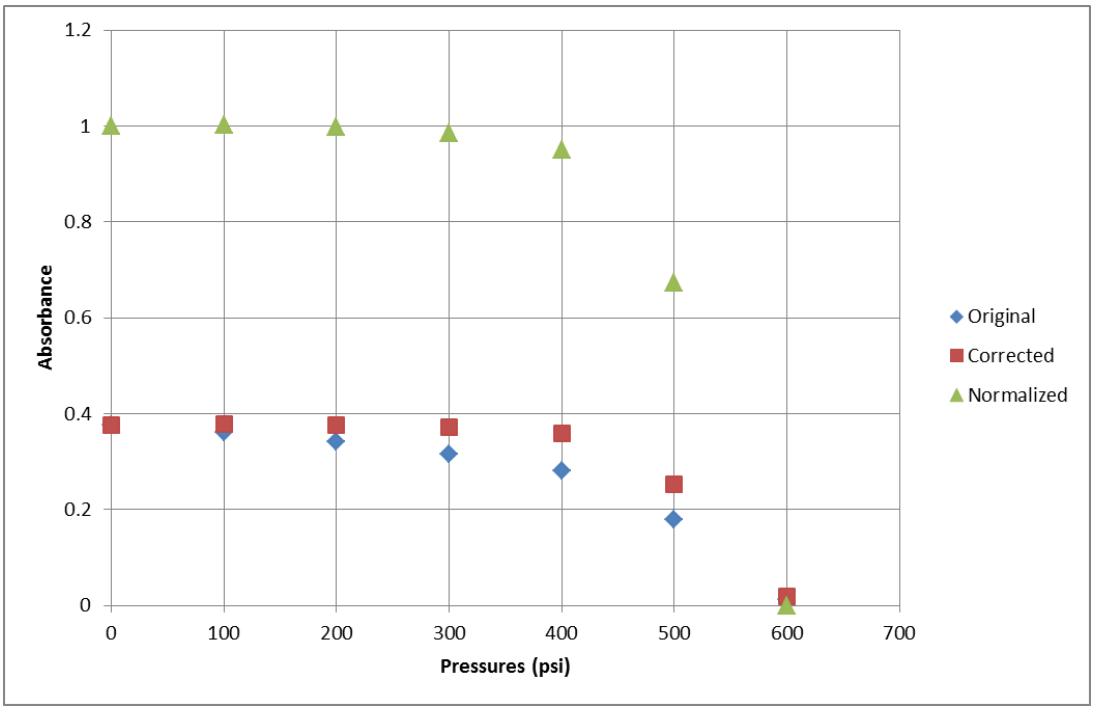

Figure A1.1 Example of the final result from precipitation curve correction and normalization.

Appendix 2

A2. HR-TEM images for dodecanethiol coated gold nanoparticles.

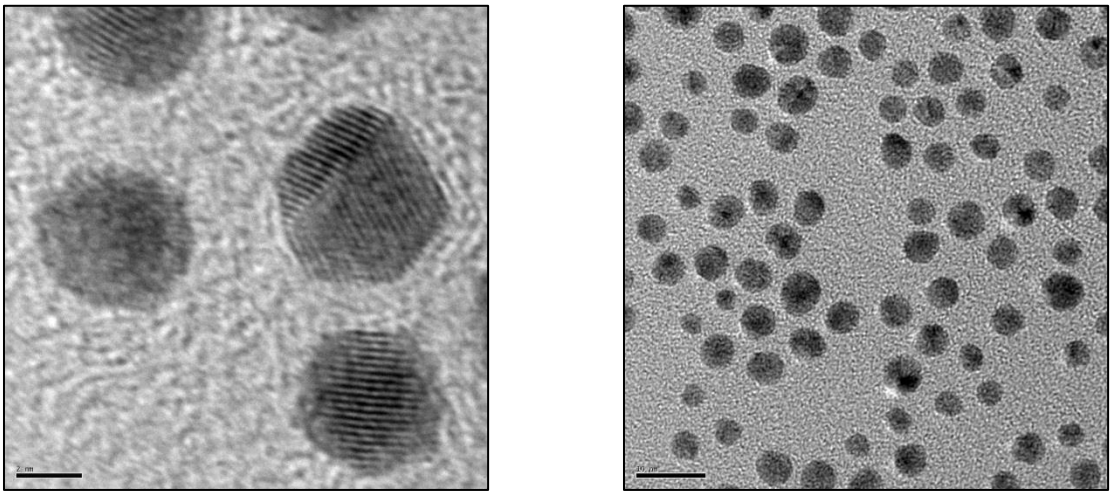

Figure A2.1 High Resolution TEM images of dodecanethiol coated gold nanoparticles. *Left:* at 1.5M X, *Right:* at 300K X

Appendix 3

A3. Calculating liquid holdup, entrainment and packing characteristics in a packed cascaded vessel

Step 1: Calculate surface area and volume of a single packing using its dimensions. Multiply that by the number of packings added to the column to give total surface area of the packings (SA_p) and total volume occupied by the packing material.

Step 2: Total available surface area in contact with the solvent (SA_T) is the total area of packings (SA_p) + area of wall in contact with the solvent (SA_w).

Step 3: (SA_w) = 2 × π × radius of column × length of column in contact with the solvent (L_s).

Step 4: This total surface area could be then compared to the initial surface area of the unpacked column (Where L_s for 20mL of hexane ≈ 7cm)

Step 5: To calculate entrainment, the column was first filled with the packing being investigated. The column along with the packing material was then weighed on a weighing scale to determine the weight of the packed column. The bottom of the column was then sealed using a rubber stopper and 20 mL of hexane was slowly added to the column from the top. After all the hexane was added to the system, the height of the solvent in the system was noted (L_s).

Step 6: The system was then drained of the hexane from the bottom of the column by removing the rubber stopper. The system was then immediately weighed on the scale to determine the increase in system weight caused by entrained solvent. Volume of solvent entrained was then calculated by using the density of the solvent.

Step 7: Calculate all tabulated parameters using the methods described above.

Appendix 4

A4. Additional catalyst characterization results

Table A4.1 TPR results

Catalyst	Stage 1		Stage 2						Peak area ratio*	Degree of Fe_2O_3 reduction (%)
	Temperature (center)	Area	Temperature (center)	Area	Temperature (center)	Area	Temperature (center)	Area		
G10Al	284	1.82	476	8.22	NA	NA	NA	NA	4.52	50.1
G10Si	274	1.92	480	9.68	NA	NA	NA	NA	5.04	51.6
i10Al	355	4.06	487	0.04	602	0.69	782	0.26	0.24	33.8
i10Si	366	3.88	485	2.93	593	3.55	NA	NA	1.67	42.2

Stage 1: the reduction of Fe_2O_3 to Fe_3O_4
Stage 2: the subsequent reduction of Fe_3O_4 to metallic iron
Peak area ratio = area of the peak in stage 1/area of the peaks in stage 2

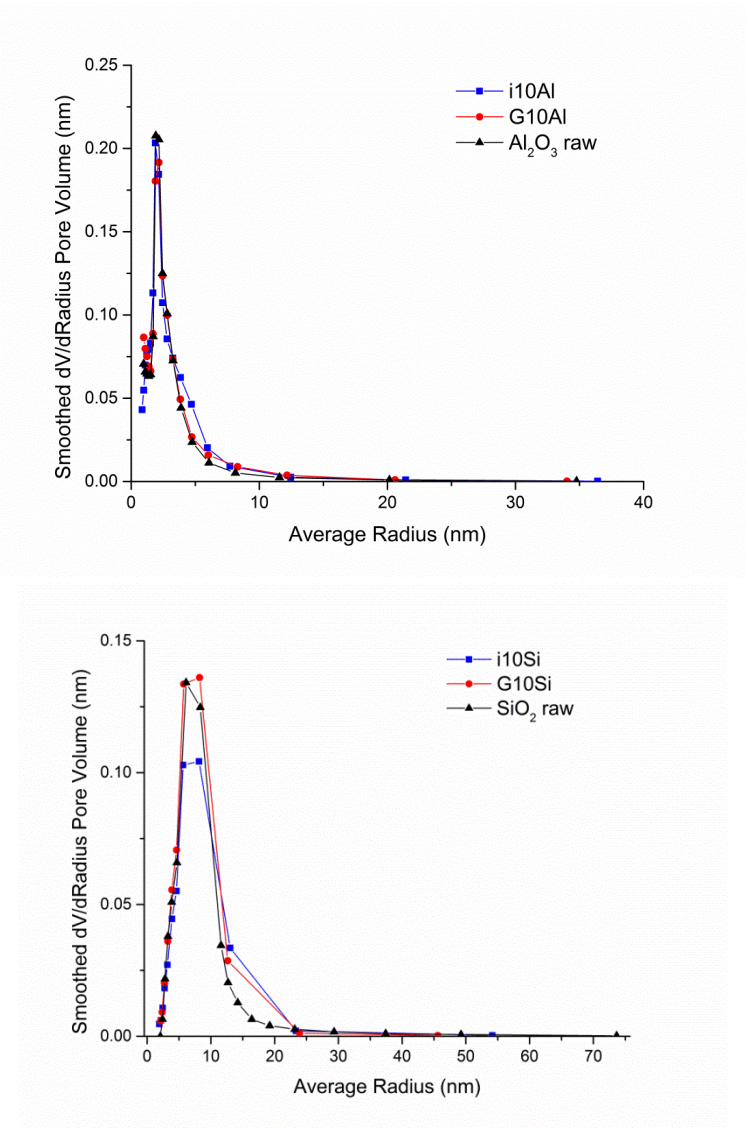

Figure A4.1 Pore size distribution for the raw support materials and four catalysts prepared by GXL and incipient wetness method, calculated from the BJH desorption branch of the isotherm

Appendix 5

A5. List of Publications and Presentations

List of Publications

1. Pranav S. Vengsarkar & Christopher B. Roberts, 'Solid-stabilized emulsion formation using stearoyl lactylate coated iron oxide nanoparticles', *J. Nanoparticle Res.* **2014**, 16, 2627

2. Pranav S. Vengsarkar & Christopher B. Roberts, 'Effect of Ligand and Solvent Structure on Size-Selective Nanoparticle Dispersability and Fractionation in Gas-Expanded Liquid (GXL) Systems', *The Journal of Physical Chemistry C* **2013** 117 (27), 14362-14373

3. Pranav S. Vengsarkar, Rui Xu & Christopher B. Roberts, 'Deposition of iron oxide nanoparticles onto an oxidic support using a gas-expanded liquid process to generate a Fischer-Tropsch catalyst', *Submitted to Applied Catalysis A*

4. Pranav S. Vengsarkar, Rui Xu & Christopher B. Roberts, 'Scalable fractionation of iron oxide nanoparticles using a CO_2 gas-expanded liquid system', S*ubmitted to Nanotechnology*

5. Pranav S. Vengsarkar, & Christopher B. Roberts, 'UV-Vis studies and size-selective precipitation of spherical iron oxide nanoparticles using gas-expanded liquids', *To be submitted to Journal of Nanoparticle Research*

6. Rui Xu, Pranav S. Vengsarkar, & Christopher B. Roberts, 'Fischer Tropsch Synthesis over Supported Nano-Iron Catalysts Synthesized By Gas-Expanded Liquid Deposition Technique', To be s*ubmitted to ACS Catalysis*

7. Vengsarkar, P. S., Boice, J. N., Roberts, C. B.; 'Tunable Steric Stabilization Effects on Size-Selective Nanoparticle Dispersability in Gas Expanded Liquid Systems', *Proceedings of the 10th International Symposium on Supercritical Fluids (ISSF), San Francisco, CA,* **2012***, http://issf2012.com/handouts/documents/133_004.pdf*

8. Boice, J. N., Vengsarkar, P. S., Roberts, C. B.; 'Nanoparticle Dispersability in a DMSO/CO_2-Gas Expanded Liquid System', *Proceedings of the 10th International Symposium on Supercritical Fluids (ISSF), San Francisco, CA,* **2012***, http://issf2012.com/handouts/documents/305_000.pdf*

List of Presentations

1. Vengsarkar, P. S., Xu, Rui & Roberts, C. B..; 'Application-scale size-selective fractionation of iron oxide nanoparticles using CO_2-expanded liquids', *ACS Annual Spring Meeting, Denver, CO, 2015*

2. Vengsarkar, P. S., & Roberts, C. B..; 'Synthesis of stearoyl lactylate coated iron oxide nanoparticles with self-assembled bilayers for use in the formation of solid-stabilized emulsions', *(Poster presentation),Gulf of Mexico: Oil Spill & Ecosystem Conference, Houston, TX, 2015*

3. Vengsarkar, P. S., Xu, Rui & Roberts, C. B..; 'Controlled Deposition of Iron Oxide Nanoparticles Using a Novel Gas-Expanded Liquid (GXL) Process to Generate Supported Fischer-Tropsch Catalysts', *AIChE Annual Meeting, Atlanta, GA, 2014*

4. Xu, Rui, Vengsarkar, P. S., & Roberts, C. B.; 'Fischer Tropsch Synthesis over Supported Nano-Iron Catalysts Synthesized By Gas-Expanded Liquid Deposition Technique', *AIChE Annual Meeting, Atlanta, GA, 2014*

5. Jie Jhong, Vengsarkar, P. S., Roberts, C. B. & Ashurst, W.R; 'Characterization of Gas-Expanded Liquid-Deposited Nanofilms with Size-Controlled Gold and Iron Oxide Nanoparticles', *AIChE Annual Meeting, Atlanta, GA, 2014*

6. Vengsarkar, P. S. & Roberts, C. B.; 'Bilayer coated magnetic nanoparticles for oil spill remediation', *Auburn University Graduate School Fall 2014 3-Minute Thesis Competition, Auburn, AL, 2014*

7. Vengsarkar, P. S. & Roberts, C. B.; 'Gas-expanded liquids (GXLs) in nanoparticle processing and other applications', *Auburn University Department of Chemical Engineering Fall 2014 Seminar , Auburn, AL, 2014*

8. Xu, Rui, Vengsarkar, P. S., & Roberts, C. B.; 'Deposition of iron oxide nanoparticles onto an oxidic support using a gas-expanded liquid (GXL) process to generate Fischer-Tropsch catalyst', *(Poster presentation), Gordon Catalysis Conference, New London, NH, 2014*

9. Vengsarkar, P. S., Xu, Rui & Roberts, C. B.; 'Preparation of a supported Fischer-Tropsch catalyst using a novel Gas-eXpanded Liquid (GXL) process and its application in the generation of Fischer-Tropsch syncrude',*Auburn University*

Research Week, Auburn, AL, 2014 (Outstanding Oral Presentation in Engineering Award)

10. Vengsarkar, P. S. & Roberts, C. B.; 'Synthesis of iron oxide nanoparticles coated with novel surfactant bilayers and their application in stabilizing oil-in-water emulsions', *ACS Spring Meeting, Dallas, TX, 2014*

11. Vengsarkar, P. S. & Roberts, C. B.; 'Pickering Emulsion Formation using Iron Oxide Nanoparticles Stabilized with Novel Surfactant Bilayers', *Gulf of Mexico: Oil Spill & Ecosystem Conference, Mobile, AL, 2014*

12. Vengsarkar, P. S. & Roberts, C. B.; 'Synthesis of Surfactant Bilayer-Coated Iron Oxide Nanoparticles for the Stabilization of Oil-in-Water Emulsions', *AIChE Annual Meeting, San Francisco, CA, 2013*

13. Vengsarkar, P. S. & Roberts, C. B.; 'Augmenting the Size-Selective Fractionation of Metal and Metal Oxide Nanoparticles Using a Modified Gas-Expanded Liquid Process', *(Poster Presentation), AIChE Annual Meeting, San Francisco, CA, 2013*

14. Vengsarkar, P. S. & Roberts, C. B.; 'Enhanced Size-Selective Fractionation of Gold Nanoparticles using a Packed Column based Gas-Expanded Liquid Process', *(Poster Presentation), Auburn University Graduate Engineering Research Showcase, Auburn, AL, 2013*

15. Vengsarkar, P. S. & Roberts, C. B.; 'Investigating the Effects of Nanoparticle Size on Pickering Emulsion Formation and Stability', *(Poster Presentation), Gulf of Mexico: Oil Spill & Ecosystem Conference, New Orleans, LA, 2013*

16. Vengsarkar, P. S., Duggan, J. N., Roberts, C. B.; 'Manipulating Size-Selective Dispersability of Gold Nanoparticles in Gas Expanded Liquid Systems Using Ligand/Solvent Steric Effects', *AIChE Annual Meeting, Pittsburgh, PA, 2012*

17. Vengsarkar, P. S., Duggan, J. N., Roberts, C. B.; 'Tunable Steric Stabilization Effects on Iron Oxide Nanoparticle Dispersability in Gas Expanded Liquid Systems',*(Poster Presentation), AIChE Annual Meeting, Pittsburgh, PA, 2012*

18. Duggan, J. N., Vengsarkar, P. S., Roberts, C. B.; 'Tunable Assembly of Metallic and Magnetic Nanoparticle Clusters in DMSO Solvent Systems', *AIChE Annual Meeting, Pittsburgh, PA, 2012*

19. Duggan, J. N., Vengsarkar, P. S., Roberts, C. B.; 'Exploring the Dispersibility of Gold Nanoparticles in DMSO Using Gas-Expanded Liquid Systems',*(Poster Presentation), AIChE Annual Meeting, Pittsburgh, PA, 2012*

20. Vengsarkar, P. S., Duggan, J. N., Roberts, C. B.; 'Influence of Solvent/Ligand Steric Effects on CO_2 Induced Nanoparticle Precipitation and Size-Selective Fractionation',*(Poster Presentation), Auburn University Graduate Engineering Research Showcase, Auburn, AL, 2012*

21. Duggan, J. N., Vengsarkar, P. S., Roberts, C. B.; 'Dispersibility of Gold Nanoparticles in a DMSO/CO_2 Gas Expanded Liquid System ', *(Poster Presentation), Auburn University Graduate Engineering Research Showcase, Auburn, AL, 2012*

22. Vengsarkar, P. S., Boice, J. N., Roberts, C. B.; 'Tunable Steric Stabilization Effects on Size-Selective Nanoparticle Dispersability in Gas Expanded Liquid Systems', *10^{th} International Symposium on Supercritical Fluids (ISSF), San Francisco, CA, 2012*

23. Boice, J. N., Vengsarkar, P. S., Roberts, C. B.; 'Nanoparticle Dispersibility in a DMSO/CO_2-Gas Expanded Liquid System', *10^{th} International Symposium on Supercritical Fluids (ISSF), San Francisco, CA, 2012*

24. Vengsarkar, P. S., Saunders, S. R., Roberts, C. B.; 'Influence of Solvent Steric Effects on CO_2 induced nanoparticle precipitation', *(Poster Presentation), AIChE Annual Meeting, Pittsburgh, PA, 2011*

25. Vengsarkar, P. S., Saunders, S. R & Roberts, C. B.; 'Control of CO_2 Induced nanoparticle precipitation using Solvent Steric Effects',*(Poster Presentation), Auburn University Graduate Engineering Research Showcase, Auburn, AL, 2011*

26. Vengsarkar, P. S., Saunders, S. R & Roberts, C. B.; 'Size Selective Processing of Metallic Nanoparticles Using Subcritical CO_2',*(Poster Presentation), Auburn University Graduate Scholars Forum, Auburn, AL, 2011*